

**UNIVERSIDADE DE SÃO PAULO
INSTITUTO DE FÍSICA DE SÃO CARLOS**

Willian Massashi Hisano Natori

$j = 3/2$ **Quantum Spin-Orbital Liquids**

São Carlos

2018

Willian Massashi Hisano Natori

$j = 3/2$ Quantum Spin-Orbital Liquids

Thesis presented to the Graduate Program in Physics at the Instituto de Física de São Carlos, Universidade de São Paulo, to obtain the degree of Doctor in Science.

Concentration area: Basic Physics

Advisor: Prof. Dr. Rodrigo Gonçalves Pereira

Corrected Version
(Original version available at the Program Unit)

São Carlos
2018

I AUTHORIZE THE REPRODUCTION AND DISSEMINATION OF TOTAL OR PARTIAL COPIES OF THIS DOCUMENT, BY CONVENCIONAL OR ELECTRONIC MEDIA FOR STUDY OR RESEARCH PURPOSE, SINCE IT IS REFERENCED.

Natori, Willian Massashi Hisano
j = 3/2 Quantum Spin-Orbital Liquids / Willian
Massashi Hisano Natori; advisor Rodrigo Gonçalves Pereira -
revised version -- São Carlos 2018.
178 p.

Thesis (Doctorate - Graduate Program in Física Básica) -
- Instituto de Física de São Carlos, Universidade de São
Paulo - Brasil , 2018.

1. Quantum Spin Orbital Liquids. 2. heavy ion Mott
Insulators. 3. Parton Mean-Field Theory. 4. Variational
Monte Carlo. 5. Resonant Inelastic X-Ray Scattering. I.
Pereira, Rodrigo Gonçalves, advisor. II. Title.

ACKNOWLEDGEMENTS

There are a lot of people to acknowledge for several kinds of contribution for this thesis. Firstly, I thank my supervisor Rodrigo Pereira for the good advices and supervision throughout these years. The questions he proposed and his intuition for interesting physical problems were very useful to obtain the results I present in this thesis. I also thank his patience to discuss even technical details of the calculations, and for his capacity to detect my mistakes. At the same time, his capacity to realize when I have stumbled upon something interesting allowed me to write the articles that form the foundations of this thesis. I finally thank him for pointing out interesting and important problems in strongly correlated systems and allowed me to work with themes that are still under development.

I must also thank the important collaboration of two other professors in Brazil. First, I thank professor Eric Andrade, who performed the Variational Monte Carlo calculations for the quantum spin orbital liquids. This work was not only necessary to complete the studies of these phases, but it also allowed me to dedicate part of my time to study other themes that are part of the thesis, such as the experimental responses of a quantum spin liquid and the derivation of minimal microscopic models. I also thank professor Eduardo Miranda for the proposal of the problems that were investigated here and for supporting me with reference letters more than once.

I also thank professor Maria Daghofer for hosting me in Stuttgart during the year of 2016. This period has shaped the research interests of the second half of this PhD, more focused on microscopic models and experimental probes. Meeting the academic environment in Germany was an extremely important experience for me, and was only possible thanks to her generosity. I extend thanks to people I met in this period and that helped me there at some point (or at least made my stay in Stuttgart more interesting): Daniel Huerga, George Jackeli, Hans-Rainer Trebin, Jan Lotze, Jonas Heverhagen, Judit Romhányi, Michael Schmid, Mirco Marahrens, Pavel Anisimov, Ralph Hübner, Stephan Humeniuk, Teresa Feldmaier, and Ulrike Mergenthaler. Danke sehr!

Concerning Brazilian institutions, I thank the IFSC community for allowing me to study here throughout these five years. Thank you for keeping an organized environment that helped me learning the necessary skills for research and getting the necessary books and articles to complete it. To finish the academic acknowledgements, I thank Fapesp for its grant that allowed me to complete this work.

I would also extend the acknowledgements to my family for all the support throughout these years. In special, I would like to thank my father, for his help in certain credit card transactions, and my brother, for being a good roommate and for giving me free rides to the bus

station.

Finally, I would like to give thanks to God and to the Seventh-Day Adventist communities in São Carlos and Stuttgart. As stated by the book of Ecclesiastes, there are infinitely many books one can read, because the number of themes that we can dedicate our thoughts are also infinite. If this causes frustration in relation to the finitude of life and our steady state of ignorance, this is also a testimony of the number of things that can give us a sense of awe about this world. I am grateful to add one more book about the complexity of phenomena observed even in the simplest things that exist.

*“Of making many books there is no end; and much study is a weariness of the flesh
Let us hear the conclusion of the whole matter: Fear God,
and keep his commandments: for this is the whole duty of man.”
Ecclesiastes 12:12,13*

ABSTRACT

NATORI, W. $j = 3/2$ **Quantum Spin-Orbital Liquids**. 2018. 178p. Thesis (Doctor in Science) - Instituto de Física de São Carlos, Universidade de São Paulo, São Carlos, 2018.

Quantum spin liquids (QSLs) are strongly correlated systems displaying fascinating phenomena like long-range entanglement and fractionalized excitations. The research on these states has since its beginning followed trends generated by the synthesis of new compounds and the construction of new theoretical tools. In coherence with this history, a manifold of new results about QSLs were established during the past decade due to studies on the integrable Kitaev model on the honeycomb lattice. This $j = 1/2$ model displays bond-dependent and anisotropic exchanges that are essential to stabilize its QSL ground state with Majorana fermion excitations and emergent Z_2 gauge field. Even more interestingly, this model is relevant to understand the magnetism of a certain class of $4/5d^5$ Mott insulators with specific lattice constraints, t_{2g} orbital degeneracy and strong spin-orbit coupling (SOC). This mechanism defining these so-called Kitaev materials can be applied to similar compounds based on transition metal ions in different electronic configurations. In this thesis, I investigate minimal models for two types of $4/5d^1$ Mott insulators: the ones on the ordered double perovskite structure (ODP) and the ones isostructural to the Kitaev materials. Their effective models generically show bond-dependent and anisotropic interactions involving multipoles of an effective $j = 3/2$ angular momentum. Such degrees of freedom are conveniently written in terms of pseudospin s and pseudo-orbital τ operators resembling spin and orbital operators of Kugel-Khomskii models with twofold orbital degeneracy. Despite their anisotropy, the two realistic models display continuous global symmetries in the limit of vanishing Hund's coupling enhancing quantum fluctuations and possibly stabilizing a QSL phase. Parton mean-field theory was used to propose fermionic QSLs that will be called quantum spin-orbital liquids (QSOLs) due their dependence with s and τ . On ODPs, I studied a chiral QSOL with Majorana fermion excitations and a gapless spectrum characterized by nodal lines along the edges of the Brillouin zone. These nodal lines are topological defects of a non-Abelian Berry connection and the system exhibits dispersing surface states. Several experimental responses of the chiral QSOL within the mean-field approximation are compared with the experimental data available for the spin liquid candidate Ba_2YMoO_6 . Moreover, based on a symmetry analysis, I discuss the operators involved in resonant inelastic X-ray scattering (RIXS) amplitudes for $4/5d^1$ Mott insulators and show that the RIXS cross sections allow one to selectively probe pseudospin and pseudo-orbital degrees of freedom. For the chiral spin-orbital liquid in particular, these cross sections provide information about the spectrum for different flavors of Majorana fermions. The model for materials isostructural to the Kitaev materials has an emergent $SU(4)$ symmetry that is made explicit by means of a Klein transformation on pseudospin degrees of freedom. The model is known to stabilize a QSOL on the honeycomb lattice and instigated the investigation of QSOLs on a generalization of this lattice to three dimensions. Parton mean-field theory was used once again to propose the liquid states, and a

variational Monte Carlo (VMC) method was used to compute the energies of the projected wave functions. The numerical results show that the lowest-energy QSOL corresponds to a zero-flux state with a Fermi surface of four-color fermionic partons. Further VMC computations also revealed that this state is stable against formation of plaquette ordering (tetramerization). The energy of this QSOL is highly competitive even when Hund's coupling induced perturbations are included, as shown by comparison with simple ordered states. Extensions and perspectives for future work are discussed in the end of this thesis.

Keywords: Quantum Spin Orbital Liquids. heavy ion Mott Insulators. Parton Mean-Field Theory. Variational Monte Carlo. Resonant Inelastic X-Ray Scattering.

RESUMO

NATORI, W. **Líquidos spin-orbitais quânticos** $j = 3/2$. 2018. 178p. Tese (Doutor em Ciências) - Instituto de Física de São Carlos, Universidade de São Paulo, São Carlos, 2018.

Líquidos de spin quânticos (QSLs) são sistemas fortemente correlacionados que apresentam fenômenos fascinantes como emaranhamento de longo alcance e excitações fracionárias. A pesquisa a respeito destes estados seguiu tendências geradas pela síntese de novos compostos e construção de novas técnicas teóricas desde seu princípio. Coerentemente com essa história, uma variedade de novos resultados a respeito de líquidos de spin foram estabelecidos na última década graças a estudos feitos sobre o modelo integrável de Kitaev na rede colmeia. Este modelo de spins $j = 1/2$ apresenta interações de troca anisotrópicas e direcionalmente dependentes que são essenciais para estabilizar um estado fundamental do tipo QSL com férmions de Majorana e campo de gauge Z_2 emergente. Ainda mais interessante, este modelo é relevante para se entender o magnetismo de uma certa classe de isolantes de Mott baseados em metais de transição na configuração $4/5d^5$ em redes específicas, degenerescência orbital t_{2g} e acoplamento spin-órbita forte (SOC). Esse mecanismo que define os chamados materiais do tipo Kitaev podem ser aplicados a compostos baseados em metais de transição em configurações eletrônicas diferentes. Nesta tese, eu investigo modelos mínimos para dois tipos de isolantes de Mott do tipo $4/5d^1$: os que se apresentam na estrutura perovskita dupla ordenada (ODP) e os isostruturais aos materiais do tipo Kitaev. Seus modelos efetivos genericamente apresentam interações multipolares anisotrópicas e direcionalmente dependentes de um momento angular efetivo $j = 3/2$. Estes graus de liberdade são convenientemente escritos em termos de operadores de pseudospin s e pseudo-orbital τ semelhantes a operadores de spin e orbital de modelos do tipo Kugel-Khomskii com orbitais duplamente degenerados. Apesar da anisotropia, esses dois modelos realísticos apresentam simetrias globais contínuas no limite de acoplamento de Hund nulo que incrementam flutuações quânticas e possivelmente estabilizam uma fase do tipo QSL. A teoria de campo médio com partons foi usada para propor QSLs fermiônicos que serão chamados de líquidos spin-orbitais quânticos (QSOLs) devido à dependência deles com s e τ . Em ODPs, eu estudei um líquido de spin quiral com excitações do tipo férmion de Majorana e um espectro sem gap caracterizado por linhas nodais ao longo das arestas da zona de Brillouin. Essas linhas nodais são defeitos topológicos de uma conexão de Berry não-abeliana e o sistema apresenta estados de superfície dispersivos. Várias respostas experimentais foram calculadas para o QSOL quiral dentro da aproximação de campo médio e comparadas com os dados experimentais disponíveis para o candidato a líquido de spin Ba_2YMoO_6 . Além disso, baseado em uma análise de simetria, discuto os operadores envolvidos nas amplitudes de espalhamento de raios-x ressonante para isolantes de Mott na configuração $4/5d^1$ e mostro que seções de choque de RIXS permitem estudar seletivamente os graus de liberdade de pseudospins e pseudo-orbitais. Para o caso particular do líquido spin-orbital quiral, essas seções de choque nos fornecem informações sobre

o espectro de diferentes sabores de férmions de Majorana. Esse modelo possui uma simetria $SU(4)$ emergente que é tornada explícita através de uma transformações de Klein nos graus de liberdade de pseudospin. Sabe-se que este modelo estabiliza um QSOL na rede colmeia, o que instigou uma investigação de QSOLs na generalização desta rede em três dimensões. A teoria de campo médio com partons foi usada novamente para propor estes líquidos quânticos, e o método de Monte Carlo Variacional (VMC) foi usado para calcular as energias das funções de onda projetadas. Os resultados numéricos mostraram que o QSOL de menor energia corresponde a um estado de fluxo-zero com superfície de Fermi envolvendo partons fermiônicos de quatro cores. Cálculos adicionais com VMC também demonstraram que este estado é estável à formação de ordem de plaquetas (tetramerização). A energia deste QSOL é altamente competitiva mesmo quando perturbações induzidas pelo acoplamento de Hund são incluídas, o que é mostrado através da comparação com estados ordenados simples. Extensões e perspectivas para trabalhos futuros são discutidas no final desta tese.

Palavras-chave: líquidos spin-orbitais quânticos. Isolantes de Mott baseados em íons pesados. Teoria de Campo Médio com Partons. Método de Monte Carlo Variacional. Espalhamento de Raios-X Inelástico Ressonante.

LIST OF FIGURES

<p>Figure 1 – The concept of Goldstone modes is depicted using a ferromagnetic state as an example. The states $0\rangle$ and $\phi\rangle$ are degenerate ground states connected to each other by a global spin rotation. $\phi(i)\rangle$ is not the ground state but a low-excited state, since it is defined through a slowly varying $\phi(i)$ function. Source: By the author.</p>	35
<p>Figure 2 – (a) Octahedral environment created by negatively charged ions (red spheres) surrounding the transition metal ion (blue sphere). (b) The e_g and t_{2g} orbitals generated out of the lifting of the fivefold degeneracy of the d orbitals by a octahedral crystal field. (c) Superexchange path connecting two neighboring transition metal ions on a square lattice. This is an ideal representation of the CuO_2 planes of high-T_c superconductors. Source: By the author.</p>	40
<p>Figure 3 – (a) VBS state on the square lattice and (b) RVB state as the linear combination of several VBS states. Source: By the author.</p>	41
<p>Figure 4 – Four examples of frustrated lattices (a) the triangular lattice, (b) the kagome lattice, (c) the fcc lattice, and (d) the pyrochlore lattice. Source: By the author.</p>	42
<p>Figure 5 – Scheme of the lifting of degeneracy for d electrons under crystal-field and tetragonal distortion. The electrons of a $3d^9$ fill up these levels in such a way that the valence electrons are given by $d_{x^2-y^2}$ orbitals. Source: By the author.</p>	43
<p>Figure 6 – Representations of QSL <i>Ansätze</i> on the square lattice with real order parameters. Here, $\chi_{ij} > 0$ if the line is full, and $\chi_{ij} < 0$ along dashed lines. Source: By the author.</p>	47
<p>Figure 7 – Representation on the chiral spin liquid state with zero-flux on the square plaquettes and $\pi/2$ flux on the triangular plaquettes. Source: By the author.</p>	49
<p>Figure 8 – Effect of the large spin-orbit coupling in (a) d^1 and (b) d^5 electron systems. Source: Adapted from NATORI; DAGHOFER; PEREIRA. (1)</p>	52
<p>Figure 9 – (a) representation of the honeycomb model. The different color on the links correspond to different Kitaev interactions. (b) The Brillouin zone of the honeycomb lattice. (c) Phase diagram of the Kitaev model in the case $J_x + J_y + J_z = 1$. Source: By the author.</p>	57

Figure 10 – Kmetko-Smith diagram indicating the increasing of localization as a function of the position in the periodic table. Source: COLEMAN. (2)	65
Figure 11 – (a) structure of the rock-salt structure of ordered double perovskite compounds. The B' elements form a fcc lattice. (b) The active orbitals depend upon the overlap of d and p orbitals along the bonds connecting two sites. (c) Representation of active orbitals along a path perpendicular to the z -axis on Kitaev materials. Source: NATORI; DAGHOFER; PEREIRA (1); NATORI; ANDRADE; PEREIRA. (3)	69
Figure 12 – Density profiles of the eigenstates of the spin-orbit coupling Hamiltonian. Source: NATORI; DAGHOFER; PEREIRA. (1)	75
Figure 13 – (a) Eight-point basis for the hyperhoneycomb lattice. The symbols (circle or triangle) display the two sublattices forming the hyperhoneycomb lattice, and shows the points where the rotations on pseudo-orbitals should be applied. The different colors, on the other hand, correspond to the four sublattice division associated with the Klein transformation. (b) The Brillouin zone of the base-centered orthorhombic lattice. Source: NATORI; ANDRADE; PEREIRA. (3)	86
Figure 14 – (Color online) (a) Diagrammatic representation of the most symmetric gauge choices on an elementary tetrahedron. The arrow pointing from site i to site j represents that $\phi_{ij} = +1$ (and $\phi_{ji} = -1$ in the opposite direction). Notice that the two Ansätze are conjugated by time reversal. (b) Representation of the Z_2 fluxes of the ansatz on the fcc lattice. The flux through each face of a green (red) tetrahedron is positive (negative) when the sites are oriented counterclockwise with respect to a normal vector pointing outward. Source: NATORI, DAGHOFER, PEREIRA. (1)	94
Figure 15 – (a) First Brillouin zone of the cubic lattice highlighting the Fermi lines (orange lines). (b) Dispersion for different fermion flavors. Source: NATORI; DAGHOFER; PEREIRA. (1)	97
Figure 16 – Spin-wave spectrum for the two-color ordered states along the high symmetry lines of the (a) hexagonal lattice and (b) the hyperhoneycomb lattice. Source: By the author.	100
Figure 17 – Representation of the stripy order on the honeycomb lattice, which is equivalent to one of the possible two-color ordered states discussed in this section. The blue (red) arrows symbolize $j^z = 3/2$ ($j^z = -3/2$) states. Source: By the author.	102

Figure 18 – Representation of the (a) zero-flux and (b) π -flux states. Each vertex corresponds to a basis point of the hyperhoneycomb lattice as labeled in Fig. 13a. Solid (dashed) lines represent bonds with $\chi_{ij} = +1$ ($\chi_{ij} = -1$).	
Source: NATORI; ANDRADE; PEREIRA. (3)	105
Figure 19 – Mean-field dispersion of fermions in the (a) zero-flux and (b) π -flux states. The dashed line marks the Fermi level at quarter filling. The high symmetry points of the Brillouin zone are specified in Fig. 20. The energy scale in this plot is set by $ \chi_{ij} = 1$.	
Source: NATORI; ANDRADE; PEREIRA. (3)	107
Figure 20 – (a) Brillouin zone of the base-centered orthorhombic lattice. (b) Fermi surface of the zero-flux state. Different colors represent different bands in Eq. (4.57).	
Source: NATORI; ANDRADE; PEREIRA. (3)	107
Figure 21 – VMC ground state energy, per site and in units of J , for the different mean-field states as a function of the inverse of the particle number. The dashed lines are linear extrapolations to the data.	
Source: NATORI; ANDRADE; PEREIRA. (3)	110
Figure 22 – Fig.(a) gives a representation of a fully tetramerized state on the hyperhoneycomb lattice in real space, where the magenta bonds indicate the localization of the tetramers. Figures (b), (c) and (d) give the dispersion relations for different values of ϵ and t and show how they induce gap opening. The ϵ parameter also induces the breaking of particle-hole symmetry.	
Source: NATORI; ANDRADE; PEREIRA (3)	112
Figure 23 – Energy per site calculated with VMC as a function of the tetramerization order parameter (Eq. (4.74)). The number of sites is $N = 8L^3$, where L is given by the inset. The minimum of the energy was found at $r = 0$, which shows that the zero-flux QSOL is stable against tetramerization.	
Source: By the author.	112
Figure 24 – Energy of the stripy order and the QSOLs based on complex fermions as a function of the parameter $\eta = J_H/U$ for the Hamiltonian given by Eq. (3.68). The stripy order energy was calculated using LFWT, while the QSOL energy is determined with VMC.	
Source: By the author.	113
Figure 25 – (a) Absolute value of the order parameters of the chiral spin-orbital liquid as a function of temperature. (b) Magnetic specific heat per site calculated within the mean-field theory.	
Source: NATORI; DAGHOFER; PEREIRA. (1)	119
Figure 26 – Spin lattice relaxation rate of the chiral spin liquid state as a function of the temperature.	
Source: NATORI; DAGHOFER; PEREIRA. (1)	125

Figure 27 – (a) First Brillouin zone of the fcc lattice. (b) Dynamical structure factor (in arbitrary units) probed by inelastic neutron scattering. (c) Result after integration over $1.5\text{\AA}^{-1} < Q < 1.8\text{\AA}^{-1}$.	
Source: NATORI; DAGHOFER; PEREIRA (1)	126
Figure 28 – Schematic diagram of a RIXS experiment at the L_2 edge, featuring specifically the possibility of pseudo-orbital flip. The absorbed photon creates a core $2p$ hole, which is subject to strong spin-orbit coupling. This highly unstable state decays before a d electron can tunnel to or from the ion, generating a spin-orbital excitation and an emitted photon.	
Source: NATORI; DAGHOFER; PEREIRA. (1)	132
Figure 29 – RIXS cross section (in arbitrary units) probing (a) s , (b) $s\tau_y$, (c) τ_x and (d) τ_z operators along the high symmetry directions of the Brillouin zone of the fcc lattice.	
Source: NATORI; DAGHOFER; PEREIRA. (1)	133
Figure 30 – Axes of symmetry of a cube related to the O symmetry group.	
Source: By the author	157
Figure 31 – Spectrum of the chiral spin-orbital liquid Ansatz for double perovskites in a slab geometry with open boundary conditions in the (111) direction. The surface states are indicated by the thick red lines in the middle of the gap between the M and K points.	
Source: NATORI; ANDRADE; MIRANDA; PEREIRA (4)	170

LIST OF TABLES

Table 1 – Operators describing active multipoles within a cubic Γ_8 quartet. Bars over functions of \mathbf{J} indicate the symmetrization with respect to all the possible permutations of the indices, e.g., $\overline{j_x j_y^2} = j_x j_y^2 + j_y j_x j_y + j_y^2 j_x$. The operators $\tau^{xy}, \tau^{yz}, \tau^{zx}, \bar{\tau}^{xy}, \bar{\tau}^{yz}, \bar{\tau}^{zx}$ are explicitly given in Eq. (3.46)	77
Table 2 – Table containing the number of Kitaev bonds on the elementary plaquettes of the three-dimensional generalizations of the honeycomb lattice	84
Table 3 – VMC ground state energy, per site, for the different mean-field states.	109
Table 4 – Character Table of the O group	158
Table 5 – Klein four-group multiplication rules.	161
Table 6 – Coefficients of the scattering operators in Eq. G.4 as a function of the angle parameter φ . The columns with the cubic limit values are obtained by taking $\varphi = \arcsin(1/\sqrt{3})$	178

LIST OF ABBREVIATIONS AND ACRONYMS

BCS	Bardeen-Cooper-Schrieffer
BZ	Brillouin zone
DSF	Dynamic Structure Factor
FRG	Functional Renormalization Group
GMM	Gamma Matrix Model
HPT	Holstein-Primakoff Transformation
IGG	Invariant Gauge Group
INS	Inelastic Neutron Scattering
iPEPS	infinite Projected Entangled Pair States
LFWT	Linear Flavor Wave Theory
LSMA	Lieb-Schultz-Mattis-Affleck
MFT	Mean Field Theory
NMR	Nuclear Magnetic Resonance
pf-FRG	Pseudofermion Functional Renormalization Group
PSG	Projective Symmetry Group
QSL	Quantum Spin Liquid
QSOL	Quantum Spin Orbital Liquid
RVB	Resonant Valence Bond
RIXS	Resonant Inelastic X-Ray Scattering
SOC	Spin-Orbit Coupling
SSB	Spontaneous Symmetry Breaking
VBS	Valence Bond Solid
VMC	Variational Monte Carlo

LIST OF SYMBOLS

σ^a	Pauli Matrices
Γ^a	Gamma Matrices
U	Hubbard-U parameter
J_H	Hund's coupling
η	ratio J_H/U
Θ	time-reversal operator

CONTENTS

1	INTRODUCTION	25
2	HISTORICAL AND CONCEPTUAL BACKGROUND FOR QUANTUM SPIN LIQUIDS	31
2.1	The Landau's paradigm of phase transition	32
2.2	Historical Development of Quantum Spin Liquids	36
2.2.1	Modeling Mott insulators	37
2.2.2	First wave of Quantum Spin Liquids: Mott insulators in frustrated lattices	41
2.2.3	Second wave: high- T_c superconductors and fractionalization	43
2.2.4	Third wave: exactly solvable models and implementation in heavy transition metal ion Mott insulators	50
2.2.4.1	Spin-Orbital Physics in Real Compounds	50
2.2.4.2	Kitaev Model exact solution	55
2.3	Defining Quantum Spin Liquids	58
3	QUANTUM COMPASS MODELS IN TRANSITION METAL OXIDES	63
3.1	Qualitative Discussion of the $j = 3/2$ Spin-Orbital Models	63
3.2	Kugel-Khomskii model for t_{2g} degenerate systems	65
3.2.1	General Formulas for the Derivation of t_{2g} Kugel-Khomskii models in d^1 systems	65
3.2.2	Effective Kugel-Khomskii Model on the fcc lattice	68
3.2.2.1	Ordered Double Perovskites	68
3.2.2.2	Effective Kugel-Khomskii Model of ordered double perovskites	69
3.2.3	Effective Kugel-Khomskii Model on generalized honeycomb lattices	71
3.3	Strong Spin-Orbit Coupling in Transition Metal Ions	74
3.3.1	Degrees of Freedom in the Strong Spin-Orbit Coupling Limit	74
3.3.2	Symmetry analysis of the multipole operators	76
3.3.3	Double perovskite model in the strong spin-orbit coupling limit	78
3.3.4	Generalized Honeycomb Models in the strong spin-orbit coupling limit	81
3.3.4.1	The hyperhoneycomb lattice	84
3.4	Heuristic Argument in favor of a $j = 3/2$ Quantum Spin Orbital Liquid	86
4	PARTON THEORIES TO QUANTUM SPIN LIQUIDS	89
4.1	Parton Constructions	89
4.1.1	Complex Fermions	90

4.1.2	Majorana Fermions	90
4.2	Parton Mean Field Theory	91
4.2.1	Mean-Field Theory of the Chiral Spin-Orbital Liquid with Nodal Lines	91
4.2.2	Spin-Orbital Liquids on the Hyperhoneycomb Lattices	98
4.2.2.1	Linear Flavor Wave Theory	98
4.2.2.2	Parton Mean Field Theory	103
4.2.3	Variational Monte Carlo Study of the SU(4)-symmetric Spin-Orbital Liquids	106
5	EXPERIMENTAL PROBES TO QUANTUM SPIN LIQUIDS	115
5.1	Experimental responses of the chiral QSOL to well-established probes	117
5.1.1	Specific Heat	117
5.1.2	Magnetic Susceptibility	121
5.1.3	Nuclear Magnetic Resonance	123
5.1.4	Inelastic Neutron Scattering	126
5.2	Resonant Inelastic X-Ray Scattering	128
5.2.1	Derivation and symmetry analysis of RIXS scattering operators	129
5.2.2	L-edge RIXS cross section of the chiral spin-orbital liquid	132
6	CONCLUSIONS AND OUTLOOK	137
	BIBLIOGRAPHY	143
	APPENDIX	155
	APPENDIX A – ANALYSIS OF THE MULTIPOLE OPERATORS UNDER O_h OPERATIONS	157
	APPENDIX B – KLEIN TRANSFORMATIONS	161
	APPENDIX C – PSEUDOSPIN AND PSEUDO-ORBITAL OPERATORS IN TERMS OF SU(4) GENERATORS	165
	APPENDIX D – SYMMETRY AND TOPOLOGICAL PROPERTIES OF THE CHIRAL SPIN-ORBITAL LIQUID WITH NODAL LINES	167
	APPENDIX E – VARIATIONAL MONTE CARLO CALCULATION OF THE CHIRAL SPIN-ORBITAL LIQUID	171

APPENDIX F – COMPUTATION OF PARTON MEAN-FIELD CORRELATION FUNCTIONS	173
APPENDIX G – RIXS SCATTERING OPERATORS UNDER TETRAGONAL DISTORTION	177

1 INTRODUCTION

Emergent phenomena have been highly discussed in the sciences and the Philosophy of Science for their relevance in fields like chemistry, sociology, psychology, biology, and physics. (5) Emergentism is often contrasted with reductionism. Broadly speaking, reductionists claim that everything can be *reduced to* the fundamental constituents of the world. Emergentists reject this assertion and affirm that, as these fundamental constituents assemble, they develop novel entities, properties and laws, as well as patterns of collective behavior that are non-reducible. Such a brief characterization of the debate leaves room for a lot of equivocation. Scientists, and philosophers alike, generally diverge on the meaning of *reducing* something to its smallest parts, and the criterion to affirm that something is non-reducible is sometimes loosely stated.

One way to reduce the ambiguity of the debate is to state whether one considers reductionism and emergentism as ontological or epistemological constructs. Narrowing to Physics, this distinction can be used to talk about reductionism and emergentism not as contradictory, but complementary concepts. A physicist can assert that every aspect of the physical reality is composed of fundamental constituents like elementary particles or strings that interact with each other, i.e., a reductionist ontology. But without contradicting this statement, he can also affirm an epistemological emergentism, in the sense that (i) one is unable to reconstruct the laws governing a many-particle system from the knowledge of the equations of motion of their constituents, (ii) emergent phenomena is sometimes needed to gain some understanding of the properties of the fundamental constituents, and (iii) certain properties and phenomena cannot be well-defined in finite systems, but only in the limit of infinite number of constituents, and yet they describe experimental results. (6–9) Although this pragmatic view does not exhaust the debates between emergentists and reductionists, it does avoid internal contradictions and it uses the terms in a meaningful way. Such view of emergence and reduction will be presupposed throughout this thesis.

This thesis is devoted to study a topic that gains insights both from the reductionist and emergentist perspective: the proposal of quantum spin liquids (QSLs) ground states in solid state platforms. A QSL is an elusive phase in the context of quantum magnetism that is still not confirmed experimentally. In the emergent viewpoint, QSLs present a plethora of emergent phenomena such as fractional excitations, emergent gauge fields and topological order. (10, 11) In the reductionist perspective, the search for QSLs has followed trends in the synthesis of Mott insulators since their proposal (12) and their theoretical modeling was always dependent upon the (reductionist) knowledge of the microscopic physics of these compounds. A similar interplay between reduction and emergence can be observed in the field of topological phases of matter. The topological invariants characterizing these states are only well-defined for many-body systems and depend on global (not local) structures of a real space or momentum space

manifold. (13–15) However, the history of this field in the last decade is closely related with the synthesis of weakly correlated materials composed by ions with strong spin-orbit coupling. Like in the case of the QSLs, the analysis of the microscopic physics guided the synthesis of compounds characterized by emergent phenomena defying the canonical understanding of matter.

The key importance of strong spin-orbit coupling (SOC) connects these two branches of research, although such importance appears in different ways. In Mott insulators, a strong SOC induces anisotropic and bond-dependent exchange interactions between (pseudo)spin degrees of freedom. The phase diagrams of these models differ radically from the one obtained for the isotropic Heisenberg model on the same lattice, and often include the possibility of QSL states. The so-called Kitaev materials constitute the most important examples of compounds with this behavior. (16–18) They were first proposed in a seminal paper from Jackeli and Khaliullin (19), which demonstrated that Mott insulators based on heavy $4d^5$ or $5d^5$ ions forming some specific lattices would implement the integrable Kitaev model. (20) This $j = 1/2$ model is described by Ising-like couplings in different quantization axis according to the bond direction. A simple spin representation can be used to integrate the model and prove that its ground state is a Majorana fermion QSL interacting with a static Z_2 emergent gauge field. (20, 21) On the other hand, SOC was also found to be essential to the emergence of the first examples of topological phases of matter akin to the quantum spin Hall effect. In this class of materials, SOC promotes a band inversion of states of different symmetry (22–25) that indicates a phase transition between trivial and nontrivial topological states.

Although the Physics of $4/5d^5$ Mott insulators has been deservedly more explored due to the combination of simplicity and theoretical relevance of the Kitaev model, there is no lack of interesting physical phenomena emerging in $4/5d$ systems in other electronic configurations. (26) Many such examples are found in compounds presenting the double perovskite structure with stoichiometric formula $A_2BB'O_6$. (27) Interesting compounds to study exotic emergent magnetic phases are found in double perovskites in which A is an alkali ion, B is a nonmagnetic ion, and B' is a heavy transition metal the $4/5d^n$ configuration. The effective angular moments J varies according to the electronic configuration number n , the crystal-field environment, the spin-orbit coupling, and the Hund's coupling. (28) Both the Kitaev materials and the double perovskites display an octahedral environment that energetically favors the t_{2g} orbitals. In contrast to what happens to the e_g orbitals, the projection of the angular momentum operator \mathbf{L} over the t_{2g} manifold leads to an $l = 1$ effective angular momentum \mathbf{l} . The $4/5d^n$ species are heavy transition metal ions and display significant spin-orbit coupling. In the limiting case, only the physics of the lowest energy manifold obtained from the SOC involving electronic spins and t_{2g} orbitals can be considered. The $4/5d^5$ is the simplest case in these circumstances: the local degrees of freedom can be thought as single holes occupying a $j = 1/2$ state. The $4/5d^1$ case constitutes the simplest example after that, in which the local physics is described by a single electron within a $j = 3/2$ manifold. (29)

The first detailed study of the effective model describing double perovskites with $4/5d^1$ magnetic ion was performed by Ref. (29) The derivation of the effective spin-orbital model studied in this article follows closely the methodology developed by Jackeli and Khaliullin in their proposal of the Kitaev materials. The effective model displays direction-dependent and anisotropic interactions in analogy to the Kitaev model. However, the interactions does not happen between the quantization axis of the effective angular j , i.e., the dipoles of j . The total Hamiltonian is rather expressed in terms of interactions between multipoles of $j = 3/2$. A variational mean-field theory was performed over the model and explained the stability of some exotic phases observed in some double perovskites (30–38) in a much more satisfactorily way than the isotropic Heisenberg models.

Ref. (29) also showed that certain regions of the phase diagram were dominated by quantum fluctuations, implying that good quantum spin liquid candidates could be found among this class of compounds. Inspection showed that the quantum fluctuations were maximized at a special case in which the model displays an SU(2) global symmetry. In accordance with these theoretical results, the ordered double perovskite Ba_2YMoO_6 displayed no measured crystal distortion and absence of any magnetic order down to temperatures of 2K (much lower than its Curie-Weiss temperature ranging between -91K and -160K). (30–33) Preliminary studies of valence bond solids and fermionic quantum spin liquids were already performed on the spin-orbital model in Ref. (29), but there was much room for improvement.

More recently, QSLs were also proposed on compounds isostructural to the Kitaev materials by the replacement of the d^5 by d^1 species. (3, 39) The Jackeli-Khaliullin mechanism leads to a Hamiltonian displaying the same bond-dependence of the interactions that is observed on the Kitaev model, and the complicated interactions between $j = 3/2$ multipoles that appear in the double perovskite spin-orbital model. But in the limit of vanishing Hund's coupling, this model displays an emergent SU(4) symmetry. Previous studies of this highly symmetrical model showed that its ground state is dominated by quantum fluctuations (40), and in some cases is most likely to host a quantum spin liquid. (41–43) The compound $\alpha\text{-ZrCl}_3$, in which the Zr ions form a honeycomb lattice, is an example of material that can be described through this model and is thus a spin liquid candidate. (39) Similar compounds were proposed to be synthesized in metal-organic frameworks. (39)

This thesis is devoted to study the modeling, proposal, and experimental verification of $j = 3/2$ quantum spin liquids on $4/5d^1$ Mott insulators. In Chapter 2 I give a conceptual and historical background to QSLs. The first difficulty to study quantum spin liquids is that this concept has evolved over time and was formulated in different ways by different authors. There are several lines of study on QSLs and it is not possible to cover all of them coherently within this thesis. I chose then to start with a historical background organized in terms of epochs inaugurated by certain benchmarks and a selection of subsequent works connected with these benchmarks. I restricted the papers to subjects related with my original contributions discussed

in the subsequent chapters. After this background, I make a synthesis of the accepted QSL definition and how these phases are studied on practice.

My original results are presented and discussed in chapters 3, 4 and 5. Chapter 3 starts with a presentation of the local physics of $4/5d^1$ Mott insulators. One result of this doctoral work was the development of $s = 1/2$ pseudospin s and pseudo-orbital τ operators that faithfully describe the physics inside the $j = 3/2$ manifold. (1, 4) After developing the necessary technology to understand the electronic degrees of freedom, the chapter gives a general algorithm to derive effective models for the studied compounds. These models resemble the Kugel-Khomskii models that describe the physics of Mott insulators retaining twofold orbital degeneracy. (44, 45) The QSLs proposed on these effective models will be then called *quantum spin-orbital liquids* (QSOLs). The derivation of spin-orbital models on the ordered double perovskite and Kitaev material structures will serve as concrete examples of how the algorithm can be applied. This chapter ends by giving the arguments in favor of possible QSL ground state in these models. Chapter 4 main goal is to propose specific fermionic QSOLs and study their mean field dispersion and the energetics after a projection to the physical Hilbert space. This so-called Gutzwiller projection is implemented using the Variational Monte Carlo (VMC) technique. (46) The VMC calculations were implemented by prof. Eric Andrade of the Institute of Physics of Sao Carlos, and were included for completeness. Finally, in Chapter 5 I provide the response functions of the QSOL proposed for ordered double perovskites and compare the theory with the experimental data available for the spin liquid candidate Ba_2YMoO_6 . (30–33) Since there were still no experimental results available for the compounds isostructural to the Kitaev materials, the analysis of the proposed QSOL was left for future work.

Particularly important, in Chapter 5 I derive the L -edge resonant inelastic x-ray scattering (RIXS) operators for $4/5d^1$ compounds retaining the cubic symmetry using the fast-collision approximation. RIXS is a promising tool to analyze strongly correlated systems as a complementary tool to inelastic neutron scattering (INS). (47–52) One of the RIXS potential strength is the possibility to probe different electronic degrees of freedom by adjusting the photon polarization. This feature is at the same time a weakness, since the control of the photon final polarization is normally unattainable in actual experiments and it leads to a very complex theoretical modeling. Aided by symmetry principles (47, 51) I demonstrate that RIXS can directly probe the pseudospin and pseudo-orbital operators (s, τ), whereas INS probes only the total angular momentum \mathbf{j} . This is an important distinction for the proposed QSOL, since it displays an $\text{SU}(2)$ symmetry on s rotations, but not on \mathbf{j} . Such distinction leads to qualitatively different responses of these two spectroscopic techniques and gives an example of how RIXS can provide experimental information about QSOLs that are inaccessible to INS.

Chapter 6 summarizes the results and gives my conclusions regarding this work. Overall, this thesis shows how $4/5d^1$ Mott insulators can be modeled and how possible QSOL ground states in this compounds are investigated, both theoretically and experimentally. I close the thesis

with open questions and promising extensions of the present work.

2 HISTORICAL AND CONCEPTUAL BACKGROUND FOR QUANTUM SPIN LIQUIDS

Quantum spin liquid is an almost fifty-year-old concept (12) whose accepted definition and experimental motivations changed over time. The first challenge to study this phase is, oddly enough, to give a proper QSL definition encompassing the different contexts in which this phase was proposed. For example, one common definition for QSL is that of a magnetic insulator that does not order down to zero temperature due to strong quantum fluctuations. (10) But as emphasized by Ref. (10) itself, since this definition focus on what a QSL is *not*, one cannot propose a smoking-gun experiment to confirm a QSL state. A more positive definition of QSL was given in Ref. (11) and conceives QSLs as long-range entangled states in the context of magnetism. This definition and its connection to the more usual view of QSL will be discussed by the end of this chapter in Section 2.3.

This chapter introduces recurring themes appearing in the original results of this thesis. Section 2.1 gives a brief account of the Landau's theory of phase transitions that grounded the paradigmatic understanding of phases in Condensed Matter during most of the 20th century. Although the present work is mostly concerned with phases lying outside this paradigm, some of the concepts developed here will still be used. For example, the notion of QSL as a disordered state is indeed incomplete, but absence of magnetic order can still be a good indicator of a QSL ground state. A method to argue in favor of a QSL ground state of a model is then to prove that ordered states are energetically uncompetitive or unstable using spin-wave analysis (and their extensions). This methodology will be applied in the next chapters. The specific heat analysis of the QSL defined on double perovskites also utilizes concepts of the Landau theory.

Section 2.2 lists some historical benchmarks of the theory and experiments on quantum spin liquids. It starts with the history of Mott insulators accompanied by the fundamentals of their modeling. I subdivided the search for QSLs in solid state in three periods. They should not be interpreted as rigidly defined periods indicating the start and end of the search of QSLs in a certain type of compound. Nevertheless, the periods point out important developments of studies on spin liquid states. An extended discussion of the honeycomb Kitaev model (20) was given in the middle of this section. The Kitaev model provides a unique strongly correlated model that is integrable (20) with ensured Majorana QSL ground state (21) hosting anyonic excitations, and possible implementations in solid state platforms - the so-called Kitaev materials. (16–18) The Kitaev model and the research in Kitaev materials will be used as a of gold standard to indicate the merits and limitations of our research.

2.1 The Landau's paradigm of phase transition

The spontaneous symmetry breaking (SSB) in many-body systems was one of the Anderson's example of emergent phenomena in his influential 1972 article. (6) A SSB happens whenever the many-particle system transits from a state displaying the full symmetry of the many-body Hamiltonian to another with smaller symmetry. Several divergences on thermodynamical quantities are experimentally observed in the transition point. These divergences are indicatives of singularities in the system free energy, which are only possible when defined on the thermodynamic limit, i.e., taking the limit in which the number of particles goes to infinity. Strictly speaking, SSBs would never be observed in nature. This is in strong contrast to the many instances of symmetry breaking that are specially important in Condensed Matter Physics.

The most elementary SSB example given by Anderson was the formation of regular crystals. In principle, the state of any (non-relativistic) quantum many-body system can be determined by finding the eigenstates and eigenfunctions of the Hamiltonian

$$\begin{aligned}
 H = & -\frac{\hbar^2}{2m} \sum_j \nabla_j^2 - \frac{\hbar^2}{2M} \sum_\alpha \nabla_\alpha^2 \\
 & - \sum_j \sum_\alpha \frac{Z_\alpha e^2}{|\mathbf{r}_j - \mathbf{R}_\alpha|} + \frac{1}{2} \sum_{\alpha \neq \beta} \frac{Z_\alpha Z_\beta e^2}{|\mathbf{R}_\beta - \mathbf{R}_\alpha|} + \frac{1}{2} \sum_{j \neq k} \frac{e^2}{|\mathbf{r}_j - \mathbf{r}_k|}
 \end{aligned} \tag{2.1}$$

where the Greek letters label the nuclei and the Latin letters label the electrons. The first line in Eq. (2.1) refers to the kinetic energy of electrons and nuclei while the second contains the electrostatic potential among all the particles of the system. Eq. (2.1) is extremely general and is invariant under any translation. However, the nuclei of crystals present themselves tightly bound to certain positions in space and form a lattice structure with discrete translation invariance. In other words, crystals spontaneously break the translation symmetry of Eq. (2.1). The concept of SSBs goes beyond this structural example and extends to describe the formation of other patterns in the internal structure of a solid such as the formation of magnetic order or superconductivity.

Landau's theory of phase transition is the most well-developed conceptual framework to understand phase transitions based upon SSBs. The theory assumed that transitions displaying SSBs are not governed by microscopic details and can be studied solely from symmetry principles. Two basic concepts are introduced: the *(local) order parameter* and the *Landau's free energy* Φ . The order parameter spans a representation of the group of symmetry of the most symmetric phase and is used as a quantifier of the phase transition: it is zero in the most symmetric phase, and nonzero after the symmetry breaking. The free energy Φ is defined at the neighborhood of the critical temperature and expressed as a polynomial of the order parameter, in which the coefficients for each order in this polynomial depends on experimentally controllable parameters. Thermodynamical quantities (e.g., specific heat, magnetization, magnetic susceptibility, etc) near criticality are evaluated from Φ in terms of the controllable parameters and the so-called

critical exponents can be evaluated. Landau's theory predicts that very different systems from a microscopical standpoint would display the same critical exponents, provided that the number of spatial dimensions of the systems, and the symmetries of the high-symmetry and low-symmetry phases were coincident. These exponents assemble models with different microscopic physics and form universality classes.

Let us illustrate the concepts of Landau's theory in the simplest spin model: the Ising model on a square lattice

$$H_{\text{Isign}} = J \sum_{\langle ij \rangle} \sigma_i \sigma_j - h \sum_i \sigma_i, \quad (2.2)$$

in which J is the exchange constant, h is an applied magnetic field and σ is a component of the spin in a fixed direction. To simplify the discussion, consider $J < 0$ and $h = 0$. It is clear that the model will display an ordered ground state at zero temperature that is characterized by the alignment of all spins in a fixed orientation, the so-called ferromagnetic state. Notice that this ferromagnetic ground state breaks the $\sigma_i \rightarrow -\sigma_i$ symmetry of the Ising Hamiltonian. Thermal fluctuations destroy this order at high temperatures and the state becomes paramagnetic, which is the high-symmetry state. The order parameter distinguishing the two phases is the magnetization $M = \langle \sigma_i \rangle$, which is zero at the paramagnetic phase and finite for any temperature lower than a critical temperature T_c . Near T_c , the phenomenology of the phase transition can be studied through a Landau free energy given by the following polynomial

$$\Phi(t, M, h) = \Phi_0 + a_2 t M^2 + a_4 M^4 - h M, \quad (2.3)$$

in which Φ_0 , a_2 and a_4 are constants and $t = (T - T_c)/T_c$ is the reduced temperature. The value of the order parameter M is obtained by minimizing the Φ function. Several critical exponents of the theory can be computed in this process. For example, the magnetization vanishes like $M \sim (-t)^\beta = (-t)^{1/2}$ for $T < T_c$ within the mean-field approximation. Besides thermodynamical quantities, the inclusion of fluctuations in this formalism allows the computation of critical exponents related with correlation functions.

There is also one important phenomenon associated with the SSB of continuous symmetries that cannot be discussed using the Ising model. Let us then introduce the Heisenberg model

$$H_{\text{Hei}} = J \sum_{\langle ij \rangle} \left(\mathbf{S}_i \cdot \mathbf{S}_j + \frac{n_i n_j}{4} \right), \quad (2.4)$$

where J is the exchange constant, \mathbf{S}_i is the spin operator at a lattice site i , n_i is the occupation number of the site i and the brackets $\langle \dots \rangle$ indicate that i and j are nearest-neighbor sites. In Mott insulators, the occupation number is fixed; here we consider $n_i = 1$. In contrast to the Ising model, the relevance of all spin axes of quantization makes H_{Hei} a quantum model. Nevertheless, if $J < 0$, we know that the exact ground state is ferromagnetic, e.g., $|0\rangle = \otimes_i |\uparrow_i\rangle$, where $S_i^z |\uparrow_i\rangle = \frac{1}{2} |\uparrow_i\rangle$. This differs from the corresponding Ising model ground state because it present a continuous, not a discrete, degeneracy. Any state $|\phi\rangle$ given by $|\phi\rangle = \exp(i \sum_i \phi \cdot \mathbf{S}_i) |0\rangle$ with

ϕ constant is also a ground state of Eq. (2.4) due to this SU(2) symmetry. In other words, the ground state $|0\rangle$ breaks the continuous SU(2) symmetry of the spins associated with H_{Hei} .

The presence of a continuum of degenerate ground states provides an intuitive picture to understand the presence of gapless excitations in systems breaking continuous symmetries. Since $|0\rangle$ and $|\phi\rangle$ display the same energy, it is possible to evolve the system from one to another without inputting energy. Consider now a state $|\phi(i)\rangle = \exp(i \sum_i \phi(i) \cdot \mathbf{S}_i) |0\rangle$, in which $\phi(i)$ is a real function. The energy difference between $|\phi(i)\rangle$ and $|0\rangle$ must be small if $\phi(i)$ varies slowly (see Fig. 1). This intuition can be formalized in the language of quantum field theory and can be stated as follows: if a Hamiltonian displays a continuous symmetry, either the ground state retains the symmetry, or it will present gapless bosonic excitations. (53) Such excitations are often called *Goldstone modes*.

Interestingly enough, a methodology to study bosonic excitations for spin systems presenting SSB was developed many years before this theorem and constitutes the basis of the spin-wave analysis or linear spin-wave theory. (54) The first step is to represent the spin S operators using the Holstein-Primakoff transformation, which is the following for the ferromagnetic state

$$S_i^z = S - b_i^\dagger b_i, \quad S_i^+ = \sqrt{2S - b_i^\dagger b_i} b_i, \quad S_i^- = b_i \sqrt{2S - b_i^\dagger b_i}, \quad (2.5)$$

where b_i is a boson operator at the site i . Eq. (2.5) is used to rewrite the Heisenberg model as a bosonic Hamiltonian, and the ferromagnetic ordered state $|\psi_{\text{fer}}\rangle$ is the ‘‘vacuum’’ of the theory, i.e., $b_i |\psi_{\text{fer}}\rangle = 0$ for all i . Assuming that $S \gg \langle b_i^\dagger b_i \rangle$ in a self-consistent computation, we pick only the quadratic terms that allows an exact diagonalization. The excitations in this spin-wave analysis disperse in accordance with the lattice symmetry and are called *magnons*. These excitations can be measured through the differential cross section of magnetic inelastic neutron scattering (INS). For a $S = 1/2$ spin system, this cross section is proportional to the dynamic structure factor (DSF) (55)

$$S(\mathbf{q}, \omega) = \frac{1}{N} \sum_{\mathbf{R}_i, \mathbf{R}_j} \sum_{a,b} e^{-i\mathbf{q} \cdot (\mathbf{R}_i - \mathbf{R}_j)} \int_{-\infty}^{\infty} dt e^{i\omega t} \langle 0 | S_i^a(t) S_j^b(0) | 0 \rangle. \quad (2.6)$$

The magnetic interaction of the neutron on the ferromagnetic ground state induces spin flips on the sites i and j and generate the magnons. Only one magnetic mode can be excited by a neutron transferring energy $\hbar\omega$ and momentum \mathbf{q} . The cross sections will then display a sharp peak of the transferred energy for a given value of transferred momenta. This allows the experimental measurement of the magnon dispersion. Other quasi-particles related to magnetic excitations are generally measured with magnetic INS up to today. Further discussions of this topic will be done in more detail in Chapter 5.

Landau’s theory, its extensions and generalizations were so successful in describing phases of matter that led to the question if they could describe all possible phases. One of the first important counter-examples of phase transitions without local order parameter was found

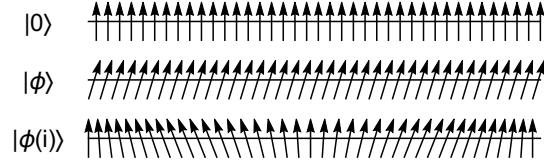


Figure 1 – The concept of Goldstone modes is depicted using a ferromagnetic state as an example. The states $|0\rangle$ and $|\phi\rangle$ are degenerate ground states connected to each other by a global spin rotation. $|\phi(i)\rangle$ is not the ground state but a low-excited state, since it is defined through a slowly varying $\phi(i)$ function.

Source: By the author.

through the Ising lattice gauge theory. (56,57) In contrast to the Ising model, Wegner's lattice theory places the spin variables on the links and defines operators P_i as products of the spins on the links forming lattice plaquettes. More explicitly, on the square lattice

$$\begin{aligned} H_{\text{Wegner}} &= J \sum_i \sigma(i, \hat{x}) \sigma(i + \hat{x}, \hat{y}) \sigma(i + \hat{x} + \hat{y}, -\hat{x}) \sigma(i + \hat{y}, -\hat{y}) \\ &\equiv J \sum_i P_i, \end{aligned} \quad (2.7)$$

in which $\sigma(i, \hat{x})$ is a spin placed between the sites i and $i + \hat{x}$. Consider a fixed site i of the lattice and let us label the links connected to this point by (i, \hat{a}) . A gauge transformation $G(i)$ is defined as follows

$$G(i) : \sigma(i, \hat{a}) \mapsto -\sigma(i, \hat{a}). \quad (2.8)$$

Notice that this transformation changes the sign of two links of the plaquettes containing the site i . Therefore, $G(i)$ leaves the plaquette operators and the whole Hamiltonian invariant.

The spins are not left invariant under gauge transformations, and thus they cannot be used to label the physical states of this theory. This leads to the question of how many states are there in the Hilbert space of H_{Wegner} . Following (58), we consider the instructive case of the action of gauge transformations on a single plaquette. Since there are four links on a square, there are $2^4 = 16$ possible configurations for the σ variables. There are also four sites on a square plaquette with $2^4 = 16$ combinations of gauge transformations (2.8) and identity transformations $E(i) : \sigma(i, \hat{a}) \mapsto \sigma(i, \hat{a})$. Notice that the operations

$$\begin{aligned} e(i) &= E(i)E(i + \hat{x})E(i + \hat{x} + \hat{y})E(i + \hat{y}), \\ g(i) &= G(i)G(i + \hat{x})G(i + \hat{x} + \hat{y})G(i + \hat{y}), \end{aligned} \quad (2.9)$$

leave all spins σ invariant. One can also attribute to the set $\{e(i), g(i)\}$ the structure of a group by defining the composition as the group operation. This is the so called *invariant gauge group* (IGG) of the plaquette. Given a fixed spin configuration, the IGG says that the 16 gauge operations will induce $16/2 = 8$ gauge equivalent configurations. Therefore, there are $16/8 = 2$ different gauge-equivalent classes, each corresponding to a physical state. How can we label the two states of this plaquette? The states must be labeled by a gauge invariant quantity, which turns out to be

the product of spins around the plaquette, i.e., the operator P_i . The physical states correspond to the two possibilities $P_i = \pm 1$. Turning back to the lattice problem, one can show that any product of spins around a closed contour C is also gauge-invariant, and useful to label a physical state. A phase transition of the Hamiltonian (2.7) can be defined by monitoring average values of extended loops inside the lattice. (56,57) Since these loops are not local order parameters, it lies outside the Landau's theory.

I will state some results for the Wegner Z_2 gauge theory on the square lattice for completeness. (58) The IGG in this case will still display two elements corresponding to the application of $E(i)$ or $G(i)$ at every one of the N sites of the lattice. The number of physical states is 2×2^N , but the N plaquettes can label only $2^N/2$ states (since they must satisfy a global constraint). The multiplicative factor 4 is related to the four possible configurations of the two inequivalent *global* loops that cross the whole lattice in the \hat{x} or \hat{y} direction. This has an important consequence when analyzing Eq. (2.7). One could think that there would be a single ground state defined by $P_i = +1$ for a ferromagnetic coupling $J < 0$. However, the ground state is fourfold degenerate and they cannot be distinguished by variables defined only when considering the lattice as a whole. This kind of degeneracy is the so-called *topological degeneracy* and cannot be lifted by local perturbations.

The topological degeneracy is the defining feature of the concept of *topological order*, a form of order that does not display SSB and is not studied with Landau's formalism. This concept was introduced by Wen in the context of chiral spin liquids (59), and is useful to classify other states like the fractional quantum Hall effect, resonant valence bond states, and even superconductors (see discussion of the Chapter 8 in Ref. (60)). A simple example of an integrable quantum model with topological degeneracy and Z_2 gauge fields was developed by Kitaev in 2003 (61) and is called the "toric-code model". Besides topological order, this model is also useful to understand spin fractionalization and anyonic excitations (see the discussion in Ref. (11) for a pedagogical introduction to the model). The topological order is a very important concept to understand spin liquids in general, but since the QSLs studied in this thesis will be all gapless, it will not be further discussed.

2.2 Historical Development of Quantum Spin Liquids

Let us step back to the general many-body Hamiltonian (2.1). It is not possible to find exact solutions to Eq. (2.1) of a system with N electrons and nuclei, where N is of the order of the Avogadro's number, since the dimension of the Hilbert space grows exponentially with N . Hence, if we want to use the knowledge of fundamental quantum mechanics to study everyday matter, we are forced to apply some approximations. A vital part of the work in Theoretical Condensed Matter consists in identifying the dominating physics in a solid state system and of formulating minimal models describing the physics of real compounds at least in a qualitative

correct way.

The band theory of solids was the first successful theory of Condensed Matter Physics and also one of the first successes of Schrödinger's formalism to quantum mechanics. Its first approximation uses the fact that the nuclei are much slower than the electrons, and treat the total wavefunction $|\psi\rangle$ as a direct product of an electronic and a nuclear state. This is the famous Born-Oppenheimer approximation that allows us to first treat the nuclei as immobile charged particles located exactly at lattice points.

The second approximation to formulate band theory is the neglect of repulsion among electrons arising from the Coulomb interaction. The problem of N interacting electrons is then simplified to a problem of finding the N lowest energy eigenstates and energies of a non-interacting Schrödinger equation. The potential acting on the electrons is produced by static nuclei at fixed positions and display the lattice symmetry. The energy levels of this problem can be approximated by continua of energies that can be distinguished from each other either because of their physical origin or because of energy gaps. Each continuum of energies is called a *band*. Band theory was well-succeeded to explain several properties of solids and provided the first framework allowing a good distinction between metals and insulators. A metal would be a solid whose highest occupied energy levels happens to be in the middle of a band. The excitation to an unoccupied energy level would cost no energy and, therefore, the solid would be a good conductor. An insulator is an electronic system whose highest occupied energy levels constitute a filled band and present an energy gap separating this band from the lowest energy band of unoccupied states.

Band theory was challenged already in 1937 by reports of the insulating state of certain d -based transition metal oxides with partially filled valence band. (62) Soon after these experiments, Mott and Peierls proposed that the insulating state of these compounds must be explained by strong electrostatic repulsion between the electrons. (63) Large Coulomb interactions can prevent the electron from moving throughout the lattice and localize it at the neighborhood of an ion. These observations mark the beginning of the field of *strongly correlated systems*. By that time, there were two available frameworks to study solid state physics. The first was band theory, which described well electrons with extended wavefunctions. The second was the Heitler-London approximation, which took the atomic limit as the starting point. In the following decades, Mott had done important works that improved the understanding of correlation-driven insulating compounds. (64–66) Hence, they are now generically called *Mott insulators*.

2.2.1 Modeling Mott insulators

We are now going to describe the ideas to derive effective models describing the electronic behavior of Mott insulators. These models assume the Born-Oppenheimer approximation just like the band theory. What they cannot neglect is the relevance of the inter-electronic interaction,

which must be inserted in this problem. One feature realized in the earliest Mott insulators was that the d atomic orbitals that seemed to dominate the electronic physics were much more localized than the s and p orbitals. The first step to describe a Mott insulator is then to consider electrons localized near the lattice sites of an ideal crystal with lattice parameters greater than the characteristic radius of the d orbitals.

The next approximation is to consider that the interactions between electrons can be replaced by a repulsive potential with spherical symmetry acting only in a small neighborhood of every lattice site. (67) All models presented in this thesis assume the validity of this mean field theory for atoms. This problem is diagonalizable again and its eigenfunctions are orbitals that will be labeled by φ . Radial quantum numbers can still be defined and associated with the number of nodes and energy of the orbital wave functions. Since the symmetry is still spherical, the orbitals are labeled with the same orbital (l) and magnetic (m) quantum numbers of the hydrogen atom. The number l distinguishes between different eigenfunctions of \mathbf{L}^2 , where

$$\mathbf{L} = \mathbf{r} \times \mathbf{p} = -i\hbar \mathbf{r} \times \nabla. \quad (2.10)$$

Relevant electronic phenomena occur only for electrons in the outermost shell. The relevant orbitals for transition metal compounds will always present $l = 2$. These orbitals are five-fold degenerate and these degenerate levels are labeled by $m = -2, -1, \dots, 2$ and correspond to angular distributions of the orbital wavefunctions described by the spherical harmonics $Y_m^2(\theta, \phi)$.

$$\varphi_{(m)}(\mathbf{r}) = R(r)Y_m^2(\theta, \phi) \quad (2.11)$$

The transition metal ion is normally surrounded by six negatively charged ions (e.g., oxygen O^{2-}) in real compounds. The charged ions generate an effective electric field that is often called the *crystal field*. I will be mostly concerned with an ideal case where the negative ions are equidistant from the transition metal and form an octahedral environment with local symmetry given by the O_h group 2a. The crystal field in this case generates an additional term for the orbital Hamiltonian that reads (68)

$$H_{CF} = C \left(x^4 + y^4 + z^4 - \frac{3}{5}r^4 \right), \quad (2.12)$$

where C is a constant determined by the configuration of the surrounding ions. H_{CF} breaks the spherical symmetry of the Coulomb potential and lifts the degeneracy of the d orbitals. An analysis of the orbitals using the character tables of O_h shows the splitting of the five orbitals into a doublet (67–70)

$$\begin{aligned} d_{x^2-y^2} &\propto \frac{\sqrt{3}}{2} \frac{x^2 - y^2}{r^2} \\ d_{3z^2-r^2} &\propto \frac{1}{2} \frac{3z^2 - r^2}{r^2} \end{aligned} \quad (2.13)$$

forming the basis of the E_g irreducible representation (irrep) and a triplet

$$\begin{aligned} d_{xy} &\propto \sqrt{3} \frac{xy}{r}, \\ d_{yz} &\propto \sqrt{3} \frac{yz}{r}, \\ d_{zx} &\propto \sqrt{3} \frac{zx}{r}, \end{aligned} \quad (2.14)$$

forming the basis of the T_{2g} representation. These are generally called e_g and t_{2g} orbitals, respectively (see Fig. 2b). Besides lifting of the degeneracy, the crystal field also causes the (partial) nullification of the effective angular momentum (*quenching*). This is often made intuitive by the observation that the orbitals in Eq. (2.13) and Eq. (2.14) are real (apart from a constant phase factor). (67) The \mathbf{L}_j operator, on the other hand, is purely imaginary (see Eq. (2.10)). Since \mathbf{L}_j is also hermitian, its mean values must take real values. Thus,

$$\langle \mathbf{L}_j \rangle = \int d^3\mathbf{r} \psi_j^*(\mathbf{r}) \mathbf{L}_j \psi_j(\mathbf{r}) = 0, \quad (2.15)$$

where ψ_j is the wavefunction of either an e_g or t_{2g} orbital centered at \mathbf{R}_j . It is important to point out that this argument concerns the average of the \mathbf{L}_j operator for a specific set of wavefunctions. Later in this chapter, the fact that the angular momentum operator is not totally quenched in the manifold of states spanned by the t_{2g} orbitals will be very important.

It was soon realized that Mott insulators had not only anomalous electrical conductivity properties, but also unusual magnetic behavior. There were indications that the magnetic phenomena in Mott insulators could be well-described through studies on the Heisenberg model (Eq. (2.4)). These observations created two problems for theoretical physicists. The first one was to explain why the exchange coupling was normally antiferromagnetic ($J > 0$). The second was to explain how it could occur considering the large distance between the magnetic ions and the localized nature of their orbitals. The latter problem motivated Anderson to develop a theory of *superexchange* to explain the antiferromagnetism. (71) Consider for example a transition metal oxide whose electrons are solely in the $d_{x^2-y^2}$ orbital (see Eq. 2.13). The d orbital hybridizes with the p orbitals of the oxygen ions surrounding it (see Fig. 2c). The absence of electric conductivity means that the electrons do not move throughout the lattice. Nevertheless, the orbital hybridization allows virtual electron transfers between neighboring sites (“hopping”). If charge fluctuations do not occur, the net result of these transfers will be expressed in terms of interactions between spin and orbital degrees of freedom.

The theory of superexchange was matured later by Anderson himself (72) who gave an explanation for the antiferromagnetic nature of the exchange constants. First, he introduced a model of singly occupied ions that treated both the kinetic process of the electrons and the on-site interactions. His model is equivalent to the *Hubbard model* (73), which is written as

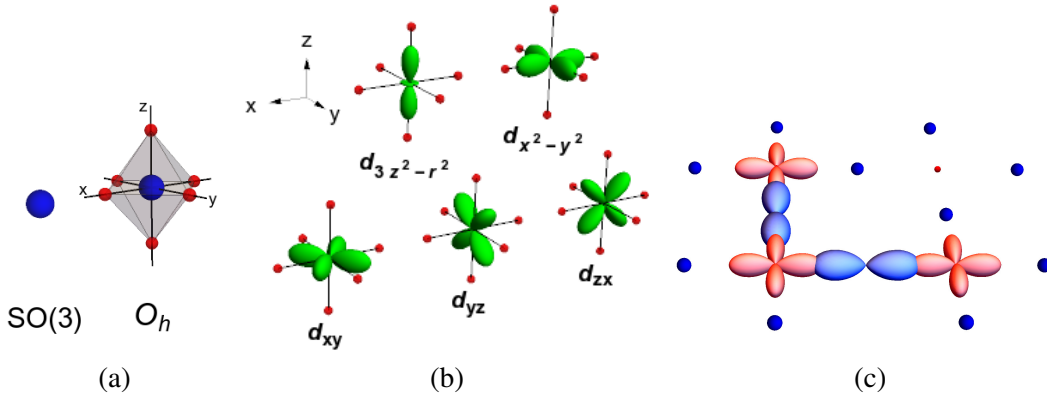


Figure 2 – (a) Octahedral environment created by negatively charged ions (red spheres) surrounding the transition metal ion (blue sphere). (b) The e_g and t_{2g} orbitals generated out of the lifting of the fivefold degeneracy of the d orbitals by a octahedral crystal field. (c) Superexchange path connecting two neighboring transition metal ions on a square lattice. This is an ideal representation of the CuO_2 planes of high- T_c superconductors. Source: By the author.

follows in second quantization:

$$H_{\text{Hub}} = -\sum_{\langle ij \rangle} t_{ij} (c_i^\dagger c_j + h.c.) + U \sum_i n_{i\uparrow} n_{i\downarrow}, \quad (2.16)$$

where c_i is a (fermionic) operator that annihilates the orbital at the lattice site i and $\langle ij \rangle$ label the pairs of nearest neighboring sites. If $\varphi_{i\sigma}(\mathbf{r})$ is the wavefunction of the orbital localized at the site i , the Hubbard- U parameter reads:

$$U = \int d\mathbf{r} d\mathbf{r}' \varphi_{i\sigma}^*(\mathbf{r}) \varphi_{i\sigma}(\mathbf{r}) \frac{e^2}{|\mathbf{r} - \mathbf{r}'|} \varphi_{i\bar{\sigma}}^*(\mathbf{r}') \varphi_{i\bar{\sigma}}(\mathbf{r}'). \quad (2.17)$$

The hopping parameters t_{ij} depend upon the hybridization of the d wavefunctions explained above. At $U = 0$, this model ground state describes a metal as characterized by band theory. In the limit $U/t \rightarrow \infty$, the ground state is composed by localized electrons described by Heitler-London theory. In the regime where U is strong enough to ensure localization, but not to hinder virtual electron transfers, Anderson showed how an antiferromagnetic Heisenberg model can be derived with a second order perturbation theory of the kinetic part of H_{Hub} , leading to $J \sim \frac{t^2}{U}$.

Anderson's article posed a well-stated problem to understand the magnetism of several Mott insulators: what is the ground state of the $S=1/2$ antiferromagnetic Heisenberg model? One suggestion was that the classical ground state could be stabilized and one would verify a ground state with spontaneously broken symmetry. This ground state in bipartite lattices is characterized by all spins aligned in one orientation on one sublattice and in the opposite sense on the other. This is the so-called the Néel state. (74) A spin-wave analysis can be made in analogy with the ferromagnetic case (Eq. (2.5)), but this time one should consider two bosons and define the spin transformation in such a way that $|\psi_{\text{Néel}}\rangle$ is the new vacuum.

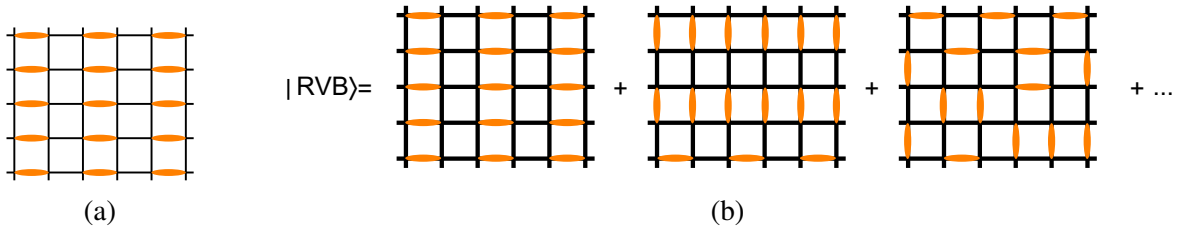


Figure 3 – (a) VBS state on the square lattice and (b) RVB state as the linear combination of several VBS states.

Source: By the author.

Although a Néel ground state to the Heisenberg model makes sense for classical spins, the situation changes when considering it as a quantum model. The state $|\psi_{\text{Néel}}\rangle$ is not even an eigenstate of H_{Hei} ! In fact, it can be shown that the (antiferromagnetic) Heisenberg model in finite systems will display an entangled singlet ground state. (75) We then ask ourselves if there could be some case in which the singlet ground state is preserved in the thermodynamic limit. This is one of the fundamental ideas behind quantum spin liquids.

2.2.2 First wave of Quantum Spin Liquids: Mott insulators in frustrated lattices

In 1973 (12) Anderson wrote the article that introduced the concept of quantum spin liquids, and gave the resonant valence bond (RVB) as the first example of these states. Anderson's main motivation was a Pauling's proposal of studying the electronic behavior of solids by an extension of the concept of resonating valence bonds from small molecules (e.g., benzene) to a whole lattice. The electrons would be delocalized throughout the compound and would be constantly moving around it in an entangled manner. Although the original idea was to build an alternative framework to study metals, it was soon realized that such state would be insulating. More specifically, it would be a Mott insulator, since it is characterized by an insulating behavior explained by strong electronic correlations.

A pictorial representation of the RVB state is given in Fig. 3. Instead of giving a definite spin state for each site of the lattice, we place singlet

$$|\psi_{\text{singlet}}\rangle = \frac{|\uparrow_i\downarrow_j\rangle - |\downarrow_i\uparrow_j\rangle}{\sqrt{2}}$$

on the links of the lattice in such a way that all sites are covered. A singlet configuration built out of this rule is called a *valence bond solid* (VBS). The RVB is a linear combination of a macroscopic number of VBS states and it distinguishes sharply from the VBS when considering the entanglement between the sites. While the singlets and the VBS states display only entanglement between nearest neighbors, a state generated by a linear combination of VBS presents long-range entangled spins. (67) The resulting state is neither a trivial paramagnet,

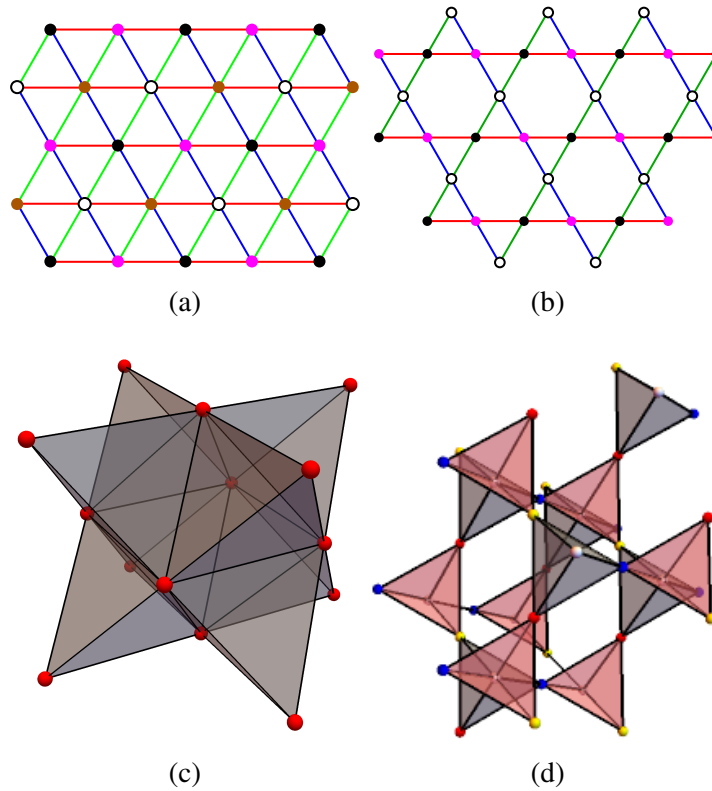


Figure 4 – Four examples of frustrated lattices (a) the triangular lattice, (b) the kagome lattice, (c) the fcc lattice, and (d) the pyrochlore lattice.
Source: By the author.

nor magnetically ordered like the ferromagnetic or the Néel state. In other words, the RVB is a macroscopic singlet state.

Anderson investigated the RVB state on the $S = 1/2$ Heisenberg model on the triangular lattice (12, 76) and found that the RVB displayed a lower energy when compared with the ordered state of lesser energy. It was soon realized that magnetically disordered states were favored in lattices that displayed *geometrical frustration*. The concept of geometrical frustration is readily understood by the antiferromagnetic Ising model ($J > 0, h = 0$ in Eq. (2.2)) on a single triangle. (10) The ground state of this triangle is six-fold degenerate and it is impossible to minimize the interaction energy of all links simultaneously. The interactions cannot be simultaneously satisfied; for this reason, they are called *frustrated*.

Quantum Monte Carlo and exact diagonalization methods applied on the Heisenberg model on the triangular lattice have shown that it present a long-range ordered ground state. (77) Although Anderson's original proposal for QSL was not successful, it did point out to the possibility of QSLs in other frustrated lattices like the kagomé, the fcc, and the pyrochlore, as shown in Figure 4. The search for QSLs in frustrated lattices continues to this day and was revitalized by the synthesis of new Mott insulators on the kagomé lattice like herbertsmithite (78), kapellasite (79), or $\text{Ca}_{10}\text{Cr}_7\text{O}_{28}$ (80).

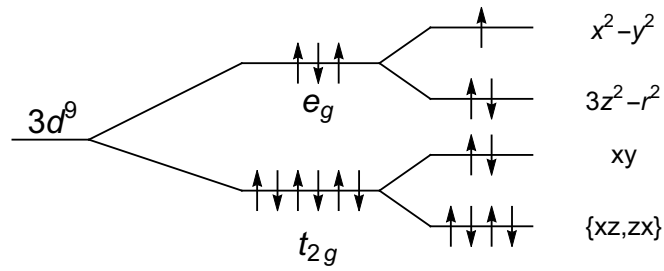


Figure 5 – Scheme of the lifting of degeneracy for d electrons under crystal-field and tetragonal distortion. The electrons of a $3d^9$ fill up these levels in such a way that the valence electrons are given by $d_{x^2-y^2}$ orbitals.

Source: By the author.

2.2.3 Second wave: high- T_c superconductors and fractionalization

The second wave of studies on QSLs was pioneered once again by Anderson in 1987 (81), this time inspired by studies on high- T_c superconductors. In 1986, it was found that doping the Mott insulator lanthanum copper oxides (La_2CuO_4) led to a superconducting phase at temperatures near $T \sim 30\text{K}$ (82); this anomalous behavior could not be explained by the pairing mechanism of electrons of the BCS theory. (83) The proposed explanations for high- T_c superconductivity forms a field of its own and will not be explored here. It is instructive, however, to use the discussion of the Mott insulating phase of cuprates to introduce some concepts.

The low-energy structure of the the undoped cooper oxide is well-described by a single band of $3d^9$ cooper ions and structural studies on La_2CuO_4 showed that these compounds are arranged in the layered perovskite structure. (84) This structure can be constructed by first picturing each Cu^{2+} ion surrounded by six O^{2-} ions in a octahedral environment (Fig. 2a). The crystal field generated by the oxygen ions lift the degeneracy of the d orbital into triply degenerate t_{2g} orbitals and doubly degenerate e_g orbitals (Fig. 2b). Neighboring octahedra share a corner in such a way that the structure is formed by stacked CuO_2 layers (Fig. 2c) that sandwich two LaO planes.

The octahedral environment does not preserve its complete symmetry but undergoes a tetragonal distortion due to the Jahn-Teller effect. (85) The orbital degeneracy will be lifted again as indicated in Fig. 5, implying that the valence band of the cooper oxides will be given by a singly occupied $d_{x^2-y^2}$ orbital. The minimal model for the Mott insulating phase of high- T_c superconductors considers that the low-energy physics of these oxides are described by weakly coupled CuO_2 layers. The Hamiltonian describing each plane is simply the Hubbard model in Eq. (2.16) on a square lattice. Other effects, like interlayer interactions, are included perturbatively.

Considering this background, Ref. (81) start the study of the CuO_2 planes physics with the Heisenberg model (Eq. (2.4)). This is indeed appropriate for undoped samples, since the localized $3d$ orbitals of the cooper ions have a large interaction parameter U and that this valence band would be half-filled. Anderson showed that the RVB state is related with the BCS

wavefunction projected to the space with $N/2$ Cooper pairs (where N is the number of lattice sites). As a follow-up article, Baskaran, Zou and Anderson did the mean field theory of the RVB state by explicitly making a BCS decoupling over the Heisenberg and the $t - J$ models. (86) This work identified quasiparticle fermionic operators, whose different combinations could account for charge or spin excitations. The spin excitations discussed in Ref. (86) exemplify what is now called *spinons* in QSLs, and the quasiparticle operators define the *parton* constructions. They also pointed out that the spin liquid would be found at intermediate values of U . Reducing the value of U leads to the enhancement of virtual transfers of electrons in different sites and favor the onset of a QSL state.

Controversies about the nature of the RVB ground state and its excitations started still in the year of 1987. In June of this year, Kivelson and collaborators proposed that the excitations of the RVB state would be topological and its ground state would display a topological order. (87) These topological excitations were compared with solitons in the conjugate polymer polyacetylene (88): they would be created in pairs by the breaking of a bond and would constitute an extended mobile defect. The elementary spin excitations would be spin-1/2 fermions and the charged excitations would be spinless bosons in coherence with. (86) In November of 1987, Kalmeyer and Laughlin proposed that a bosonic Laughlin wavefunction for the Fractional Quantum Hall Effect (FQHE) would be a trial wavefunction as good as the BCS to describe the RVB state. (89) The elementary spin excitations were also spin-1/2 particles, but they could obey either a fermionic or a *fractional* statistics. The idea of fractional statistics can be conceived when one inserts the concept of a Berry phase in the analysis of the statistics of a given particle. (90) A certain kind of particle is said to be a boson (fermion) when the accumulated Berry phase obtained through the exchange of two indistinguishable particles is zero (π). If the accumulated Berry phase is neither zero nor π , the particle is said to possess a fractional statistics and is called *anyon* (91) In 1988, Laughlin proposed that the spin excitations would be fractional indeed. (92) To complete this controversy, Read and Chakraborty proposed bosonic spinons for the RVB state. (93)

The inconclusiveness of the debate with regard to the statistics of the spin-1/2 excitations of the RVB state explains the different proposals for parton operators found in the literature. The fundamental idea about partons is to rewrite the spin operators in terms of canonical bosons and fermions subject to a constraint that restricts the parton Hilbert space to another that is isomorphic to the spin Hilbert space. (11) The idea behind these particles is very formal, and they should not be misread as canonical electron operators or magnons. The first parton constructions were justified through large- N approximation. (93, 94) It is known that the mean-field and the exact results of these theories coincide for $N \rightarrow \infty$. If $N = 2$ was sufficiently large, the parton mean field theory for $S = 1/2$ QSLs would lead to at least qualitatively correct results. This gives the basis to the fermionic parton construction proposed by Affleck and Marston. (94)

Let us focus on the fermionic partons for $S = 1/2$ spins in the $N = 2$ limit. The spin

operators are represented through the fermions

$$\mathbf{S}_i = \frac{1}{2} \sum_{\alpha, \beta = \uparrow, \downarrow} f_{\alpha, i}^\dagger \boldsymbol{\sigma}_{\alpha\beta} f_{\beta, i}, \quad (2.18)$$

where $\boldsymbol{\sigma}$ are the Pauli matrices and i is a lattice site. The $f_\alpha, f_\alpha^\dagger$ operators satisfy the same anti-commutative algebra of the electrons. However, they are subject to the following constraint

$$\sum_{\alpha} f_{\alpha, i}^\dagger f_{\alpha, i} \equiv n_i = 1, \quad \forall i \text{ on the lattice.} \quad (2.19)$$

The reason for Eq. (2.19) is to ensure the isomorphism between the parton and the spin Hilbert spaces. There are four states generated by the fermions that form the set $\{|0\rangle, |\uparrow\rangle, |\downarrow\rangle, |\uparrow, \downarrow\rangle\}$. On the other hand, the basis of the Hilbert space of a single site of the Heisenberg model is spanned by two vectors $|\uparrow\rangle$ and $|\downarrow\rangle$. Eq. (2.19) is then necessary to ensure an exact mapping between the parton and spin states; this feature is very general for all parton representations.

Partons are the starting point to mean-field theories for quantum spin liquids. (58) Consider the Heisenberg model in Eq. (2.4). This Hamiltonian in terms of the partons in Eq. (2.18) reads

$$H = \frac{J}{2} \sum_{\langle ij \rangle} \sum_{\alpha, \beta = \uparrow, \downarrow} f_{\alpha, i}^\dagger f_{\beta, i} f_{\beta, j}^\dagger f_{\alpha, j} = -\frac{J}{2} \sum_{\langle ij \rangle} \sum_{\alpha, \beta = \uparrow, \downarrow} f_{\alpha, i}^\dagger f_{\alpha, j} f_{\beta, j}^\dagger f_{\beta, i}. \quad (2.20)$$

The order parameters χ_{ij} for QSLs are defined out of the mean values

$$\chi_{ij} = \left\langle f_{\alpha, i}^\dagger f_{\alpha, j} \right\rangle \quad (2.21)$$

obtained from a self-consistent condition of the following mean-field Hamiltonian

$$H_{\text{MFT}} = -\frac{J}{2} \sum_{\langle ij \rangle} \sum_{\alpha = \uparrow, \downarrow} \left(\chi_{ij} f_{\alpha, i}^\dagger f_{\alpha, j} + h.c. \right) + \frac{J}{2} \sum_{\langle ij \rangle} |\chi_{ij}|^2. \quad (2.22)$$

The values obtained for χ_{ij} define one QSL Ansatz. The translation symmetry of the lattice is used to write the H_{MFT} in the Fourier space. The resulting Hamiltonian have the form

$$H_{\text{MFT}} = \frac{J}{2} \sum_{\langle ij \rangle} |\chi_{ij}|^2 + \sum_{\mathbf{k}} \sum_{\alpha = \uparrow, \downarrow} \epsilon_{\mathbf{k}} f_{\alpha, \mathbf{k}}^\dagger f_{\alpha, \mathbf{k}}, \quad (2.23)$$

where $\epsilon_{\mathbf{k}}$ is an energy dispersion depending on the lattice, J and χ_{ij} . This dispersion is formally equal to the bands observed in noninteracting electrons.

Parton mean field theory (MFT) is different from mean-field theories in Landau's framework since it changes the Hilbert space of the interacting Hamiltonian. More explicitly, the constraint (2.19) that defines the exact mapping between the spin and parton Hilbert spaces are satisfied only on average

$$\sum_{\alpha} \langle f_{\alpha}^\dagger f_{\alpha} \rangle = 1, \quad (2.24)$$

but not exactly. The wavefunction $|\Psi_{\text{MFT}}\rangle$ of the ground state of Eq. (2.22) is, therefore, not even qualitatively correct. The fundamental reason for this is that the partons cannot be treated as quasi-particles. This point is better understood by making an analogy with the Wegner's model. Just like the spins on the links are not themselves physical, but just part of the plaquette operators P_i , so are the $f_{\alpha,i}$ operators unphysical. These are just formal constructs to represent the physical variables and can be thought of as *part* of the spins.

Proceeding with the analogy between Wegner's model and partons, we can also define a Z_2 gauge transformation for the partons like

$$f_{\alpha,i}^\dagger \rightarrow -f_{\alpha,i}^\dagger, f_{\alpha,i} \rightarrow -f_{\alpha,i}. \quad (2.25)$$

This transformation leaves Eq. (2.18) and Eq. (2.19) invariant. In other words, it does not change the physical variables of our problem. Notice that these transformations are local gauge transformations, i.e., they can be made site by site without changing the physics of the system. This has an important consequence for the order parameters. The transformation (2.25) implies that the order parameter in Eq. (2.21) must transform like

$$\chi_{ij} \rightarrow -\chi_{ij}, \quad (2.26)$$

where j is any nearest neighbor of i . Parton MFT is equivalent to keeping a gauge field fixed. One more analogy with Wegner's theory can be done by stating that the gauge fluxes around elementary plaquettes as physical quantities of our theory. Consider first the case in which $\chi_{ij} \in \mathbb{R}$. The Z_2 gauge flux around a plaquette p , ϕ_p , is given by

$$e^{i\phi_p} = \prod_{\langle ij \rangle \in p} \text{sign}(\chi_{ij}). \quad (2.27)$$

Notice that ϕ_p is always zero or $\pi \pmod{2\pi}$ and is invariant under gauge transformations (2.25). Now, take the case where χ_{ij} is an imaginary number and define the variable $s_{ij} = \pm 1$ such that $\chi_{ij} = i s_{ij} |\chi_{ij}|$. The values of s_{ij} obey the constraint $s_{ji} = -s_{ij}$ and define a directionality between the sites. In analogy to Eq. (2.27), the flux is now defined by

$$e^{i\phi_p} = \prod_{\langle ij \rangle \in p} (i s_{ij}). \quad (2.28)$$

Notice that if the elementary plaquettes possess an even number of links, the value of ϕ_p will once again be zero or π . However, if the number of links is odd, $\phi_p = \pm \frac{\pi}{2}$.

Equation (2.26) has an important consequence for the analysis of the symmetry of a QSL Ansatz that is better illustrated through a simple example. Consider first the zero-flux Ansatz with real order parameters depicted in Fig. (6a), which clearly displays all the lattice symmetries of the Heisenberg model. The QSL described by the wavefunction $|\Psi_{\text{MFT}}\rangle$ is (trivially) translationally invariant. Contrast this case with the π -flux Ansatz in Fig. (6b), whose mean-field Hamiltonian

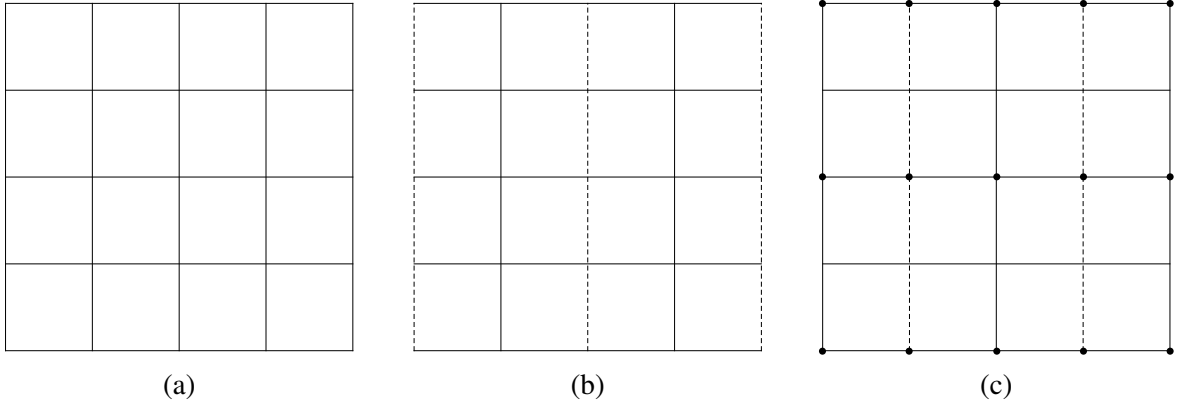


Figure 6 – Representations of QSL *Ansätze* on the square lattice with real order parameters. Here, $\chi_{ij} > 0$ if the line is full, and $\chi_{ij} < 0$ along dashed lines. Source: By the author.

breaks translation symmetry along the \hat{x} direction. The mean-field wavefunction $|\Psi_{\text{MFT}}\rangle$ will also break translation symmetry. However, the physical wavefunction $|\Psi\rangle$ given by (see Eq. (2.19))

$$|\Psi\rangle = \mathcal{P} |\Psi_{\text{MFT}}\rangle = \prod_i n_i (2 - n_i) |\Psi_{\text{MFT}}\rangle \quad (2.29)$$

does not break any symmetry. One way to understand this is to interpret \mathcal{P} as the operator enforcing all gauge transformations (2.25) on $|\Psi_{\text{MFT}}\rangle$, in such a way that $|\Psi\rangle$ is a linear combination of the mean-field ground states of all mean-field Hamiltonians that are physically equivalent to the π -flux *Ansatz*. An analogy can be done with the VBS and RVB states discussed in subsection 2.2.2. The wavefunction $|\Psi_{\text{MFT}}\rangle$ is akin to the VBS state, while $|\Psi\rangle$ is the highly entangled state corresponding to a linear combination of a macroscopic number of less entangled functions.

Another way to understand the translational invariance of the QSL is by verifying that the π -flux *Ansatz* can be recovered from a translation in the \hat{x} direction by a gauge transformation. This is illustrated in Fig. (6c), where the dots represent the sites where the gauge transformation will be applied. In general, the *Ansätze* will not display the symmetry indicated by the mean-field Hamiltonian, but their total symmetry will be given by a combination of the mean-field and gauge symmetries. The group of all transformations that keep an *Ansatz* invariant is called *projective symmetry groups* (PSG). (58, 60)

Do all the proposed QSLs up until this point preserve all the symmetries of the original Hamiltonian? Wen and collaborators pointed out that QSLs with excitations obeying fractional statistics cannot preserve time-reversal (T) and inversion (P) symmetries, since a particle with θ statistics must transform into one with $-\theta$ statistics under these operations. This is the case for a QSL based on FQHE wavefunctions like (92), which is an exemplar of a *chiral quantum spin liquid* (CQSL). (95) A realistic proposal for a CQSL to explain the physics of the cuprates was also discussed in Ref. (95) The experimental motivation for this proposal was the observation

that doping-enhanced second-neighbor interactions between spins. The Heisenberg model in this case will read:

$$H_{JJ'} = J \sum_{\langle ij \rangle} \mathbf{S}_i \cdot \mathbf{S}_j + J' \sum_{\langle\langle ij \rangle\rangle} \mathbf{S}_i \cdot \mathbf{S}_j, \quad (2.30)$$

in which $\langle\langle ij \rangle\rangle$ are the pairs of second-nearest-neighbor sites. The new term introduces frustration on the square lattice and creates instabilities to the ordered Néel state. A fermionic parton mean field decoupling for this model (without terms proportional to $|\chi_{ij}|^2$) reads

$$H_{\text{MFT}} = -\frac{J}{2} \sum_{\langle ij \rangle} \sum_{\alpha=\uparrow,\downarrow} \left(\chi_{ij}^{(1)} f_{\alpha,i}^\dagger f_{\alpha,j} + h.c. \right) - \frac{J'}{2} \sum_{\langle\langle ij \rangle\rangle} \sum_{\alpha=\uparrow,\downarrow} \left(\chi_{ij}^{(2)} f_{\alpha,i}^\dagger f_{\alpha,j} + h.c. \right), \quad (2.31)$$

where $\chi_{ij}^{(1)}$ and $\chi_{ij}^{(2)}$ are the order parameters giving the first and second-nearest neighbors "hoppings" of the theory. Consider now the case where these parameters are imaginary. Figure (7) illustrates an example of how to represent such Ansätze; there, the arrows point in the direction where $s_{ij} = +1$. The translation symmetry of this Ansatz is the same as the π -flux discussed above (see Fig. 6b); therefore, the physical wavefunction is also invariant under lattice translations.

It is easy to verify that the Ansatz in Figure (7) represents a chiral spin liquid. The directionality on the links connecting the sites impel us to fix a handedness in order to unambiguously define fluxes around triangular plaquettes. If we fix the counterclockwise orientation, this QSL is characterized by $\phi_p = \pi/2$ for all triangles on the lattice, and $\phi_p = 0$ for all squares. Notice that all hoppings are reversed by reflection, where the mirror is placed at the line $x = 1/2$. This implies the breaking of the parity symmetry. Furthermore, the time-reversal operator reverses the orientations of all hoppings and change the fluxes around the triangles to $-\pi/2$. The Ansatz then breaks P and T , but not PT , and is therefore chiral. This symmetry breaking allow us to define a type of local order parameter for quantum spin liquids (60, 95)

$$E_{ijk} = \mathbf{S}_i \cdot (\mathbf{S}_j \times \mathbf{S}_k), \quad (2.32)$$

where i, j and k are sites forming a triangle ordered according to a counterclockwise prescription. For a chiral spin liquid, $\langle E_{ijk} \rangle \sim \chi_{ij} \chi_{jk} \chi_{ki} \neq 0$. This parameter, however, does not define the state of the system in the same way the magnetization defines a magnetic ordering for the Ising or Heisenberg models. The physical wavefunction is still given by a highly entangled state determined by Eq. (2.29).

A last development I want to discuss from this period is the method to enforce the exact constraints (2.19) on $|\Psi_{\text{MFT}}\rangle$ and then calculate exact physical observables for $|\Psi\rangle$ at zero temperature: the *Variational Monte Carlo* (VMC) method. (46) The VMC was originally designed by Gutzwiller to study correlations on ferromagnetic materials by projecting a Fermi sea metallic state to the Hilbert space of states obeying a defined local condition. (96) Such problem can be immediately translated to the problem of QSLs described by partons, since we

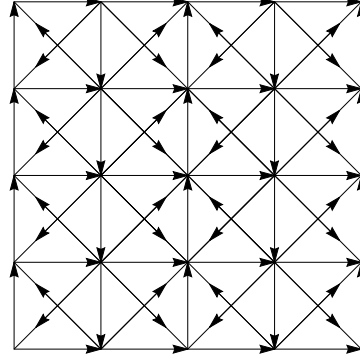


Figure 7 – Representation on the chiral spin liquid state with zero-flux on the square plaquettes and $\pi/2$ flux on the triangular plaquettes.
Source: By the author.

have a wavefunction $|\Psi_{\text{MFT}}\rangle$ similar to wavefunctions for electrons in solids and a local constraint. The VMC goal is to evaluate expectation values of an operator

$$\langle \mathcal{O} \rangle = \frac{\langle \Psi | \mathcal{O} | \Psi \rangle}{\langle \Psi | \Psi \rangle}, \quad (2.33)$$

where $|\Psi\rangle$ is the projected wavefunction. Let $\{|\alpha\rangle\}$ be the set of states obeying the desired constraint. The average $\langle \mathcal{O} \rangle$ can be rewritten in terms of the matrix elements $\langle \alpha | \mathcal{O} | \beta \rangle$ as follows

$$\begin{aligned} \langle \mathcal{O} \rangle &= \sum_{\alpha, \beta} \langle \alpha | \mathcal{O} | \beta \rangle \frac{\langle \Psi | \alpha \rangle \langle \beta | \Psi \rangle}{\langle \Psi | \Psi \rangle} \\ &= \sum_{\alpha} \left(\sum_{\beta} \langle \alpha | \mathcal{O} | \beta \rangle \frac{\langle \beta | \Psi \rangle}{\langle \alpha | \Psi \rangle} \right) \frac{|\langle \alpha | \Psi \rangle|^2}{\langle \Psi | \Psi \rangle} \\ &\equiv \sum_{\alpha} f(\alpha) p(\alpha). \end{aligned} \quad (2.34)$$

The $p(\alpha) \equiv |\langle \alpha | \Psi \rangle|^2 / \langle \Psi | \Psi \rangle$ obey the properties

$$p(\alpha) \geq 0, \text{ and } \sum_{\alpha} p(\alpha) = 1, \quad (2.35)$$

and can be thus considered probabilities. The functions $f(\alpha)$ will be given by

$$f(\alpha) = \sum_{\beta} \langle \alpha | \mathcal{O} | \beta \rangle \frac{\langle \beta | \Psi \rangle}{\langle \alpha | \Psi \rangle} \quad (2.36)$$

and gives the contribution of a state $|\alpha\rangle$ to the average $\langle \mathcal{O} \rangle$.

The idea behind the VMC is that Eq. (2.34) can be evaluated by performing a random walk over the states $\{|\alpha\rangle\}$. A starting state $|\alpha_1\rangle$ is fixed at the beginning of the computation. The transition between this configuration $|\alpha_1\rangle$ to another $|\alpha_2\rangle$ occurs with a probability given by a Monte Carlo weight factor $T(\alpha_1 \rightarrow \alpha_2)$ that reads

$$T(\alpha_1 \rightarrow \alpha_2) = \min \left(1, \frac{p(\alpha_2)}{p(\alpha_1)} \right). \quad (2.37)$$

This is the well-known Metropolis algorithm. This procedure generates a chain of accepted states $\{|\alpha_1\rangle, |\alpha_2\rangle, \dots, |\alpha_{N_{MC}}\rangle\}$ and allow us to estimate

$$\langle \mathcal{O} \rangle \approx \frac{1}{N_{MC}} \sum_{i=1}^{N_{MC}} f(\alpha_i). \quad (2.38)$$

The accuracy of $\langle \mathcal{O} \rangle$ increases with the number of configurations evaluated with the Monte Carlo method, N_{MC} . It is necessary to run $N_b > 1$ independent estimates in order to estimate the error, that is, the average computed with VMC reads

$$\langle \mathcal{O} \rangle_{\text{VMC}} = \frac{1}{N_b} \sum_{l=1}^{N_b} \langle \mathcal{O} \rangle_l, \quad (2.39)$$

where $\langle \mathcal{O} \rangle_l$ is the estimate average of the l -th Monte Carlo run. The error will be given by

$$\delta \langle \mathcal{O} \rangle_{\text{VMC}} = \sqrt{\frac{1}{N_b - 1} \sum_{l=1}^{N_b} (\langle \mathcal{O} \rangle_{\text{VMC}} - \langle \mathcal{O} \rangle_l)^2}. \quad (2.40)$$

More specific details of the implementation of VMC to study QSLs will be given in Chapter 4.

2.2.4 Third wave: exactly solvable models and implementation in heavy transition metal ion Mott insulators

The third wave of studies on QSLs is the one in progress today and is characterized by the development of better tools to study QSLs and by the several proposals of candidate compounds for a QSL ground state. It is not possible to cover all the work that has been done in this period covering approximately 20 years. Therefore, I focused on a subset of studies with general applicability and those that are relevant to this thesis. The goal of this section is to provide the background of the exactly solvable Kitaev model on the honeycomb lattice (20) and the physics of the Kitaev materials. (16–18)

2.2.4.1 Spin-Orbital Physics in Real Compounds

The synthesis of compounds displaying spin-orbital physics and the development of theories describing their magnetism have a history that runs in parallel with the three waves of studies on QSLs. The first article that called attention to the effects of the symmetry of the orbitals on the superexchange between transition metal ions was written by Kanamori already in 1959. (97) Using transition metal oxides as examples, Kanamori already emphasized that charge transfers necessary for superexchange processes can only occur if the d magnetic orbitals and the p oxygen orbitals overlap. This in turn depends on the charge distribution of these orbitals, the environment generating the crystal field, and the lattice describing the arrangement of transition metal ions. Such mechanism is implied in the theory of superexchange developed by Anderson and applied to the physics of cuprates.

The cuprates exemplify the class of Mott insulators that are locally described by only one type of orbital; would a qualitatively different physics emerge in compounds retaining orbital degeneracy? An affirmative answer to this question is expected because the physics involving the orbitals would be subject by the mechanism investigated by Kanamori. This would lead to effective models with orbital operators depending on the charge distribution of the relevant orbitals and the geometry of the lattice, which are qualitatively different from the Heisenberg model. A good starting point important to study these models is the review about orbitally degenerate materials written in 1982 by Kugel and Khomskii. (44) Kugel and Khomskii derived effective Hamiltonians for e_g and t_{2g} degenerate orbital systems and proved the large anisotropy on the orbital-dependent terms. The importance of this review led these effective models retaining orbital degeneracy to be called Kugel-Khomskii models.

The review by Kugel and Khomskii also discusses how e_g and t_{2g} systems would be different in regard to the effects of spin-orbit coupling (SOC). The e_g states are effectively $l = 0$ and the SOC is irrelevant for them. On the other hand, the d_{xy} , d_{yz} and d_{zx} can be arranged into an effective angular momentum operator \mathbf{l} ,

$$\mathbf{l} = \mathcal{P}_{t_{2g}} \mathbf{L}_{(2)} \mathcal{P}_{t_{2g}} = -\mathbf{L}_{(1)} \quad (2.41)$$

with $\mathcal{P}_{t_{2g}}$ being the projection operator to the t_{2g} orbitals and $\mathbf{L}_{(l)}$ being the angular momentum operator of elementary quantum mechanics with orbital quantum number l . A basis for \mathbf{l} obeying Eq. (2.41) is given by

$$|l_z = 0\rangle = |d_{xy}\rangle, \quad |l_z = \pm 1\rangle = \mp \frac{1}{\sqrt{2}} (|d_{zx}\rangle \pm i |d_{yz}\rangle). \quad (2.42)$$

The SOC in t_{2g} systems can be then modeled by the Hamiltonian

$$H_{\text{SOC}} = \lambda \mathcal{P}_{t_{2g}} \mathbf{L}_{(2)} \cdot \mathbf{S} \mathcal{P}_{t_{2g}} = -\lambda \mathbf{l} \cdot \mathbf{S}, \quad (2.43)$$

where λ is the spin-orbit coupling constant of the transition metal. The value of λ scales with Z^4 , where Z is the atomic number. The spin-orbit coupling is, therefore, expected to be more relevant in Mott insulators based on heavier ions.

Equation (2.43) finds immediate usage to describe the state of singly occupied ions in the electronic configurations d^1 and d^5 . The former case is equivalent to each site occupied by a single electron, while the second correspond to sites occupied by a single hole. The starting point is to give explicit forms for the annihilation operators of the eigenstates of l^z in terms of d_{xy} , d_{yz} and d_{zx} :

$$d_{0\sigma} = d_{xy,\sigma}, \quad d_{1\sigma} = -\frac{1}{\sqrt{2}}(d_{yz,\sigma} + id_{zx,\sigma}), \quad d_{-1,\sigma} = \frac{1}{\sqrt{2}}(d_{yz,\sigma} - id_{zx,\sigma}). \quad (2.44)$$

Eq. (2.43) has six eigenstates that can be subdivided into a $j = 1/2$ doublet and a $j = 3/2$ quartet. Since H_{SOC} is time-reversal invariant, the eigenstates are Kramers's degenerate. In terms

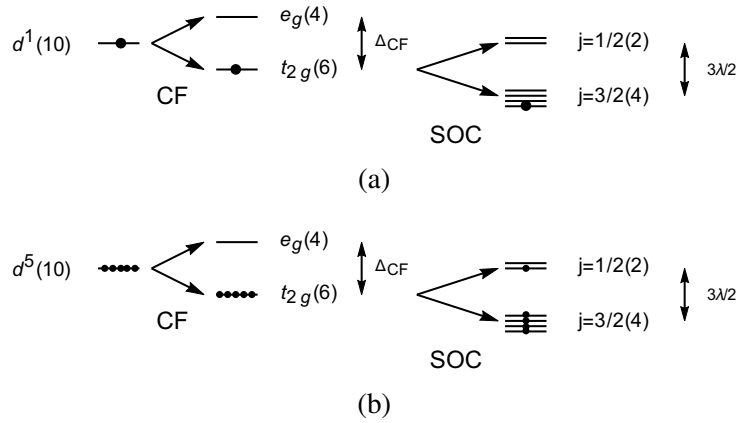


Figure 8 – Effect of the large spin-orbit coupling in (a) d^1 and (b) d^5 electron systems.
Source: Adapted from NATORI; DAGHOFER; PEREIRA. (1)

of Eq. (2.44) reads (49, 98)

$$A_s = 2s \left(\frac{1}{\sqrt{3}} d_{0,-s} - \sqrt{\frac{2}{3}} d_{-2s,s} \right), \quad (2.45a)$$

$$B_s = \sqrt{\frac{2}{3}} d_{0,-s} + \frac{1}{\sqrt{3}} d_{-2s,s}, \quad (2.45b)$$

$$C_s = d_{2s,s}, \quad (2.45c)$$

where $s = \uparrow, \downarrow = \pm 1/2$ distinguishes between Kramers-degenerate states. Note that, due to the combination of spin and orbital degrees of freedom induced by H_{SOC} , the index s in A_s and B_s is not the same as the actual spin eigenvalue in the d operators on the right-hand side of Eqs. (2.45). The B and C states are energetically favored and correspond to the $j = 3/2$ states, where $\mathbf{j} = \mathbf{l} + \mathbf{S}$ is the total angular momentum. They are separated from the A orbitals by a factor of $3\lambda/2$. In the limit $\lambda \rightarrow \infty$, the d^1 compounds are described by the physics of the B and C orbitals, while the d^5 compounds are equivalent to a system with no orbital degeneracy and a $s = 1/2$ pseudospin s (see Fig. 8).

Another important article discussing spin-orbital physics in connection with experimental results was written by Khaliullin in 2005. (99) Khaliullin made a survey of transition metal compounds including some that were synthesized after the Kugel-Khomskii review. Mainly motivated by the synthesis of layered cobalt oxides, this paper made an important discussion on the effects of spin-orbit coupling on CoO_2 triangular layers. The cobalt ions are in the $3d^5$ electronic configuration, and Khaliullin argued that the large λ limit discussed above could be applied for these compounds. The bond-dependent and anisotropic nature of the unprojected spin-orbital model is also transferred to the pseudospins s on this restricted space. For this particular compound, the model in the large- λ limit reads

$$H_{\text{CoO}_2} = J \sum_{\langle ij \rangle_\gamma} \tilde{\mathbf{s}}_i \cdot \tilde{\mathbf{s}}_j, \quad (2.46)$$

where γ labels the three different bond directions on the triangular lattice (see the different colors for the links in Fig. 4a). The \tilde{s}_i are defined by introducing a four sublattice division of the triangular lattice and applying distinct rotations on s_i according to the sublattice containing i . More explicitly,

$$\tilde{s}_i = \begin{cases} s_i, & \text{if } i \in A, \\ (-s_i^x, -s_i^y, s_i^z), & \text{if } i \in B, \\ (s_i^x, -s_i^y, -s_i^z), & \text{if } i \in C, \\ (-s_i^x, s_i^y, -s_i^z), & \text{if } i \in D. \end{cases} \quad (2.47)$$

Figure 4a gives a representation of these four sublattices with different colors. Interestingly enough, the highly-anisotropic and bond-dependent H_{CoO_2} could be written like the antiferromagnetic Heisenberg model on the triangular lattice with an adequate sublattice transformation. (12)

A converging point of all the topics reported in the third wave of studies is found on an exactly solvable model proposed by Kitaev in a seminal paper published in 2006. (20) This seemingly simple model reads

$$H_K = -J_x \sum_{\langle jk \rangle_x} \sigma_j^x \sigma_k^x - J_y \sum_{\langle jk \rangle_y} \sigma_j^y \sigma_k^y - J_z \sum_{\langle jk \rangle_z} \sigma_j^z \sigma_k^z, \quad (2.48)$$

where j, k are points of the honeycomb lattice and $\langle jk \rangle_\gamma$ links are analogous to the ones discussed on the triangular lattice in Eq. (2.46) (see Fig. 9a). There are two interesting historical curiosities about the model (2.48). First, Kugel and Khomskii have written this Hamiltonian on the cubic lattice to discuss the simplest case of an e_g orbital Hamiltonian with exchange frustration (see Eq. (34) of Ref. (44)) In their qualitative discussion, they relate this model to a classical model of magnetic needles, like compasses. This justifies the terminology *quantum compass model* for spin models with anisotropic and bond dependent interactions between spins. The second curiosity is that Kitaev was not mainly interested in discussing quantum spin liquids but the theory of anyons. He does mention that anyons were proposed to be found in RVB states, as discussed in Subsection 2.2.3 and the similarities between the RVB and the gapped phase of H_K . However, the assertion that the ground state of the model was a quantum spin liquid was first made by Baskaran in 2007 (21) as a result of the study of spin fractionalization in this model. Ref. (21) also showed how the spin-spin correlations of the Kitaev model are restricted to nearest neighbors, implying absence of magnetic long-range order.

The earlier work of Khaliullin in cobalt oxides have shown that d^5 compounds retaining t_{2g} orbital degeneracy and with strong SOC could host $S = 1/2$ Hamiltonian with anisotropic and bond-dependent interactions. (99) This was the first hint to proposals of solid state implementations of the Kitaev model. In 2009, Jackeli and Khaliullin demonstrated that the Kitaev model would be the effective Hamiltonian of Mott insulators with magnetic ions B in the referred electronic configuration and arranged in lattices formed by edge-sharing BO_6 regular octahedra. (19) This crystalline structure led to bond-dependent interactions exactly like in Fig. 9a. The combination

of two different exchange paths in this geometry with the projection to the lowest $j = 1/2$ manifold defined by SOC leads exactly to Eq. (2.48) in the isotropic case $J_x = J_y = J_z$.

Jackeli and Khaliullin explicitly proposed that compounds with stoichiometric formula A_2BO_3 , where A is an alkali ion and B is a $4/5d^5$ ion, would implement the Kitaev model on the honeycomb lattice. It took just one year to synthesize the first exemplar of such compounds, Na_2IrO_3 . (100) Another iridate (α - Li_2IrO_3) was synthesized by the same group two years later. (101) These were the two first recognized examples of Kitaev materials (16–18), i.e., real compounds in which the Kitaev model is relevant to describe their magnetism. Two years later, it was recognized that the compound α - $RuCl_3$ was another example of a Kitaev on the honeycomb lattice with distinct chemical composition. (102)

One theoretical development of the Kitaev model was the realization that it was also integrable in some tricoordinate three dimensional lattices. (103–108) The possible tricoordinated lattices are already known and were classified in Ref. (109) Ref. (107) studied the Kitaev model on all tricoordinated lattices with equal bond length and whose elementary closed paths runs over the same number of sites p . The dimensionality, different number of links for the elementary plaquettes and symmetries of these generalized honeycomb lattices lead to qualitatively different QSLs. Turning back to the materials, it is geometrically possible to find the B ion in some of these lattices for A_2BO_3 oxides with edge-sharing BO_6 octahedra. There are currently two exemplars of three dimensional Kitaev materials: the γ - Li_2IrO_3 (110) on the stripy-honeycomb lattice and the β - Li_2IrO_3 (111) on the hyperhoneycomb lattice.

All the mentioned Kitaev materials so far display some kind of magnetic order. This was expected from the study of minimal effective models that add direct overlap between d -orbitals, and superexchange terms from second and third neighbors. (112–115) Analyzing this seemingly disappointing result was an important step to synthesize the best candidate for a Kitaev QSL known so far. The following heuristic argument was made based on the ordered states presented in α - Li_2IrO_3 and Na_2IrO_3 . The sodium-based iridate display a zigzag but the lithium-based iridate displays an incommensurate magnetic order. It was then postulated that the smaller the weight of the alkali metal, the more disordered the phase of the Kitaev material would be. A hydrogen-based iridate would then be a strong QSL candidate. The compound $H_3LiIr_2O_6$ (116) was synthesized following this intuition. It indeed showed a nuclear magnetic resonance and specific heat responses that are compatible with a QSL. It also does not show any magnetic order down to temperatures of 0.05K, in spite of its exchange constants of order $J \sim 100K$. Further experiments must be done to confirm this assertion, but it is probable that the Kitaev model led to the discovery of a phase of quantum matter postulated 45 years ago!

Even if $H_3LiIr_2O_6$ is shown to be a QSL, this does not mean the end of studies in Kitaev materials. There are ongoing investigations about a possible QSL induced in α - $RuCl_3$ by the application of a magnetic field. (117–119) Quantum chemistry calculations also showed that the application of pressure can increase the relative importance of the Kitaev model in relation to

its perturbations. (120) It was also recently proposed that d^7 compounds could also host Kitaev materials. (121, 122) Finally, implementations of the Kitaev model in metal-organic frameworks are possible and remain unexplored. (108) All these routes indicate that Kitaev materials will continue to be a flourishing subject in the upcoming years.

2.2.4.2 Kitaev Model exact solution

In this subsection, I discuss the exact solution to the Kitaev model on the honeycomb lattice. The Kitaev model is a model with bond-dependent Ising interactions involving mutually perpendicular easy-axes (see Eq. (2.48)). The feature that gives a quantum character to the Kitaev model is the different spin quantization axes along inequivalent bonds. Spin models are not exactly solvable in general and the proposal of QSLs are normally done using mean-field parton theories discussed in Subsection 2.2.3. The key point of the integrability of the Kitaev model on the honeycomb lattice (and its three-dimensional generalizations) is its macroscopic number of conserved quantities that are associated with plaquette operators defined as follows:

$$W_p = \sigma_1^z \sigma_2^x \sigma_3^y \sigma_4^z \sigma_5^x \sigma_6^y, \quad (2.49)$$

where the sites 1 to 6 are shown in figure 9a. The axis of quantization associated with a given site is equal to the label of the bond connected to this site pointing outward the plaquette. It is straightforward to verify that any plaquette operator defined by the same convention will commute with the Kitaev model, i.e., $[H_K, W_p] = 0$ and with each other, i.e., $[W_p, W_{p'}] = 0$. This allows us to separate H_K into sectors defined by fixed eigenvalues of the plaquette operators $w_p = \pm 1$ like

$$H_K = \bigoplus_{w_1, \dots, w_m} H_{K; w_1, \dots, w_m}, \quad (2.50)$$

in which $H_{K; w_1, \dots, w_m}$ is the sector of the Kitaev model where the plaquette operator W_i has a fixed value w_i .

In practice, the model is integrated through a Majorana parton representation of the spins. A Majorana fermion f is a particle that is its own antiparticle, i.e., $f = f^\dagger$, and were first proposed as real solutions of the Dirac equation. (123) In accordance with Kitaev's original paper (20), the four Majorana flavors are labeled by

$$c_i, b_i^x, b_i^y, b_i^z \text{ with } \{b_i^a, b_j^{a'}\} = 2\delta_{ij}\delta_{aa'}, \{b_i^a, c_j\} = 0 \text{ and } \{c_i, c_j\} = 2\delta_{ij}. \quad (2.51)$$

This parton representation of the spins also enlarges the Hilbert space and introduces non-physical states. In order to find the constraint to the physical Hilbert space, Kitaev first wrote the spins in terms of Majorana fermions as follows

$$\sigma_i^a = ib_i^a c_i. \quad (2.52)$$

The Majorana fermion representation of the product $\sigma^x \sigma^y \sigma^z$ leads to the operator iD_i for each i site, where

$$D_i = b_i^x b_i^y b_i^z c_i. \quad (2.53)$$

Since $\sigma^x \sigma^y \sigma^z = i$, the physical Hilbert space \mathcal{H} is defined as follows

$$|\psi\rangle \in \mathcal{H} \text{ if and only if } D_i |\psi\rangle = |\psi\rangle, \forall i. \quad (2.54)$$

The algebra of the Majorana flavors (2.51), the spin representation (2.52) and the constraint (2.53) imply that the Majorana representation of the spins satisfy the algebra of the Pauli matrices $[\sigma^a, \sigma^b] = 2i\epsilon^{abc}\sigma^c$.

The Kitaev model (Eq. (2.48)) in terms of Majorana fermions is given by

$$H_K = i \sum_{\langle ij \rangle_a} J_a \hat{u}_{\langle ij \rangle_a} c_i c_j \quad (2.55)$$

with

$$\hat{u}_{\langle ij \rangle_a} \equiv i b_i^a b_j^a. \quad (2.56)$$

It can be shown that $\hat{u}_{\langle ij \rangle_a}$ display ± 1 eigenvalues and that they transform under D_i like $D_i \hat{u}_{\langle ij \rangle_a} D_i = -\hat{u}_{\langle ij \rangle_a}$. In other words, they are Z_2 gauge operators. These operators also commutes with each other $[\hat{u}_{\langle ij \rangle_a}, \hat{u}_{\langle i'j' \rangle_{a'}}] = 0$ and with the Kitaev model $[\hat{u}_{\langle ij \rangle_a}, H_K] = 0$. Therefore, they can be fixed and used to distinguish different sectors of Eq. (2.50) by fixing their eigenvalues $u_{\langle ij \rangle_a}$. These $u_{\langle ij \rangle_a}$ values defines a static Z_2 gauge field similar to the bond variables of Wegner's model in Eq. (2.7). The values of $u_{\langle ij \rangle_a}$ are related to the eigenvalues of the plaquette operators by

$$w_p = \prod_{\langle ij \rangle \in \partial p} u_{\langle ij \rangle_a}, \quad i \in \text{even sublattice and } j \in \text{odd sublattice}. \quad (2.57)$$

It is clear that w_p is not altered by Z_2 gauge transformations and plays the same role as the plaquette operators P_i in Eq. (2.7).

The Hamiltonian in Eq. (2.55) after fixing the $u_{\langle ij \rangle_a}$ values is quadratic on the c_i operators, and therefore diagonalizable. A theorem proved by Lieb (124) implies that, on the honeycomb lattice, the ground state of (2.55) lies on the sector presenting $w_p = +1$ for all plaquettes. After fixing the gauge variables and fix the problem to the ground state sector, one can diagonalize H_K with the usual Fourier transformation and diagonalize the Hamiltonian in the reciprocal space. Let N be the total number of sites of the lattice in such a way that the even sublattice A and the odd sublattice B have $N/2$ sites. The translation vectors of the honeycomb lattice are given by

$$\mathbf{a}_1 = \frac{1}{2}(3, \sqrt{3}), \quad \mathbf{a}_2 = \frac{1}{2}(3, -\sqrt{3}), \quad (2.58)$$

with corresponding reciprocal lattice vectors

$$\mathbf{b}_1 = \frac{2\pi}{3} \left(1, \sqrt{3}\right), \quad \mathbf{b}_2 = \frac{2\pi}{3} \left(1, -\sqrt{3}\right). \quad (2.59)$$

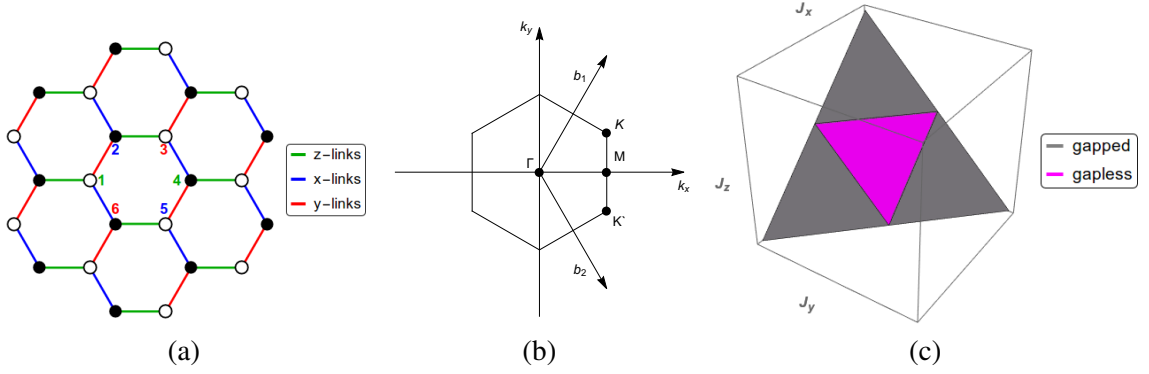


Figure 9 – (a) representation of the honeycomb model. The different color on the links correspond to different Kitaev interactions. (b) The Brillouin zone of the honeycomb lattice. (c) Phase diagram of the Kitaev model in the case $J_x + J_y + J_z = 1$. Source: By the author.

The Fourier transform then reads

$$c_{\mathbf{k},A} = \frac{1}{\sqrt{N}} \sum_{i_A} c_{i_A} \exp(i\mathbf{k} \cdot \mathbf{r}_{i_A}), \quad c_{\mathbf{k},B} = \frac{1}{\sqrt{N}} \sum_{i_B} c_{i_B} \exp(i\mathbf{k} \cdot \mathbf{r}_{i_B}), \quad (2.60)$$

where \mathbf{k} is a vector of the Brillouin zone (BZ) displayed in Fig. 9b and the normalization factor was chosen in such a way that $\{c_{\mathbf{k},X}, c_{\mathbf{k}',Y}\} = \delta_{X,Y} \delta_{\mathbf{k},-\mathbf{k}'}$. In order to make the operators $c_{\mathbf{k},X}$ obey the canonical fermion algebra, the Brillouin zone is cut into two halves and chose one of them that is called $\frac{1}{2}BZ$. Such splitting must obey the property $\mathbf{k} \in \frac{1}{2}BZ$ the vector $-\mathbf{k}$ is inside the other half of the BZ. Then

$$c_{i_X} = \sqrt{\frac{2}{N}} \sum_{\mathbf{k} \in \frac{1}{2}BZ} \left(c_{\mathbf{k},X} \exp(-i\mathbf{k} \cdot \mathbf{r}_{i_X}) + c_{\mathbf{k},X}^\dagger \exp(i\mathbf{k} \cdot \mathbf{r}_{i_X}) \right), \quad (2.61)$$

in which $c_{\mathbf{k},X}^\dagger = c_{-\mathbf{k},X}$. Substituting Eq. (2.61) in Eq. (2.55), the problem of finding the eigenstates and eigenvalues is reduced to the diagonalization of a 2×2 matrix. The spectrum of Majorana fermions is given by

$$\epsilon_{\mathbf{k}} = \pm \left| \sum_a J_a e^{i\mathbf{k} \cdot \delta_a} \right|, \quad (2.62)$$

where

$$\delta_z = \hat{\mathbf{x}}, \quad \delta_x = -\frac{1}{2}\hat{\mathbf{x}} + \frac{\sqrt{3}}{2}\hat{\mathbf{y}}, \quad \delta_y = -\frac{1}{2}\hat{\mathbf{x}} - \frac{\sqrt{3}}{2}\hat{\mathbf{y}} \quad (2.63)$$

are the nearest neighbor vectors connecting points of the sublattice A to the sublattice B (see Fig. 9a). The band dispersion (2.62) will be gapped or gapless according to the values of the coupling constants J_a . It can be shown that the Majorana spectrum will be gapless if and only if it satisfies the triangular inequality

$$|J_x| \leq |J_y| + |J_z|, \quad |J_y| \leq |J_x| + |J_z|, \quad |J_z| \leq |J_x| + |J_y|. \quad (2.64)$$

A phase diagram distinguishing gapped and gapless phases is shown in Figure 9c.

One could naively expect that the ground state of the Kitaev model would be given by the Fermi sea of negative energy Majorana fermions coupled with the static Z_2 gauge field. However, such state is still unphysical since it does not obey the constraint in Eq. (2.53). A physical state $|\Phi_{\text{phys}}\rangle$ is obtained out of the mean field state $|\Phi\rangle$ by using the projection operator \mathcal{P} as follows

$$\mathcal{P}|\Phi\rangle = \prod_j \frac{1 + D_j}{2} |\Phi\rangle = |\Phi_{\text{phys}}\rangle. \quad (2.65)$$

Since the eigenvalues of $D_j = \pm 1$, it is clear that $|\Phi_{\text{phys}}\rangle$ satisfies Eq. (2.53) and provides an eigenstate of the Kitaev model. One important point is that, for several operators \mathcal{O} , the average of the projected wavefunction coincides with the unprojected one, i.e., $\langle\Phi|\mathcal{P}\mathcal{O}\mathcal{P}|\Phi\rangle = \langle\Phi|\mathcal{O}|\Phi\rangle$. (125) This is made clearer by introducing complex fermion operators $\chi_{\langle ij \rangle_a}^\dagger, \chi_{\langle ij \rangle_a}$ on the links (21)

$$\chi_{\langle ij \rangle_a}^\dagger = \frac{1}{2}(b_i^a - ib_j^a), \quad \chi_{\langle ij \rangle_a} = \frac{1}{2}(b_i^a + ib_j^a), \quad (2.66)$$

and complex matter fermions given by (21)

$$f_{\mathbf{r}} = \frac{1}{2}(c_{A\mathbf{r}} + ic_{B\mathbf{r}}) \quad \text{and} \quad f_{\mathbf{r}}^\dagger = \frac{1}{2}(c_{A\mathbf{r}} - ic_{B\mathbf{r}}). \quad (2.67)$$

If the operator \mathcal{O} does not change the bond fermion number $\chi_{\langle ij \rangle_a}^\dagger \chi_{\langle ij \rangle_a}$, then (125)

$$\langle\Phi|\mathcal{P}\mathcal{O}\mathcal{P}|\Phi\rangle = \langle\Phi|\mathcal{O}|\Phi\rangle. \quad (2.68)$$

The equation above is valid for several important operators, like the Hamiltonian itself and the spin-spin correlators. That way the Kitaev model avoids the necessity for a Gutzwiller projection like it happens for QSLs defined through mean-field parton theories.

The combination of integrability and implementation in solid state systems turned the Kitaev model onto a paradigmatic model to study QSLs. Its exact solution and ultra-short spin correlation allowed for the first time the computation of several QSL dynamical correlation functions that can be measured through spectroscopic probes. (125–131) Its thermodynamics were also rigorously explored and allowed the investigation of thermal phase transitions of fractionalized particles. (132–134) The discovery of Kitaev materials generated a new focus for the search on solid state platforms for quantum spin liquids. It is probably not an overstatement to say that the Kitaev model plays for the theory of quantum spin liquids a role similar to the one of the electron gas in the theory of metals. Both of them provide simple models with exactly known solutions upon which one can calculate experimental responses. The qualitative features of these responses are then expected to be observed if such state is observed in real materials.

2.3 Defining Quantum Spin Liquids

I provided the necessary historical background to understand the evolution of the research on quantum spin liquids driving to the Kitaev model and the Kitaev materials in Section 2.2.

It is clear that QSLs are magnetic states to be found in Mott insulators that do not display conventional orders like ferromagnetic order or Néel state. It is also clear that QSLs are very diverse. QSL states were proposed based on BCS wavefunctions, fractional quantum Hall states and several parton theories. Their spectrum of excitations can be bosonic, fermionic or fractional, and accompany Z_2 , $U(1)$ or $SU(2)$ emergent gauge fields. They were predicted to occur in compounds with frustrated lattices and low-spin effective models, compounds in unfrustrated lattices and doping, and compounds retaining orbital degeneracy. Is it possible to find a proper definition of quantum spin liquids that account for all this variety?

The most positive definition of QSLs grounded on fundamental concepts of quantum mechanics states that QSLs are many-body states displaying long-range entanglement in the context of magnetism. (11) This notion is already implied in the original definition of the RVB state and the projected parton wavefunctions. In practice, since there is still no experimental probe to many-body entanglement, we must look for other features of quantum spin liquids. It was earlier stated that QSLs were associated for a long time with absence of spin order. Although this is not considered to be correct anymore, lack of order can be related with many-body entanglement, making the absence of long-range order a feature of a good spin liquid candidate. The link between QSLs and absence of order is given by the Lieb-Schultz-Mattis-Affleck (LSMA) theorem. (135) The LSMA theorem proves that the ground state of local spin Hamiltonians on lattices with $SU(2)$ symmetry, total half-integer spin per unit cell and periodic boundary conditions are either gapless or present topological order. This theorem was initially proved for spin chains with $SU(2)$ symmetry and was later generalized for other systems. For example, Oshikawa (136) required a lesser symmetry $U(1)$ equivalent to the conservation of the particle number. In this case, the spectrum would be always gapless, except for an integer particle number per unit cell of the ground state.

The LSMA theorem provides strong constraints on the ground state of a spin system. There is the possibility that the ground state displays a topological order and is, therefore, nontrivial. Another possibility is that a SSB occurred and the excitations are bosonic Goldstone modes. But, what if the gapless excitations appear and there is no observed magnetic order? Since this gapless excitation is not a Goldstone mode, and the disordered state is not compatible with the trivial paramagnetic state, the ground state must be highly entangled. The combination of disordered ground state and gapless excitations in a strongly interacting spin system is then a good indication of quantum spin liquids.

The discussion above relates with another definition, namely that QSLs are macroscopic spin states displaying *fractional excitations*. (69) These excitations must be contrasted with the usual ones, which are written in terms of linear combinations of local excitations like the magnons mentioned in Section 2.1. In spin systems, this means that the usual excitations carries effectively an integer spin, since each local excitation change the values of the spin by an integer $\Delta S^z = \pm 1, \dots, \pm 2S$. A fractional excitation must be created by a nonlocal operator, e.g., a string.

Fractional excitations are never created alone, and this explains the absence of observed order in the dynamical structure factor of QSLs.

Let us illustrate a necessary condition for fractionalization to occur through the $S = 1/2$ fermionic spinon. Consider first the VBS state already presented in Figure 3. If one singlet is broken, that results in one dangling spin up and other spin down, each of which confined in a different site. This dangling spins correspond to the spinons, which are always created in pairs by local excitations. To move the spins away from each other, the configuration of the dimers throughout the whole lattice must be rearranged in this process. The necessary energy to take the spinons infinitely apart from each other is also infinite and they are said to be confined - hence, they are not relevant excitations of the VBS. The situation is different in the RVB state. A RVB is equivalent to a linear combination of a macroscopic number of VBS configurations. After creating the same pair of dangling spins in a RVB, they can move away from each other by changing the weight factor of the VBS configurations that already define the RVB state. In this case, it takes only a finite energy cost to let the spins infinitely apart from each other and they are said to be *deconfined*. In this case each of them can be called a spinon that clearly carries $S = 1/2$ spin. This deconfinement is only possible because of the highly entangled nature of the RVB state.

Consider now how the inelastic neutron scattering of spinons would differ from the spectrum of magnons. The magnon dispersion can be measured through INS and the energy of the excitation $\hbar\omega$ is found to be a well-defined function of the transferred momentum \mathbf{q} . The spinons also display a well defined dispersion relation $\hbar\omega_{\mathbf{k}}$, but the fact that they are always created in pairs generate a great difference to their dynamical structure factor. Consider a QSL ground state with $S = 1/2$ spinon excitations probed with INS, and let us fix the transferred momentum and energy to $(\mathbf{q}, \hbar\omega)$. This will generate two spinons, and momentum conservation ensures that one will have momentum \mathbf{k} and other $\mathbf{q} - \mathbf{k}$. However, for a given pair of transferred energy and momentum, there are usually many pairs of excitations obeying the condition $\omega = \omega_{\mathbf{q}-\mathbf{k}} + \omega_{\mathbf{k}}$. For this reason, the DSF of QSLs is often “blurred” in contrast to the definite lines observed in ordered states.

The Majorana fermions and the Z_2 gauge flux excitations (visons) on the Kitaev model are other examples of fractionalized excitations. (21) It can be shown that a spin excitation on the Kitaev spin liquid must produce at least a pair of visons and other Majorana fermion c . This has an important physical consequence for neutron scattering experiments: it means that a gap Δ related to the formation of the vison pair will be always observed on the dynamical structure factor (Eq. 2.6) even if the QSL is on the gapless phase. (125–129) The dynamics observed in INS experiments for the Kitaev model must then consider excited states of the sector with two visons: this partly explains the eight year difference between the exact solution of the Kitaev model and the computation of the exact dynamic factor. Such gap was proved to be robust against a Heisenberg-like perturbation, but not for all perturbations allowed by symmetry. (137)

Therefore, it is generically not expected to appear in Kitaev materials, even if they are in the QSL phase.

A very important discovery concerning the experimental probes for QSLs was that the Majorana gapless spectrum of the Kitaev model can be observed with other spectroscopic technique, namely, resonant inelastic x-ray scattering (RIXS). (130, 131) RIXS is a photon-in photon-out spectroscopic technique that uncovers elementary excitations of solids through the analysis of the energy, momentum, and polarization of the incident and scattered photon. (48) Recent advancements in RIXS instrumentation are making this a viable technique to investigate the dynamics of strongly correlated systems. This technique will be discussed in detail in Chapter 5, since the analysis of its scattering for $4/5d^1$ Mott insulators constituted a great part of my original work. Here I point out that RIXS is a technique based upon local excitations. It is thus very significant that it can be used to probe fractionalized excitations depending on many-body entanglement like Majorana fermions. Chapter 5 will give other examples of other potential results of RIXS as a probe of quantum spin orbital liquids in contrast to the INS responses.

3 QUANTUM COMPASS MODELS IN TRANSITION METAL OXIDES

This chapter is devoted to make explicit the derivation of spin-orbital models for $4d^1$ and $5d^1$ based Mott insulators together with an analysis of their fundamental degrees of freedom. I emphasized in Chapter 2 how the search for QSLs have been brought to a new focus on Mott insulators retaining orbital degeneracy, displaying strong spin-orbit coupling, and described by bond-dependent exchange interactions. The $4/5d^5$ Mott insulators were justifiably more investigated than compounds with different electronic configurations since the proposal of the Kitaev materials. (19)

But the mechanism discussed in Ref. (19) is not restricted to d^5 ions and was successfully applied to derive $j = 3/2$ models on $4/5d^1$ magnetic insulators. (29) The model was proposed to describe the physics of ordered double perovskites, where the magnetic ions are arranged on a fcc lattice. The interactions are anisotropic and bond-dependent like in the Kitaev case, but they are not restricted to dipole interactions. Interactions between quadrupoles and octupoles of $j = 3/2$ effective angular momentum were essential to the physics of this model. It was also shown that these unusual interactions were essential to stabilize certain exotic ordered phases observed in double perovskites. (34–38) More relevant to this thesis, it was also shown that a certain limit of the model was dominated by quantum fluctuations and could display a QSL ground state. This was further supported by experiments on the compound Ba_2YMoO_6 arguing in favor of either a valence-bond glass or a collective spin-singlet ground state. (30–33) In summary, there were theoretical and experimental evidence that $j = 3/2$ magnetic insulators induced by strong spin-orbit coupling could promote a QSL state.

3.1 Qualitative Discussion of the $j = 3/2$ Spin-Orbital Models

I start by giving some orders of magnitude of important parameters describing the compounds to be studied here. This discussion will also serve as a justification for the methodology of the model derivation. The Kmetko-Smith diagram (138) depicted in Fig. 10 gives the first general guidance to order the strength of electronic correlation for f , $4d$ or $5d$ electrons. This diagram shows that f electrons are in general more localized than their d counterparts, implying a larger value of the Hubbard- U parameter. The electronic localization also increases with the decrease of the number of nodes of the radial part of the orbital function. The diagram then indicates that $4d$ and $5d$ systems would drive to the Mott insulators with lower values of electronic correlation. These intermediate strength of the electronic interaction actually favor a spin liquid state, as indicated by the earliest studies of the RVB state on cuprates. (86)

As stated in Chapter 2, the electronic correlation of systems retaining orbital degeneracy is qualitatively different from the correlation of nondegenerate orbitals. This chapter will give

the explicit calculations supporting this statement. Let the Greek indexes α, β, γ and δ label the atomic orbitals and σ, σ' label the spin. Hereafter, the orbital labels will be restricted to t_{2g} states (Eq. (2.14)), and $\sigma = \uparrow, \downarrow$ is always the electronic spin. I also apply the ordering convention $xy < yz < zx$ used in other works. (1, 139) The interaction between two electrons (or holes) at an atom is written like

$$H_{\text{int}} = \frac{1}{2} \sum_{\sigma\sigma'} \sum_{\alpha\beta\gamma\delta} \langle \alpha\beta | \hat{V} | \gamma\delta \rangle d_{\alpha\sigma}^\dagger d_{\beta\sigma'}^\dagger d_{\delta\sigma'} d_{\gamma\sigma}, \quad (3.1)$$

where \hat{V} is the Coulomb interaction between the electrons. The matrix elements $\langle \alpha\beta | \hat{V} | \gamma\delta \rangle$ in Eq. (3.1) have a special meaning when at least two of the four orbitals are equal. These are

$$U = \langle \alpha\alpha | \hat{V} | \alpha\alpha \rangle \quad (3.2a)$$

$$U' = \langle \alpha\beta | \hat{V} | \alpha\beta \rangle \quad (3.2b)$$

$$J_H = \langle \alpha\beta | \hat{V} | \beta\alpha \rangle = \langle \alpha\alpha | \hat{V} | \beta\beta \rangle. \quad (3.2c)$$

The parameter U is just the same interaction parameter of the Hubbard model, U' is the direct electrostatic interaction between two electrons occupying different orbitals, and J_H is the so-called Hund's coupling. They are evaluated using the Racah parameters in the limit of an isolated atom, whose explicit evaluation leads to $U = U' + 2J_H$. (68) Only parameters given in terms of U and J_H are taken into account in deriving most effective models for transition metal oxides, and the same will be the case for this thesis. H_{int} is then written like

$$\begin{aligned} H_{\text{int}} = & U \sum_{\alpha} n_{i\alpha\uparrow} n_{i\alpha\downarrow} \\ & + (U - 2J_H) \sum_{\sigma} \sum_{\beta < \alpha} n_{i\alpha\sigma} n_{i\beta\bar{\sigma}} + (U - 3J_H) \sum_{\sigma} \sum_{\beta < \alpha} n_{i\alpha\sigma} n_{i\beta\sigma} \\ & - J_H \sum_{\beta < \alpha} \left(d_{i\alpha\uparrow}^\dagger d_{i\alpha\downarrow}^\dagger d_{i\beta\downarrow}^\dagger d_{i\beta\uparrow} - d_{i\alpha\downarrow}^\dagger d_{i\alpha\uparrow}^\dagger d_{i\beta\uparrow}^\dagger d_{i\beta\downarrow} + h.c. \right). \end{aligned} \quad (3.3)$$

The models derived in this thesis followed a methodology to discover the effective Hamiltonian of heavy transition metal Mott insulators that is sometimes dubbed Jackeli-Khaliullin mechanism. (17) The starting point is the derivation of a t_{2g} Kugel-Khomskii Hamiltonian \mathcal{H}_{KK} with arbitrary spin-orbit coupling constant (λ). The \mathcal{H}_{KK} Hamiltonian for d^1 and d^5 systems differ only on the interpretation of the fermionic operators: they represent electrons for the d^1 systems and holes for the d^5 systems. In both cases, the t_{2g} orbitals generate an effective $l = 1$ angular momentum operator (see Eq. (2.41)). The effect of SOC on the t_{2g} orbitals is described by the Hamiltonian H_{SOC} written in Eq. (2.43) and was described in Subsection 2.2.4.1. I recall here that the $j = 3/2$ manifold is energetically favored for d^1 electron systems and a projection of \mathcal{H}_{KK} to this manifold is valid for λ much greater than the hopping parameter (see Fig. 8).

Since the correlation involves direct electrostatic repulsion, Hund's coupling and SOC the phenomena emerging in $4d$ and $5d$ transition metal oxides depends upon the relation between

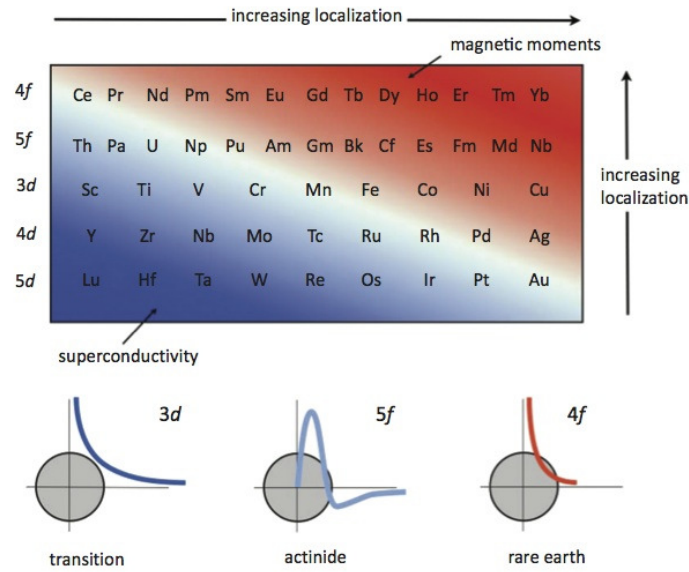


Figure 10 – Kmetko-Smith diagram indicating the increasing of localization as a function of the position in the periodic table.

Source: COLEMAN. (2)

the parameters U , J_H and λ . It was recently pointed out that the Jackeli-Khaliullin mechanism is rigorously justified only if the energy difference between e_g and t_{2g} states (often labeled $10Dq$ (68)) and the Hund's coupling is much larger than SOC. (140) The estimation of these parameters for electrons in solid state is very difficult because of the mixing between d and p orbitals in these crystals and the screening due to the electrons surrounding the ion. (68) Ideally, they can be extracted through quantum chemistry calculations combined with the experimental data extracted from real materials. Nevertheless, the literature present consistently some typical values for these parameters. The crystal-field splitting $10Dq$ of $3d$ to $5d$ compounds ranges between 2-4 eV (increasing with the atomic mass). (52) The typical values of the Hubbard and Hund's coupling electrons are $U \sim 0.5 - 3\text{eV}$ and $J_H \sim 0.5\text{eV}$ for $5d$ elements. (141) $4d$ elements display $J_H \sim 0.6 - 0.7\text{eV}$ (141) and greater values for the Hubbard interaction when comparing with $5d$ ions. (138) The estimated value of the SOC parameter for $4d$ ions is $\lambda \sim 0.1 - 0.4\text{eV}$. (52) These values allow us to argue that $\lambda \ll U, J_H, 10Dq$ in many $4d$ and $5d$ compounds. In the following, I assume that the parameters are within the range where the Jackeli-Khaliullin mechanism is valid.

3.2 Kugel-Khomskii model for t_{2g} degenerate systems

3.2.1 General Formulas for the Derivation of t_{2g} Kugel-Khomskii models in d^1 systems

This section will provide the derivation of the Kugel-Khomskii Hamiltonian for $4d^1$ and $5d^1$ magnetic Mott insulators in cubic double perovskites and generalized honeycomb lattices. Before working out the physically motivated examples, let me state some general features of this

derivation and fix a notation. I start with the multi-orbital Hubbard model that is written as a sum of two terms

$$\hat{H} = \hat{H}_0 + \hat{T}, \quad (3.4)$$

where \hat{H}_0 is the onsite interaction Hamiltonian and \hat{T} is the bond-dependent hopping Hamiltonian. \hat{H}_0 is always given by the sum of Eq. (3.1) on each site of the lattice

$$\hat{H}_0 = \sum_i \hat{H}_{\text{int},i}, \quad (3.5)$$

while the hopping Hamiltonian is generically given by

$$\hat{T} = - \sum_{\langle ij \rangle_\gamma} \sum_{\gamma, \sigma} t_{ij, \alpha\beta}^{(\gamma)} d_{i, \alpha, \sigma}^\dagger d_{j, \beta, \sigma} + h.c.. \quad (3.6)$$

While the terms α and β still label the orbitals in Eq. (3.6), the label γ now refers to different bond directions of the lattice. The hopping parameters $t_{ij, \alpha\beta}^{(\gamma)}$ now indicate that the hopping between two nearest neighbors will depend upon the active orbitals and the bond direction. The exact values of these coefficients will depend upon the relative position between the sites i and j .

The first assumption of the effective models is that the correlations in \hat{H}_0 are strong enough to localize the electrons and hinder charge fluctuations. The low-energy physics will be then derived through second-order perturbation theory, in which \hat{T} is the perturbation. Described this way, the procedure is identical to the derivation of the Heisenberg model from the single-orbital Hubbard model. The first factor causing differences arises from the bond and orbital dependence of the $t_{ij, \alpha\beta}^{(\gamma)}$ parameters, which already implies a bond-dependent and orbitally anisotropic effective Hamiltonian. The second factor refers to the Hund's coupling dependent electronic interactions (see Eq. (3.3)). The third difference comes from the projection to the $j = 3/2$ manifold generated by SOC.

In practical calculations, I derive the effective models concerning two sites connected by each of the non-equivalent bond γ , and then sum these two site Hamiltonians throughout the lattice. It is then possible to give the explicit bases for the initial, intermediate, and final states, since we are dealing with a two-site problem. Let me start by stating a basis for the intermediate state. It reads

$$\begin{aligned} \mathbb{B} &= \{ |xy_\uparrow xy_\downarrow, 0\rangle, |yz_\uparrow yz_\downarrow, 0\rangle, |zx_\uparrow zx_\downarrow, 0\rangle, \\ &|xy_\uparrow yz_\downarrow, 0\rangle, |xy_\downarrow yz_\uparrow, 0\rangle, |xy_\uparrow zx_\downarrow, 0\rangle, |xy_\downarrow zx_\uparrow, 0\rangle, |yz_\uparrow zx_\downarrow, 0\rangle, |yz_\downarrow zx_\uparrow, 0\rangle, \\ &|xy_\uparrow yz_\uparrow, 0\rangle, |xy_\uparrow zx_\uparrow, 0\rangle, |yz_\uparrow zx_\uparrow, 0\rangle, |xy_\downarrow yz_\downarrow, 0\rangle, |xy_\downarrow zx_\downarrow, 0\rangle, |yz_\downarrow zx_\downarrow, 0\rangle, \\ &|0, xy_\uparrow xy_\downarrow\rangle, |0, yz_\uparrow yz_\downarrow\rangle, \dots, |0, yz_\downarrow zx_\downarrow\rangle \} \\ &= \{|1\rangle, |2\rangle, |3\rangle, \dots, |30\rangle\}. \end{aligned} \quad (3.7)$$

Let H_0 be the matrix $(H_0)_{\alpha\beta} \equiv \langle \alpha | \hat{H}_0 | \beta \rangle$, where $|\alpha\rangle, |\beta\rangle \in \mathbf{B}$. The order of this basis was especially chosen so that H_0 can be written in a block diagonal form

$$H_0 = \begin{pmatrix} 1 & 0 \\ 0 & 1 \end{pmatrix} \otimes \begin{pmatrix} H_3 & & & \\ & H_2 & & \\ & & H_2 & \\ & & & H_2 \\ & & & & (U - 3J_H)\mathbb{I}_{6 \times 6} \end{pmatrix}, \quad (3.8)$$

where the H_3 and H_2 matrices are given respectively by

$$H_3 = \begin{pmatrix} U & J_H & J_H \\ J_H & U & J_H \\ J_H & J_H & U \end{pmatrix}, \quad H_2 = \begin{pmatrix} U - 2J_H & -J_H \\ -J_H & U - 2J_H \end{pmatrix}. \quad (3.9)$$

It is now straightforward to find the eigenvectors of H_0 . Twelve of them are made explicit by the third line of the states of the basis \mathbf{B} (Eq. 3.7). All these states are characterized by electrons occupying different orbitals, but displaying spins with the same orientation. These states display the lowest possible eigenvalues $U - 3J_H$ and illustrates the idea that Hund's coupling favors ferromagnetism between electrons in different orbitals. Three of the eigenvectors of H_0 related with the matrices H_3 are given by:

$$|\psi_{U+2J_H, H_3}\rangle = \frac{1}{\sqrt{3}} (|xy_\uparrow xy_\downarrow, 0\rangle + |yz_\uparrow yz_\downarrow, 0\rangle + |zx_\uparrow zx_\downarrow, 0\rangle) \quad (3.10a)$$

$$|\psi_{U-J_H, H_3}^1\rangle = \frac{1}{\sqrt{2}} (|xy_\uparrow xy_\downarrow, 0\rangle - |yz_\uparrow yz_\downarrow, 0\rangle), \quad (3.10b)$$

$$|\psi_{U-J_H, H_3}^2\rangle = \frac{1}{\sqrt{6}} (|xy_\uparrow xy_\downarrow, 0\rangle + |yz_\uparrow yz_\downarrow, 0\rangle - 2|zx_\uparrow zx_\downarrow, 0\rangle). \quad (3.10c)$$

The other three eigenvectors are obtained by simply changing the doubly occupancy to the other site. Finally, two examples of eigenvectors associated with the matrix H_2 are given by

$$|\psi_{U-3J_H, H_2}\rangle = \frac{1}{\sqrt{2}} (|xy_\uparrow yz_\downarrow, 0\rangle + |xy_\downarrow yz_\uparrow, 0\rangle), \quad (3.11a)$$

$$|\psi_{U-J_H, H_2}\rangle = \frac{1}{\sqrt{2}} (|xy_\uparrow yz_\downarrow, 0\rangle - |xy_\downarrow yz_\uparrow, 0\rangle), \quad (3.11b)$$

and the other eigenvectors are derived by analogy.

The matrix H_{eff}^γ describing the effective Hamiltonian along the bond γ is obtained through the matrix equation

$$H_{\text{eff}}^\gamma = T_{\text{hop}}^\gamma U_{\text{int}} T_{\text{hop}}^{\gamma\dagger}, \quad (3.12)$$

where T_{hop}^γ is the matrix generated by the compound dependent parameters $t_{ij, \alpha\beta}^{(\gamma)}$ in Eq. (3.6) and connects the final states to the doubly occupied intermediate state. The U_{int} matrix results from

the second order perturbation theory and reads

$$U_{\text{int}} = -\sum_{\alpha} \frac{|\alpha\rangle\langle\alpha|}{E_{\alpha}}, \quad (3.13)$$

in which $|\alpha\rangle$ labels the eigenvectors of H_0 discussed above. U_{int} can be written explicitly by first defining the following ratios

$$r_1 = \frac{1}{1-3\eta}, \quad r_2 = \frac{1}{1-\eta}, \quad r_3 = \frac{1}{1+2\eta}, \quad (3.14)$$

in which $\eta = J_H/U$. Then, the U_{int} operator of a double occupied site reads

$$U_{\text{int}} = -\frac{2r_2 + r_3}{3U} \sum_{\alpha} |\alpha_{\uparrow}\alpha_{\downarrow}\rangle \langle\alpha_{\uparrow}\alpha_{\downarrow}| - \frac{r_1 + r_2}{2U} \sum_{\sigma,\sigma',\alpha} |\alpha_{\sigma}(\alpha-1)_{\sigma'}\rangle \langle\alpha_{\sigma}(\alpha-1)_{\sigma'}| \\ - \frac{r_3 - r_2}{3U} \sum_{\alpha \neq \beta} |\alpha_{\uparrow}\alpha_{\downarrow}\rangle \langle\beta_{\uparrow}\beta_{\downarrow}| - \frac{r_1 - r_2}{2U} \sum_{\sigma,\sigma',\alpha} |\alpha_{\sigma}(\alpha-1)_{\sigma'}\rangle \langle\alpha_{\sigma'}(\alpha-1)_{\sigma}|, \quad (3.15)$$

where $|\alpha_{\uparrow}\alpha_{\downarrow}\rangle \langle\alpha_{\uparrow}\alpha_{\downarrow}| = |\alpha_{\uparrow}\alpha_{\downarrow}, 0\rangle \langle\alpha_{\uparrow}\alpha_{\downarrow}, 0| + |0, \alpha_{\uparrow}\alpha_{\downarrow}\rangle \langle 0, \alpha_{\uparrow}\alpha_{\downarrow}|$, etc. Equation (3.12) is the most general expression for t_{2g} Kugel-Khomskii models for singly occupied sites. The next two subsections will apply this equation to derive the minimal Kugel-Khomskii models for two types of existent compounds.

3.2.2 Effective Kugel-Khomskii Model on the fcc lattice

3.2.2.1 Ordered Double Perovskites

I start with the derivation of the minimal model for the magnetism of insulating ordered double perovskites. First, let us understand the structure of these oxides. Consider first compounds in the usual perovskite arrangement with stoichiometric formula ABO_3 . In this formula, A corresponds to an alkaline earth metal or lanthanide, B is a transition metal ion, and O is the oxygen. The structure of the perovskites can be formed starting from the ions B. Each of them are surrounded by six oxygen anions forming an octahedral environment. This environment is then surrounded by eight A cations forming a cubic lattice with crystallographic axis parallel to the vectors connecting the ion B to the oxygens. An ordered double perovskite structure is formed by a partial cation substitution replacing half of the B ions by another species B' . The resulting stoichiometric formula will be always $A_2BB'O_6$, but the cations B and B' can order in three different ways: a rock-salt arrangement, a layered structure, and a columnar ordering. (27) The rock-salt structure is the most common among the three and in this case the cation B and B' are located on a fcc lattice (see Fig. 11a). Several ordered double perovskite compounds were already synthesized with B, B' in different oxidation states and electronic configurations resulting in a great variety of electric, magnetic and thermoelectric phenomena. (27) In this thesis, I focus on rock-salt double perovskites in which B is a nonmagnetic ion and B' is a magnetic ion in a $4d^1$ or $5d^1$ configuration.

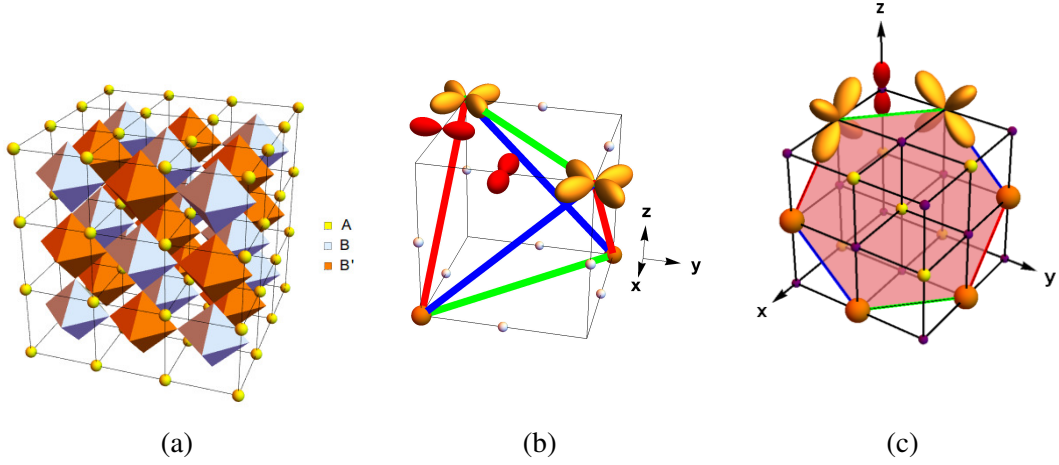


Figure 11 – (a) structure of the rock-salt structure of ordered double perovskite compounds. The B' elements form a fcc lattice. (b) The active orbitals depend upon the overlap of d and p orbitals along the bonds connecting two sites. (c) Representation of active orbitals along a path perpendicular to the z -axis on Kitaev materials. Source: NATORI; DAGHOFER; PEREIRA (1); NATORI; ANDRADE; PEREIRA. (3)

The magnetic interaction in double perovskites arises mainly from superexchange, since the large B'-B' separation weakens direct d - d overlap. There are two conditions for the occurrence of the hopping processes: (i) the t_{2g} orbitals must overlap with a p orbital, and (ii) the two p orbitals in the middle of the path connecting two neighbors must overlap with each other. As indicated by Figure (11b), these two requirements strongly restrict the allowed exchange by selecting the active orbitals in a given bond. To clarify this point, consider the three axis parallel to the primitive vectors of the cubic lattice of the A specie. Let $\gamma = x, y, z$ label the axes; if i and j are nearest neighbors forming a bond perpendicular to γ we find

$$\hat{T}_{ij}^{\gamma} = -t \sum_{\sigma} (d_{i,\gamma,\sigma}^{\dagger} d_{j,\gamma,\sigma} + d_{j,\gamma,\sigma}^{\dagger} d_{i,\gamma,\sigma}), \quad (3.16)$$

where $d_{i,\gamma,\sigma}^{\dagger}$ creates an electron with spin σ and orbital $\alpha\beta$ ($\epsilon_{\alpha\beta\gamma} = 1$) at the site i . In terms of the general notation in Eq. (3.6), Eq. (3.16) states that $t_{ij,\alpha\beta}^{(\gamma)} = 0$ except when $\alpha = \beta = \gamma$.

3.2.2.2 Effective Kugel-Khomskii Model of ordered double perovskites

After finding the hopping Hamiltonian for double perovskites, one can use Eq. (3.12) to find the effective Kugel-Khomskii model of ordered double perovskites. I choose to detail the derivation for bonds on the xy planes for concreteness; the results for different direction γ 's will be obtained by simple change of orbital and planes. The symmetry constraints on Eq. (3.12) also implies that not all two-site states $|\delta_{\sigma}, \epsilon_{\sigma'}\rangle \equiv d_{j,\delta_{\sigma}}^{\dagger} d_{i,\epsilon_{\sigma'}}^{\dagger} |0\rangle$ will contribute to the effective

Hamiltonian. \hat{T}_{ij}^z forces at least one site to be occupied by a xy orbital, otherwise $\hat{T}_{ij}^z |\psi_{ij}\rangle = 0$. I divide the space of states obeying this condition into two subspaces as follows:

1. The subspace spanned by

$$\mathfrak{B}_{xy,xy} = \{|xy_\uparrow, xy_\uparrow\rangle, |xy_\downarrow, xy_\downarrow\rangle, |xy_\uparrow, xy_\downarrow\rangle, |xy_\downarrow, xy_\uparrow\rangle\},$$

in which the both sites are occupied by xy orbitals. The matrix H_{eff}^z in this ordered basis reads

$$[H_{\text{KK}}^z]_{xy,xy} = -\frac{2t^2}{3U}(2r_2 + r_3) \begin{pmatrix} 0 & 0 & 0 & 0 \\ 0 & 0 & 0 & 0 \\ 0 & 0 & 1 & -1 \\ 0 & 0 & -1 & 1 \end{pmatrix}.$$

This can be translated into the following spin-orbital Hamiltonian

$$(H_{\text{KK}}^z)_{xy,xy} = \frac{J}{3}(2r_2 + r_3) \left(\mathbf{S}_i \cdot \mathbf{S}_j - \frac{1}{4} \right) n_{i,xy} n_{j,xy}, \quad (3.17)$$

where

$$J = \frac{4t^2}{U}, \quad (3.18)$$

and

$$n_{i,xy} = d_{i,xy,\uparrow}^\dagger d_{i,xy,\uparrow} + d_{i,xy,\downarrow}^\dagger d_{i,xy,\downarrow}, \quad (3.19a)$$

$$S_i^a n_{i,xy} = \frac{1}{2} \sum_{\sigma,\sigma'} (\sigma^a)_{\sigma,\sigma'} d_{i,xy,\sigma}^\dagger d_{i,xy,\sigma'}. \quad (3.19b)$$

2. The subspace spanned by

$$\mathfrak{B}_{xy,\beta} = \{|xy_\uparrow, \beta_\downarrow\rangle, |xy_\downarrow, \beta_\uparrow\rangle, |\beta_\downarrow, xy_\uparrow\rangle, |\beta_\uparrow, xy_\downarrow\rangle, |xy_\uparrow, \beta_\uparrow\rangle, |xy_\downarrow, \beta_\downarrow\rangle, |\beta_\uparrow, xy_\uparrow\rangle, |\beta_\downarrow, xy_\downarrow\rangle\},$$

where $\beta = yz, zx$. The states in $\mathfrak{B}_{xy,\beta}$ contain one site occupied by xy and other by a different orbital. Notice that the first four vectors in $\mathfrak{B}_{xy,\beta}$ have antiparallel spins, while the remaining states have parallel spins. The matrix of the effective Kugel-Khomskii Hamiltonian in this subspace is written as

$$[H_{\text{KK}}^z]_{xy,\beta} = -\frac{J}{8} \begin{pmatrix} (r_1 + r_2)\mathbb{I}_{4 \times 4} + (r_1 - r_2)\mathbb{I}_{2 \times 2} \otimes \sigma_x & \\ & 2r_1\mathbb{I}_{4 \times 4} \end{pmatrix}.$$

The matrix above can be translated in terms of spin-orbital operators as follows

$$(H_{\text{KK}}^z)_{xy,\beta} = \left[-\frac{J}{4}r_1 \left(\mathbf{S}_i \cdot \mathbf{S}_j + \frac{3}{4} \right) + \frac{J}{4}r_2 \left(\mathbf{S}_i \cdot \mathbf{S}_j - \frac{1}{4} \right) \right] (n_{i,xy} n_{j,\beta} + n_{i,\beta} n_{j,xy}), \quad (3.20)$$

where the number operators $n_{i,\beta}$ and the projected spins $S_i^a n_{i,\beta}$ are defined in analogy to Eq. (3.19).

The sum of $(H_{\text{KK}}^z)_{xy,xy}$, $(H_{\text{KK}}^z)_{xy,yz}$, and $(H_{\text{KK}}^z)_{xy,zx}$ with the single-occupancy condition

$$n_{xy} + n_{yz} + n_{zx} = 1, \quad (3.21)$$

leads to the effective Hamiltonian

$$\begin{aligned} H_{\text{KK}}^{(z)} = & J_{\text{eff}} \left(\mathbf{S}_i \cdot \mathbf{S}_j + \frac{1}{4} \right) n_{i,xy} n_{j,xy} + V n_{i,xy} n_{j,xy} \\ & - J' \mathbf{S}_i \cdot \mathbf{S}_j (n_{i,xy} \bar{n}_{j,xy} + \bar{n}_{i,xy} n_{j,xy}) - \frac{J}{16} (3r_1 + r_2) (n_{i,xy} + n_{j,xy}), \end{aligned} \quad (3.22)$$

where $\bar{n}_{i,xy} = n_{i,yz} + n_{i,zx} = 1 - n_{i,xy}$. The coupling constants are explicitly given by

$$J_{\text{eff}} = \frac{1}{3} (2J_2 + J_3), \quad (3.23a)$$

$$V = \frac{1}{4} \left(\frac{3}{2} J_1 - \frac{5}{6} J_2 - \frac{2}{3} J_3 \right), \quad (3.23b)$$

$$J' = \frac{1}{4} (J_1 - J_2), \quad (3.23c)$$

where $J_i \equiv J r_i$. Notice that all constants in Eq. (3.23) vanish in the limit $J_H/U \rightarrow 0$ with the exception of J_{eff} . The Kugel-Khomskii model describing the magnetism of $4d^1$ and $5d^1$ ordered double perovskites, apart from an unimportant constant term, is given by (139)

$$\begin{aligned} H_{\text{KK,ODP}} = & J_{\text{eff}} \sum_{\langle ij \rangle_\gamma} \left(\mathbf{S}_i \cdot \mathbf{S}_j + \frac{1}{4} \right) n_{i,\gamma} n_{j,\gamma} \\ & + V \sum_{\langle ij \rangle_\gamma} n_{i,\gamma} n_{j,\gamma} \\ & - J' \sum_{\langle ij \rangle_\gamma} \mathbf{S}_i \cdot \mathbf{S}_j (n_{i,\gamma} \bar{n}_{j,\gamma} + \bar{n}_{i,\gamma} n_{j,\gamma}). \end{aligned} \quad (3.24)$$

I end up the subsection pointing out that the effective spin-orbital model derived in Ref. (29) took into account only the states of the basis $\mathfrak{B}_{\gamma,\gamma}$ when deriving the antiferromagnetic exchange. The model in Ref. (29) is thus incomplete, as well as the one studied in Ref. (4). The result was corrected in follow-up articles. (1, 139)

3.2.3 Effective Kugel-Khomskii Model on generalized honeycomb lattices

I now consider the Kugel-Khomskii model derived for Kitaev materials. The defining feature of the crystal structure of these compounds is the edge-sharing of the BO_6 octahedra, where B is a $4/5d^5$ transition metal ion. This geometric feature restrict the virtual electron transfers allowed by symmetry, and is the major responsible for the bond-dependent interactions (see Fig. 11c for an illustration on the honeycomb lattice). The hopping Hamiltonian depending on the orbital and the bond-direction then reads

$$\hat{T} = -t \sum_{\gamma} \sum_{\langle ij \rangle_\gamma} \sum_{\sigma} (d_{i,\alpha,\sigma}^\dagger d_{j,\beta,\sigma} + d_{i,\beta,\sigma}^\dagger d_{j,\alpha,\sigma} + h.c.), \quad (3.25)$$

in which I am following the notation implied by Eq. (3.6).

The Kugel-Khomskii model for the bonds perpendicular to the z axis will be derived explicitly. In sharp contrast to the case of double perovskites, the hopping operator between two nearest neighbor sites, $\hat{T}_{ij}^{(z)}$, annihilates any two-site state of the form $|xy_\sigma, xy_{\sigma'}\rangle$. The hopping also “flips” the orbitals instead of retaining them; thus, operators like $n_{i,\gamma}$ or $\bar{n}_{i,\gamma}$ are not expected. Following the analysis for the double perovskite, I divide the relevant states to the derivation of the Kugel-Khomskii model into three parts

1. Consider first the states $\mathfrak{B}_{yz,zx} = \{|yz_\uparrow, zx_\downarrow\rangle, |yz_\downarrow, zx_\uparrow\rangle, |zx_\uparrow, yz_\downarrow\rangle, |zx_\downarrow, yz_\uparrow\rangle\}$. The hopping leads to an intermediate state given either by $|yz_\uparrow yz_\downarrow\rangle$ or $|zx_\uparrow zx_\downarrow\rangle$. If I consider Eqs. (3.15) and (3.25), I find

$$\begin{aligned} \hat{T}_{ij}^{(z)} U_{\text{int}} \hat{T}_{ij}^{(z)} |yz_\sigma, zx_{\bar{\sigma}}\rangle &= \frac{J}{6} (2r_2 + r_3) (|yz_{\bar{\sigma}}, zx_\sigma\rangle - |yz_\sigma, zx_{\bar{\sigma}}\rangle) \\ &+ \frac{J}{6} (r_2 - r_3) (|zx_\sigma, yz_{\bar{\sigma}}\rangle - |zx_{\bar{\sigma}}, yz_\sigma\rangle) \\ &= \frac{J}{4} [(r_1 + r_2) - (r_1 - r_2)] (|yz_{\bar{\sigma}}, zx_\sigma\rangle - |yz_\sigma, zx_{\bar{\sigma}}\rangle) \\ &+ \frac{J}{6} (r_2 - r_3) (|zx_\sigma, yz_{\bar{\sigma}}\rangle - |zx_{\bar{\sigma}}, yz_\sigma\rangle + |yz_\sigma, zx_{\bar{\sigma}}\rangle - |yz_{\bar{\sigma}}, zx_\sigma\rangle). \end{aligned} \quad (3.26)$$

The other terms are obtained by making the exchange $yz \longleftrightarrow zx$. It is useful to define the operators

$$\pi_i^{0(\gamma)} = \sum_{\sigma} \left(d_{i,\alpha,\sigma}^\dagger d_{i,\alpha,\sigma} + d_{i,\beta,\sigma}^\dagger d_{i,\beta,\sigma} \right), \quad (3.27a)$$

$$\pi_i^{x(\gamma)} = \frac{1}{2} \sum_{\sigma} \left(d_{i,\beta,\sigma}^\dagger d_{i,\alpha,\sigma} + d_{i,\alpha,\sigma}^\dagger d_{i,\beta,\sigma} \right) \equiv \frac{1}{2} \sum_{\sigma} \sum_{\delta,\delta' \in \{\alpha,\beta\}} \sigma_{\delta,\delta'}^x d_{i,\delta,\sigma}^\dagger d_{i,\delta',\sigma}, \quad (3.27b)$$

$$\pi_i^{y(\gamma)} = \frac{i}{2} \sum_{\sigma} \left(-d_{i,\beta,\sigma}^\dagger d_{i,\alpha,\sigma} + d_{i,\alpha,\sigma}^\dagger d_{i,\beta,\sigma} \right) \equiv \frac{1}{2} \sum_{\sigma} \sum_{\delta,\delta' \in \{\alpha,\beta\}} \sigma_{\delta,\delta'}^y d_{i,\delta,\sigma}^\dagger d_{i,\delta',\sigma}, \quad (3.27c)$$

$$\pi_i^{z(\gamma)} = \frac{1}{2} \sum_{\sigma} \left(d_{i,\beta,\sigma}^\dagger d_{i,\beta,\sigma} - d_{i,\alpha,\sigma}^\dagger d_{i,\alpha,\sigma} \right) \equiv \frac{1}{2} \sum_{\sigma} \sum_{\delta,\delta' \in \{\alpha,\beta\}} \sigma_{\delta,\delta'}^z d_{i,\delta,\sigma}^\dagger d_{i,\delta',\sigma}, \quad (3.27d)$$

$$S_i^a \pi_i^{b(\gamma)} = \frac{1}{4} \sum_{\sigma,\sigma'} \sum_{\delta,\delta' \in \{\alpha,\beta\}} \sigma_{\sigma,\sigma'}^a \sigma_{\delta,\delta'}^b d_{i,\delta,\sigma}^\dagger d_{i,\delta',\sigma'}. \quad (3.27e)$$

Then, by defining the operator

$$B_{ij}^{(\gamma)} = \pi_i^{x(\gamma)} \pi_j^{x(\gamma)} + \pi_i^{y(\gamma)} \pi_j^{y(\gamma)} - \pi_i^{z(\gamma)} \pi_j^{z(\gamma)} + \frac{1}{4} \pi_i^{0(\gamma)} \pi_j^{0(\gamma)}, \quad (3.28)$$

it is possible to write (99)

$$(H_{\text{KK}}^z)_{yz_\sigma, zx_{\bar{\sigma}}} = \mathcal{H}_{\alpha,\beta,\sigma,\bar{\sigma}}^{(z)} - \frac{2}{3} (J_2 - J_3) \left(\mathbf{S}_i \cdot \mathbf{S}_j - \frac{1}{4} \right) B_{ij}^{(z)} \quad (3.29)$$

A part of $(H_{\text{KK}}^z)_{yz_\sigma, zx_{\bar{\sigma}}}$ was labeled $\mathcal{H}_{\alpha,\beta,\sigma,\bar{\sigma}}^{(z)}$ and was not written in terms of π and $S\pi$ operators. This will be summed with other terms to be derived later.

2. Next I consider the eight states given by $\mathfrak{B}_{(yz)^2, (zx)^2} = \{|yz_\sigma, yz_{\sigma'}\rangle, |zx_\sigma, zx_{\sigma'}\rangle\}$. The intermediate state have the form $|zx_\sigma yz_{\sigma'}\rangle$, and the second order perturbation theory leads to the following equations

$$\begin{aligned} \hat{T}_{ij}^{(z)} U_{\text{int}} \hat{T}_{ij}^{(z)} |yz_\sigma, yz_{\sigma'}\rangle &= -\frac{J_1 + J_2}{4} (|yz_\sigma, yz_{\sigma'}\rangle - |zx_{\sigma'}, zx_\sigma\rangle) \\ &\quad - \frac{J_1 - J_2}{4} (|yz_{\sigma'}, yz_\sigma\rangle - |zx_\sigma, zx_{\sigma'}\rangle), \end{aligned} \quad (3.30a)$$

$$\begin{aligned} \hat{T}_{ij}^{(z)} U_{\text{int}} \hat{T}_{ij}^{(z)} |zx_\sigma, zx_{\sigma'}\rangle &= -\frac{J_1 + J_2}{4} (|zx_\sigma, zx_{\sigma'}\rangle - |yz_{\sigma'}, yz_\sigma\rangle) \\ &\quad - \frac{J_1 - J_2}{4} (|zx_{\sigma'}, zx_\sigma\rangle - |yz_\sigma, yz_{\sigma'}\rangle). \end{aligned} \quad (3.30b)$$

This part of the Kugel-Khomskii Hamiltonian will be called $\mathcal{H}_{(yz)^2, (zx)^2}^{(z)}$ and will be subdivided in two parts

$$\mathcal{H}_{(yz)^2, (zx)^2}^{(z)} = \mathcal{H}_{\text{I}} + \mathcal{H}_{\text{two-flips}}, \quad (3.31)$$

where \mathcal{H}_{I} concerns with the parts of $\mathcal{H}_{(yz)^2, (zx)^2}^{(z)}$ in which the orbitals are kept fixed, while $\mathcal{H}_{\text{two-flips}}$ changes the orbitals of the two sites.

3. Finally, I consider the 16 states $\{|xy_\sigma, zx_{\sigma'}\rangle, |xy_\sigma, yz_{\sigma'}\rangle, |zx_{\sigma'}, xy_\sigma\rangle, |yz_{\sigma'}, xy_\sigma\rangle\}$ that contain one site occupied by a xy orbital. The doubly occupied intermediate state is given by $|xy_\sigma yz_{\sigma'}\rangle$ or $|xy_\sigma zx_{\sigma'}\rangle$. Second order perturbation theory leads to

$$\hat{T}_{ij}^{(z)} U_{\text{int}} \hat{T}_{ij}^{(z)} |xy_\sigma, zx_{\sigma'}\rangle = -\frac{J}{8} (r_1 + r_2) |xy_\sigma, zx_{\sigma'}\rangle - \frac{J}{8} (r_1 - r_2) |xy_{\sigma'}, zx_\sigma\rangle, \quad (3.32)$$

and the other terms are given by analogy. I find

$$(H_{\text{KK}}^z)_{xy} = -\frac{J_1 + J_2}{8} (\pi_i^{0(\gamma)} \mathcal{P}_j^z + \mathcal{P}_i^z \pi_j^{0(\gamma)}) - \frac{J_1 - J_2}{4} \left(\mathbf{S}_i \cdot \mathbf{S}_j + \frac{1}{4} \right) (\pi_i^{0(\gamma)} \mathcal{P}_j^z + \mathcal{P}_i^z \pi_j^{0(\gamma)}) \quad (3.33)$$

where $\mathcal{P}_i^\gamma = \sum_\sigma d_{i,\gamma,\sigma}^\dagger d_{i,\gamma,\sigma}$, and its combinations with the spin operators are analogous to the ones defined for $\pi^{a(\gamma)}$.

In contrast to the case of the double perovskite, it is not straightforward to write all terms of the Hamiltonian as combinations of spin and number operators. The simplifications are only possible when summing parts of the Hamiltonian in the three different basis with each other. The sum of the \mathcal{H}_{I} in Eq. (3.31) with the Hamiltonian $(H_{\text{KK}}^z)_{xy}$ will give

$$\begin{aligned} \mathcal{H}' &= \mathcal{H}_{\text{I}} + (H_{\text{KK}}^z)_{xy} \\ &= -\frac{1}{8} (J_1 + J_2) (\pi_i^{0(\gamma)} + \pi_j^{0(\gamma)}) - \frac{1}{4} (J_1 - J_2) \left(\mathbf{S}_i \cdot \mathbf{S}_j + \frac{1}{4} \right) (\pi_i^{0(\gamma)} + \pi_j^{0(\gamma)}). \end{aligned} \quad (3.34)$$

Also, the sum of $\mathcal{H}_{\alpha,\beta,\sigma,\bar{\sigma}}^{(z)}$ and $\mathcal{H}_{\text{two-flips}}$ gives

$$\begin{aligned} \mathcal{H}'' &= \mathcal{H}_{\alpha,\beta,\sigma,\bar{\sigma}}^{(z)} + \mathcal{H}_{\text{two-flips}} \\ &= (J_1 + J_2) \left(\mathbf{S}_i \cdot \mathbf{S}_j + \frac{1}{4} \right) A_{ij}^{(z)} + \frac{J_1 - J_2}{2} A_{ij}^{(z)}, \end{aligned} \quad (3.35)$$

where

$$A_{ij}^{(\gamma)} = \pi_i^{x(\gamma)} \pi_j^{x(\gamma)} - \pi_i^{y(\gamma)} \pi_j^{y(\gamma)} - \pi_i^{z(\gamma)} \pi_j^{z(\gamma)} + \frac{1}{4} \pi_i^{0(\gamma)} \pi_j^{0(\gamma)}. \quad (3.36)$$

The Kugel-Khomskii Hamiltonian $H_{\text{KK,KM}}$ is obtained by gathering all the terms written above and is expressed by (142)

$$\begin{aligned} H_{\text{KK,KM}} = & \frac{J_1 + J_2}{2} \sum_{\langle ij \rangle_\gamma} \left(2\mathbf{S}_i \cdot \mathbf{S}_j + \frac{1}{2} \right) A_{ij}^{(\gamma)} \\ & - \frac{J_2 - J_3}{3} \sum_{\langle ij \rangle_\gamma} \left(2\mathbf{S}_i \cdot \mathbf{S}_j - \frac{1}{2} \right) B_{ij}^{(\gamma)} \\ & + \frac{J_1 - J_2}{2} \sum_{\langle ij \rangle_\gamma} \left[A_{ij}^{(\gamma)} - \frac{1}{2} \left(\mathbf{S}_i \pi_i^{0(\gamma)} \cdot \mathbf{S}_j + \mathbf{S}_i \cdot \mathbf{S}_j \pi_j^{0(\gamma)} \right) \right]. \end{aligned} \quad (3.37)$$

The terms proportional to $\pi_i^{0(\gamma)}$ were neglected in Eq. (3.37), since their sum will give a constant due to Eq. (3.21).

I emphasize that this Kugel-Khomskii Hamiltonian is valid for t_{2g} systems characterized by singly occupied ions in the characteristic lattices of Kitaev materials, whether they are d^1 or d^5 compounds. The only difference is on whether the creation and annihilation operators used to express the spin-orbital operators are electrons or holes.

3.3 Strong Spin-Orbit Coupling in Transition Metal Ions

It is easy to verify that the Kugel-Khomskii Hamiltonians in Eq. (3.24) and Eq. (3.37) display a global SU(2) symmetry related to a global rotation of the electronic spin. The bond-dependent parts of the Hamiltonians are related to the orbital operators $\pi^{(\gamma)}$ and their physical origin traces back to the spatial distribution of the orbital wavefunctions. Now, I study the effect of including the spin-orbit coupling Eq. (2.43) in the limit of large λ for the Kugel-Khomskii models studied above.

3.3.1 Degrees of Freedom in the Strong Spin-Orbit Coupling Limit

The eigenstates of the spin-orbit coupling Hamiltonian (Eq. (2.43)) were already discussed in Subsection 2.2.4.1. Let us now focus on the $j = 3/2$, or equivalently, the B_s and C_s orbitals in Eq. (2.45). The expression for these orbitals in terms of annihilation operators of l^z eigenstates will be repeated for convenience:

$$B_s = \sqrt{\frac{2}{3}} d_{0,-s} + \frac{1}{\sqrt{3}} d_{-2s,s}, \quad (3.38a)$$

$$C_s = d_{2s,s}. \quad (3.38b)$$

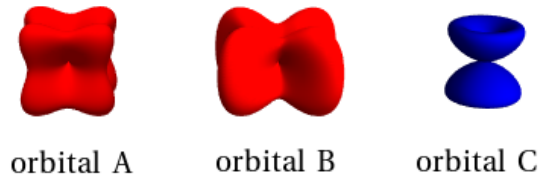


Figure 12 – Density profiles of the eigenstates of the spin-orbit coupling Hamiltonian.
Source: NATORI; DAGHOFER; PEREIRA. (1)

A sketch of the electronic distribution for these orbitals is given in Fig. 12. The B and C states are degenerate in the absence of distortion and are equivalent to the eigenstates $|j, m_j\rangle$ of \mathbf{j}^2 and j^z as follows:

$$|B_\uparrow\rangle = \left| \frac{3}{2}, -\frac{1}{2} \right\rangle, \quad (3.39a)$$

$$|B_\downarrow\rangle = \left| \frac{3}{2}, \frac{1}{2} \right\rangle, \quad (3.39b)$$

$$|C_\uparrow\rangle = \left| \frac{3}{2}, \frac{3}{2} \right\rangle, \quad (3.39c)$$

$$|C_\downarrow\rangle = \left| \frac{3}{2}, -\frac{3}{2} \right\rangle. \quad (3.39d)$$

It is sometimes convenient to work with the states on the $j = 3/2$ subspace in terms of two $s = 1/2$ pseudospin operators acting on the $\{B, C\}$ orbitals and the $s = \uparrow, \downarrow$ index for Kramers's pairs. (4) The pseudospin indices are straightforwardly derived. I also define a pseudo-orbital index τ like:

$$\tau = \begin{cases} -\frac{1}{2}, & \text{for } B, \\ +\frac{1}{2}, & \text{for } C. \end{cases} \quad (3.40)$$

In terms of $|s, \tau\rangle$ vectors, $|B_s\rangle$ and $|C_s\rangle$ are given by

$$|B_\uparrow\rangle = \left| \frac{1}{2}, -\frac{1}{2} \right\rangle, \quad (3.41a)$$

$$|B_\downarrow\rangle = \left| -\frac{1}{2}, -\frac{1}{2} \right\rangle, \quad (3.41b)$$

$$|C_\uparrow\rangle = \left| \frac{1}{2}, \frac{1}{2} \right\rangle, \quad (3.41c)$$

$$|C_\downarrow\rangle = \left| -\frac{1}{2}, \frac{1}{2} \right\rangle. \quad (3.41d)$$

A simple relation between the indices m_j , s and τ can be derived by comparing Eq. (3.39) and Eq. (3.41). This relation is formalized by defining the operators s^z and τ^z through their action on $|s, \tau\rangle$ vectors:

$$s^z |s, \tau\rangle = s |s, \tau\rangle, \quad (3.42a)$$

$$\tau^z |s, \tau\rangle = \tau |s, \tau\rangle. \quad (3.42b)$$

The j^z operator then reads

$$j^z = s^z + 4s^z\tau^z. \quad (3.43)$$

The fifteen operators $\{s^a, \tau^b, s^a\tau^b\}$ are then defined in second quantization as:

$$s^a = \frac{1}{2}\xi^\dagger(\mathbb{I} \otimes \sigma^a)\xi, \quad (3.44a)$$

$$\tau^a = \frac{1}{2}\xi^\dagger(\sigma^a \otimes \mathbb{I})\xi, \quad (3.44b)$$

$$s^a\tau^b = \frac{1}{4}\xi^\dagger(\sigma^b \otimes \sigma^a)\xi, \quad (3.44c)$$

where $\xi \equiv (C_\uparrow, C_\downarrow, B_\uparrow, B_\downarrow)^t$, σ^a are Pauli matrices and \mathbb{I} is the 2×2 identity matrix. The pseudospin and pseudo-orbital operators obey the SU(2) algebra while commuting with each other:

$$[s^a, s^b] = i\epsilon^{abc}s^c, \quad (3.45a)$$

$$[\tau^a, \tau^b] = i\epsilon^{abc}\tau^c, \quad (3.45b)$$

$$[s^a, \tau^b] = 0. \quad (3.45c)$$

Similar spin and orbital operators are used to describe Kugel-Khomskii models for e_g orbitals without SOC. (40–43, 143–146) These models possess an operator \mathbf{S} for the electronic spin and an orbital operator \mathbf{T} acting on the space of the orbitals $d_{3z^2-r^2}$ and $d_{x^2-y^2}$. The operators \mathbf{s} and $\boldsymbol{\tau}$ defined here have the same mathematical properties, but they act on different Hilbert spaces. The “spins” of the \mathbf{s} operator label the Kramers pairs in Eq. (2.45), and the orbitals $\{B, C\}$ forming the Hilbert space of $\boldsymbol{\tau}$ are linear combinations of t_{2g} orbitals.

3.3.2 Symmetry analysis of the multipole operators

The operators $(\mathbf{s}, \boldsymbol{\tau})$ can be used to rewrite any $j = 3/2$ Hermitian operator. I have explicitly calculated the expressions for all multipoles and explicit them in Table 1. (1) Auxiliary linear combinations of τ^x and τ^z were introduced to facilitate the expression of some operators. They read as follows:

$$\tau^{xy} = \tau^z, \quad (3.46a)$$

$$\tau^{yz(zx)} = \frac{1}{2}(-\tau^z \pm \sqrt{3}\tau^x), \quad (3.46b)$$

$$\bar{\tau}^{xy} = \tau^x, \quad (3.46c)$$

$$\bar{\tau}^{yz(zx)} = -\frac{1}{2}(\pm\sqrt{3}\tau^z + \tau^x). \quad (3.46d)$$

According to Table 1, \mathbf{s} is a linear combination of dipole and octupole moments of \mathbf{J} in the Γ_4 representation. Similarly, τ^x and τ^z correspond to quadrupoles in the Γ_3 representation. The component τ^y appears separately as a one-dimensional representation Γ_2 . The symmetry analysis

Table 1 – Operators describing active multipoles within a cubic Γ_8 quartet. Bars over functions of \mathbf{J} indicate the symmetrization with respect to all the possible permutations of the indices, e.g., $\overline{j_x j_y^2} = j_x j_y^2 + j_y j_x j_y + j_y^2 j_x$. The operators τ^{xy} , τ^{yz} , τ^{zx} , $\overline{\tau^{xy}}$, $\overline{\tau^{yz}}$, $\overline{\tau^{zx}}$ are explicitly given in Eq. (3.46)

Moment	Symmetry	\mathbf{j} multipoles	$(\mathbf{s}, \boldsymbol{\tau})$ multipoles
Dipoles	Γ_4	j^x	$s^x(1 + 4\tau^{yz})$
		j^y	$-s^y(1 + 4\tau^{xz})$
		j^z	$s^z(1 + 4\tau^{xy})$
Quadrupoles	Γ_3	$Q_{3z^2-r^2} = [3(j^z)^2 - \mathbf{j}^2] / \sqrt{3} \equiv \hat{O}_2^0$	$2\sqrt{3}\tau^z$
		$Q_{x^2-y^2} = (j^x)^2 - (j^y)^2 \equiv \hat{O}_2^2$	$2\sqrt{3}\tau^x$
	Γ_5	$Q_{xy} = \frac{1}{2}j^x j^y \equiv \hat{O}_2^{-2}$	$2\sqrt{3}s^z \tau^y$
		$Q_{yz} = \frac{1}{2}j^y j^z \equiv \hat{O}_2^{-1}$	$2\sqrt{3}s^x \tau^y$
		$Q_{xz} = \frac{1}{2}j^x j^z \equiv \hat{O}_2^1$	$-2\sqrt{3}s^y \tau^y$
	Octupoles	Γ_2	$T^{xyz} = \frac{\sqrt{15}}{6} \overline{j^x j^y j^z}$
Γ_4		$T_a^x = (j^x)^3 - \frac{1}{2}(\overline{j^x(j^y)^2} + \overline{(j^z)^2 j^x})$	$3s^x(1 - \tau^{yz})$
		$T_a^y = (j^y)^3 - \frac{1}{2}(\overline{j^y(j^z)^2} + \overline{(j^x)^2 j^y})$	$-3s^y(1 - \tau^{xz})$
		$T_a^z = (j^z)^3 - \frac{1}{2}(\overline{j^z(j^x)^2} + \overline{(j^y)^2 j^z})$	$3s^z(1 - \tau^{xy})$
Γ_5		$T_b^x = \frac{\sqrt{15}}{6} [\overline{j^x(j^y)^2} - \overline{(j^z)^2 j^x}]$	$3\sqrt{5}s^x \overline{\tau^{yz}}$
		$T_b^y = \frac{\sqrt{15}}{6} [\overline{j^y(j^z)^2} - \overline{(j^x)^2 j^y}]$	$-3\sqrt{5}s^y \overline{\tau^{xz}}$
	$T_b^z = \frac{\sqrt{15}}{6} [\overline{j^z(j^x)^2} - \overline{(j^y)^2 j^z}]$	$3\sqrt{5}s^z \overline{\tau^{xy}}$	

Source: Adapted from NATORI; DAGHOFER; PEREIRA (1); SANTINI et al. (147); SHIINA et al. (148)

of these operators leading to this splitting in terms of irreducible representations is presented in Appendix A.

I now discuss the effect of conjugation of time-reversal operator Θ over \mathbf{s} and $\boldsymbol{\tau}$. Each pseudospin component s^α is a linear combination of the components of the dipole J^α and the octupole T_a^α . From $\Theta^{-1}\mathbf{J}\Theta = -\mathbf{J}$ and $\Theta^{-1}\mathbf{T}_a\Theta = -\mathbf{T}_a$, it is clear that \mathbf{s} is odd under time reversal. The τ^y also differs from (τ^x, τ^z) with respect to time-reversal. While the quadrupoles are even under Θ , τ^y is reversed by this operation, that is:

$$\Theta^{-1}\mathbf{s}\Theta = -\mathbf{s}, \quad \Theta^{-1}\boldsymbol{\tau}\Theta = (\tau^x, -\tau^y, \tau^z). \quad (3.47)$$

This implies that $s\tau^y$ is even under time reversal. Consequently, it does not couple with a magnetic field in contrast to $s\tau^x$ and $s\tau^z$.

The symmetry considerations are also important to understand what can be experimentally measured with magnetic INS. The interaction of the neutron spin and the sample is equivalent to a coupling between an effective magnetic field and the degrees of freedom of the magnet; hence, the neutron couple only to operators that are odd under time-reversal. The discussion here shows that τ^x , τ^z and $s\tau^y$ cannot couple to a magnetic field, and therefore are not measured through neutron scattering. Furthermore, INS does not couple to the pseudospins, but to the dipoles \mathbf{j} . Part of the motivation to investigate RIXS responses was to verify if this new technique could be

used to investigate the dynamics of the pseudospins and pseudo-orbital directly. I have found that this is in principle possible, provided that the polarizations are controlled. (1)

3.3.3 Double perovskite model in the strong spin-orbit coupling limit

Up until now, the Hamiltonian describing the magnetism of ordered double perovskites is given by

$$H = H_{\text{KK,ODP}} - \lambda \sum_i \mathbf{l}_i \cdot \mathbf{S}_i, \quad (3.48)$$

where $H_{\text{KK,ODP}}$ is in Eq. (3.24). Taking the large λ limit, we project H to the states $|s^z, \tau^z\rangle$ described in the previous subsection. This process is tedious, but straightforward. Let us fix a notation: any \mathcal{O} operator is projected to the $j = 3/2$ manifold through the projector $\mathcal{P}_{3/2}$ and we will denote it $\tilde{\mathcal{O}} \equiv \mathcal{P}_{3/2} \mathcal{O} \mathcal{P}_{3/2}$. For double perovskites, the operators will arise from projections of the number operator of a γ orbital, $n_{i,\gamma}$, or the spin residing in this orbital $\mathbf{S}_{i,\gamma}$. They are explicitly given by (29):

$$\tilde{n}_{i,\gamma} = \frac{2}{3} \left(\frac{1}{2} - \tau_i^{\alpha\beta} \right), \quad (3.49a)$$

$$\begin{aligned} \tilde{\mathbf{S}}_{i,xy} &= \frac{2}{3} s_i^x \left(\frac{1}{2} - \tau_i^{xy} \right) \hat{\mathbf{x}} - \frac{2}{3} s_i^y \left(\frac{1}{2} - \tau_i^{xy} \right) \hat{\mathbf{y}} - \frac{2}{3} s_i^z \left(\frac{1}{2} - \tau_i^{xy} \right) \hat{\mathbf{z}} \\ &= \left(\frac{2J_i^x + T_{a,i}^x}{15} \right) \hat{\mathbf{x}} + \left(\frac{2J_i^y + T_{a,i}^y}{15} \right) \hat{\mathbf{y}} + \left(\frac{J_i^z - 2T_{a,i}^z}{15} \right) \hat{\mathbf{z}} \\ &\quad + \frac{\sqrt{15}}{45} T_{b,i}^x \hat{\mathbf{x}} - \frac{\sqrt{15}}{45} T_{b,i}^y \hat{\mathbf{y}}, \end{aligned} \quad (3.49b)$$

$$\begin{aligned} \tilde{\mathbf{S}}_{i,yz} &= -\frac{2}{3} s_i^x \left(\frac{1}{2} - \tau_i^{yz} \right) \hat{\mathbf{x}} - \frac{2}{3} s_i^y \left(\frac{1}{2} - \tau_i^{yz} \right) \hat{\mathbf{y}} + \frac{2}{3} s_i^z \left(\frac{1}{2} - \tau_i^{yz} \right) \hat{\mathbf{z}} \\ &= \left(\frac{J_i^x - 2T_{a,i}^x}{15} \right) \hat{\mathbf{x}} + \left(\frac{2J_i^y + T_{a,i}^y}{15} \right) \hat{\mathbf{y}} + \left(\frac{2J_i^z + T_{a,i}^z}{15} \right) \hat{\mathbf{z}} \\ &\quad + \frac{\sqrt{15}}{45} T_{b,i}^y \hat{\mathbf{y}} - \frac{\sqrt{15}}{45} T_{b,i}^z \hat{\mathbf{z}}, \end{aligned} \quad (3.49c)$$

$$\begin{aligned} \tilde{\mathbf{S}}_{i,zx} &= \frac{2}{3} s_i^x \left(\frac{1}{2} - \tau_i^{zx} \right) \hat{\mathbf{x}} + \frac{2}{3} s_i^y \left(\frac{1}{2} - \tau_i^{zx} \right) \hat{\mathbf{y}} + \frac{2}{3} s_i^z \left(\frac{1}{2} - \tau_i^{zx} \right) \hat{\mathbf{z}} \\ &= \left(\frac{2J_i^x + T_{a,i}^x}{15} \right) \hat{\mathbf{x}} + \left(\frac{J_i^y - 2T_{a,i}^y}{15} \right) \hat{\mathbf{y}} + \left(\frac{2J_i^z + T_{a,i}^z}{15} \right) \hat{\mathbf{z}} \\ &\quad + \frac{\sqrt{15}}{45} T_{b,i}^z \hat{\mathbf{z}} - \frac{\sqrt{15}}{45} T_{b,i}^x \hat{\mathbf{x}}. \end{aligned} \quad (3.49d)$$

Notice that the projection of the spin operator $\mathbf{S} = \mathbf{S}_{xy} + \mathbf{S}_{yz} + \mathbf{S}_{zx}$ is directly proportional to the $j = 3/2$ angular momentum operator and is given by

$$\mathcal{P}_{3/2} \mathbf{S} \mathcal{P}_{3/2} = \frac{1}{3} \mathbf{J}. \quad (3.50)$$

Substituting Eq. (3.49) in Eq. (3.24), the effective model is written as

$$\mathcal{H}_{\text{ODP}} = \mathcal{H}_{\text{SU}(2)} + \mathcal{H}_V + \mathcal{H}_{\text{fer}}, \quad (3.51)$$

in which

$$\mathcal{H}_{\text{SU}(2)} = \frac{4}{9} J_{\text{eff}} \sum_{\langle ij \rangle_\gamma} \left(\mathbf{s}_i \cdot \mathbf{s}_j + \frac{1}{4} \right) \left(\frac{1}{2} - \tau_i^{\alpha\beta} \right) \left(\frac{1}{2} - \tau_j^{\alpha\beta} \right), \quad (3.52)$$

$$\mathcal{H}_V = \frac{4}{9} V \sum_{\langle ij \rangle_\gamma} \left(\frac{1}{2} - \tau_i^{\alpha\beta} \right) \left(\frac{1}{2} - \tau_j^{\alpha\beta} \right), \quad (3.53)$$

$$\begin{aligned} \mathcal{H}_{\text{fer}} = & \frac{8}{9} J' \sum_{\langle ij \rangle_\gamma} \mathbf{s}_i \cdot \mathbf{s}_j \left(\frac{1}{2} - \tau_i^{\alpha\beta} \right) \left(\frac{1}{2} - \tau_j^{\alpha\beta} \right) \\ & - \frac{J'}{45} \sum_{\langle ij \rangle_\gamma} (4\mathbf{J}_i \cdot \mathbf{J}_j - 2J_i^\gamma J_j^\gamma + \mathbf{T}_{a,i} \cdot \mathbf{J}_j + \mathbf{J}_i \cdot \mathbf{T}_{a,j} - 3T_{a,i}^\gamma J_j^\gamma - 3J_i^\gamma T_{a,j}^\gamma) \\ & - \frac{\sqrt{15}J'}{135} \sum_{\langle ij \rangle_\gamma} (T_{b,i}^\alpha J_j^\alpha + J_i^\alpha T_{b,j}^\alpha - T_{b,i}^\beta J_j^\beta - J_i^\beta T_{b,j}^\beta). \end{aligned} \quad (3.54)$$

Here I used the Levi-Civita symbol and assumed $\epsilon_{\alpha\beta\gamma} = 1$. In these equations, the coupling constants J_{eff} , V and J' were defined in Eq. (3.23) and the operators τ^γ were defined in Eq. (3.46).

The $\mathcal{H}_{\text{SU}(2)}$ makes the hidden SU(2) symmetry found in Ref. (29) explicit. The operator

$$\mathbf{s}_{\text{tot}} = \sum_i \mathbf{s}_i \quad (3.55)$$

is a conserved quantity, i.e., $[\mathcal{H}_{\text{SU}(2)}, \mathbf{s}_{\text{tot}}] = 0$. The $\left(\frac{1}{2} - \tau_i^{\alpha\beta} \right) \left(\frac{1}{2} - \tau_j^{\alpha\beta} \right)$ operators are formally identical to the operators of the 120° compass models (45), which were first discussed as part of the Hamiltonian of e_g Kugel-Khomskii models in cubic lattices. (44, 99, 143) This similarity is explained because the transformations of (τ^x, τ^z) under the rotations of the cubic group O are exactly the same as the ones of $d_{x^2-y^2}$ and $d_{3z^2-r^2}$ under the same operations (see Appendix A and Ref. (69)) \mathcal{H}_V is similar to the term derived from the interaction between electric quadrupoles in double perovskites Ref. (29), but this time generated by a non-vanishing Hund's coupling of the $4/5 d^1$ ion. The \mathcal{H}_{fer} is formally the ‘‘ferromagnetic’’ Hamiltonian discussed in Ref. (29), and clearly display an anisotropy both on the pseudo-orbital and the pseudospin operators. Its first line is similar to $\mathcal{H}_{\text{SU}(2)}$ and is still invariant under Eq. (3.55). The second line displays the interactions between dipoles and octupoles in the Γ_4 irreducible representation. Finally, the third line is the interaction between the effective angular momentum \mathbf{J} and the Γ_5 octupole. It can be checked that this interaction is consistent with the O_h symmetry.

I must warn about some differences between the Hamiltonian derived in this work and the one studied in Ref. (29). As stated in Subsection 3.2.2.2, the model derivation in Ref. (29)

was incomplete. The SU(2)-symmetric limit in this case reads

$$\mathcal{H}'_{SU(2)} = K \sum_{\langle ij \rangle_\gamma} \left(\mathbf{s}_i \cdot \mathbf{s}_j - \frac{1}{4} \right) \left(\frac{1}{2} - \tau_i^{\alpha\beta} \right) \left(\frac{1}{2} - \tau_j^{\alpha\beta} \right), \quad (3.56)$$

where $K \propto t^2/U$. Ref. (29) neglected the part of the effective Hamiltonian given by Eq. (3.20). The projection of Eq. (3.20) to the $j = 3/2$ manifold (and $J_H = 0$) gives rise to a pure quadrupolar interaction that explains the difference between Eq. (3.56) and Eq. (3.52). The origin of the quadrupolar and ferromagnetic interactions is also explained differently. In the derivation discussed in this thesis, I only considered the in-site electrostatic interaction to construct the model. The model in Ref. (29) attributed the quadrupolar Hamiltonian to the electric quadrupole-quadrupole interactions of the extended molecular orbitals surrounding the $4/5d$ orbitals. The so-called ferromagnetic term was attributed to the electrostatic repulsion in the oxygen sites, not in the transition metal ions. The results displayed here complement the previous work on double perovskites and give an alternative explanation for the previously derived multipolar interactions.

After stating the difference between the model derived here and in Ref. (29), I still find that the two models are conceptually very similar and that some of the physical aspects discussed in (29) will be valid in our study. This subsection then closes with a summary of some arguments used in favor of a possible QSOL ground state of $\mathcal{H}'_{SU(2)}$. (29) A variational analysis of possible mean-field states was first performed with a strong anisotropy term

$$\mathcal{H}_{\text{ani}} = -D \sum_i (J_i^z)^2 = -D \sum_i (s_i^z (1 + 4\tau_i^z))^2. \quad (3.57)$$

The parameter D obeys the condition $|D| \gg J_{\text{eff}}, J', V$ and $|D| \ll \lambda$. Notice that $D > 0$ favors states with $\tau^z = +1/2$ (C orbitals), while $D < 0$ favors $\tau^z = -1/2$ (B orbitals), i.e., the anisotropy favors a “ferromagnetic” quadrupolar order. The Hamiltonian in Eq. (3.51) in this limit depends only on \mathbf{s} and ordered states can be proposed using the Luttinger-Tisza method (149), which replaces the pseudospins by classical variables and find the ground state of this lattice problem. The ground states found through this methodology comprise two-sublattice structure with an ordering wave vector equivalent to $\mathbf{Q} = 2\pi(1, 0, 0)$. Four different ordered states were defined with this methodology. We will be interested only in the limit of vanishing Hund’s coupling $\mathcal{H}'_{SU(2)}$. A state favoring $\tau^z = +1/2$ ($J^z = +3/2$) with a Néel order on the (s^x, s^y) -plane was found. The correction to the order parameter of this state was found to be greater than the maximal physical value of this parameter at $\mathcal{H}'_{SU(2)}$. Therefore, the mean field theory was found to be at least quantitatively invalid and a ground state incorporating quantum fluctuations could be proposed. It is reasonable to consider that the enhancement of fluctuations is directly associated with the global SU(2) symmetry, which is the same for $\mathcal{H}'_{SU(2)}$ and $\mathcal{H}_{SU(2)}$. This is the result used in considering the possibility of a QSOL in double perovskites in Refs. (1, 4)

3.3.4 Generalized Honeycomb Models in the strong spin-orbit coupling limit

I now turn to the model describing the magnetism of Kitaev material-like compounds that are either in the honeycomb lattice or one of its generalizations. The starting point is

$$H = H_{\text{KK,KM}} - \lambda \sum_i \mathbf{l}_i \cdot \mathbf{S}_i, \quad (3.58)$$

where $H_{\text{KK,KM}}$ was given in Eq. (3.37). The strong SOC limit justifies a projection to the $j = 3/2$ manifold. Following the same arguments given in Subsection 3.3.3, the derived Hamiltonian becomes

$$\begin{aligned} \mathcal{H}_{\text{KM}} = & J_a \sum_{\langle ij \rangle_\gamma} \left[2 (2s_i^\gamma s_j^\gamma - \mathbf{s}_i \cdot \mathbf{s}_j) + \frac{1}{2} \right] \left[2 (2\tau_i^y \tau_j^y - \boldsymbol{\tau}_i \cdot \boldsymbol{\tau}_j) + \frac{1}{2} \right] \\ & + J_b \sum_{\langle ij \rangle_\gamma} \left[2 (2s_i^\gamma s_j^\gamma - \mathbf{s}_i \cdot \mathbf{s}_j) - \frac{1}{2} \right] \left[2\boldsymbol{\tau}_i \cdot \boldsymbol{\tau}_j - \frac{1}{2} \right] \\ & - 2J_c \sum_{\langle ij \rangle_\gamma} \left(\tau_i^{\beta\gamma} \tau_j^{\gamma\alpha} + \tau_i^{\gamma\alpha} \tau_j^{\beta\gamma} \right) \\ & + 12J_c \sum_{\langle ij \rangle_\gamma} s_i^\gamma s_j^\gamma \tau_i^y \tau_j^y \\ & - \frac{3}{5} J_c \sum_{\langle ij \rangle_\gamma} (2J_i^\gamma J_j^\gamma + \mathbf{J}_i \cdot \mathbf{J}_j) + \frac{J_c}{10} \sum_{\langle ij \rangle_\gamma} (\mathbf{T}_{a,i} \cdot \mathbf{J}_j - 3T_{a,i}^\gamma J_j^\gamma + (i \longleftrightarrow j)) \\ & + J_c \frac{\sqrt{15}}{30} \sum_{\langle ij \rangle_\gamma} \left(T_{b,i}^\alpha J_j^\alpha - T_{b,i}^\beta J_j^\beta + (i \longleftrightarrow j) \right), \end{aligned} \quad (3.59)$$

in which I conveniently used a mixture of $(\mathbf{s}, \boldsymbol{\tau})$ operators and the multipoles given in Table 1. The coupling constants are defined by

$$J_a = \frac{J_1 + J_2}{12}, \quad (3.60)$$

$$J_b = \frac{J_2 - J_3}{18}, \quad (3.61)$$

$$J_c = \frac{J_1 - J_2}{18}. \quad (3.62)$$

Eq. (3.59) is considerably more complicated than the equivalent spin-orbital for double perovskites. A good starting point to analyze it is from the vanishing Hund's coupling limit, where $J_b = J_c = 0$. In this limit, I found

$$\mathcal{H}_{\text{SU(4)}} = K \sum_{\langle ij \rangle_\gamma} \left[2 (2s_i^\gamma s_j^\gamma - \mathbf{s}_i \cdot \mathbf{s}_j) + \frac{1}{2} \right] \left[2 (2\tau_i^y \tau_j^y - \boldsymbol{\tau}_i \cdot \boldsymbol{\tau}_j) + \frac{1}{2} \right], \quad (3.63)$$

where $K = 2t^2/(3U) = J/6$.

A transformation on the pseudospin and pseudo-orbital operators can be used to uncover the SU(4) symmetry of Eq. (3.63) that was suggested by its label $\mathcal{H}_{\text{SU}(4)}$. For clarity, let us focus on the usual honeycomb lattice at this point. We know that the four-sublattice rotation trick originally defined for the triangular lattice (see Eq. (2.47)) can also be defined on the honeycomb, where it reads

$$\tilde{\mathbf{s}}_i = \begin{cases} \mathbf{s}_i, & \text{if } i \in A_1, \\ (-s_i^x, -s_i^y, s_i^z), & \text{if } i \in A_2, \\ (s_i^x, -s_i^y, -s_i^z), & \text{if } i \in A_3, \\ (-s_i^x, s_i^y, -s_i^z), & \text{if } i \in A_4. \end{cases} \quad (3.64)$$

The four sublattices can be visualized in Fig. 9a and are indicated by different symbols. Since the honeycomb lattice is also bipartite, it is possible to define a two-sublattice transformation on $\boldsymbol{\tau}$ like

$$\tilde{\boldsymbol{\tau}}_i = \begin{cases} \boldsymbol{\tau}_i, & i \in A_r \text{ with } r \text{ odd}, \\ (-\tau_i^x, \tau_i^y, -\tau_i^z), & i \in A_r \text{ with } r \text{ even}. \end{cases} \quad (3.65)$$

Applying Eq. (3.64) and Eq. (3.65) on Eq. (3.63)

$$\mathcal{H}_{\text{SU}(4)} = K \sum_{\langle ij \rangle} \left(2\tilde{\mathbf{s}}_i \cdot \tilde{\mathbf{s}}_j + \frac{1}{2} \right) \left(2\tilde{\boldsymbol{\tau}}_i \cdot \tilde{\boldsymbol{\tau}}_j + \frac{1}{2} \right). \quad (3.66)$$

This is the familiar form of SU(4)-symmetric spin-orbital models as studied, for instance, in Refs. (40, 41, 43, 146, 150, 151), and is sometimes called the SU(4) Heisenberg model. This large symmetry can be verified by first confirming that the set $\{\tilde{s}_i^\alpha, \tilde{\tau}_i^\beta, \tilde{s}_i^\alpha \tilde{\tau}_i^\beta\}$ constitute the 15 generators of the SU(4) group and then checking that $\sum_i \tilde{s}_i^\alpha, \sum_i \tilde{\tau}_i^\beta, \sum_i \tilde{s}_i^\alpha \tilde{\tau}_i^\beta$ are conserved quantities. (40) The work discussed here distinguishes itself from all the previous ones, since the others had Mott insulators with doubly degenerate orbitals and negligible SOC as the starting point. Here, the starting point was a triply degenerate t_{2g} orbital and the strong spin-orbit coupling plays an essential role in the emergence of the SU(4) symmetry in the $j = 3/2$ subspace.

This model emergent symmetry in the limit of vanishing Hund's coupling was independently discussed in Ref. (39) through a complementary approach. In that work, a gauge transformation was applied on the $j = 3/2$ orbitals to demonstrate that the Hubbard model (with $J_H = 0$) display a global SU(4) symmetry. This was used as a starting point to generalize the LSMA theorem generalization previously discovered by Oshikawa. (136) A LSMA constraint was derived for systems with arbitrary SU(N) symmetry, and then specialized for models in lattices with nonsymmorphic symmetries observed on the three-dimensional generalizations of the honeycomb lattice. It was then shown that the LSMA constraint would apply for several of these lattices and ensure a nontrivial ground state, that is, a state with topological order, SSB, or gapless QSOL. A specific compound implementing the model (α -ZrCl₃) was referred in that paper. Following the work of one of the authors on alternative implementations of the Kitaev

model (108), metal-organic frameworks was mentioned as structures that could be engineered to implement this model.

The work discussed here gives a geometrical approach to understand the emergence of the SU(4) symmetry and discusses the effects of the Hund's coupling perturbations. In regard to the first issue, I showed that the emergent symmetry appears in models defined on bipartite lattices and that allows a spatially dependent spin transformation like Eq. (3.64). The bipartite lattice condition is satisfied by all tricoordinated and tridimensional lattices studied for Kitaev materials, with the exception of a lattice dubbed (9,3)a. (107) The possibility of defining a transformation like (3.64) is less evident. The selective rotation of the spin degree of freedom on four sublattices is formally known as Klein transformation due to the mapping of lattice links and on-site pseudospin rotations with the discrete Klein group. (152, 153) The details of the Klein transformation are worked out in Appendix B. Here I state only the final result: a Klein transformation can be defined if any closed loop, containing N_x x bonds, N_y y bonds and N_z z bonds satisfy

$$N_x, N_y, \text{ and } N_z \text{ all even or all odd.} \quad (3.67)$$

For example, the Klein transformation could be defined on the triangular lattice, where $N_x = N_y = N_z = 1$, and on the honeycomb lattice, where $N_x = N_y = N_z = 2$. The information of the Supplemental material of Ref. (39) allows me to easily check that the Klein condition (3.67) is satisfied for all lattices presented in that paper. The numbers N_x , N_y and N_z for some three-dimensional honeycomb lattices are given in 2.

Let me end this section by returning to the complete Hamiltonian Eq. (3.59). Since the SU(4) symmetry appears in the rotated frame, it is convenient to write the Hund's coupling perturbations in terms of these operators. The Hamiltonian (3.59) reads

$$\begin{aligned} \mathcal{H}_{\text{KM}} = & (J_a - J_b) \sum_{\langle ij \rangle_\gamma} \left(2\tilde{\mathbf{s}}_i \cdot \tilde{\mathbf{s}}_j + \frac{1}{2} \right) \left(2\tilde{\boldsymbol{\tau}}_i \cdot \tilde{\boldsymbol{\tau}}_j + \frac{1}{2} \right) \\ & + J_b \sum_{\langle ij \rangle} \left[8\tilde{\mathbf{s}}_i \cdot \tilde{\mathbf{s}}_j \tilde{\tau}_i^x \tilde{\tau}_j^x + 2(\tilde{\tau}_i^x \tilde{\tau}_j^x + \tilde{\tau}_i^z \tilde{\tau}_j^z) + \frac{1}{2} \right] \\ & + 12J_c \sum_{\langle ij \rangle_\gamma} \tilde{s}_i^\gamma \tilde{s}_j^\gamma \tilde{\tau}_i^y \tilde{\tau}_j^y + 24J_c \sum_{\langle ij \rangle_\gamma} \tilde{s}_i^\gamma \tilde{s}_j^\gamma \tilde{\tau}_i^{\alpha\beta} \tilde{\tau}_j^{\alpha\beta} \\ & - 3J_c \sum_{\langle ij \rangle_\gamma} \tilde{s}_i^\gamma \tilde{s}_j^\gamma - 9J_c \sum_{\langle ij \rangle_\gamma} \tilde{s}_i^\gamma \tilde{s}_j^\gamma (\tilde{\tau}_i^{\alpha\beta} - \tilde{\tau}_j^{\alpha\beta}) \\ & - 8J_c \sum_{\langle ij \rangle_\gamma} \left(\tilde{s}_i^\alpha \tilde{s}_j^\alpha \tilde{\tau}_i^{\beta\gamma} \tilde{\tau}_j^{\beta\gamma} + \tilde{s}_i^\beta \tilde{s}_j^\beta \tilde{\tau}_i^{\gamma\alpha} \tilde{\tau}_j^{\gamma\alpha} \right) \\ & + 4J_c \sum_{\langle ij \rangle_\gamma} \left(\tilde{s}_i^\alpha \tilde{s}_j^\alpha + \tilde{s}_i^\beta \tilde{s}_j^\beta - \frac{1}{2} \right) \left(\tilde{\tau}_i^{\beta\gamma} \tilde{\tau}_j^{\gamma\alpha} + \tilde{\tau}_i^{\gamma\alpha} \tilde{\tau}_j^{\beta\gamma} \right) \\ & + \sqrt{3}J_c \sum_{\langle ij \rangle_\gamma} \left[\tilde{s}_i^\alpha \tilde{s}_j^\alpha (\tilde{\tau}_i^{\alpha\beta} - \tilde{\tau}_j^{\alpha\beta}) - \tilde{s}_i^\beta \tilde{s}_j^\beta (\tilde{\tau}_i^{\alpha\beta} - \tilde{\tau}_j^{\alpha\beta}) \right], \end{aligned} \quad (3.68)$$

Table 2 – Table containing the number of Kitaev bonds on the elementary plaquettes of the three-dimensional generalizations of the honeycomb lattice

Well's notation	Lattice name	Number of Kitaev bonds (N_x, N_y, N_z) on elementary plaquettes
(10,3)-a	Hyperoctagon	$N_x = 4, N_y = 2, N_z = 4$ or $N_x = 4, N_y = 4, N_z = 2$
(10,3)-b	Hyperhoneycomb	$N_x = 4, N_y = 2, N_z = 4$ or $N_x = 2, N_y = 4, N_z = 4$
(10,3)-d	-	$N_x = 4, N_y = 2, N_z = 4$ or $N_x = 4, N_y = 4, N_z = 2$
nonuniform	$8^2.10$ -a	$N_x = 2, N_y = 2, N_z = 4$ or $N_x = 4, N_y = 4, N_z = 2$
(8,3)-b	hyperhexagon	$N_x = 2, N_y = 2, N_z = 4$
nonuniform	Stripyhoneycomb	$N_x = 4, N_y = 4, N_z = 6$ or $N_x = 4, N_y = 4, N_z = 4$

Source: By the author.

where the $i(j)$ sites are assumed to be in odd (even) lattices. The first line is just the SU(4) model discussed above. The second line is another bond-independent Hamiltonian in terms of the rotated variables and concerns quadrupolar interactions. The third line is an exactly solvable $j = 3/2$ model that has the same conserved quantities as the Kitaev model. Its exact solution can be found using the integration method discussed for a generalization of the Kitaev model to a system with SU(2) symmetry. (154) Apart from the Kitaev model, all the remaining terms have no simple physical interpretation. The Eq. (3.68) will be reconsidered in the study of linear flavor wave theory (LFWT) and VMC to be performed in the next chapter.

3.3.4.1 The hyperhoneycomb lattice

I emphasize that the model (3.68) is valid not only for the honeycomb lattice, but for any structure associated with a Kitaev material with a bipartite lattice that also allows for a Klein transformation. For concreteness, I consider an important example that was first proposed by Mandal and Surendran on theoretical grounds. (103) Their main interest was on the geometrical conditions of a lattice supporting the integrability of the Kitaev model. The previous works in two dimensions made them realize that there were two pertinent features characterizing these lattices (i) they were tricoordinated and (ii) two links of the same type must not be connected to the same site. They then showed that by selective elimination of sites of the cubic lattice one could generate another lattice satisfying the two geometrical conditions in three dimensions.

This lattice is currently known as the *hyperhoneycomb lattice*. Mandal's work was the precursor for other three-dimensional generalizations of the Kitaev model in other lattices. (104–108) Even more interesting, the hyperhoneycomb structure is physically relevant as demonstrated by the synthesis of the Kitaev material $\beta\text{-Li}_2\text{IrO}_3$. (111)

The position of the points of the hyperhoneycomb lattice is usually given in terms of a face-centered orthorhombic lattice with four-point basis. (103, 107, 155) I will use an alternative description in this thesis for convenience of calculations that will be realized in Chapter 4. The hyperhoneycomb is then given by a base-centered orthorhombic lattice with an eight-point basis. The primitive vectors will be taken to be

$$\mathbf{a}_1 = (2, 4, 0), \quad \mathbf{a}_2 = (-2, 2, 0), \quad \mathbf{a}_3 = (0, 0, 4), \quad (3.69)$$

whereas the basis points are given by

$$\begin{aligned} \mathbf{M}_1 : (0, 0, 0), & \quad \mathbf{M}_2 : (1, 1, 0), & \quad \mathbf{M}_3 : (1, 2, 1), & \quad \mathbf{M}_4 : (2, 3, 1), \\ \mathbf{M}_5 : (3, 3, 2), & \quad \mathbf{M}_6 : (4, 4, 2), & \quad \mathbf{M}_7 : (4, 5, 3), & \quad \mathbf{M}_8 : (5, 6, 3). \end{aligned} \quad (3.70)$$

These conventions to the hyperhoneycomb lattice are illustrated on Fig. 13a. I represented the different sublattices introduced by Klein transformations (Eq. (2.47)) with different colors. The disks and triangles in this figure show that the lattice is bipartite. The eight points \mathbf{M}_i form a zigzag chain structure inside the orthorhombic unit cell (Fig. 13a). This basis choice is also useful to reveal that the hyperhoneycomb can be constructed by coupling zigzag chains formed by $\mathbf{M}_1 - \mathbf{M}_4$ points connected with chains formed by $\mathbf{M}_5 - \mathbf{M}_8$ points.

The nearest-neighbor vectors of the hyperhoneycomb are given by

$$\begin{aligned} \boldsymbol{\delta}_z &= (1, 1, 0), \\ \boldsymbol{\delta}'_x &= (0, -1, 1), \\ \boldsymbol{\delta}'_y &= (-1, 0, -1), \\ \boldsymbol{\delta}''_x &= (0, -1, -1), \\ \boldsymbol{\delta}''_y &= (-1, 0, 1), \end{aligned} \quad (3.71)$$

It is notable that the x and y links on the hyperhoneycomb cannot be described with a single displacement vector in contrast to the honeycomb lattice. The relation between points in an odd sublattice i and an even sublattice j is symbolically given by the following equations:

$$1 : 2 = 1 + \boldsymbol{\delta}_z; \quad 4 = 1 + \boldsymbol{\delta}'_x; \quad 8 = 1 + \boldsymbol{\delta}'_y; \quad (3.72a)$$

$$3 : 4 = 3 + \boldsymbol{\delta}_z; \quad 2 = 3 + \boldsymbol{\delta}''_x; \quad 6 = 3 + \boldsymbol{\delta}''_y; \quad (3.72b)$$

$$5 : 6 = 5 + \boldsymbol{\delta}_z; \quad 8 = 5 + \boldsymbol{\delta}'_x; \quad 4 = 5 + \boldsymbol{\delta}'_y; \quad (3.72c)$$

$$7 : 8 = 7 + \boldsymbol{\delta}_z; \quad 6 = 7 + \boldsymbol{\delta}''_x; \quad 2 = 7 + \boldsymbol{\delta}''_y. \quad (3.72d)$$

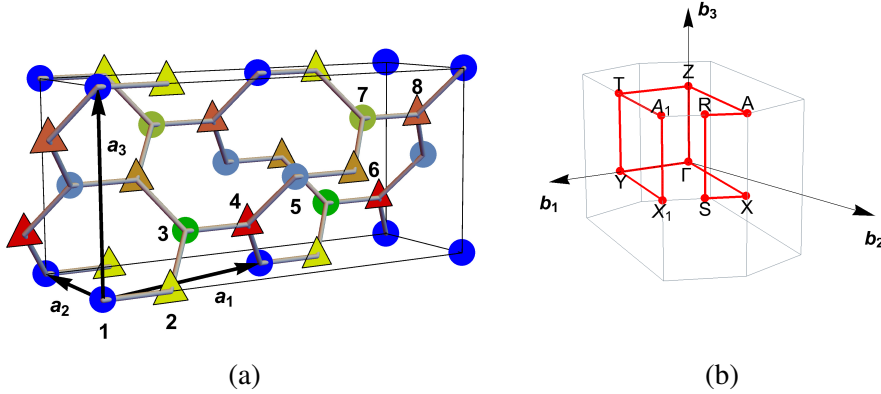


Figure 13 – (a) Eight-point basis for the hyperhoneycomb lattice. The symbols (circle or triangle) display the two sublattices forming the hyperhoneycomb lattice, and shows the points where the rotations on pseudo-orbitals should be applied. The different colors, on the other hand, correspond to the four sublattice division associated with the Klein transformation. (b) The Brillouin zone of the base-centered orthorhombic lattice. Source: NATORI; ANDRADE; PEREIRA. (3)

The Brillouin zone of the base-centered orthorhombic lattice is shown in Fig 13b with highlighted high-symmetry paths and points. The primitive vectors of the reciprocal lattice are

$$\mathbf{b}_1 = \left(\frac{\pi}{3}, \frac{\pi}{3}, 0 \right), \mathbf{b}_2 = \left(-\frac{2\pi}{3}, \frac{\pi}{3}, 0 \right), \mathbf{b}_3 = \left(0, 0, \frac{\pi}{2} \right). \quad (3.73)$$

The high-symmetry paths are $\Gamma \rightarrow X \rightarrow S \rightarrow R \rightarrow A \rightarrow Z \rightarrow \Gamma \rightarrow Y \rightarrow X_1 \rightarrow A_1 \rightarrow T \rightarrow Y$ and $Z \rightarrow T$. These points are given by $\Gamma = (0, 0, 0)$, $X = \left(-\frac{5\pi}{18}, \frac{5\pi}{18}, 0 \right)$, $S = \left(-\frac{\pi}{6}, \frac{\pi}{3}, 0 \right)$, $R = \left(-\frac{\pi}{6}, \frac{\pi}{3}, \frac{\pi}{4} \right)$, $A = \left(-\frac{5\pi}{18}, \frac{5\pi}{18}, \frac{\pi}{4} \right)$, $Z = \left(0, 0, \frac{\pi}{4} \right)$, $Y = \left(\frac{\pi}{6}, \frac{\pi}{6}, 0 \right)$, $X_1 = \left(-\frac{\pi}{18}, \frac{7\pi}{18}, 0 \right)$, $A_1 = \left(-\frac{\pi}{18}, \frac{7\pi}{18}, \frac{\pi}{4} \right)$ and $T = \left(\frac{\pi}{6}, \frac{\pi}{6}, \frac{\pi}{4} \right)$.

Part of the work in the next chapter is to argue in favor of a QSOL ground state for the SU(4) Heisenberg model on the hyperhoneycomb lattice. The motivation for this study was the realization that this model hosts such liquid ground state on the parent honeycomb lattice. (42) The complexity of the hyperhoneycomb lattice does not allow one to use all the numerical techniques studied in Ref. (42) However, it was possible to demonstrate that the energies calculated with LFWT and VMC for the two lattices were close to each other for equivalent states. This allowed us to argue in favor of a QSOL ground state for this three-dimensional lattice as well.

3.4 Heuristic Argument in favor of a $j = 3/2$ Quantum Spin Orbital Liquid

I end this chapter by giving the rationale behind the proposal of QSOLs in $j = 3/2$ models. Previous studies of isotropic Heisenberg models led to the erroneous idea that models described by larger spin- S values would be more classical than its $S = 1/2$ counterparts. The loophole

of this argument is that it neglects the possibility of multipole interactions between larger spin operators that can induce exotic order, or even quantum spin liquids. This can be understood by considering the two-site SU(4) Heisenberg model:

$$H = \left(2\mathbf{s}_i \cdot \mathbf{s}_j + \frac{1}{2} \right) \left(2\boldsymbol{\tau}_i \cdot \boldsymbol{\tau}_j + \frac{1}{2} \right). \quad (3.74)$$

This model is exactly solvable and it turns out that it has a sixfold degenerate ground state. (40) If they are written in terms of the $j^z = \pm 3/2, \pm 1/2$ index, they are expressed like:

$$\left| \psi_{(j_i^z, j_j^z), -} \right\rangle = \frac{1}{\sqrt{2}} \left(|j_i^z; j_j^{z'}\rangle - |j_i^{z'}; j_j^z\rangle \right), \quad (3.75)$$

where $j^z > j^{z'}$. Compare these multiplets with the singlet of the SU(2) Heisenberg model, $\frac{1}{\sqrt{2}} (|\uparrow_i; \downarrow_j\rangle - |\downarrow_i; \uparrow_j\rangle)$. The multiplets relate nearest neighbors whose spins differ by $\Delta j^z = \pm 3, \pm 2, \pm 1$ instead of only $\Delta S^z = \pm 1$. Multipole operators in general lead to this delocalization of the spin component of the wavefunction, and therefore favor exotic magnetic states. (26) The argument is also valid for the SU(2) symmetric limit found for double perovskites, where the interactions involving both spins and orbitals lead to this delocalization.

Another argument can be given that is specially important for the SU(4) symmetric Hamiltonian in Eq. (3.66). The large-N approach to the parton theory shows that SU(N) symmetries for larger values of N favor quantum disordered states. (94) The larger symmetries cannot be implemented in a small spin system, but they are available for systems with higher values of the angular momentum like $j = 3/2$. This result has further support of a previous numerical study of the SU(4) Heisenberg model on the honeycomb lattice showed compelling evidence in favor of a QSOL ground state with fermionic excitations. The next chapter will show how QSOLs can be proposed and studied with parton mean field theory and how their energetics can be computed with VMC calculations.

4 PARTON THEORIES TO QUANTUM SPIN LIQUIDS

The previous chapter showed how realistic effective models for $j = 3/2$ systems generally display bond-dependent interactions between multipoles and, at the same time, remarkably large continuous symmetries. The studies on the Kitaev model and the SU(N) symmetric models in the large-N limit suggest that the derived effective theories can support QSOL ground states. Unfortunately, they are not integrable like the Kitaev model and QSOL states must be studied by performing parton mean-field theories and wavefunction projection with VMC (see the discussion in Subsection 2.2.3). I present how this procedure was implemented for the models under investigation in this chapter.

4.1 Parton Constructions

Spin operators can be formally represented using canonical bosons, canonical fermions, or Majorana fermions subject to a constraint to differentiate between physical and unphysical states (see discussion in Subsection 2.2.3). This is the starting point of a mean-field theory that is always constrained by the definition of some order parameters. Two problems arise in this context. First, which parton representation should be chosen out of the possibilities? The answer is clear only for integrable models, but it is in general less clear for an arbitrary system. Second, which decoupling should we choose? As an illustration, the example discussed on the Heisenberg model in Subsection 2.2.3 led the mean-field theory to resemble band theory for electrons in second quantization (see Eq. (2.22)). However, a BCS-like decoupling with order parameters $\chi_{ij} = \langle f_{\alpha,i} f_{\alpha,j} \rangle$ could be equally well-defined and there is no *a priori* reason to prefer one over the other.

Experimental data can point out to a bosonic or fermionic theory as more adequate to describe a QSL (or QSOL) state. The QSLs obtained through bosonic parton theory are generally gapped, except when the system is tuned to quantum critical point. (11) Following this reasoning, the experimental data of the magnetic specific heat of the QSOL candidate Ba_2YMoO_6 did not obey Arrhenius law (30, 31), indicating that the best QSOL describing it would be gapless and fermionic. Bosonic parton theories were also found to be inadequate to treat the SU(4) Heisenberg model appearing on the Kitaev-like materials. (41) Fermionic theories also have the additional advantage that the partons are not inherently unstable to condensation, which makes them simpler and more adequate for an initial exploratory study. For these reasons, the QSOLs studied in this thesis are all fermionic. This section is solely devoted to present the parton representations used to explore the $j = 3/2$ QSOLs.

4.1.1 Complex Fermions

The parton representation of the $j = 3/2$ states employing canonical (complex) fermions (40, 145) is more straightforward to explain. It is convenient to represent the $|\frac{3}{2}, j^z\rangle$ vectors in terms of the pseudospins and pseudo-orbitals $|s^z, \tau^z\rangle$ (see Eq.(3.39) and Eq.(3.41)). The $|s^z, \tau^z\rangle$ vectors are then labeled again with four indices that are called ‘‘colors’’:

$$\begin{aligned} |1\rangle &= \left| \frac{1}{2}, \frac{1}{2} \right\rangle, & |2\rangle &= \left| -\frac{1}{2}, \frac{1}{2} \right\rangle, \\ |3\rangle &= \left| \frac{1}{2}, -\frac{1}{2} \right\rangle, & |4\rangle &= \left| -\frac{1}{2}, -\frac{1}{2} \right\rangle. \end{aligned} \quad (4.1)$$

The vector states are generated by applying a fermion creation operator f_m^\dagger ($m = 1, \dots, 4$) to the vacuum: $|m\rangle = f_m^\dagger|0\rangle$. The fifteen SU(4) generators S_m^n act on a basis state $|p\rangle$ according to the relation $S_m^n|p\rangle = \delta_{n,p}|m\rangle$. The second-quantized representation of these generators is

$$S_m^n(i) = f_{i,m}^\dagger f_{i,n}. \quad (4.2)$$

It is possible to demonstrate that all 15 operators s^a , τ^b and $s^a\tau^b$ are linearly independent combinations of S_m^n (see their explicit forms in Appendix C). That is how one can argue that s^a , τ^b and $s^a\tau^b$ are generators of the SU(4). (40)

If the colors in Eq. (4.1) are defined in terms of the rotated operators $(\tilde{s}, \tilde{\tau})$ the SU(4) symmetry of Eq. (3.66) becomes evident

$$\mathcal{H}_{\text{SU}(4)} = K \sum_{\langle ij \rangle} S_m^n(i) S_n^m(j). \quad (4.3)$$

Finally, the parton theory must be associated with a constraint defining the physical Hilbert space. In the present case, each site i of the lattice is occupied by a single color m , leading to

$$\sum_m f_{i,m}^\dagger f_{i,m} = 1. \quad (4.4)$$

4.1.2 Majorana Fermions

The defining feature of a Majorana fermion η is that its creation and annihilation operators coincide ($\eta^\dagger = \eta$). The fact that Majorana fermions first appeared as real solutions of the Dirac equation (123) and the relation between taking the adjoint and complex conjugation explains why they are sometimes called ‘‘real fermions’’. Therefore, parton theories based on Majorana fermions are not normally used to represent complex groups like SU(N) but SO(N) rotation groups. For example, six Majorana flavors can be used to represent the 15 generators of the SO(6) due to the isomorphism between this group and SU(4). (41) In practice, the Majorana representation is applied to the \mathbf{s} and $\boldsymbol{\tau}$ operators obeying the algebra in Eqs. (3.45) in the

following way (41, 156–159)

$$\begin{aligned}s^a &= -\frac{i}{4}\epsilon^{abc}\eta^b\eta^c, \\ \tau^a &= -\frac{i}{4}\epsilon^{abc}\theta^b\theta^c,\end{aligned}\tag{4.5}$$

where $a = x, y, z = 1, 2, 3$ for the Majorana fermion flavors. The six Majorana fermions $\zeta^a \in \{\eta^a, \theta^a\}$ obey $(\zeta^a)^\dagger = \zeta^a$ and $\{\zeta^a, \zeta^b\} = 2\delta^{ab}$. This representation has a Z_2 gauge structure because the sign of the fermions can be changed ($\eta^a \rightarrow -\eta^a$ and $\theta^a \rightarrow -\theta^a$) without modifying the local physical operators. However, in contrast to the case of canonical fermions, it is not possible to make the change $\eta^a \rightarrow \eta^a e^{i\phi}$ since this would lead to $(\eta^a)^\dagger \neq \eta^a$.

The local constraint to identify the physical state at each site i is:

$$i\eta_i^1\eta_i^2\eta_i^3\theta_i^1\theta_i^2\theta_i^3 = 1.\tag{4.6}$$

Under this condition, one can also write $s_i^a\tau_i^b = -\frac{i}{4}\eta_i^a\theta_i^b$. The energetics of a QSOL is computed only after a Gutzwiller projection of the mean-field wavefunction. At this point, it is convenient to combine the Majorana flavors into complex fermions and rewrite the constraint in terms of local occupation numbers. The most convenient complex fermion definition for the SU(4) Heisenberg model is

$$c_{i,\gamma} = \frac{1}{2}(\eta_i^\gamma - i\theta_i^\gamma).\tag{4.7}$$

The vector of these particles will be called $\mathbf{c}_i = (c_{i,x}, c_{i,y}, c_{i,z})$. Eq. (4.6) then reads

$$\prod_{\gamma=x,y,z} (1 - 2c_{i,\gamma}^\dagger c_{i,\gamma}) = 1 \quad \forall i.\tag{4.8}$$

This equation implies that a state is in the physical Hilbert space only if each site is occupied by an even number of particles (zero or two). This will play an important role in the implementation of the VMC algorithm in Subsection 4.2.3.

4.2 Parton Mean Field Theory

4.2.1 Mean-Field Theory of the Chiral Spin-Orbital Liquid with Nodal Lines

The study of QSOLs on double perovskites was restricted to Majorana fermions, since QSOLs with complex fermions were already studied in Ref. (29) Other motivation was given by the Kitaev model; it was an interesting question to understand what would be the features of a QSOL based on Majorana fermions in a model displaying bond-directional interactions. Finally, the mean-field spectrum displayed nontrivial topological features and its experimental responses at low-temperatures were consistent with the experiments. (4)

The Majorana representation in Eq. (4.5) can be used to rewrite the effective model for double perovskites in the $J_H \rightarrow 0$ limit (Eq. (3.52)) like

$$\begin{aligned}
H_{\text{eff}} = & \frac{J}{36} \sum_{\langle i,j \rangle_\gamma} \left[\sum_{a < b} \eta_i^a \eta_j^a \eta_i^b \eta_j^b \right. \\
& + (\eta_i^2 \eta_i^3 \eta_j^1 + \eta_i^3 \eta_i^1 \eta_j^2 + \eta_i^1 \eta_i^2 \eta_j^3) \bar{\theta}_j^{\alpha\beta} + (i \leftrightarrow j) \\
& \left. + \boldsymbol{\eta}_i \cdot \boldsymbol{\eta}_j \bar{\theta}_i^{\alpha\beta} \bar{\theta}_j^{\alpha\beta} + \theta_i^{\alpha\beta} \theta_j^{\alpha\beta} \theta_i^2 \theta_j^2 \right] + \frac{NJ}{24}. \tag{4.9}
\end{aligned}$$

The fermions $\theta^{\alpha\beta}$ and $\bar{\theta}^{\alpha\beta}$ label linear combinations of θ^1 and θ^3 that appear in writing $\tau^{\alpha\beta}$ and $s^a \tau^{\alpha\beta}$ operators using the Majorana representation (see Eqs. (3.46)):

$$\theta^{xy} = \theta^1, \tag{4.10}$$

$$\theta^{yz(zx)} = -\frac{1}{2}(\theta^1 \pm \sqrt{3}\theta^3), \tag{4.11}$$

$$\bar{\theta}^{xy} = \theta^3, \tag{4.12}$$

$$\bar{\theta}^{yz(zx)} = \frac{1}{2}(-\theta^3 \pm \sqrt{3}\theta^1). \tag{4.13}$$

Let us analyze some symmetries of the Hamiltonian. In general, a six-component column vector of Majorana fermions $\zeta = (\eta^1, \dots, \theta^3)^t$ can be defined. In principle, the flavors could transform according to the transformation

$$\zeta' = R\zeta, \tag{4.14}$$

where R is an SO(6) matrix. The Hamiltonian in Eq. (4.9) is not invariant under global SO(6) transformations, but it remains invariant under transformations of a considerably large subset. Such subset includes global rotations of the form $R = R_\eta \oplus I_\theta$, where R_η corresponds to an SO(3) rotation of the vector $\boldsymbol{\eta} = (\eta^1, \eta^2, \eta^3)$, and I_θ is the identity matrix in the θ sector. This corresponds to the global SU(2) invariance of Hamiltonian (3.52) expressed in terms of Majorana fermions. Moreover, there is a Z_3 symmetry generated by the transformation $R = I_\eta \oplus M_\theta$, where M_θ is the $2\pi/3$ rotation matrix acting on the two-component vector (θ^1, θ^3) leaving θ^2 invariant.

The action of time reversal Θ on Eq. (4.9) follows from the symmetry properties of \mathbf{s} and $\boldsymbol{\tau}$ discussed in Subsection 3.3.2. Based on Eq. (4.5), Θ is defined as the complex conjugation supplemented by $\Theta^{-1}\theta^2\Theta = -\theta^2$, while leaving the other flavors invariant. With this rule, the Hamiltonian in Eq. (4.9) is explicitly time-reversal invariant.

The expectation values of the bond operators $\langle \zeta_i^a \zeta_j^b \rangle$ are the chosen order parameters of this MFT. Since the fcc lattice contains triangular plaquettes, a Majorana QSOL necessarily breaks time-reversal and reflection symmetries. (160) The action of time-reversal was discussed in Subsection 3.3.2; the parity transformation P will be defined by the reflection by a symmetry plane of the fcc lattice and inverts all flux orientations in the mean-field ansatz (see Fig. 14b).

Any Majorana QSOL on the fcc lattice will be necessarily chiral, similar to the case discussed in Subsection 2.2.3 on the square lattice. The MFT can then preserve at most the $SO(3)$, Z_3 and some point-group symmetries.

In this work, I chose to study *Ansätze* preserving the largest number of symmetries, and this principle guided the choice of order parameters. To preserve the $SO(3)$ symmetry, the state must remain invariant under any global rotation of \mathbf{s} . Consequently, all order parameters of the type $\langle \eta_i^a \eta_j^b \rangle$ with $a \neq b$ must vanish, and the order parameters of different flavors must be equal: $\langle \eta_i^a \eta_j^a \rangle = \langle \eta_i^b \eta_j^b \rangle$, for $a, b = 1, 2, 3$. Similarly, $\langle \eta_i^a \theta_j^b \rangle$ vanishes for any pair (a, b) . The Z_3 symmetry rotates the $\tau^{\alpha\beta}$ operators among themselves. Thus, requiring Z_3 invariance implies that $\langle \theta^{\alpha\beta} \theta^2 \rangle$ must also be zero. Applying these restrictions, the mean-field decoupling of Eq. (4.9) leads to

$$\begin{aligned}
H_{\text{MF}} = & \frac{J}{36} \sum_{\langle i,j \rangle_\gamma} (3u_{ij}^2 + 3u_{ij}\bar{w}_{ij} + w_{ij}v_{ij}) \\
& + \frac{J}{36} \sum_{\langle i,j \rangle_\gamma} \left[i(2u_{ij} + \bar{w}_{ij}^{\alpha\beta}) \boldsymbol{\eta}_i \cdot \boldsymbol{\eta}_j \right. \\
& \left. + 3iu_{ij}\bar{\theta}_i^{\alpha\beta}\bar{\theta}_j^{\alpha\beta} + iw_{ij}^{\alpha\beta}\theta_i^2\theta_j^2 + iv_{ij}\theta_i^{\alpha\beta}\theta_j^{\alpha\beta} \right], \quad (4.15)
\end{aligned}$$

where $iu_{ij} = \langle \eta_i^a \eta_j^a \rangle$, $iv_{ij} = \langle \theta_i^2 \theta_j^2 \rangle$, $iw_{ij}^{\alpha\beta} = \langle \theta_i^{\alpha\beta} \theta_j^{\alpha\beta} \rangle$ and $i\bar{w}_{ij}^{\alpha\beta} = \langle \bar{\theta}_i^{\alpha\beta} \bar{\theta}_j^{\alpha\beta} \rangle$. Notice that all quadratic terms are diagonal in the flavor index except those involving θ^1 and θ^3 . Moreover, the decoupled terms for η^a and θ^2 fermions differ only by the corresponding mean-field amplitudes.

Since the projected wavefunctions of the *Ansätze* are invariant under translation symmetry, the magnitude of the order parameters must be uniform:

$$u_{ij} = u\phi_{ij}, \quad (4.16a)$$

$$v_{ij} = v\phi_{ij}, \quad (4.16b)$$

$$w_{ij}^{\alpha\beta} = w\phi_{ij} \quad \text{for } \langle i, j \rangle_\gamma, \quad (4.16c)$$

$$\bar{w}_{ij}^{\alpha\beta} = \bar{w}\phi_{ij} \quad \text{for } \langle i, j \rangle_\gamma, \quad (4.16d)$$

where $\phi_{ij} = \pm 1$ are Z_2 link variables. The Majorana fermion anticommutation relations ensure that $\phi_{ij} = -\phi_{ji}$. This intrinsic orientation for the links makes it convenient to subdivide the fcc lattice into four cubic sublattices and label them with the index $X = 1, 2, 3, 4$. These labels also correspond to the vertices of the elementary tetrahedra forming the fcc lattice (see Figure 14b).

The orientation of ϕ_{ij} between sublattices can be represented on a plane as shown in Fig. 14a. The inequivalent classes for QSOL mean field theories can be discovered with an analysis similar to the one done for Wegner's model (see Section 2.1). With two possible values for each ϕ_{ij} , there are in total $2^6 = 64$ different ‘‘hopping’’ configurations. The total number of gauge transformations available in Fig. 14a is $2^4 = 16$. On the other hand, the IGG is composed by two elements: either the application of the identity or of the gauge transformation to all sites.

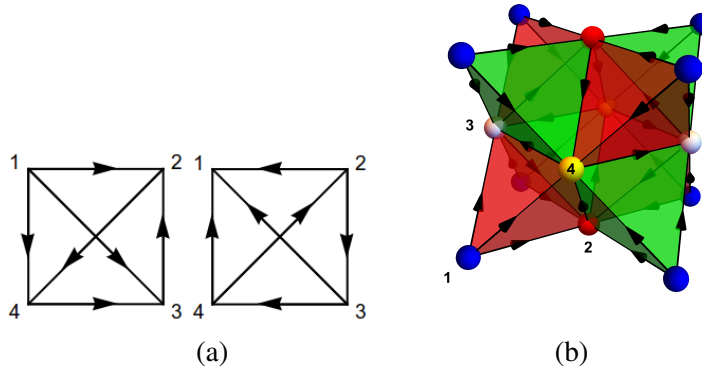


Figure 14 – (Color online) (a) Diagrammatic representation of the most symmetric gauge choices on an elementary tetrahedron. The arrow pointing from site i to site j represents that $\phi_{ij} = +1$ (and $\phi_{ji} = -1$ in the opposite direction). Notice that the two Ansätze are conjugated by time reversal. (b) Representation of the Z_2 fluxes of the ansatz on the fcc lattice. The flux through each face of a green (red) tetrahedron is positive (negative) when the sites are oriented counterclockwise with respect to a normal vector pointing outward.

Source: NATORI, DAGHOFER, PEREIRA. (1)

Therefore, each hopping configuration is gauge equivalent to eight different ones, and the 64 possibilities can be grouped into eight non-gauge-equivalent Ansätze.

The eight physically distinct Ansätze are labeled by the gauge-invariant Z_2 fluxes through the elementary plaquettes. The flux for this problem on the fcc lattice is $\chi_{ijk} \equiv -i\phi_{ij}\phi_{jk}\phi_{ki}$, where (i, j, k) are three sites forming a face of a tetrahedron oriented clockwise with respect to an outward normal vector. This flux is closely related to the scalar spin chirality of $S = 1/2$ QSLs (58, 60, 95, 161) discussed in Subsection 2.2.3. Using Eq. (4.5), the operator is given by

$$\mathbf{s}_i \cdot (\mathbf{s}_j \times \mathbf{s}_k) = -\frac{i}{8} \epsilon_{abc} \eta_i^a \eta_j^a \eta_j^b \eta_k^c \eta_k^c \eta_i^c. \quad (4.17)$$

Compared to Eq. (2.32), Eq. (4.17) differs only because it is written in terms of pseudospins instead of electronic spins. Its mean value for the QSOL is given by

$$\langle \mathbf{s}_i \cdot (\mathbf{s}_j \times \mathbf{s}_k) \rangle = \frac{3}{8} u_{ij} u_{jk} u_{ki} = \frac{3}{8} i u^3 \chi_{ijk}. \quad (4.18)$$

Eq. (4.18) gives a relation between the parton mean-field order parameter, the Z_2 flux, and the chiral order parameter. As a final remark, the fluxes χ_{ijk} through the faces of the tetrahedra are not all independent. If the sites on any given face are oriented in the same manner, the four fluxes obey the relation $\prod_{r=1}^4 \chi_r = 1$, where r labels the faces of the tetrahedron.

Time-reversal plays an important role in choosing the mean-field theory, since it relates pairs of non-equivalent gauge configurations (see Fig. 14a). In terms of Z_2 fluxes, Θ inverts χ_{ijk} of every elementary plaquette of the lattice. Although not related by gauge transformations, two gauge choices related by Θ lead to degenerate mean-field ground states. Still guided by symmetry principles, only the most symmetric Ansätze with respect to the chiral order parameter (4.17)

are studied. Their main feature is the same Z_2 flux through all faces of a given tetrahedron. The imposition of translation invariance implies that two tetrahedra sharing an edge have opposite Z_2 fluxes (see Fig. 14b). In other words, the *Ansatz* is a staggered-flux Majorana QSL, where the staggering occurs between nearest-neighbor tetrahedra.

The mean-field Hamiltonian is solved using the Fourier mode expansion

$$\zeta_{\mathbf{k}X}^a = \sqrt{\frac{2}{N}} \sum_{j \in X} \zeta_{jX}^a e^{-i\mathbf{k} \cdot \mathbf{R}_j}, \quad (4.19)$$

where $X = 1, 2, 3, 4$ is the sublattice index and N is the total number of sites in the fcc lattice. The positions of the sites in sublattice X in units of the lattice parameter are

$$\mathbf{R}_j = (n_x, n_y, n_z) + \boldsymbol{\delta}_X, \quad n_a \in \mathbb{Z}, \quad (4.20)$$

with $\boldsymbol{\delta}_1 = (0, 0, 0)$, $\boldsymbol{\delta}_2 = (1/2, 1/2, 0)$, $\boldsymbol{\delta}_3 = (0, 1/2, 1/2)$, and $\boldsymbol{\delta}_4 = (1/2, 0, 1/2)$. The operators $\zeta_{\mathbf{k}X}^a$ obey $(\zeta_{\mathbf{k}X}^a)^\dagger = \zeta_{-\mathbf{k}X}^a$ and $\{\zeta_{\mathbf{k}X}^a, \zeta_{\mathbf{k}'X'}^a\} = \delta_{\mathbf{k}, -\mathbf{k}'} \delta_{X, X'}$. As a general feature of Majorana fermions, the $\zeta_{\mathbf{k}X}^a$ can be treated as complex fermions with well-defined occupation numbers if the first Brillouin zone of the cubic lattice is divided into two halves that are mapped into each other through inversion (see the case of the Kitaev model in Subsection 2.2.4.2). Only one of these halves is taken into account and will be called $\frac{1}{2}\text{BZ}$. It is worth pointing out that the PSG analysis shows that the mean-field ansatz is invariant under translations on the fcc lattice. (4) This can be understood intuitively by noting that translations by $\boldsymbol{\delta}_X$ exchange the sublattices but do not change the signs of the gauge-invariant fluxes represented in Fig. 14b.

The mean-field Hamiltonian in Eq. (4.15) can be rewritten in the form

$$\begin{aligned} H_{\text{MF}} = & \frac{NJ}{2} \left(u^2 + u\bar{w} + \frac{vw}{3} \right) \\ & + \frac{J}{18} \sum_{\mathbf{k} \in \frac{1}{2}\text{BZ}} \left[(2u + \bar{w}) \sum_{a=1}^3 (\eta_{\mathbf{k}}^a)^\dagger \mathcal{H}_1(\mathbf{k}) \eta_{\mathbf{k}}^a \right. \\ & \left. + w (\theta_{\mathbf{k}}^2)^\dagger \mathcal{H}_1(\mathbf{k}) \theta_{\mathbf{k}}^2 + (\Psi_{\mathbf{k}})^\dagger \mathcal{H}_2(\mathbf{k}) \Psi_{\mathbf{k}} \right], \end{aligned} \quad (4.21)$$

where $\zeta_{\mathbf{k}} = (\zeta_{\mathbf{k},1}, \zeta_{\mathbf{k},2}, \zeta_{\mathbf{k},3}, \zeta_{\mathbf{k},4})^t$ for $\zeta \in \{\eta^a, \theta^2\}$ are four-component spinors, and $\Psi_{\mathbf{k}} = (\theta_{\mathbf{k}1}^1, \theta_{\mathbf{k}2}^1, \dots, \theta_{\mathbf{k}4}^3)^t$ is an eight-component spinor. To find the ground state of Eq. (4.21), I first explicit the 4×4 matrix $\mathcal{H}_1(\mathbf{k})$

$$\mathcal{H}_1(\mathbf{k}) = \mathbf{h}(\mathbf{k}) \cdot \boldsymbol{\Sigma}, \quad (4.22)$$

in which

$$\begin{aligned} \mathbf{h}(\mathbf{k}) = & (h_1(\mathbf{k}), h_2(\mathbf{k}), h_3(\mathbf{k})) \\ = & 4 \left(\cos \frac{k_x}{2} \cos \frac{k_y}{2}, \cos \frac{k_y}{2} \cos \frac{k_z}{2}, \cos \frac{k_x}{2} \cos \frac{k_z}{2} \right), \end{aligned} \quad (4.23)$$

and

$$\begin{aligned}\Sigma &= (\Sigma_1, \Sigma_2, \Sigma_3) \\ &= (-\sigma^z \otimes \sigma^y, -\sigma^y \otimes \mathbb{I}, -\sigma^x \otimes \sigma^y).\end{aligned}\quad (4.24)$$

Using the property $(A \otimes B)(C \otimes D) = AB \otimes CD$, it is easy to verify that these Σ matrices obey the Clifford algebra $\{\Sigma^a, \Sigma^b\} = 2\delta^{ab}$ and their commutation relations are the same as of the Pauli matrices. This has an important implication for the form of the eigenvalues of \mathcal{H}_1 . Let $U_{\mathbf{k}}$ be the unitary matrix that diagonalizes it

$$U_{\mathbf{k}}^\dagger \mathcal{H}_1(\mathbf{k}) U_{\mathbf{k}} = \Lambda_1(\mathbf{k}). \quad (4.25)$$

This implies that the eigenvalues of $\mathcal{H}_1(\mathbf{k})$ will be $\pm |\mathbf{h}(\mathbf{k})|$, leading to bands that are doubly degenerate for all values of \mathbf{k} .

Several interesting symmetry and topological characteristics of the mean-field ground state of \mathcal{H}_1 were studied in Ref. (4). I decided to report them explicitly in Appendix D instead of giving them in the main text, since the focus of the thesis is the study of how to propose QSOLs and study their experimental responses. First, a PSG analysis was performed on the *Ansatz* and it was found that the QSOL display a discrete symmetry isomorphic to O_h . These symmetry operators are given by combinations of the spatial operations, gauge transformations and application of the Θ operator. Second, the symmetry operator that explains the twofold degeneracy of the Hamiltonian was explicitly found and is given by the combination of two C_4 rotations. This symmetry operator also subdivides the eigenstates into two different sectors in analogy to the chirality of Weyl fermions in massless Dirac equations. (162) Third, the Fermi surface is given by nodal lines along the edges of the cubic Brillouin zone and are associated with a nontrivial generalized Berry phase (or Zak phase). (163, 164) This draws a relation between the chiral QSOL and the bands of the weakly correlated line-node semimetals and superconductors. (165–167) Finally, dispersing edge states were found for the model with open boundary conditions in the (111) direction.

Let us now return to the problem of formulating and solving the self-consistent equations fixing the mean-field Hamiltonian (Eq. (4.21)). The order parameters u and v are determined simply by:

$$\begin{aligned}u &= -i \langle \eta_{j,1}^1 \eta_{j+\delta_{2,2}}^1 \rangle \\ &= \frac{16}{N} \text{Im} \sum_{\mathbf{k}} e^{i\mathbf{k} \cdot \delta_2} \sum_{\lambda=1}^4 (U_{\mathbf{k}})_{2\lambda} (U_{\mathbf{k}}^\dagger)_{\lambda 1} \langle (\tilde{\eta}_{\mathbf{k}\lambda}^1)^\dagger \tilde{\eta}_{\mathbf{k}\lambda}^1 \rangle,\end{aligned}\quad (4.26)$$

$$\begin{aligned}v &= -i \langle \theta_{j,1}^2 \theta_{j+\delta_{2,2}}^2 \rangle \\ &= \frac{16}{N} \text{Im} \sum_{\mathbf{k}} e^{i\mathbf{k} \cdot \delta_2} \sum_{\lambda=1}^4 (U_{\mathbf{k}})_{2\lambda} (U_{\mathbf{k}}^\dagger)_{\lambda 1} \langle (\tilde{\theta}_{\mathbf{k}\lambda}^2)^\dagger \tilde{\theta}_{\mathbf{k}\lambda}^2 \rangle,\end{aligned}\quad (4.27)$$

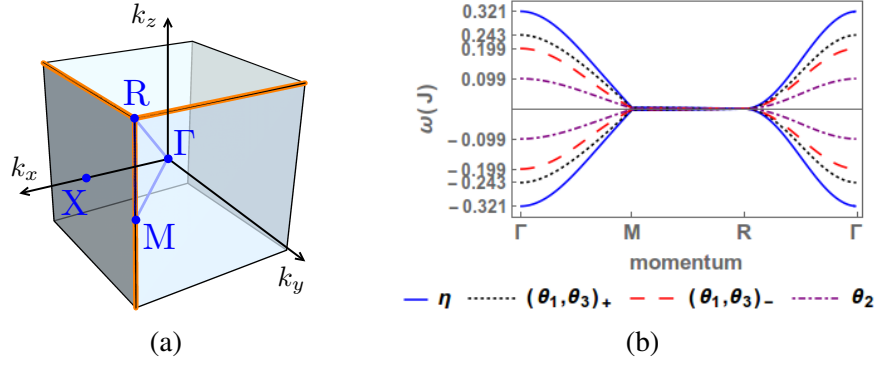


Figure 15 – (a) First Brillouin zone of the cubic lattice highlighting the Fermi lines (orange lines). (b) Dispersion for different fermion flavors.
Source: NATORI; DAGHOFER; PEREIRA. (1)

where the sum over \mathbf{k} is restricted to $\mathbf{k} \in \frac{1}{2}\text{BZ}$ and $U_{\mathbf{k}}$ was given by Eq. (D.16). At zero temperature, the average occupation of the single-particle states is

$$\langle (\tilde{\eta}_{\mathbf{k}\lambda}^a)^\dagger \tilde{\eta}_{\mathbf{k}\lambda}^a \rangle = \Theta(-\epsilon_{\mathbf{k}\lambda}^{(\eta)}), \quad (4.28)$$

$$\langle (\tilde{\theta}_{\mathbf{k}\lambda}^2)^\dagger \tilde{\theta}_{\mathbf{k}\lambda}^2 \rangle = \Theta(-\epsilon_{\mathbf{k}\lambda}^{(\theta^2)}), \quad (4.29)$$

where $\Theta(x)$ is the Heaviside step function and

$$\epsilon_{\mathbf{k}\lambda}^{(\eta)} = \frac{J(2u + \bar{w})}{18} |\mathbf{h}(\mathbf{k})| C_\lambda, \quad (4.30)$$

$$\epsilon_{\mathbf{k}\lambda}^{(\theta^2)} = \frac{Jw}{18} |\mathbf{h}(\mathbf{k})| C_\lambda, \quad (4.31)$$

are the dispersion relations of the η and θ^2 fermions, respectively, with $C_\lambda = -1$ for $\lambda = 1, 2$ and $C_\lambda = +1$ for $\lambda = 3, 4$.

The expressions for u and v coincide at zero temperature, except possibly for a sign depending on the relative sign between the parameters $2u + \bar{w}$ and w . Without loss of generality, $u > 0$ was fixed. This corresponds to fix the sign of the Θ -symmetry-breaking order parameter in Eq. (4.17). As discussed in Ref. (4), the two cases $v = u$ or $v = -u$ give rise to two different Ansätze, with different expressions for the 8×8 matrix $\mathcal{H}_2(\mathbf{k})$. This thesis will deal only with the case $v = u$ because this case led to the smaller mean field energy. In this case, self-consistency of the mean-field equations implies $2u + \bar{w} > 0$ and $w > 0$.

Having fixed $\text{sgn}(uv) > 0$, the 8×8 matrix $\mathcal{H}_2(\mathbf{k})$ in Eq. (4.21) is given by

$$\mathcal{H}_2(\mathbf{k}) = \begin{pmatrix} \mathcal{H}_{\theta_1\theta_1}(\mathbf{k}) & \mathcal{H}_{\theta_1\theta_3}(\mathbf{k}) \\ \mathcal{H}_{\theta_1\theta_3}(\mathbf{k}) & \mathcal{H}_{\theta_3\theta_3}(\mathbf{k}) \end{pmatrix}, \quad (4.32)$$

in which

$$\begin{aligned}
\mathcal{H}_{\theta_1\theta_1}(\mathbf{k}) &= v h_1(\mathbf{k})\Sigma_1 + \frac{9u+v}{4} [h_2(\mathbf{k})\Sigma_2 + h_3(\mathbf{k})\Sigma_3], \\
\mathcal{H}_{\theta_3\theta_3}(\mathbf{k}) &= 3u h_1(\mathbf{k})\Sigma_1 + \frac{3}{4}(u+v) [h_2(\mathbf{k})\Sigma_2 + h_3(\mathbf{k})\Sigma_3], \\
\mathcal{H}_{\theta_1\theta_3}(\mathbf{k}) &= \frac{\sqrt{3}}{4}(3u-v) [-h_2(\mathbf{k})\Sigma_2 + h_3(\mathbf{k})\Sigma_3].
\end{aligned} \tag{4.33}$$

The unitary matrix diagonalizing $\mathcal{H}_2(\mathbf{k})$ is called $V_{\mathbf{k}}$

$$V_{\mathbf{k}}^\dagger \mathcal{H}_2(\mathbf{k}) V_{\mathbf{k}} = \Lambda_2(\mathbf{k}), \tag{4.34}$$

and was found numerically. The order parameters w and \bar{w} can be calculated similarly to Eq. (4.27), using the components of $V_{\mathbf{k}}$ instead of $U_{\mathbf{k}}$. The values of the order parameters found numerically at zero temperature were $u = v \approx 0.258$, $w \approx 0.16$ and $\bar{w} \approx 0.318$.

The mean field dispersion of the Majorana fermions using these order parameters is shown in Fig. (15b). The nodal line containing the points connecting $M = (\pi, \pi, 0)$ and $R = (\pi, \pi, \pi)$ displayed in Fig. (15b) are parameterized by $\mathbf{k} = (\pi, \pi, k_z)$. The dispersion in the neighborhood of these nodes is linear (1, 4) with the exception of the point of intersection of the three nodal lines, R . The band touching is quadratic at R and display an anisotropic dispersion $\epsilon_{\pm}(R + \mathbf{p}) \propto \sqrt{p_x^2 p_y^2 + p_y^2 p_z^2 + p_z^2 p_x^2}$. These are important points to study the low-temperature physics of the chiral QSOL in the next chapter.

A VMC calculation of the chiral spin-orbital liquid was performed in Ref. (4). However, as stated in Subsection 3.2.2, this work was done over the incomplete effective model and will be omitted in the main text for clarity. The interested reader can follow the algorithm to compute the energy of this QSOL with VMC in Appendix E.

4.2.2 Spin-Orbital Liquids on the Hyperhoneycomb Lattices

This subsection concerns the QSOLs in the model defined on the hyperhoneycomb lattices with special attention to the limit with SU(4) global symmetry. I first study a LFWT of this model in order to fix an ordered state energy to compare with the proposed QSOLs and to show how most of the simple ordered states are actually unstable under Hund's coupling perturbations. Then, I give some details of the parton mean field theories and discuss the obtained Fermi surfaces. I finally give the VMC analysis of the QSOL energetics. The numerical work was performed by Prof. Eric Andrade and is reproduced here with his permission.

4.2.2.1 Linear Flavor Wave Theory

To fix a notation, I first study the ‘‘Néel’’ state on the honeycomb lattice and reproduce the results of Ref. (168) with regard to magnon dispersion, zero-point fluctuations and the correction

to the order parameter. The technical information concerning the honeycomb lattice was already given in Subsection 2.2.4.2 and will not be repeated here. The color notation and the generators of the SU(4) were discussed in Subsection 4.1.1; this discussion remains valid with the sole difference that it must be adapted to state vectors given in terms of the rotated pseudospins and pseudo-orbitals $|\tilde{s}^z, \tilde{\tau}^z\rangle$.

Let the sites on the even sublattice (A) be occupied by the color $|\alpha\rangle$, and the ones on the odd sublattice (B) by the color $|\beta\rangle$ obeying the orthogonality condition $\langle\alpha|\beta\rangle = 0$. The SU(4) Heisenberg model in terms of the generators in Eq. (4.2) is given by 4.3. The Holstein-Primakoff transformation (HPT) for the two-color ordered state reads

$$S_\alpha^\alpha(i) = 1 - \sum_{\gamma \neq \alpha} b_{\gamma,i}^\dagger b_{\gamma,i}, S_\beta^\beta(j) = 1 - \sum_{\delta \neq \beta} b_{\delta,j}^\dagger b_{\delta,j}, \quad (4.35a)$$

$$S_\gamma^\alpha(i) = b_{\gamma,i}^\dagger \sqrt{1 - \sum_{\epsilon \neq \alpha} b_{\epsilon,i}^\dagger b_{\epsilon,i}}, S_\delta^\beta(j) = b_{\delta,j}^\dagger \sqrt{1 - \sum_{\phi \neq \beta} b_{\phi,j}^\dagger b_{\phi,j}}, \quad (4.35b)$$

$$S_\gamma^\epsilon(i) = b_{\gamma,i}^\dagger b_{\epsilon,i}, S_\delta^\phi(j) = b_{\delta,j}^\dagger b_{\phi,j}, \quad (4.35c)$$

in which $\gamma, \epsilon \neq \alpha$ and $\delta, \phi \neq \beta$. A special property of the SU(4) symmetric point is that the results for flavor-wave dispersion, zero-point energy correction and order parameter correction are independent of the chosen colors α and β . To linear order in bosonic operators, the SU(4) model is given by (42)

$$H_{ij} \equiv S_n^m(i) S_m^n(j) \approx \left(b_{\beta i}^\dagger b_{\beta i} + b_{\alpha j}^\dagger b_{\alpha j} + b_{\beta i}^\dagger b_{\alpha j}^\dagger + b_{\beta i} b_{\alpha j} \right) \equiv \left(Z_{ij}^\dagger Z_{ij} - 1 \right), \quad (4.36)$$

where $Z_{ij}^\dagger = b_{\alpha j}^\dagger + b_{\beta i}$. In momentum space, the LFWT Hamiltonian is

$$H_{fw} = -\frac{3}{2}NK + K \sum_{\mathbf{k}} \psi_{\mathbf{k}}^\dagger H_{\mathbf{k}}^{AFM} \psi_{\mathbf{k}}, \quad (4.37)$$

in which $\psi_{\mathbf{k}}$ is the spinor

$$\psi_{\mathbf{k}} = \begin{pmatrix} b_{\alpha, -\mathbf{k}, B}^\dagger \\ b_{\beta \mathbf{k}, A} \end{pmatrix}. \quad (4.38)$$

The diagonalization of H_{fw} is obtained by introducing a simple Bogouliubov transformation

$$\begin{pmatrix} c_{-\mathbf{k}}^\dagger \\ d_{\mathbf{k}} \end{pmatrix} = M_{\mathbf{k}} \psi_{\mathbf{k}}. \quad (4.39)$$

The matrices $M_{\mathbf{k}}$ must be chosen in such a way that $M_{\mathbf{k}}^\dagger H_{\mathbf{k}}^{AFM} M_{\mathbf{k}}$ is diagonal and $c_{\mathbf{k}}$ and $d_{\mathbf{k}}$ obey the canonical boson commutation relations. This is accomplished by:

$$M_{\mathbf{k}} = \begin{pmatrix} \cosh \theta_{\mathbf{k}} & \sinh \theta_{\mathbf{k}} e^{-i\phi_{\mathbf{k}}} \\ \sinh \theta_{\mathbf{k}} e^{i\phi_{\mathbf{k}}} & \cosh \theta_{\mathbf{k}} \end{pmatrix} \equiv \begin{pmatrix} u_{\mathbf{k}} & v_{\mathbf{k}} e^{-i\phi_{\mathbf{k}}} \\ v_{\mathbf{k}} e^{i\phi_{\mathbf{k}}} & u_{\mathbf{k}} \end{pmatrix}, \quad (4.40)$$

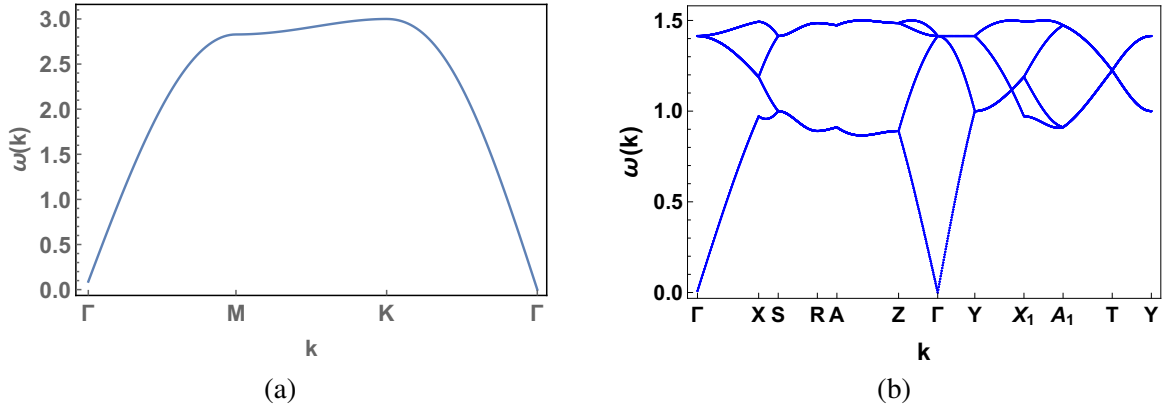


Figure 16 – Spin-wave spectrum for the two-color ordered states along the high symmetry lines of the (a) hexagonal lattice and (b) the hyperhoneycomb lattice.
Source: By the author.

in which

$$f(\mathbf{k}) \equiv \sum_{i=1}^3 e^{i\mathbf{k}\cdot\delta_i}. \quad (4.41)$$

The parameters $\theta_{\mathbf{k}}$ and $\phi_{\mathbf{k}}$ are determined by the equations

$$\tanh 2\theta_{\mathbf{k}} = -\frac{|f(\mathbf{k})|}{3}, \quad (4.42a)$$

$$\exp(i\phi_{\mathbf{k}}) = \frac{f(\mathbf{k})}{|f(\mathbf{k})|}. \quad (4.42b)$$

Finally, the diagonalized H_{fw} reads

$$\begin{aligned} H_{fw} &= -\frac{3}{2}NK + K \sum_{\mathbf{k}} \epsilon_{\mathbf{k}} \left(c_{-\mathbf{k}} c_{-\mathbf{k}}^{\dagger} + d_{\mathbf{k}}^{\dagger} d_{\mathbf{k}} \right) \\ &= -\frac{3}{2}NK + K \sum_{\mathbf{k}} \epsilon_{\mathbf{k}} + K \sum_{\mathbf{k}} \epsilon_{\mathbf{k}} \left(c_{\mathbf{k}}^{\dagger} c_{\mathbf{k}} + d_{\mathbf{k}}^{\dagger} d_{\mathbf{k}} \right), \end{aligned} \quad (4.43)$$

where the spectrum of excitations are

$$\epsilon_{\mathbf{k}} = \sqrt{9 - |f(\mathbf{k})|^2}. \quad (4.44)$$

The dispersion relations along the high symmetry lines is displayed in Fig. 16a. Notice the presence of Goldstone modes displaying a linear behavior for long wavelengths fluctuations, as expected by the SSB of a continuous symmetry. The LFWT dispersion also allows the computation of the zero-point fluctuations and to estimate the energy of the two-color ordered state:

$$E^0 = -\frac{3}{2}K + \frac{3\sqrt{3}}{16\pi^2}K \int d^2k \epsilon_{\mathbf{k}} \approx -0.314K. \quad (4.45)$$

Finally, the correction to the order parameter due to spin-orbital fluctuations ΔM is

$$\Delta M = \frac{1}{N} \left\langle \sum_{i \in A} b_{\beta i}^\dagger b_{\beta i} + \sum_{j \in B} b_{\alpha j}^\dagger b_{\alpha j} \right\rangle = \frac{1}{N} \left\langle \sum_{\mathbf{k}} \left(b_{\alpha \mathbf{k}}^\dagger b_{\alpha \mathbf{k}} + b_{\beta \mathbf{k}}^\dagger b_{\beta \mathbf{k}} \right) \right\rangle, \quad (4.46)$$

where the mean value is the expectation value calculated on the vacuum of the HP bosons. By labeling $\mathcal{Q}_{\mathbf{k}} \equiv M_{\mathbf{k}}^{-1}$, the correction of the order parameter is given by

$$\begin{aligned} \Delta M &= \frac{1}{N} \left\langle \sum_{\mathbf{k}} \left[\begin{pmatrix} c_{-\mathbf{k}} & d_{\mathbf{k}}^\dagger \end{pmatrix} \left(\mathcal{Q}_{\mathbf{k}}^\dagger \mathcal{Q}_{\mathbf{k}} \right) \begin{pmatrix} c_{-\mathbf{k}}^\dagger \\ d_{\mathbf{k}} \end{pmatrix} - 1 \right] \right\rangle \\ &= \frac{1}{2N} \sum_{\mathbf{k}} \sum_{i=1}^2 \left[\mathcal{Q}_{\mathbf{k}}^\dagger \mathcal{Q}_{\mathbf{k}} \right]_{ii} - \frac{1}{2}. \\ &= \frac{1}{N} \sum_{\mathbf{k}} \cosh(2\theta_{\mathbf{k}}) - \frac{1}{2} = \frac{1}{N} \sum_{\mathbf{k}} \frac{3}{\epsilon_{\mathbf{k}}} - \frac{1}{2} \approx 0.258. \end{aligned} \quad (4.47)$$

The values of E_{AFM}^0 and ΔM reproduce the results of Ref. (168) [by fixing the large- M parameter of that paper to $M = 1$]. It is interesting to notice that the correction of the order parameter is rather small and what makes this an uncompetitive state is its large energy in relation to the QSOLs investigated in Ref. (42)

The steps to use LFWT on the hyperhoneycomb lattice are formally the same. The difference is that I was not able to find a closed formula for $M_{\mathbf{k}}$ and $\mathcal{Q}_{\mathbf{k}}$, which were computed numerically using standard methods to diagonalize many-body bosonic Hamiltonians. (169) Using the notation for the hyperhoneycomb lattice fixed in Subsection 3.3.4.1, I also find Eq. 4.37 (but this time, on the hyperhoneycomb lattice).

The flavor wave excitations display closed forms. If I define

$$f_1(\mathbf{k}) = 2 \cos(k_x - k_y) \cos(2k_z), \quad (4.48a)$$

$$\begin{aligned} f_2(\mathbf{k}) &= 5 - \cos[2(k_x - k_y)] + 2 \cos[2(2k_x + k_y)] \\ &\quad + 2 \cos[2(k_x + 2k_y)] - 2 \cos(4k_z) \sin^2(k_x - k_y), \end{aligned} \quad (4.48b)$$

$$f_3(\mathbf{k}) = 8 \cos(2k_x + k_y) \cos(k_x + 2k_y) \cos(2k_z), \quad (4.48c)$$

the expressions for the excitations reads

$$\epsilon_1(\mathbf{k}) = \sqrt{6 - f_1(\mathbf{k}) - \sqrt{f_2(\mathbf{k}) + f_3(\mathbf{k})}}, \quad (4.49a)$$

$$\epsilon_2(\mathbf{k}) = \sqrt{6 - f_1(\mathbf{k}) + \sqrt{f_2(\mathbf{k}) + f_3(\mathbf{k})}}, \quad (4.49b)$$

$$\epsilon_3(\mathbf{k}) = \sqrt{6 + f_1(\mathbf{k}) - \sqrt{f_2(\mathbf{k}) - f_3(\mathbf{k})}}, \quad (4.49c)$$

$$\epsilon_4(\mathbf{k}) = \sqrt{6 + f_1(\mathbf{k}) + \sqrt{f_2(\mathbf{k}) - f_3(\mathbf{k})}}. \quad (4.49d)$$

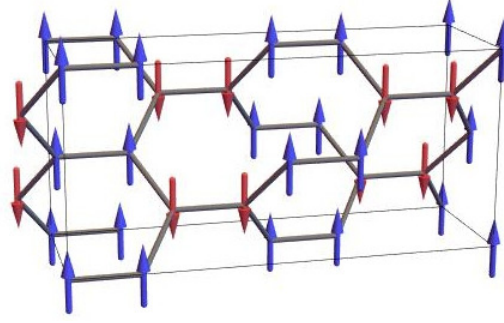


Figure 17 – Representation of the stripy order on the honeycomb lattice, which is equivalent to one of the possible two-color ordered states discussed in this section. The blue (red) arrows symbolize $j^z = 3/2$ ($j^z = -3/2$) states.

Source: By the author.

The diagonal LFWT Hamiltonian is explicitly given by

$$H_{fw} = -\frac{3}{2}NK + J \sum_{\mathbf{k}} \sum_{i=1}^4 \epsilon_i(\mathbf{k}) + K \sum_{\mathbf{k}} \sum_{i=1}^4 \epsilon_{\mathbf{k}} \left(\gamma_{i,\mathbf{k}}^\dagger \gamma_{i,\mathbf{k}} + \delta_{i,\mathbf{k}}^\dagger \delta_{i,\mathbf{k}} \right). \quad (4.50)$$

Including the zero-point fluctuations, the energy of the two-color state per particle reads

$$E_{\text{two-color}}^0 \approx -0.3079K, \quad (4.51)$$

and the correction to the order parameter is very small

$$\Delta M \approx 0.0282(4). \quad (4.52)$$

The difference in one order of magnitude to this correction is in line with the fact that quantum fluctuations in two dimensions are stronger than in three dimensions. It is also noticeable that the energy of this ordered state is very close on the two lattices. As will be shown, the energy $E_{\text{two-color}}^0$ is much higher than the energy of the QSOL states, making it uncompetitive for the ground state.

I recall that the LFWT is being performed with the $|\tilde{s}^z, \tilde{\tau}^z\rangle$ vectors; its physical picture is more immediately obtained by rotating the vectors back to the $|s^z, \tau^z\rangle$ or $|\frac{3}{2}, j^z\rangle$ representation. The simplest (and most important) case is the ordered state with $|\tilde{s}^z, \tilde{\tau}^z\rangle = |\frac{1}{2}, \frac{1}{2}\rangle$ on the sublattices labeled with odd indices and $|\tilde{s}^z, \tilde{\tau}^z\rangle = |\frac{1}{2}, -\frac{1}{2}\rangle$ on the sublattices labeled with even indices (see Subsection 3.3.4.1). The pseudo-orbital Néel order is converted to a ferromagnetic order on τ^z . Similarly, the ferromagnetic order on \tilde{s}^z becomes the so-called stripy order on s^z . This ordered state was first discussed as an exactly solvable point of the Kitaev-Heisenberg model. (112, 155) In the present context, it is more immediate to say that the model presents a stripy order involving $j^z = \pm 3/2$ states and is represented in Fig. 17. I will return to this state at the end of this section.

Four-color ordered states were also investigated and LFWT was found to be inadequate to study them. This type of order is set by placing one distinct color at each of the four sublattices

defined by the Klein transformation. A strict LFWT calculation leads to a very low energy per site $E_{\text{four-color}}^0 = -\frac{3}{2}K$, which is lower even than the QSOLs that will be discussed below. However, this result is misleading and its origin was discussed in Ref. (170). First, the LFWT Hamiltonian is the sum of independent Hamiltonians given by Eq. (4.36). This equation also implies that the only bosons allowed to move through a given bond are the ones whose colors correspond to those on the sites connected by this bond. The set of sites in which a boson is allowed to move form a connected cluster and the zero-point energy tends to increase with the cluster size. In the case of the two-color ordered state, the connected clusters of the two bosons correspond to the whole lattice and induces the large energy correction discussed above. In contrast, the connected clusters of the four-color ordered state contain only two sites and lead to a null energy correction. Since LFWT is designed to study long-range order, it becomes inaccurate if small clusters appear. (170)

The same remarkably low energy of the four-color state was found on the honeycomb lattice, where the use of more sophisticated techniques showed that it was an artifact of the LFWT. (42) The massive degeneracy of this state was used to argue in favor of the absence of spontaneous symmetry breaking for the SU(4) model on the honeycomb lattice. Exact diagonalization and infinite projected entangled-pair state (iPEPS) calculations gave more formal arguments in favor of a QSOL ground state. Although the use of this technique was not possible on the hyperhoneycomb lattice, the same type of degeneracy was found on it and supports a ground state that does not break symmetries and encourage the study of QSOL ground states.

4.2.2.2 Parton Mean Field Theory

The QSOLs on the hyperhoneycomb lattice for the SU(4) Heisenberg model will be now studied. The studied parton mean-field theories are exactly the same as studied in Ref. (42) on the honeycomb lattice. This lattice compared the energetics obtained using exact diagonalization with the results obtained with VMC for some fermionic QSOLs. The authors argued in favor of a QSOL with complex fermion excitations and π -flux per plaquette based on the close agreement of the result obtained from exact diagonalization and the energetics of the projected wavefunction of this state. The exact diagonalization procedure is not reliable for the hyperhoneycomb lattice because of a technical complication. This method find exact results for systems limited to $N \sim 20$ sites due to the exponential growth of the Hilbert space. This is just enough to consider four distinct elementary plaquettes of the hyperhoneycomb ($N = 18$), that is, only one minimal cluster. However, It will be demonstrated that the QSOLs on the hyperhoneycomb display energies similar to the ones found on the honeycomb lattice in agreement with the LFWT result. This gives plausibility to the hypothesis that the energy ground state of the model on the hyperhoneycomb lattice will be also close to the one calculated on the honeycomb in Ref. (42), and as a result, that its ground state is also a QSOL.

I first consider the results for the QSOLs based on the canonical fermion representation.

The order parameters will be $\chi_{ij} \equiv \langle f_{im}^\dagger f_{jm} \rangle$ and lead to the following mean-field equations

$$H_{mf} = - \sum_{\langle ij \rangle} \sum_{m=1}^4 \left(\chi_{ij} f_{im}^\dagger f_{jm} + h.c. \right). \quad (4.53)$$

As usual, the flux around the plaquettes will be used to label the QSOLs. It was decided that a pragmatic approach would be followed. The mean-field theories discussed in this section serve to generate wavefunctions that will be projected to a physical Hilbert state. The projected wavefunction is a QSOL with well-defined values for the gauge fluxes and described in terms of a certain type of parton (even if it does not arise from a self-consistent mean field theory). Further studies on the optimization of the projected wavefunction will be the subject of future works.

Following (42), the QSOLs order parameters are restricted to real values and the theory is treated as if $\chi_{ij} = \pm 1$. The flux around a plaquette P is called $\phi(P)$ and will be given by

$$e^{i\phi(P)} = \prod_{\langle ij \rangle \in P} \chi_{ij}. \quad (4.54)$$

Two different *Ansätze* were investigated, one with uniform zero-flux on all plaquettes and other with π -flux per plaquettes. These are represented in Fig. 18. In this case, the numbers represent the eight sublattices of the hyperhoneycomb and the solid (dashed) lines represent order parameters with $\chi_{ij} = +1$ ($\chi_{ij} = -1$). While the zero-flux could be represented in terms of the standard four-sublattice representation of the hyperhoneycomb, the π -flux breaks the translation symmetry on the mean-field level and requires the eight-sublattice representation.

At the mean-field level, the single-occupancy constraint is imposed on average,

$$\sum_m \left\langle \Psi_{MF} \left| f_{im}^\dagger f_{im} \right| \Psi_{MF} \right\rangle = 1, \quad (4.55)$$

corresponding to a quarter-filled Fermi sea. The mean-field ground state $|\Psi_{MF}\rangle$ is determined by diagonalizing the quadratic Hamiltonian (4.53) for both zero-flux and π -flux states. In general,

$$H_f = \sum_{\mathbf{k}} \sum_{\lambda=1}^8 E_\lambda(\mathbf{k}) f_{\mathbf{k}\lambda}^\dagger f_{\mathbf{k}\lambda}, \quad (4.56)$$

where λ is the band index and $f_{\mathbf{k}\lambda}$ annihilates a fermion with momentum \mathbf{k} in band λ . The analytical expressions for the dispersion relations are possible only for the zero-flux state. The eight bands are written as $E_1 = \varepsilon_1^{++}$, $E_2 = \varepsilon_1^{+-}$, $E_3 = \varepsilon_1^{-+}$, $E_4 = \varepsilon_1^{--}$, $E_5 = \varepsilon_2^{++}$, $E_6 = \varepsilon_2^{+-}$, $E_7 = \varepsilon_2^{-+}$, $E_8 = \varepsilon_2^{--}$ where

$$\varepsilon_n^{pp'}(\mathbf{k}) = p \sqrt{g_n(\mathbf{k}) + p' \sqrt{|g_n(\mathbf{k})|^2 - |h_n(\mathbf{k})|^2}}, \quad (4.57)$$

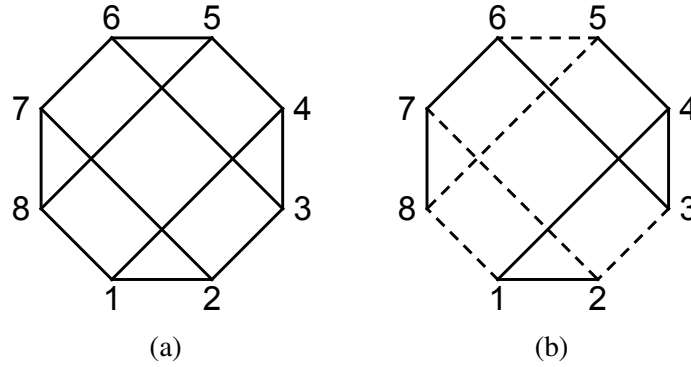


Figure 18 – Representation of the (a) zero-flux and (b) π -flux states. Each vertex corresponds to a basis point of the hyperhoneycomb lattice as labeled in Fig. 13a. Solid (dashed) lines represent bonds with $\chi_{ij} = +1$ ($\chi_{ij} = -1$).
Source: NATORI; ANDRADE; PEREIRA. (3)

with $n = 1, 2$ and $p, p' = \pm$, and the following functions are defined by

$$\begin{aligned}
 g_1(\mathbf{k}) &= 3 + 2 \cos(2k_z) \cos(k_x - k_y), \\
 h_1(\mathbf{k}) &= 2 \cos(2k_z) e^{i(k_x+k_y)} - e^{-2i(k_x+k_y)} + e^{2ik_x} + e^{2ik_y}, \\
 g_2(\mathbf{k}) &= 3 - 2 \cos(2k_z) \cos(k_x - k_y), \\
 h_2(\mathbf{k}) &= 2 \cos(2k_z) e^{i(k_x+k_y)} + e^{-2i(k_x+k_y)} - e^{2ik_x} - e^{2ik_y}.
 \end{aligned} \tag{4.58}$$

An analytical form for the dispersion of the π -flux QSOL was not found and was computed only numerically. Figure 19 shows the mean-field spectrum of the two QSOLs. Notice that in both cases the dispersions display particle-hole symmetries, as expected for bipartite lattices.

The quarter-filling condition $\langle f_{im}^\dagger f_{im} \rangle = 1/4$ determines the position of the Fermi level. The zero-flux state displays a large Fermi surface that is illustrated in Fig. 20. The vector $\mathbf{Q}_0 = (\frac{\pi}{3}, \frac{\pi}{3}, \frac{\pi}{3})$ connects the two plain pieces of the Fermi surface depicted in yellow. Since this is a reciprocal lattice vector of the Bravais lattice of the hyperhoneycomb lattice before doubling the unit cell, the Fermi surface is not nested and this QSOL is at least locally stable against (spin) density waves driven by interactions beyond the mean-field level. On the other hand, the Fermi level for the π -flux state crosses Dirac points at the high-symmetry points S, Z and T. Close inspection reveals that the dispersion in the vicinity of these Dirac points is anisotropic. The spectrum in the neighborhood of S is linear along two directions in \mathbf{k} space but quadratic in the third direction. The opposite is verified for the dispersion around the Z and T points, which is quadratic along two directions and linear in the third. Similar behavior has been discussed for Dirac semimetals in two and three dimensions. (167, 171, 172) This state may be then related with topological phases of matter protected by nonsymmorphic symmetries.

The mean-field ground state $|\Psi_{\text{MF}}\rangle$ is given by the Fermi sea of all single-fermion states with energy below the Fermi level. The constraint defining the physical Hilbert space must be imposed by a Gutzwiller projection if we are to evaluate physical quantities. For the $j = 3/2$

QSOL described by complex fermions, the projection reads

$$|\Psi_{\text{phys}}\rangle = \mathcal{P}_f |\Psi_{\text{MF}}\rangle, \quad (4.59)$$

where $\mathcal{P}_f = \prod_i \left[\frac{1}{6} n_i (2 - n_i) (3 - n_i) (4 - n_i) \right]$ and $n_i = \sum_m f_{im}^\dagger f_{im}$.

I will now briefly discuss the parton mean-field theory using Majorana fermions. In terms of the complex fermions c_i defined in Eq. (4.7), the total SU(4) Heisenberg model reads

$$H_{SU(4)} = K \sum_{\langle jl \rangle} \left[1 - \frac{1}{2} \left(i\mathbf{c}_j^\dagger \cdot \mathbf{c}_l - i\mathbf{c}_l^\dagger \cdot \mathbf{c}_j \right)^2 \right]. \quad (4.60)$$

The most straightforward mean field decoupling reads (41)

$$H_c = -i \sum_{\langle jl \rangle} \xi_{jl} \left(\mathbf{c}_j^\dagger \cdot \mathbf{c}_l - \mathbf{c}_l^\dagger \cdot \mathbf{c}_j \right), \quad (4.61)$$

where $\xi_{jl} = \langle i\mathbf{c}_j^\dagger \cdot \mathbf{c}_l - i\mathbf{c}_l^\dagger \cdot \mathbf{c}_j \rangle$ and I ignored the terms dependent only on the order parameters. The values of ξ_{jl} must be real numbers and obey $\xi_{jl} = -\xi_{lj}$. Using the property that the hyperhoneycomb lattice is bipartite, it is verifiable that the mean-field dispersion of the complex fermion QSOL and the Majorana fermion QSOL will be formally the same. To show this, define the operators $c_j = i\tilde{c}_j$, $c_l = \tilde{c}_l$. In terms of these operators

$$H_c = - \sum_{\langle jl \rangle} \xi_{jl} \left(\tilde{c}_j^\dagger \cdot \tilde{c}_l + \tilde{c}_l^\dagger \cdot \tilde{c}_j \right), \quad (4.62)$$

which is formally identical to the mean-field Hamiltonian for complex fermions. The spectrum for Majorana fermions will be the same as the one found for complex fermions. The same problems of self-consistency were found for the Majorana fermion equations and the pragmatic approach will be also used in this case.

One distinction between the Majorana fermion and the complex fermion QSOL is that the average density of c fermions is not constrained to a specific value. The $|\Psi_{\text{MF}}\rangle$ is then not constrained to a specific Fermi level and corresponds to the Fermi sea of all negative energy eigenstates in the mean-field level. The two QSOLs display Fermi surfaces given by nodal lines, a behavior also observed for the Kitaev model on the same lattice. (103, 107, 155) The Gutzwiller projection is implemented by applying the projector operator $\mathcal{P}_c = \prod_j \left[\frac{1}{2} + \frac{1}{2} \prod_\gamma \left(1 - 2c_{j\gamma}^\dagger c_{j\gamma} \right) \right]$ to impose the Z_2 constraint to the physical Hilbert space in Eq. (4.8).

4.2.3 Variational Monte Carlo Study of the SU(4)-symmetric Spin-Orbital Liquids

The local constraints are now exactly enforced by considering a Gutzwiller projection of the mean-field wave functions. (46) As a result of this computation, the zero-flux state of complex state was found to be the QSOL with lowest energy. The large Fermi surface of this

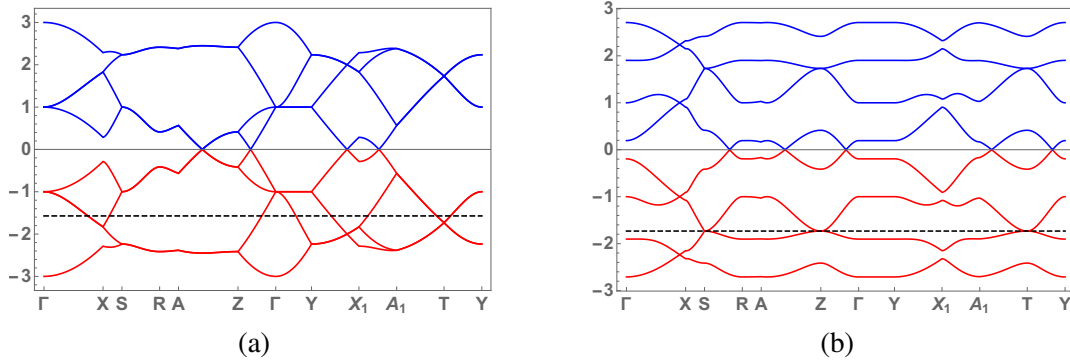


Figure 19 – Mean-field dispersion of fermions in the (a) zero-flux and (b) π -flux states. The dashed line marks the Fermi level at quarter filling. The high symmetry points of the Brillouin zone are specified in Fig. 20. The energy scale in this plot is set by $|\chi_{ij}| = 1$.

Source: NATORI; ANDRADE; PEREIRA. (3)

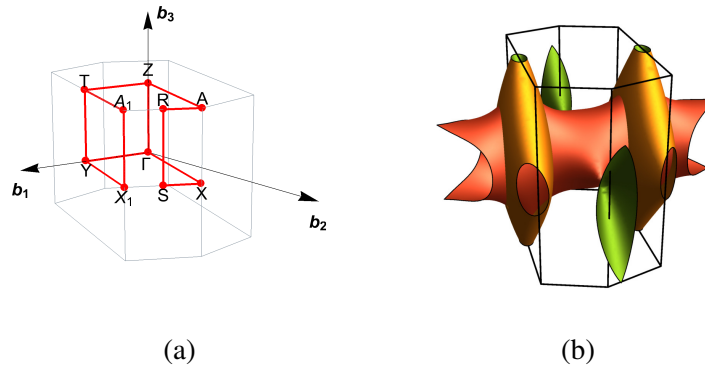


Figure 20 – (a) Brillouin zone of the base-centered orthorhombic lattice. (b) Fermi surface of the zero-flux state. Different colors represent different bands in Eq. (4.57).

Source: NATORI; ANDRADE; PEREIRA. (3)

QSOL induced us to study its stability against perturbations inducing tetramerization (43) and also the effect of J_H -induced perturbations (Eq. (3.68)) on its energetics. The principles of the VMC algorithm is the same in all cases, so that the procedure to the numerical calculations will be discussed only for the SU(4) symmetric case.

For complex fermions, the mean-field ground state from Eq. (4.53) is projected to states explicitly obeying Eq. (4.4). The first step is to generate a basis of the physically allowed real-space configurations

$$|\{i_a^1\}, \{i_b^2\}, \{i_c^3\}, \{i_d^4\}\rangle = \prod_{m=1}^4 \prod_{\mathbf{r}_{a,m}=1}^{N/4} f_m^\dagger(\mathbf{r}_{a,m}) |\emptyset\rangle, \quad (4.63)$$

where i_a^m denotes the position, at site i , of the a -th fermion with color m . The overlap of (4.63)

with the mean-field state is

$$\Psi (\{i_a^1\}, \{i_b^2\}, \{i_c^3\}, \{i_d^4\}) = \prod_{m=1}^4 \Phi [\{i^m\}], \quad (4.64)$$

in which $\Phi [\{i^m\}]$ is the Slater determinant for one fermion species

$$\Phi [\{i^m\}] = \begin{vmatrix} \zeta_1(i_1^m) & \zeta_2(i_1^m) & \cdots & \zeta_{N/4}(i_1^m) \\ \vdots & \vdots & \ddots & \vdots \\ \zeta_1(i_{N/4}^m) & \zeta_2(i_{N/4}^m) & \cdots & \zeta_{N/4}(i_{N/4}^m) \end{vmatrix}, \quad (4.65)$$

and $\zeta_\nu(i)$ is the amplitude of the fermion at site i in the ν th eigenfunction of the mean-field Hamiltonian (4.53): $\zeta_\nu(j) \equiv \langle j | \nu \rangle$.

Variational Monte Carlo calculations are carried out using this wave function. The general principles of this calculation were discussed in Subsection 2.2.3 and here I give an example of how that general procedure is applied. The number of sites considered is given by $N = 8L^3$, with $L = 3, 4, 5$, and 6 (see Subsection 3.3.4.1). The first step is to randomly assign each color at $N/4$ distinct sites of the lattice. The Monte Carlo moves consist in exchanging a random pair of sites containing distinct colors. This moves can involve sites far away — and which would not otherwise interact directly via the Hamiltonian — because this improves the sampling over the space of configurations. The Metropolis algorithm (Eq.(2.37)) provides the criterion to accept or reject these moves. Given a color configurations $\{i\}$, we can define a probability that is proportional to the weight of the wave function

$$p(\{i\}) \propto \left| \prod_{m=1}^4 \Phi [\{i^m\}] \right|^2. \quad (4.66)$$

The probability that a move from $\{i\}$ to a different $\{i'\}$ configuration occurs is

$$T(\{j\} \rightarrow \{j'\}) = \begin{cases} 1, & \text{if } p(\{j'\}) > p(\{j\}) \\ p(\{j'\})/p(\{j\}), & \text{otherwise.} \end{cases} \quad (4.67)$$

For each accepted ground state configuration, the following number is computed

$$f(\{j\}) = \sum_{\{j'\}} \langle \{j\} | H_{\text{SU}(4)} | \{j'\} \rangle \frac{\langle \{j'\} | \Psi \rangle}{\langle \{j\} | \Psi \rangle}. \quad (4.68)$$

After N_{exc} of such exchanges attempts, we are said to have performed a Monte Carlo sweep. The ground state energy E_0 calculated after the sweep is given by

$$E_0 = \frac{1}{N_{\text{MC}}} \sum_{i=1}^{N_{\text{MC}}} f(\{j\}_i), \quad (4.69)$$

where N_{MC} is the number of accepted configurations after a sweep. In fact, the first sweeps of the VMC procedure may compute unreliable values of E_0 . It is possible, for example, that the

Table 3 – VMC ground state energy, per site, for the different mean-field states.

Ansatz	E_0/N
Complex fermions zero-flux	$-0.825 (1) J$
Complex fermions π -flux	$-0.806 (2) J$
Majorana fermions zero-flux	$-0.783 (1) J$
Majorana fermions π -flux	$-0.757 (1) J$

Source: NATORI; ANDRADE; PEREIRA (3)

initial random state corresponds to a large value of $f(\{j\}_i)$ and the other states accepted with the Metropolis algorithm follow this tendency, leading to a value of E_0 much larger than the actual energy of the projected wavefunction. For this reason, N_{warm} sweeps are performed before measurements of physical quantities for “thermalization” and only then N_{mes} measurements sweeps are considered for the calculation of the mean values and the variance. In the VMC program, the typical values of these numbers are $N_{\text{exc}} \sim 10^3$ and $N_{\text{warm}} = N_{\text{mes}} \sim 10^5$.

For the Majorana fermion representation of the pseudospin and pseudo-orbital operators, the mean-field ground state from Eq. (4.61) is Gutzwiller projected. The wavefunction is already written in terms of the three complex c fermions both in the zero-flux and π -flux states. Eq. (4.8) imposes that a site can either have no c fermions, $|\emptyset\rangle$, or two c fermions. Three states are then introduced (41)

$$|X\rangle = c_y^\dagger c_z^\dagger |\emptyset\rangle, |Y\rangle = c_z^\dagger c_x^\dagger |\emptyset\rangle, |Z\rangle = c_x^\dagger c_y^\dagger |\emptyset\rangle. \quad (4.70)$$

For any given configuration of these states, specified by the real-space location of the $|X\rangle$, $|Y\rangle$, and $|Z\rangle$ states (at sites $\{x_i\}$, $\{y_j\}$, and $\{z_m\}$, respectively), the projected wave function assigns an amplitude

$$\Psi(\{x_i\}, \{y_j\}, \{z_m\}) = \Phi_z(\{x_i\}, \{y_j\}) \cdot \Phi_x(\{y_j\}, \{z_m\}) \cdot \Phi_y(\{z_m\}, \{x_i\}) \quad (4.71)$$

to it. The locations of the $|\emptyset\rangle$ states are automatically specified.

The starting point of the VMC procedure is to generate an initial state in which we populate $N/4$ randomly chosen sites with the x -state ($\{x_i\}$), $N/4$ with the y -state ($\{y_i\}$), and $N/4$ with the z -state ($\{z_i\}$), in which $\{x_i\}$, $\{y_i\}$ and $\{z_i\}$ are disjoint sets. The Monte Carlo moves consist in exchanging random pairs of sites containing distinct states often involving widely separated sites. These moves are accepted or rejected according to the usual Metropolis algorithm, much in the same way as the case of complex fermions. The probability weight of a given configuration used in Metropolis algorithm is now proportional to $|\Psi(\{x_i\}, \{y_j\}, \{z_m\})|^2$.

Figure 21 shows the VMC results for the ground state energies of all four considered Ansätze at the different system sizes. The results do not vary much with the system size and their extrapolation for $N \rightarrow \infty$ are presented in Table 3. The corresponding variational energy for the SU(4) model on the hyperhoneycomb lattice are comparable with those of the honeycomb lattice. (42) This result and the similar values of the energy for the ordered states using LFWT

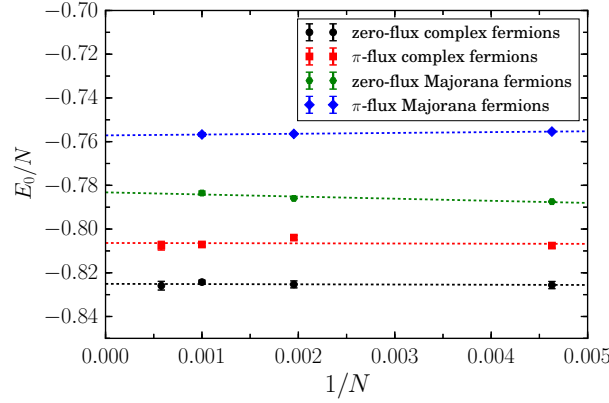


Figure 21 – VMC ground state energy, per site and in units of J , for the different mean-field states as a function of the inverse of the particle number. The dashed lines are linear extrapolations to the data.

Source: NATORI; ANDRADE; PEREIRA. (3)

reinforces the idea that the exact ground state energy on the hyperhoneycomb lattice must be similar to the one verified on the honeycomb lattice. The combination of these results indicate the feasibility of a spin-orbital liquid ground state. However, there are two significant differences. First, the projected wave function with the lowest variational energy is the zero-flux state of complex fermions with a large Fermi surface instead of the π -flux Ansatz with doubly degenerate bands and a single Dirac cone. Second, the relative energy difference between the best variational state and the next candidate, the π -flux state for complex fermions, is roughly 2%, hinting at a fiercer competition between the different variational states in the hyperhoneycomb lattice.

The large Fermi surface of the zero-flux QSOL led us to investigate the stability of this Ansatz against the so-called *tetramerization*. (43) As discussed earlier in Section 3.4, the two-site SU(4) Hamiltonian does not generate a singlet but a sixfold degenerate ground state. A singlet state must involve at least four sites (hence, it is called tetramer), whose explicit form is given by

$$|\text{Tet}\rangle = \frac{1}{\sqrt{24}} \sum_{\{ijkl\}} c_{i1}^\dagger c_{j2}^\dagger c_{k3}^\dagger c_{l4}^\dagger |0\rangle, \quad (4.72)$$

where the sum runs over all $4! = 24$ color permutations. Fig. 22a also gives a representation of a state composed by direct product of tetramers on the hyperhoneycomb lattice, which is the analogous of a VBS state on a $j = 3/2$ model. Each tetramer is centered at a site on the sublattice 1 or 6 and involves the three nearest neighbors of these sites.

The tetramer formation can be induced by localizing fermions at the neighborhood of a given site. In the case of the zero-flux QSOL, this can be induced by slightly modifying Eq. (4.53) as follows (43)

$$H_{mf} = \sum_i \epsilon_i - \sum_{\langle ij \rangle} \sum_{m=1}^4 \left(t_{ij} f_{im}^\dagger f_{jm} + h.c. \right). \quad (4.73)$$

We keep $\epsilon_i = 0$ and $t_{ij} = \chi_{ij} = 1$ for all sites and links, except when they involve a site on sublattices 1 or 6. Choosing $\epsilon_i = \epsilon < 0$ and $t_{ij} = t > 1$ in these cases induce the formation of tetramers throughout the lattice (see Fig. 22a).

Let us now define the tetramerization order parameter. Let $P_{ij} = S_n^m(i)S_n^m(j)$, in such a way that $\mathcal{H}_{\text{SU}(4)} = K \sum_{\langle ij \rangle} P_{ij}$. It is possible to distinguish two types of links in Fig. 22a: the ones inside of a tetramer (magenta bonds) and the ones connecting two different tetramers (blue bonds). Let $\langle P_a \rangle$ be the mean value of the projected wavefunction of the ground state of $H_{m,f}$ for the first type of bond, and $\langle P_b \rangle$ for the second type. The equality $\langle P_a \rangle = \langle P_b \rangle$ is found on QSOLs, while a fully tetramerized state is characterized by $\langle P_a \rangle = -1$ and $\langle P_b \rangle = 1/4$. (43) A convenient tetramerization order parameter is then given by

$$r = \frac{4}{5} (\langle P_b \rangle - \langle P_a \rangle), \quad (4.74)$$

where $r = 0$ for the QSOL and $r = 1$ for the fully tetramerized state. The $r = 0$ state is obtained by setting $\epsilon_i = 0$ and $t_{ij} = 1$ for all links and bonds. Once these two parameters are changed, they induce a different ground state wavefunction whose projection gives $r \neq 0$. Figure 22 shows how the dispersion can be modified by these parameters, including the possibility of opening a gap. For this wavefunction, it is possible to compute its ground state energy using the same procedure outlined above.

A quantum spin-orbital liquid is said to be stable against tetramerization if the energy minimum is found at $r = 0$. This is not necessarily the case for the SU(4) Heisenberg model. For example, the exact diagonalization of this model on the two-leg ladder indicated that its ground state display spontaneous plaquette formation (tetramerization) with twofold degeneracy. (173) Here, the numerical calculations performed for the zero-flux QSOL on the hyperhoneycomb lattice showed that the energy minimum occurs for the $r = 0$ point (see Fig. 23). A similar result was found in a previous study done on the honeycomb lattice. (43) Hence, it is possible to argue in favor of the QSOL stability on the hyperhoneycomb lattice.

The follow-up question was the effect of the Hund's coupling induced perturbations on the QSOL given in Eq. (3.68). These perturbations lift degeneracies of the SU(4) model and can favor ordered states. As discussed earlier, I have performed the LFWT study for two-color ordered states on the hyperhoneycomb lattice. I have found that most of these states develop complex frequencies on the LFWT dispersion when perturbations induced by infinitesimal values of η are added. The sole exceptions are the stripy ordered state displayed in Fig. 17 and the states related to it by global rotations of \tilde{s} . Complex frequencies are induced by the perturbations only for $\eta > 0.125$. Up to this value of η , LFWT can be used to give an estimative energy of the stripy ordered state as the function of the perturbation.

The energy per site of the stripy state and of the complex fermion QSOLs as a function of η is shown in Fig.(24) and indicates that the zero-flux remains the lowest energy state. Taking into account the evidence that this state is also stable against tetramerization, the result makes this

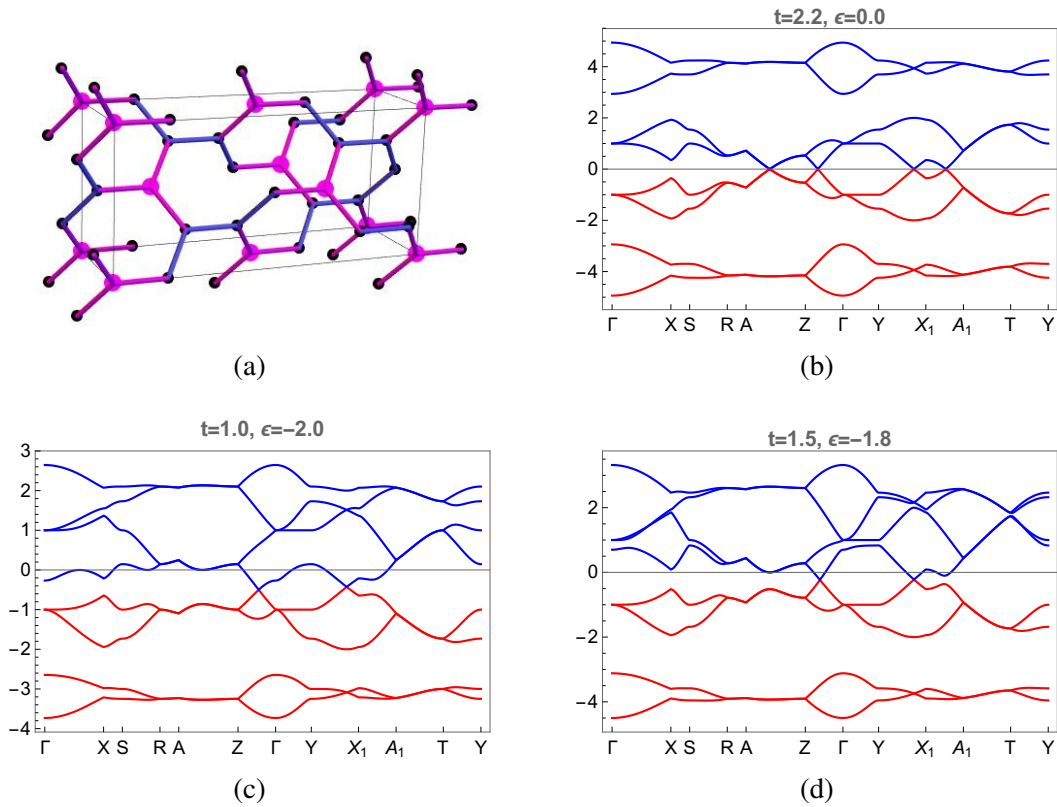


Figure 22 – Fig.(a) gives a representation of a fully tetramerized state on the hyperhoneycomb lattice in real space, where the magenta bonds indicate the localization of the tetramers. Figures (b), (c) and (d) give the dispersion relations for different values of ϵ and t and show how they induce gap opening. The ϵ parameter also induces the breaking of particle-hole symmetry.

Source: NATORI; ANDRADE; PEREIRA (3)

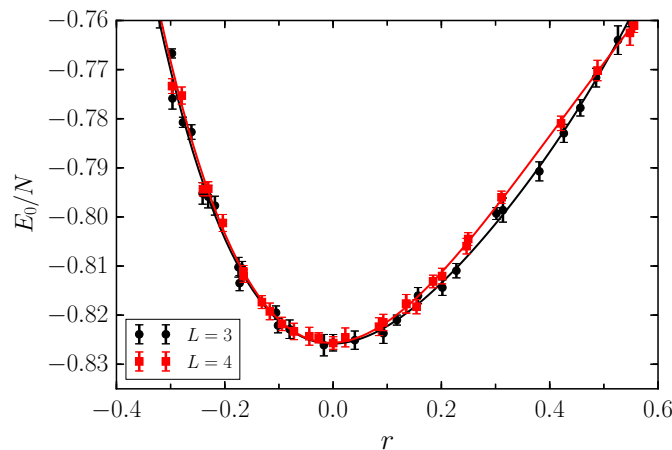


Figure 23 – Energy per site calculated with VMC as a function of the tetramerization order parameter (Eq. (4.74)). The number of sites is $N = 8L^3$, where L is given by the inset. The minimum of the energy was found at $r = 0$, which shows that the zero-flux QSOL is stable against tetramerization.

Source: By the author.

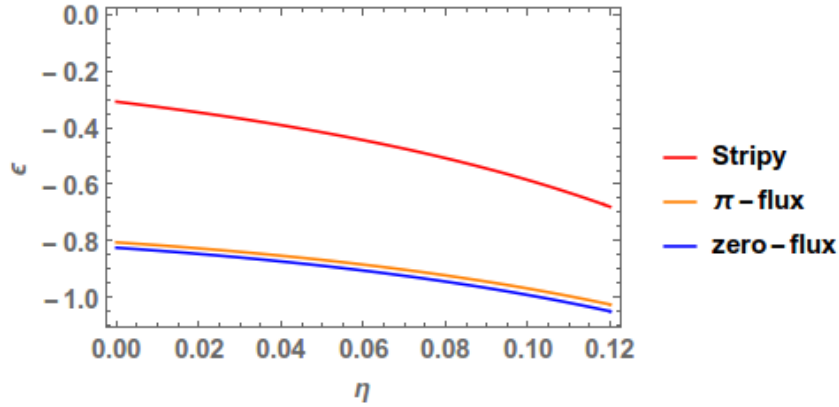


Figure 24 – Energy of the stripy order and the QSOLs based on complex fermions as a function of the parameter $\eta = J_H/U$ for the Hamiltonian given by Eq. (3.68). The stripy order energy was calculated using LFWT, while the QSOL energy is determined with VMC.

Source: By the author.

QSOL a viable candidate for the ground state of $4/5d^1$ compounds with the same lattice structure as the Kitaev materials. It must be added, however, that non-collinear ordered states and dimerized phases were not studied and it is still possible that they adequately describe the ground state of of Eq. (3.68). In fact, the Kitaev material $\beta\text{-Li}_2\text{IrO}_3$ on the hyperhoneycomb lattice displays non-collinear order of pseudospins due to interactions beyond the nearest neighbors (174) and it is possible that a spin-orbital analogous order emerges on the hypothetical compound studied here. This kind of study is more correctly done with the aid of experimental data that are still unavailable and, therefore, will be left for future work.

5 EXPERIMENTAL PROBES TO QUANTUM SPIN LIQUIDS

Physics is an experimental science and its theoretical predictions must result in phenomena that are, at least in principle, experimentally observable. This is another challenge on the study of QSLs and QSOLs. There is still no experimental probe giving a reliable measure of long-range entanglement. (11) The option to study QSLs experimentally is to compute the expected response of a proposed QSL under the usual probes to frustrated magnetism and then compare these results with the experimental data available for a spin liquid candidate.

This chapter presents the experimental responses of the chiral QSOL on double perovskites within parton mean field theory. (1) These results are compared with the experimental data of the double perovskite Ba_2YMoO_6 , which lacks observable magnetic order. This methodology must be viewed with caution. Once again: since the partons are not themselves physical, the experimental responses calculated with this approach will include responses arising from unphysical states. The theoretical technology to tackle this problem is still being developed. In fact, the Kitaev model remains the only instance of a QSL described with a parton theory whose spectroscopic (125–131) and thermodynamic responses (132–134, 175) were calculated in a numerically exact way. Some controlled approximations are possible if perturbations are added to this model (137, 142, 176), but it is still not clear how it can be applied outside this context. Nevertheless, parton theory is still used to discuss the low-temperature physics (158, 159) and dynamical structure factor (177) of QSLs. The idea is that the mean field result constitutes a good starting point to discuss the property of a QSL, and that improvements can be made by including gauge fluctuations.

Some important points pervading this chapter must be presented at this point. First, the low-temperature physics of the QSOL will be dominated by the states close to the Fermi lines. It is therefore important to calculate the density of states near these points, which in turn depend upon the Majorana fermion dispersion. As stated in the previous chapter, in the neighborhood of the R point ($\mathbf{k} = (\pi, \pi, \pi) + \mathbf{q}$, with $|\mathbf{q}| \ll 1$) the following proportionality relation is observed

$$\epsilon_{\mathbf{k}\lambda} \propto \sqrt{q_x^2 q_y^2 + q_y^2 q_z^2 + q_z^2 q_x^2}, \quad (5.1)$$

for all Majorana flavors. I write $\epsilon_{\mathbf{k}\lambda} = q^2 f_\lambda(\Omega)$, with $f_\lambda(\Omega)$ a function of the spherical angle coordinates of \mathbf{q} that also absorbs the multiplicative factor arising from the order parameters u , v , w , and \bar{w} . It will be verified that the single-particle states in the neighborhood of the R point dominate the low-energy physics due to this quadratic dispersion. This can be first realized by

computing its corresponding contribution to the density of states

$$\begin{aligned}
\rho_{\text{point}}(E) &= \sum_{\mathbf{k}, \lambda} \delta(E - \epsilon_{\mathbf{k}\lambda}) \\
&\approx \sum_{\lambda} \int d\Omega \int \frac{dq q^2}{(2\pi)^3} \delta(E - q^2 f_{\lambda}(\Omega)) \\
&= \frac{1}{2} \sqrt{E} \sum_{\lambda} \int d\Omega [f_{\lambda}(\Omega)]^{-3/2}.
\end{aligned} \tag{5.2}$$

The important point is that $\rho_{\text{point}}(E) \propto \sqrt{E}$ corresponds to a vanishing density of states characteristic of a pseudogap. On the other hand, the density of states around generic points on the nodal line parallel to the k_z axis yields

$$\begin{aligned}
\rho_{\text{line}}(E) &\approx \sum_{\lambda} \int dk_z \int d\varphi \int \frac{dp p}{(2\pi)^3} \delta(E - v_{\lambda}(k_z)p) \\
&= E \sum_{\lambda} \int_0^{\pi-\epsilon} \frac{dk_z}{4\pi^2 [v_{\lambda}(k_z)]^2},
\end{aligned} \tag{5.3}$$

where $v_{\lambda}(k_z)$ is the effective velocity of the linear dispersion around the nodal line and the integral was cut off at $|k_z - \pi| = \epsilon > 0$ to exclude the contribution from the R point. Thus, the contribution from the nodal lines to the density of states is $\rho_{\text{line}}(E) \propto E$. The comparison of Eqs. (5.2) and (5.3) suggests that the low-temperature thermodynamics of the chiral spin-orbital liquid should be governed by the quadratic band touching point.

Another point to be discussed is the total magnetic moment \mathbf{M} of the electrons in atomic d orbitals, which couple to external magnetic fields and the neutron spin in INS. For an atom, the magnetic moment in the limit of strong SOC is given by

$$\begin{aligned}
\mathbf{M} &= \mathcal{P}_{3/2} \mathcal{P}_{t_{2g}} [\mathbf{L} + 2\mathbf{S}] \mathcal{P}_{t_{2g}} \mathcal{P}_{3/2} \\
&= \mathcal{P}_{3/2} [-\mathbf{1} + 2\mathbf{S}] \mathcal{P}_{3/2},
\end{aligned}$$

where \mathbf{S} in the second line is the electronic spin of the t_{2g} orbitals. Remember that Eq. (3.50) shows that $\mathcal{P}_{3/2} \mathbf{S} \mathcal{P}_{3/2} = \frac{1}{3} \mathbf{j}$. It can also be proved that (29)

$$\mathcal{P}_{3/2} \mathbf{1} \mathcal{P}_{3/2} = \frac{2}{3} \mathbf{j}. \tag{5.4}$$

Gathering all the results would result in a vanishing magnetic moment $\mathbf{M} = 0$. The measured magnetic moments are indeed small in comparison with spin- $\frac{1}{2}$ systems without degeneracy. They are, however, not zero and are proportional to the total angular momentum \mathbf{j} . This can be explained in terms of the hybridization of the d orbitals with the p orbitals from the oxygen ions. As a result, the coupling of the electron to a magnetic field \mathbf{H} is modeled by (29)

$$\mathcal{H}_Z = -g_{\text{eff}} \mu_B \mathbf{H} \cdot \mathbf{J}, \tag{5.5}$$

where g_{eff} is the effective Landé factor and μ_B is the Bohr magneton.

This chapter is separated into two broad sections, the first concerning with the experimental responses of the chiral QSOL to techniques already available (Section 5.1) and the second is concerned with the RIXS theory for $4/5d^1$ Mott insulators (Section 5.2). An introductory discussion of each technique is given before presenting the calculations to indicate what information can be acquired for the QSOL with it.

5.1 Experimental responses of the chiral QSOL to well-established probes

5.1.1 Specific Heat

A phase transition always occur at points in which the free energy F or the partition function Z is nonanalytical. Thermal phase transitions must then be accompanied by a singularity of the specific heat, since it is given by the derivative of the free energy like

$$C_V = -T \frac{\partial^2 F}{\partial T^2}. \quad (5.6)$$

This is a very general result valid for all kinds of transition (magnetic, structural, ferroelectric, etc). Since any degree of freedom of a compound is subject to thermal fluctuation, the measurement of the magnetic specific heat is generally given by the subtraction of the lattice specific heat C_{lat} from the experimentally measured C_V . The fundamental step of this procedure is to identify a nonmagnetic compound isostructural to the QSL candidate. The specific heat measured in the nonmagnetic compound is corrected by the atomic mass of the magnetic ion of the QSL candidate, giving the C_{lat} . This procedure presupposes that the contributions to C_V in Mott insulators can be mostly attributed to phonons and magnetic excitations C_{mag} , i.e., $C_V = C_{\text{lat}} + C_{\text{mag}}$. However, it is not a priori clear if other contributions are irrelevant to C_V .

The magnetic specific heat can give us important information concerning the nature of the local degrees of freedom of a spin Hamiltonian. We know that the entropy released between the zero and T temperature is given by the integral

$$S(T) = \int_0^T \frac{C_V(T')}{T'} dT'. \quad (5.7)$$

In a spin system, we know that the number of accessible states is $\Omega = (2S + 1)^N$, where N is the number of spins and S is the effective spin. It is possible to compute $S(T)$ from the experimental data of the magnetic specific heat, and in this manner compute the value of the spin. For example, if the system has a spin $S = 3/2$, then the entropy per particle integrated from low to high temperatures must approach $k_B \ln 4$, where k_B is the Boltzmann constant. This is an important information for the Mott insulators with strong spin-orbit coupling, since it can validate or refute the projection of the Kugel-Khomskii Hamiltonian to the Hilbert space of states with an effective angular momentum. The specific heat near the critical temperature can also reveal the universality class of the model describing the compound under study. This is made by

extracting the critical exponents at the point of phase transition from the experimental data, and then comparing it with the most studied models.

The specific heat C_V of Ba_2YMoO_6 was measured by de Vries *et al.* (30) and Aharen *et al.* (31) In both experiments, the magnetic contribution was obtained by subtracting off the specific heat of the nonmagnetic compound Ba_2YNbO_6 from the total specific heat of Ba_2YMoO_6 . The measurements agree about the presence of a broad peak around 50 K. However, the reported maximal values of C_V are different: 7.5 J/mol·K in Ref. (30) versus 2.5 J/mol·K in Ref. (31) By integrating C_V out to $T \approx 200$ K, de Vries *et al.* (30) found that the entropy released is close to $k_B \ln 4$, as expected for a $j = 3/2$ system and the low-temperature behavior of C_V was interpreted as evidence for a pseudogap in magnetic excitations. (33) On the other hand, Aharen *et al.* (31) noted that the entropy lost below 50 K is lower than $k_B \ln 2$ and found an abrupt drop in the magnetic specific heat above 60 K. Disorder may be the cause of these differences, since it affects the density of states and consequently changes the specific heat. (158) Since disorder is inevitable in any synthesized compound and it is difficult to compare the level of cleanness of two different samples, extra caution must be given when analyzing specific heat data. The study of disorder effects were beyond the goals of this doctoral thesis and is left for a more specific project. The results published in Ref. (1) focused on the common observation of a broad peak in C_V and use this information to set the energy scale in our spin-orbital model.

At low temperatures $T \ll J$, the order parameters are approximately given by their zero-temperature values. The main effect of thermal fluctuations in this regime is to change the occupation of the states in a band with fixed bandwidth. Using the density of states in Eq. (5.2), the contribution of points in the neighborhood of R to C_V is given by

$$\begin{aligned} C_V(T \ll J) &= \int_0^\infty dE E \rho_{\text{point}}(E) \frac{\partial n_F}{\partial T} \\ &\propto T^{3/2} \int_0^\infty dx \frac{x^{5/2} e^x}{(1 + e^x)^2}. \end{aligned} \quad (5.8)$$

A similar calculation for the points near the nodal lines yield $C_V \propto T^2$. Thus, at sufficiently low temperatures we obtain the power-law behavior $C_V \propto T^{3/2}$.

The C_V is calculated following the method of Ref. (159), which studied a Majorana QSL on a $S = 1/2$ Heisenberg model. The mean-field theory described in Sec. 4.2.1 can be extended to $T > 0$ by replacing the average occupation of single-particle states by the Fermi-Dirac distribution:

$$\begin{aligned} \langle \tilde{\zeta}_{\mathbf{k}\lambda}^\dagger \tilde{\zeta}_{\mathbf{k}\lambda} \rangle &= n_F(\epsilon_{\mathbf{k}\lambda}^{(\zeta)}) \\ &= \left[1 + \exp(\beta \epsilon_{\mathbf{k}\lambda}^{(\zeta)}) \right]^{-1} \end{aligned} \quad (5.9)$$

where $\beta = 1/(k_B T)$. The order parameters calculated using Eq. (5.9) define a temperature-dependent mean-field Hamiltonian $H_{\text{MF}}(T)$. We fix these parameters by minimizing the free

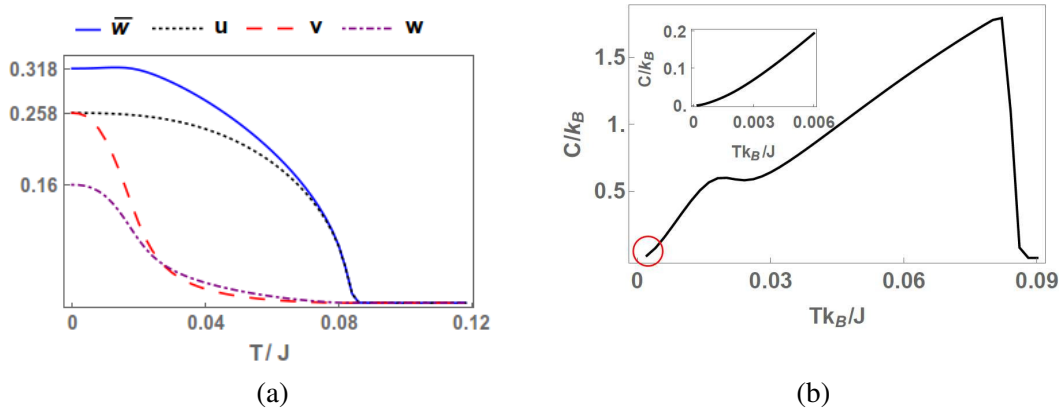


Figure 25 – (a) Absolute value of the order parameters of the chiral spin-orbital liquid as a function of temperature. (b) Magnetic specific heat per site calculated within the mean-field theory.

Source: NATORI; DAGHOFER; PEREIRA. (1)

energy,

$$F = -\frac{1}{\beta} \sum_{\mathbf{k} \in \frac{1}{2}BZ} \sum_{\lambda} \ln(1 + e^{-\beta \epsilon_{\mathbf{k}\lambda}}) + \frac{NJ}{2} \left(u^2 + u\bar{w} + \frac{vw}{3} \right), \quad (5.10)$$

and solving the self-consistent equations numerically (see textbooks on many-body theory such as (178, 179) for a derivation of this formula). The absolute values of the order parameters decrease with increasing temperature as shown in Fig. 25a.

All order parameters vanish at the same critical temperature that can be set by $k_B T_c = J/12$. The procedure is similar to the Landau theory outlined in Section 2.1 but applied for a system with more than one order parameter. Expanding (5.10) up to the fourth-order in $\beta \epsilon_{\mathbf{k}\lambda}$, the Landau free energy Φ reads

$$\begin{aligned} \Phi &\equiv \frac{\beta F}{N} \\ &= -3 \ln 2 + \frac{\mathcal{K}}{2} \left(u^2 + u\bar{w} + \frac{vw}{3} \right) \\ &\quad - 3 \left(\frac{\mathcal{K}}{36} \right)^2 (21u^2 + v^2 + w^2 + 12u\bar{w} + 3\bar{w}^2) \\ &\quad + \frac{3}{8} \left(\frac{\mathcal{K}}{36} \right)^4 [19(3u + v)^4 + 84(2u + \bar{w})^4 \\ &\quad - 24uv(11(3u + v)^2 - 39uv) + 28w^4], \end{aligned} \quad (5.11)$$

where $\mathcal{K} = \beta J$. This functional can be reorganized as follows

$$\Phi \equiv -3 \ln 2 + \Phi_2(u, v, w, \bar{w}) + \Phi_4(u, v, w, \bar{w}),$$

where Φ_2 contains the terms that are quadratic in the order parameters and Φ_4 contains the quartic terms. The quadratic term can be written in matrix form $\Phi_2 = \mathbf{t}^T M \mathbf{t}$, where $\mathbf{t}^T = (u, v, w, \bar{w})$.

Diagonalizing M , the set of eigenvalues a_n , $n = 1, \dots, 4$ are found and given by

$$\begin{aligned} a_{1,2} &= -\frac{\mathcal{K}(36 \pm \mathcal{K})}{432}, \\ a_{3,4} &= \frac{\mathcal{K}(36 - 4\mathcal{K} \pm \sqrt{2592 - 360\mathcal{K} + 13\mathcal{K}^2})}{144}, \end{aligned} \quad (5.12)$$

The eigenvalues a_2 and a_4 vanish, respectively, at the temperatures $k_B T_p = J/36$ and $k_B T_c = J/12$. The critical temperature where the numerically calculated specific heat in Fig. 25 drops to zero corresponds to the higher value $T = T_c$. The parameters u and \bar{w} vanish as $(T_c - T)^{1/2}$, as expected for primary order parameters at the mean-field level. Note that this is a well-defined second-order phase transition because a nonzero value of u implies spontaneous breaking of time reversal symmetry [see Eq. (4.18)]. On the other hand, v and w behave as secondary order parameters (180, 181) and vanish with a different critical exponent $(T_c - T)^{3/2}$ (see Fig. 25a). Fluctuations may change these critical exponents, but they were not considered in the present analysis.

The whole temperature dependence of the specific heat computed with the self-consistent approach is shown in Fig. 25b. Starting from the low-temperature limit, the $T^{3/2}$ behavior is observed. Increase of the temperature turns it into a small plateau at $k_B T \approx 0.02J$. Above this temperature, there is a regime where C_V increases approximately linear with T , followed by a sharp drop at $k_B T_c = J/12$. This is a discontinuity at the mean-field level with the same critical exponent observed in the Ising model (also within the mean-field approximation). The similarity of the C_V behavior at T_c for this two models is related with the development of a nonzero chiral order parameter (Eq.(4.18)) that breaks a discrete symmetry (time-reversal).

The lost entropy per site calculated within the parton mean-field theory is approximately $1.98k_B$, significantly higher than the expected for a $j = 3/2$ system ($k_B \ln 4 \approx 1.39k_B$). This result was anticipated since the mean-field result to overestimate the entropy since the number of microstates in this approach is higher than the actual number of physical states. This problem will be implicit in all other calculations and can be better understood by contrasting with the Kitaev model. First, there are no operators in which the mean values of the QSOL projected and unprojected wavefunction (see Eq. 2.68) are the same. At zero temperature, this problem was circumvented by using the Variational Monte Carlo (VMC) method to enforce the projection and find a better estimate of the ground state energy. (4) This method, however, is generally not used to study QSLs at finite temperatures. Second, the parton MFT implicitly assumes that the Z_2 gauge configuration in the mean-field *Ansatz* remains frozen at finite temperatures. Without this assumption, the diagonalization of the Hamiltonian would be impossible and no result would be obtained in the mean-field level. This is correct for the case of the Kitaev model, where the Z_2 gauge variables commute with the entire Hamiltonian, but it is generally incorrect for models in general.

The only calculations of thermodynamic quantities in controlled approximations of QSLs at finite temperatures were done recently for the Kitaev model, and benefit from this

model integrability. (132–134, 175) Remarkably, studies of thermodynamics of the Kitaev model (132–134, 175) found that thermal fluctuations of the Z_2 gauge field are activated at temperatures *much lower* than the bandwidth of the Majorana fermions at zero temperature. The proliferation of thermally excited visons is detected as an additional peak in the specific heat. In the case of three-dimensional QSLs (132), the lower-temperature peak in C_V is a true singularity and signals a topological phase transition predicted by Z_2 gauge theory. (182, 183)

Nevertheless, it is still possible to argue in favor of using the broad peak at higher temperature and determine the energy scale of the exchange interactions. It was found for Kitaev models that the corresponding peak in C_V is well described by the approximations of either fixing a uniform configuration or treating the Z_2 gauge field as a completely random variable. (133) I used this result and the qualitative agreement of the C_V calculated here with the experimental data obtained in Ref. (31) to give an estimative for the critical temperature $T_c \approx 70\text{K}$. This fixes the exchange coupling constant at $J \approx 72\text{ meV}$ and give the energy scale to analyze the INS and RIXS results.

5.1.2 Magnetic Susceptibility

If specific heat can be considered the most fundamental thermodynamical measurement, the magnetic susceptibility χ under uniform magnetic field is the most basic thermodynamical quantity specific to a magnetic system. It is formally defined by the derivative of the magnetization with respect to an applied field for a fixed temperature. The response of an ordered magnetic state is expected to be very different from the paramagnetic state, and therefore the transition between the disordered to the ordered state is typically accompanied by a peak or a cusp of the susceptibility at the transition point. (11) Anisotropic magnetic susceptibility give hints on the type of magnetic order displayed by the system.

It is usual to start the analysis of the susceptibility from its low and high-temperature behaviors. The low-temperature susceptibility depends upon the low-energy magnetic excitations (in analogy to the specific heat) and can also give indications of a gapped or gapless magnetic state. The magnetic susceptibility at high temperatures is given by $\chi(T) \sim A/(T - \Theta_{\text{CW}})$, where Θ_{CW} is the Curie-Weiss temperature. For strongly correlated systems, this temperature is related with the exchange constants of the Hamiltonian. If the experimental data is fitted by $\Theta_{\text{CW}} > 0$ ($\Theta_{\text{CW}} < 0$), we understand that the magnetic interactions are predominantly (antiferromagnetic) ferromagnetic. The absolute value of Θ_{CW} sets the order of magnitude expected for the phase transition. The absence of order at temperatures well-below $|\Theta_{\text{CW}}|$ is often taken as an indication of exotic magnetism. This allows us to to define the frustration parameter $f = |\Theta_{\text{CW}}|/T_o$, where T_o is the temperature of the ordering parameter. A compound with $f \gg 1$ indicates a resistance against the usual orders in a strongly correlated system and can serve as an indicator of quantum spin liquid behavior.

The magnetic susceptibility data for Ba_2YMoO_6 presented by de Vrie *et al.* (30) and Aharen *et al.* (31) are very unusual. The two papers agreed that there would be two Curie regimes (i.e., two temperature ranges in which $1/\chi$ has a linear behavior). The most immediate explanation would be the splitting of the fourfold degeneracy of the $j = 3/2$ manifold at lower temperatures, which would account for the low temperature Curie regime. Such degeneracy lifting would still retain the Kramer's degeneracy of the pseudospins and give the second Curie regime. But one consequence of lifting the pseudo-orbital degeneracy is the formation of a quadrupolar order that is accompanied by a structural transition. This explanation can be then ruled out because of the retention of the cubic symmetry in Ba_2YMoO_6 . (29)

Now, consider the susceptibility of the chiral QSOL. For simplicity, let me state the static susceptibility of a spin-1/2 system (179)

$$\chi(\mathbf{q} = 0, \omega = 0, T) = \chi(T) = - \int \frac{d^3k}{(2\pi)^3} \sum_{\omega_n} \frac{1}{(i\omega_n - \epsilon_{\mathbf{k}})^2}, \quad (5.13)$$

where ω_n is the fermionic Matsubara frequency

$$\omega_n = (2n + 1) \pi k_B T. \quad (5.14)$$

The susceptibility $\chi(T)$ can be given in terms of the density of states as follows

$$\begin{aligned} \chi(T) &= - \int d\epsilon \delta(\epsilon - \epsilon_{\mathbf{k}}) \int \frac{d^3k}{(2\pi)^3} \sum_{\omega_n} \frac{1}{(i\omega_n - \epsilon)^2} \\ &\propto - \int d\epsilon \sum_{\omega_n} \frac{\rho(\epsilon)}{(i\omega_n - \epsilon)^2} \\ &= \int d\epsilon \rho(\epsilon) \left(- \frac{\partial n_F(\epsilon, T)}{\partial T} \right) = \frac{1}{k_B T^2} \int d\epsilon \rho(\epsilon) \frac{\epsilon \exp\left(\frac{\epsilon}{k_B T}\right)}{\left[1 + \exp\left(\frac{\epsilon}{k_B T}\right)\right]^2} \end{aligned} \quad (5.15)$$

For low-temperatures, this implies that if $\rho(\epsilon) \propto \epsilon^\alpha$, then $\chi(T) \propto T^\alpha$. A similar expression can be obtained for the QSOL susceptibility leading to the same power law expression. Using Eq. (5.2), this implies $\chi(T) \propto T^{1/2}$. The QSOL low-temperature behavior, if not confirmed by the experimental data, is at least consistent with it. (30, 31)

However, the situation is different with regard to the evaluation of the Curie-Weiss temperature Θ_{CW} . Attempts to apply the self-consistent method led always to $\Theta_{\text{CW}} = 0$. Analytically, Θ_{CW} is evaluated by including a Zeeman term on a Landau free energy (in our case, Eq. (5.11)), finding the minimum of the order parameter for vanishing h , expressing this order parameter explicitly, and then evaluating the magnetic susceptibility. The order parameters of the QSOL theory, however, do not couple directly with the magnetic field like the order parameters of more usual ordered phases. Parton mean-field theory seems to be inadequate to estimate Θ_{CW} . Even in the Kitaev model, where $\chi(T)$ can be exactly calculated, Θ_{CW} is evaluated with

standard high-temperature expansions of the magnetic susceptibility. (175) That being the case, the Curie-Weiss temperature evaluated in Ref. (29) was given by $\Theta_{\text{CW}} = -\frac{J}{5}$ on the SU(2) symmetric model. If this value is accepted, this is equivalent to $\Theta_{\text{CW}} \approx -168\text{K}$, which is in the same range of Curie-Weiss temperatures found in Ref. (30) (-160K) and Ref. (31) (-219K). Thus, this result is also consistent with the experimental data.

5.1.3 Nuclear Magnetic Resonance

Nuclear magnetic resonance (NMR) is a very versatile technique based upon the hyperfine interaction between the atom nuclei and the electrons in their surroundings. The first part of an NMR experiment is to set the nuclear spins into an ordered state by applying a magnetic field pulse with intensity close to the resonance frequency ω_n of the nuclear ion under consideration. Once the magnetic pulse is over, the hyperfine interaction allows the transference of energy of the excited nuclear spins to their surrounding electrons. In general, ω_n is several orders of magnitude lower than the energy scales of the electronic degrees of freedom. The electronic modes excited by the hyperfine interaction will be then low-energy gapless excitations. Following these principles, NMR experiments on solids allow us to study excitations near Fermi surfaces from the data of nuclear spin relaxation.

There are two interesting quantities that are obtained through NMR in the context of magnetic materials: the Knight shift and the longitudinal relaxation frequency $1/T_1$. The Knight shift gives a measure of the local electronic susceptibility and can give information about inhomogeneous arrangements of the magnetic moments throughout the lattice. This quantity was not calculated for the quantum spin orbital liquid with nodal lines. Here I only state that Ref. (31) has shown that the Knight shift of Ba_2YMoO_6 was vanishingly small in contrast to what is expected for an ordered phase, giving another argument in favor of a state dominated by quantum fluctuations.

Now, let me discuss how the relaxation frequency $1/T_1$ can be computed and the information that can be obtained from it. In spin systems, the energy transfer between electrons and nuclei is mediated by the hyperfine coupling

$$H_{\text{hf}} = -\mathbf{I}_i \cdot \mathbf{B}_{\text{hf}}(i), \quad (5.16)$$

where \mathbf{I}_i is the nuclear spin at site i and $\mathbf{B}_{\text{hf}}(i)$ is the hyperfine effective field due to neighboring electrons. The excited nuclear spin in Ref. (31) was the $I = 1/2$ ^{89}Y , which couples to the $j = 3/2$ magnetic moment of Mo electronic spins. The effective field \mathbf{B}_{hf} is then written like

$$\mathbf{B}_{\text{hf}}(i) = A_0 \sum_{\delta} \mathbf{j}_{i+\delta}, \quad (5.17)$$

where δ is the relative position of the atoms of ^{89}Y and their neighboring Mo atoms, and A_0 is the constant hyperfine coupling for first-neighbor δ . Following Fermi's golden rule, the spin-lattice

relaxation rate $1/T_1$ is proportional to the density of states excited by the hyperfine interaction and the square of matrix element of H_{hf} between the ground state and the excited state. The explicit final result is

$$\frac{1}{T_1} \propto \frac{1}{1 - e^{-\beta\omega}} \sum_{\mathbf{q} \in \text{BZ}} |A(\mathbf{q})|^2 \chi''_{+-}(\mathbf{q}, \omega), \quad (5.18)$$

where ω is the resonance frequency,

$$A(\mathbf{q}) = A_0 \left[\cos\left(\frac{q_x}{2}\right) + \cos\left(\frac{q_y}{2}\right) + \cos\left(\frac{q_z}{2}\right) \right] \quad (5.19)$$

is the hyperfine interaction form factor, and $\chi''_{+-}(\mathbf{q}, \omega)$ is the spectral function given by

$$\chi''_{+-}(\mathbf{q}, \omega) = \frac{1 - e^{-\beta\omega}}{Z} \sum_{n, n'} e^{-\beta E_n} |\langle n' | j_{\mathbf{q}}^- | n \rangle|^2 \delta(\omega - E_{n'} + E_n), \quad (5.20)$$

with $|n\rangle$ being an exact eigenstate of the spin Hamiltonian with energy E_n , and $Z = \sum_n e^{-\beta E_n}$ being the partition function. Here, $j_j^- = j_j^x - i j_j^y$ is the angular momentum lowering operator at site j and $j_{\mathbf{q}}^-$ is its Fourier transform.

In order to calculate $1/T_1$, the first step was to write j_j^- in terms of \mathbf{s} and $\boldsymbol{\tau}$ according to Table 1 and relate the spectral function $\chi''_{+-}(\mathbf{q}, \omega)$ to finite-temperature correlations of free Majorana fermions. In this approach, the order parameters calculated self-consistently at finite temperature (see Subsection 5.1.1) were used to update the Hamiltonian at each temperature. Some insight can be gained if we first analyze the contribution of the η fermions to the total spectral function, since this case allows the derivation of some closed-form expressions. Using the procedure outlined in Appendix F, the η fermion contribution is given by

$$\left(\frac{1}{T_1}\right)_{\eta} \propto \int_{\text{BZ}} d^3k d^3k' \frac{|A(\mathbf{k} - \mathbf{k}')|^2 \mathcal{F}^{\eta}(\mathbf{k}, \mathbf{k}')}{\cosh^2\left(\beta \epsilon_{\mathbf{k}\mathbf{1}}^{(\eta)}/2\right)} \delta(\epsilon_{\mathbf{k}'\mathbf{1}}^{(\eta)} - \epsilon_{\mathbf{k}\mathbf{1}}^{(\eta)}), \quad (5.21)$$

where

$$\mathcal{F}^{\eta}(\mathbf{k}, \mathbf{k}') = 1 + \frac{\mathbf{h}(\mathbf{k}) \cdot \mathbf{h}(\mathbf{k}')}{|\mathbf{h}(\mathbf{k})| |\mathbf{h}(\mathbf{k}')|}. \quad (5.22)$$

At low temperatures $k_B T \ll J$, the spin-lattice relaxation rate is dominated by excitations with small momentum transfer near the quadratic band touching point. Let us denote $\mathbf{k} = (\pi, \pi, \pi) + \mathbf{q}$ and $\mathbf{k}' = (\pi, \pi, \pi) + \mathbf{q}'$, with $|\mathbf{q}|, |\mathbf{q}'| \ll 1$. In this case, the energies can be approximated by Eq. (5.1) and the vector $\mathbf{h}(\mathbf{k})$ by

$$\mathbf{h}(\mathbf{k}) \approx (q_x q_y, q_y q_z, q_x q_z) \equiv q^2 \tilde{\mathbf{h}}(\Omega), \quad (5.23)$$

where Ω is the solid angle in spherical coordinates. It is also possible to use the approximation $A(\mathbf{k} - \mathbf{k}') \approx 3$ and

$$\mathcal{F}^{\eta}(\mathbf{k}, \mathbf{k}') \approx \mathcal{F}(\Omega, \Omega') = 1 + \frac{\tilde{\mathbf{h}}(\Omega) \cdot \tilde{\mathbf{h}}(\Omega')}{|\tilde{\mathbf{h}}(\Omega)| |\tilde{\mathbf{h}}(\Omega')|}. \quad (5.24)$$

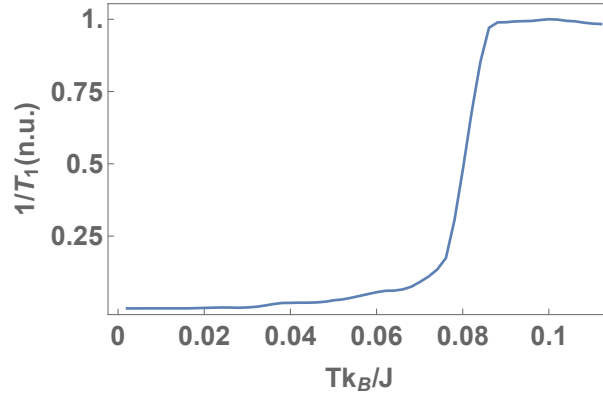


Figure 26 – Spin lattice relaxation rate of the chiral spin liquid state as a function of the temperature.

Source: NATORI; DAGHOFER; PEREIRA. (1)

Gathering all the approximations, the low-temperature spin-lattice relaxation rate is

$$\begin{aligned}
\left(\frac{1}{T_1}\right)_\eta &\propto \int d\Omega d\Omega' \mathcal{F}(\Omega, \Omega') \int dq q^2 \int dq' (q')^2 \frac{\delta(q^2 f(\Omega) - (q')^2 f(\Omega'))}{\cosh^2(\beta q^2 f(\Omega)/2)} \\
&\propto \int d\Omega d\Omega' \frac{\mathcal{F}(\Omega, \Omega') |f(\Omega)|^{1/2}}{|f(\Omega')|^{3/2}} \int dq \frac{q^3}{\cosh^2(\beta q^2 f(\Omega)/2)} \\
&\propto T^2 \int d\Omega d\Omega' \frac{\mathcal{F}(\Omega, \Omega') |f(\Omega)|^{1/2}}{|f(\Omega')|^{3/2}} \int dx \frac{x^3}{\cosh^2[x^2 f(\Omega)/2]}. \tag{5.25}
\end{aligned}$$

That is how we verify that $(1/T_1)_\eta$ scales as T^2 for $T \rightarrow 0$. A similar calculation assuming momenta near the Fermi lines leads to $(1/T_1)_\eta \propto T^3$. While this result refers to the contribution from η fermions, it also reflects the qualitative behavior of the total $1/T_1$ since the dispersion relation of the θ fermions near the Fermi lines is qualitatively the same.

The total spectral function $\chi''_{+-}(\mathbf{q}, \omega)$ was computed numerically, including the contribution from θ fermions and at arbitrary temperatures, as explained in Appendix F. The result for the spin-lattice relaxation rate is shown in Fig. 26. At low temperatures, the behavior is dominated by the R point and is described by the power law $1/T_1 \propto T^2$ discussed above. An abrupt increase of $1/T_1$ is verified near the critical temperature T_c , followed by a constant behavior at higher temperatures. This result is qualitatively consistent with the measured relaxation rate in Ref. (31). While the suppression of $1/T_1$ at low temperatures was interpreted as evidence for a gapped QSL, the experimental result is also qualitatively consistent with a pseudogap in the low-energy density of states. Considering the absence of an Arrhenius law behavior in C_V , the pseudogap interpretation better adjusts to the experimental data. Thus, the chiral spin-orbital liquid is a valid alternative to explain the spin-lattice relaxation rate of Ba_2YMoO_6 .

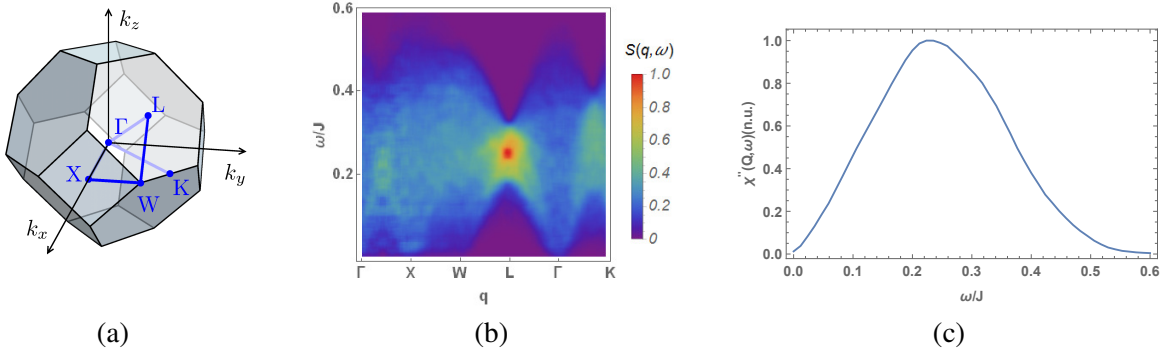


Figure 27 – (a) First Brillouin zone of the fcc lattice. (b) Dynamical structure factor (in arbitrary units) probed by inelastic neutron scattering. (c) Result after integration over $1.5\text{\AA}^{-1} < Q < 1.8\text{\AA}^{-1}$.

Source: NATORI; DAGHOFER; PEREIRA (1)

5.1.4 Inelastic Neutron Scattering

Neutron scattering is the standard probe to study magnetic ordering and excitations in condensed matter. This status can be understood by a comparison with the three measurements studied above. The three gave valuable indications of the nature of the excitations close to the Fermi surface and some information about the phase transitions and exchange constants could be extracted from the high temperature behavior. However, one could not find the full excitation structure of a magnet with these techniques. INS cross sections provides detailed information about the spin dynamics for a broad range of transferred energy and momentum, and with a good resolution of these two variables.

The neutron spin couples with the total angular momentum of the electron to a good approximation. (55) For the $4/5d^1$ Mott insulators, this implies that it measures correlations between the total magnetic moments $\mathbf{M} \propto \mathbf{j}$ (see the discussion at the beginning of this chapter). At zero temperature, the magnetic scattering cross section for polarized neutrons is proportional to one component of the dynamical structure factor

$$S^{ab}(\mathbf{q}, \omega) = \sum_{j,n} e^{-i\mathbf{q}\cdot\mathbf{R}_j} \langle g | j_j^a | n \rangle \langle n | j_j^b | g \rangle \delta(\omega - E_n + E_g), \quad (5.26)$$

where $|g\rangle$ is the ground state, \mathbf{q} and $\omega > 0$ are the momentum and energy transferred by the neutron, and $|n\rangle$ is an excited state of the many-body Hamiltonian.

I calculated the dynamical structure factor for the chiral spin-orbital liquid measured by the INS within the parton MFT formalism. It follows from $P\Theta$ and point group symmetries that $S^{ab}(\mathbf{q}, \omega) \propto \delta^{ab}$ and $S^{aa}(\mathbf{q}, \omega) = S^{aa}(-\mathbf{q}, \omega)$. Writing the operator \mathbf{j} in terms of \mathbf{s} and $\boldsymbol{\tau}$ and then Majorana fermions, generates

$$S^{aa}(\mathbf{q}, \omega) = \frac{4}{N} \sum_{n,\mathbf{k}} F_n^a(\mathbf{k}, \mathbf{q}) \delta(\omega - E_n + E_g). \quad (5.27)$$

For example, the form factor for $S^{zz}(\mathbf{q}, \omega)$ is

$$F_n^z(\mathbf{k}, \mathbf{q}) = \left| \sum_X \langle g | \eta_{\mathbf{q}-\mathbf{k}+\mathbf{G},X}^2 \eta_{\mathbf{k},X}^3 | n \rangle e^{i\mathbf{G}\cdot\delta_X} \right|^2 + 4 \left| \sum_X \langle g | \eta_{\mathbf{q}-\mathbf{k}+\mathbf{G},X}^3 \bar{\theta}_{\mathbf{k},X}^{xy} | n \rangle e^{i\mathbf{G}\cdot\delta_X} \right|^2, \quad (5.28)$$

where \mathbf{G} is a vector of the cubic reciprocal lattice chosen such that $\mathbf{q} - \mathbf{k} + \mathbf{G}$ is contained in the first Brillouin zone. The components $S^{xx}(\mathbf{q}, \omega)$ and $S^{yy}(\mathbf{q}, \omega)$ can be obtained from Eq. (5.28) by cyclic permutation of all indices $a = 1, 2, 3 = x, y, z$. Within the mean-field theory, the excited states are restricted to two-particle excitations. The form factors can be calculated using the matrix elements of $U_{\mathbf{k}}$ and $V_{\mathbf{k}}$ defined in Eqs. (4.25) and (4.34).

Figure 27b shows the dynamical structure factor $S^{xx}(\mathbf{q}, \omega)$ along the high-symmetry lines of the Brillouin zone of the fcc lattice (see Fig. 27a). The spectral weight is distributed over a continuum of fractionalized excitations, which is a general behavior of QSL dynamical structure factor (see for example (78, 177) and the discussion of 2.3). The maximum intensity is found at the L point, corresponding to momentum transfer $\mathbf{q} = (\pi, \pi, \pi)$. The energy scale at the maximum is of the order of the bandwidth of the Majorana fermions η^a and $\theta^{1,3}$ shown in Fig. 15b. Using $J \approx 72$ meV estimated from the specific heat, the peak in the dynamical structure factor appears at transferred energy $\omega \approx 0.25J \approx 18$ meV.

The theoretical results can be compared with the neutron scattering experiments reported by Carlo *et al.* (32) done in polycrystalline samples. To be consistent with the experiments performed in this reference, an average of dynamical structure factor over momenta with absolute value Q in the range $1.5\text{\AA}^{-1} < Q < 1.8\text{\AA}^{-1}$. I took the lattice spacing to be $a = 8.389\text{\AA}$ (30) and considered a sum over transferred momenta within these values of Q . In particular, this included the point $L' = a^{-1}(3\pi, 3\pi, -\pi)$ equivalent to L by a reciprocal lattice translation.

The integration leads to a single broad maximum at $\omega \approx 18$ meV displayed in Fig. 27c. This result is inconsistent with the neutron scattering cross section, which shows a three-peak structure with a pronounced magnetic peak at $\omega \approx 28$ meV and two smaller ones at 11 and 17 meV. The chiral QSOL does contain multiple energy scales associated with the nondegenerate Majorana fermion bands shown in Fig. 15b, but the bandwidths of the flavors $\eta^a, \theta^{1,3}$ are rather close to each other and lead to this single peak.

The inclusion of Z_2 gauge fluctuations to the chiral QSOL may account for the formation of new peaks. One indication of this is the broadening and shift of the spectral weight of $S(\mathbf{q}, \omega)$ caused by them in a bosonic spin liquid. (177) It must be said, however, that the gauge fluctuations in (177) were included as perturbations controlled by phenomenological parameters (i.e., without any relation to a microscopic parameter). In this case, it is difficult to estimate a value in which they are actually capturing the physics of dynamical Z_2 gauge fluxes in a QSL. Some comparison with the the dynamics of the Kitaev model is useful at this point. The exact computation of $S(\mathbf{q}, \omega)$ in this models is simplified by the fact that the Z_2 gauge flux is static. (125–129) The inclusion of dynamical gauge fluxes parting from this integrable starting

point was first considered in Ref. (137) and more formally developed only in a recent paper. (176) In summary, the effects of dynamical Z_2 gauge fluxes on the dynamical structure factor of QSLs is still an open question and their inclusion will be left for a future work.

5.2 Resonant Inelastic X-Ray Scattering

Resonant Inelastic X-Ray Scattering (RIXS) is a fast developing photon-in photon-out spectroscopic technique that has the potential to complement INS studies on frustrated magnets. (48) The energy of the incident x-ray is tuned to resonate with the energy of an atomic transition between a core and a valence level of the species under study, and this resonance enhances the photon scattering cross section. Similar to the INS, RIXS measures the dependence of the photon differential cross sections on the transferred momentum and energy that is then related to orders and excitations of certain degrees of freedom of the electrons.

Ament et al. (48) list five generic features of RIXS that make it an attractive technique to study condensed matter systems.

1. First, RIXS displays the largest scattering phase space available to study elementary excitations of all existing spectroscopic techniques.
2. Second, since it is based upon the resonance energy between specific atomic levels, this technique distinguishes between different chemical elements and atomic orbitals.
3. Third, RIXS has a penetration depth of the order $\sim 0.1 - 1\mu\text{m}$, which is enough to measure bulk properties.
4. Fourth, the sample volume to perform an experiment is smaller than the ones used in neutron scattering experiments facilitating single crystal experiments. This is justified by the stronger interactions between photons and electrons in comparison to neutrons and the higher brightness of x-ray sources in comparison to neutron sources. This can be very useful to study compounds that are difficult to synthesize, such as the $4/5d$ Mott insulators, where often only polycrystalline or powder measurements can be done (like what happened in Ref. (32))
5. The fifth RIXS general feature is the polarization dependence of its differential cross section. In theoretical terms, this means that RIXS scattering operators are strongly dependent upon the relation between initial and final polarization.

Besides these general features, RIXS can be a very useful experimental technique for materials with great neutron absorbance. This includes, for example, iridium based materials and provides the earliest link between research in Kitaev materials and RIXS theory and instrumentation.

Considering all these positive features, one could ask: why does INS remain the standard probe for strongly correlated system instead of RIXS? I provide two answers here. First, RIXS requires very bright x-ray sources in order to obtain enough scattered photons and give an spectrum with good energy and momentum resolution. Second, the technology allowing the design of experiments with fixed photon final polarization is still unavailable. This means that actual RIXS experiments measure the combination of correlation functions from different microscopic operators. A detailed theoretical analysis must then be done in parallel with the experiment in order to acquire useful data. Despite the great challenges to overcome these two problems, the fast development of RIXS instrumentation allows optimism concerning the availability of this technique to study strongly correlated systems.

This section is devoted only to the study of RIXS scattering operators and the RIXS cross section of the chiral QSOL. Subsection 5.2.1 presents the fast-collision approximation used to estimate the RIXS scattering operators. A symmetry analysis of these operators using the method described in Refs. (47, 51, 184) is also sketched. Subsection 5.2.2 presents RIXS scattering operators for $4/5d^1$ Mott insulators in the limit of strong SOC. All the calculations were done at the so-called L edge, in which the energy of the incident photon is tuned to resonate with a core p -level. A comparison with the INS results will be given by the end of this section.

5.2.1 Derivation and symmetry analysis of RIXS scattering operators

Most of this section is devoted to fix a notation and give certain orders of magnitude for the RIXS processes. Let us start with the most general many-body Hamiltonian (see Eq. (2.1)) which will be called H_0 in this section. If RIXS is used to study this system, the total Hamiltonian is given by $H = H_0 + H'$, where H' is the Hamiltonian describing the interaction between electrons and photons. (48) For brevity, I already take the starting point to be

$$H' = \sum_{i=1}^N \left[\frac{e}{m} \mathbf{A}(\mathbf{r}_i) \cdot \mathbf{p}_i + \frac{e\hbar}{2m} \boldsymbol{\sigma}_i \cdot \nabla \times \mathbf{A}(\mathbf{r}_i) \right]. \quad (5.29)$$

Here, e is the electronic charge, m is the electron mass, \mathbf{r}_i , and \mathbf{p}_i and $\boldsymbol{\sigma}_i$ are, respectively, the position, momentum and spin of the i -th electron. The interaction with the photon is mediated by the electromagnetic vector potential $\mathbf{A}(\mathbf{r})$, and only linear terms in this field were preserved. $\mathbf{A}(\mathbf{r})$ in second quantization reads

$$\mathbf{A}(\mathbf{r}) = \sum_{\mathbf{k}, \varepsilon} \frac{1}{\sqrt{2\mathcal{V}\epsilon_0\omega_{\mathbf{k}}}} \left(\varepsilon a_{\mathbf{k}, \varepsilon} e^{i\mathbf{k}\cdot\mathbf{r}} + \varepsilon^* a_{\mathbf{k}, \varepsilon}^\dagger e^{-i\mathbf{k}\cdot\mathbf{r}} \right), \quad (5.30)$$

where \mathcal{V} is the volume, ϵ_0 is the vacuum permittivity, and $a_{\mathbf{k}, \varepsilon}^\dagger$ is the creation operator for a photon with wave vector \mathbf{k} , frequency $\omega_{\mathbf{k}}$, and polarization vector ε .

The RIXS cross sections are calculated taking the interaction of a single photon with the whole system as the perturbation. Let the initial electron-photon state be $|G\rangle$ and let us label a

set of possible final states by $\{|F\rangle\}$. The energy of the x-ray photon for the RIXS study I am proposing ranges between $\sim 1 - 10\text{keV}$ and is sufficient to excite an electron from a core level to the valence band. As a result, between the initial and final state there will be a highly unstable intermediate state $|\nu\rangle$. The x-ray cross section of this process calculated up to second-order is (48)

$$I \propto \sum_F \left| \langle F | H' | G \rangle + \sum_\nu \frac{\langle F | H' | \nu \rangle \langle \nu | H' | G \rangle}{E_G - E_\nu + i\gamma_\nu} \right|^2 \times \delta(E_F - E_G), \quad (5.31)$$

in which E_ν and $1/\gamma_\nu$ are the energy and the lifetime of the intermediate state. The initial state is taken to correspond to a direct product of a many-body electronic ground state $|g\rangle$ and an incident photon state: $|G\rangle = |g\rangle \otimes |\mathbf{k}, \omega_{\mathbf{k}}, \boldsymbol{\varepsilon}\rangle$. Similarly, the final state is a direct product of an excited electronic state $|n\rangle$ with energy E_n and an emitted photon labeled by $|F\rangle = |n\rangle \otimes |\mathbf{k}', \omega_{\mathbf{k}'}, \boldsymbol{\varepsilon}'\rangle$.

The key point of the RIXS technique is that $\omega_{\mathbf{k}}$ is tuned to the energy difference between an atomic core level and a valence shell state. In terms of the notation above, the incident photon energy $\hbar\omega_{\mathbf{k}}$ is chosen so that $|E_G - E_\nu| \ll \gamma_\nu$. In this situation, the system is said to be in resonance and the second-order processes in Eq. (5.31) dominate the scattering cross section.

The RIXS cross section operators computed in this paper considered the only "direct" RIXS process using the fast collision approximation. Let me present these approximations and justify the validity of the approach a posteriori. First, the so-called "magnetic" contribution ($\propto \boldsymbol{\sigma} \cdot \nabla \times \mathbf{A}$) of H' is neglected. Second, the dipole approximation is assumed for the scattering amplitude and take $e^{i\mathbf{k}\cdot\mathbf{r}_i} \approx e^{i\mathbf{k}\cdot\mathbf{R}_i}$, where \mathbf{R}_i represents the lattice point to which the i -th electron is bound. Third, the core hole state is said to decay before it can hop to a different ion, i.e., it is localized. This approximation is known as the fast collision approximation. (48) Finally, the effects of the core-hole Coulomb potential is neglected (direct RIXS process). Within these approximations, RIXS probes only single-site operators.

The number of approximations leads to a justifiable skepticism towards this approach to compute RIXS cross sections. In fact, sophisticated numerical studies of the RIXS cross section for cuprates indicated that simpler approximations fail, specially for systems under doping. (185) The reason for this failure is that the time scales of $3d$ electrons (of order $\sim 1/\Gamma_\nu$) approach those of the intermediate $|\nu\rangle$ states. However, for $4d$ and $5d$ electrons, the γ_ν is of the order of $1 - 5\text{eV}$ for the L -edge. (186) This is much greater than the $\sim 10\text{meV}$ energy scale for the spin-orbital excitations considered in this thesis. Hence, the fast collision approximation is a good starting point to study the physics of the $4/5d$ Mott insulators.

Since only single-site operators are considered, the RIXS processes preserve the translation symmetry. Hence, the cross section will depend only on $\mathbf{q} = \mathbf{k} - \mathbf{k}'$ and $\omega = \omega_{\mathbf{k}} - \omega_{\mathbf{k}'}$, which are, respectively, the momentum and energy transferred to the sample. Equation (5.31) can then

be recast in the form

$$I(\mathbf{q}, \omega) \propto \sum_n |\langle n | \hat{O}_{\mathbf{q}} | g \rangle|^2 \delta(E_g - E_n + \hbar\omega), \quad (5.32)$$

where $\hat{O}_{\mathbf{q}}$ is the so-called scattering operator in momentum space. The latter is obtained from the Fourier transform $\hat{O}_{\mathbf{q}} = \sum_i e^{i\mathbf{q} \cdot \mathbf{R}_i} \hat{O}_i$, where

$$\hat{O}_i = \sum_{\nu} \frac{1}{i\gamma_{\nu}} \mathcal{D}_i^{\dagger}(\boldsymbol{\varepsilon}') | \nu \rangle \langle \nu | \mathcal{D}_i(\boldsymbol{\varepsilon}). \quad (5.33)$$

Here, the dipole operator

$$\mathcal{D}_i(\boldsymbol{\varepsilon}) = \boldsymbol{\varepsilon} \cdot \mathbf{r}_i \quad (5.34)$$

acts on the electronic states bound to position \mathbf{R}_i .

Equations (5.33) and (5.34) show that the RIXS cross section (5.32) depends on the initial and final polarizations $\boldsymbol{\varepsilon}$ and $\boldsymbol{\varepsilon}'$ and on the matrix elements of the electron position operator $\langle \nu | \mathbf{r} | g \rangle$ and $\langle n | \mathbf{r} | \nu \rangle$. The polarization of the incident photon can be controlled in experiments. The final polarization is far more difficult to control. Naively, one could filter the scattered photons and detect only photons at the desired final polarization. This method, however, would eliminate most of the incident photons and increase the necessary time to perform a RIXS measurement.

If the polarization concerns the photons, the matrix elements depend on details of the intermediate states for a particular compound and the probed operators will vary according to the probed system. Nevertheless, provided the final states are low-energy excitations, the scattering operators are rewritten in terms of charge, spin and orbital degrees of freedom of the valence electrons. For magnetic insulators, RIXS operators correspond to a combination of spin and orbital angular momentum. This feature makes RIXS an attractive technique to investigate magnetic insulators with strong SOC, in which spins and orbitals cannot be treated as separate degrees of freedom.

Since \hat{O}_i is in general a complicated operator, it is desirable to start our RIXS analysis by determining: (i) which polarization vectors $\boldsymbol{\varepsilon}$ and $\boldsymbol{\varepsilon}'$ we should choose to acquire the signatures of a given state; and (ii) which spin operators couple with these polarizations. The two issues can be tackled at once by an elementary symmetry analysis of Eq. (5.33). As the absorption and emission processes occur at the same ion, the operator \hat{O}_i should be invariant under operations of the point group symmetry of the site \mathbf{R}_i . The starting point is the decomposition of the scattering operator into irreducible representations of the point group, $\Gamma = \Gamma_1 \oplus \dots \oplus \Gamma_n$. A basis for these representations is then constructed in terms of the polarization factors $\boldsymbol{\varepsilon}^{\Gamma_j}$ and (pseudo)spins \mathcal{J}^{Γ_j} , in the form (47, 51, 184)

$$\hat{O}_i = \sum_{\Gamma_j=1}^n \sum_{l_j=1}^{\text{mul}(\Gamma_j)} \kappa_{\Gamma_j, l_j} \boldsymbol{\varepsilon}^{\Gamma_j, l_j} \cdot \mathcal{J}^{\Gamma_j, l_j}, \quad (5.35)$$

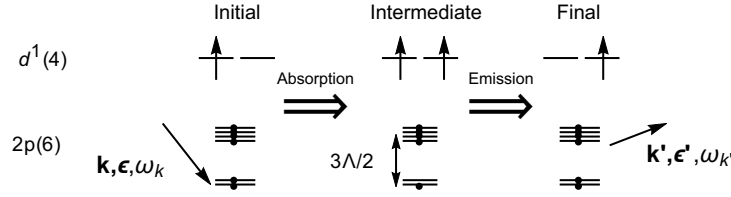


Figure 28 – Schematic diagram of a RIXS experiment at the L_2 edge, featuring specifically the possibility of pseudo-orbital flip. The absorbed photon creates a core $2p$ hole, which is subject to strong spin-orbit coupling. This highly unstable state decays before a d electron can tunnel to or from the ion, generating a spin-orbital excitation and an emitted photon.

Source: NATORI; DAGHOFER; PEREIRA. (1)

where $\text{mul}(\Gamma_j)$ is the multiplicity of the irreducible representation Γ_j , the dot represents a symmetric contraction of all indices, and κ_{Γ_j, l_j} are material specific coefficients.

The bases of the irreducible representations of the octahedral group in terms of multipoles of $j = 3/2$ moments are known (147, 148) and are reproduced in Table 1, together with their representation in terms of \mathbf{s} and $\boldsymbol{\tau}$ pseudospins. Considering that the polarization vectors transform like \mathbf{j} operators under rotations, $\varepsilon^{\Gamma_j, l_j}$ are given by:

$$P_a = \frac{i}{2} \sum_{bc} \epsilon_{abc} \varepsilon_b'^* \varepsilon_c, \quad (5.36a)$$

$$T_a = \frac{1}{2} \sum_{b \neq c} (1 - \delta_{ab})(1 - \delta_{ac}) \varepsilon_b'^* \varepsilon_c, \quad (5.36b)$$

$$Q_2 = \varepsilon_x'^* \varepsilon_x - \varepsilon_y'^* \varepsilon_y, \quad (5.36c)$$

$$Q_3 = \frac{1}{\sqrt{3}} (\varepsilon_x'^* \varepsilon_x + \varepsilon_y'^* \varepsilon_y - 2\varepsilon_z'^* \varepsilon_z), \quad (5.36d)$$

$$U = \boldsymbol{\varepsilon}'^* \cdot \boldsymbol{\varepsilon}, \quad (5.36e)$$

Here, the vector \mathbf{P} corresponds to the Γ_4 representation, \mathbf{T} to Γ_5 , Q_2 and Q_3 to Γ_3 , and U to the scalar representation. Combining Table 1 and Eqs. (5.36) in Eq. (5.35), we obtain the general form of all transition operators [except for the scalar representation, which couples with the Casimir operator $\mathbf{j}^2 = j(j+1) = \text{const.}$]. Noticing that \mathbf{s} is given by a linear combination of Γ_4 dipoles and octupoles, and (τ_x, τ_z) form a basis of the Γ_3 irreducible representation, RIXS can in principle probe pseudospin and pseudo-orbital excitations directly.

5.2.2 L-edge RIXS cross section of the chiral spin-orbital liquid

I now calculate the L -edge RIXS operators for $4d^1$ and $5d^1$ orbital systems retaining cubic symmetry explicitly, as well as the RIXS scattering cross sections for the chiral QSOL at the mean-field level. The L -edge mechanism is illustrated in Fig. 28. There the $2p$ core electrons are excited to the B and C states of Eq. (2.45). This edge was chosen because the strong SOC of

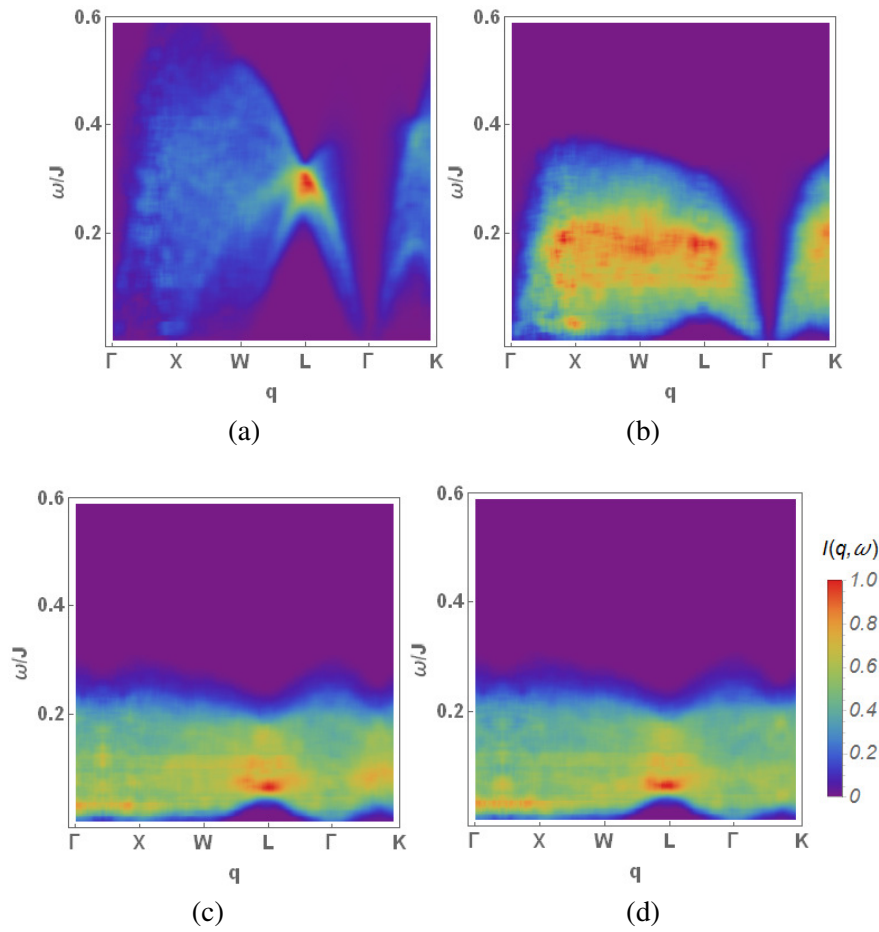


Figure 29 – RIXS cross section (in arbitrary units) probing (a) \mathbf{s} , (b) $s\tau_y$, (c) τ_x and (d) τ_z operators along the high symmetry directions of the Brillouin zone of the fcc lattice. Source: NATORI; DAGHOFER; PEREIRA. (1)

the intermediate state allows transitions between initial and final states that do not conserve the spin S^z , which allows more complicated operators to be probed. The core-hole Hamiltonian is

$$H_{\text{core}} = \Lambda \mathbf{L} \cdot \mathbf{S}, \quad (5.37)$$

where $\Lambda > 0$ is the SOC constant for the $2p$ states and \mathbf{L} is the $L = 1$ angular momentum of p electrons. Like in the d^1 valence electron, there is a lifting of the six-fold degeneracy into a doublet and a quadruplet. However, now the doublet has lower energy (see Fig. 28). We refer to the excited hole in the $j = 1/2$ ($j = 3/2$) multiplet as the resonant L_2 (L_3) edge. Since the separation between these two edges is of the order ~ 100 eV (~ 1 keV) for $4d$ ($5d$) ions (52), which is much larger than the inverse lifetime of the intermediate states (1-5 eV), the two edges can be taken as separate processes.

Most of the dipole matrix elements of Eq. (5.34) vanish by symmetry. The remaining

terms are written in second quantization as (52)

$$\begin{aligned} \mathcal{D}_i(\varepsilon) \propto & d_{xy,\sigma}^\dagger(\varepsilon_x p_{y,\sigma} + \varepsilon_y p_{x,\sigma}) + d_{yz,\sigma}^\dagger(\varepsilon_y p_{z,\sigma} + \varepsilon_z p_{y,\sigma}) \\ & + d_{zx,\sigma}^\dagger(\varepsilon_z p_{x,\sigma} + \varepsilon_x p_{z,\sigma}). \end{aligned} \quad (5.38)$$

Eq. (5.33) is further simplified by writing $\gamma_\nu \approx \gamma_\mu = \text{const.}$, with $\mu = 2, 3$, for all intermediate states in the L_μ edge. Here, γ_μ is the average decay rate of the intermediate core-hole states. This approximation, together with the others discussed in Section 5.2.1, leads to

$$\hat{\mathcal{O}}_i^{L_\mu} = \frac{1}{i\gamma_\mu} \mathcal{D}_i^\dagger(\varepsilon') \mathcal{P}_\mu \mathcal{D}_i(\varepsilon), \quad (5.39)$$

where \mathcal{P}_μ is the projection operator of the intermediate states in the L_μ edge.

Expressions for the scattering operator were derived in terms of pseudospins \mathbf{s} and $\boldsymbol{\tau}$ by taking the projection in the $j = 3/2$ subspace and using the single-occupancy constraint $\sum_\sigma (B_\sigma^\dagger B_\sigma + C_\sigma^\dagger C_\sigma) = 1$. (3) Let us study these operators in the cubic limit relevant for Ba_2YMoO_6 . For the L_2 -edge, I find

$$\begin{aligned} \hat{\mathcal{O}}_i^{L_2} \propto & \frac{1}{\sqrt{3}} \left[Q_2 \tau_i^x + Q_3 \tau_i^z - 4\mathbf{T} \cdot (\mathbf{s} \tau_i^y) - \frac{2}{\sqrt{3}} \mathbf{P} \cdot \mathbf{K}_i \right] \\ & + \text{const.}, \end{aligned} \quad (5.40)$$

where

$$\mathbf{K}_i = (s_i^x(1 - 4\tau_i^{yz}), s_i^y(1 - 4\tau_i^{xz}), s_i^z(1 - 4\tau_i^{xy})). \quad (5.41)$$

On the other hand, the scattering operator for the L_3 edge involves only the pseudospin \mathbf{s} :

$$\hat{\mathcal{O}}_i^{L_3} \propto \frac{4}{3} \mathbf{P} \cdot \mathbf{s}_i + \text{const.} \quad (5.42)$$

An independent and more general work discussing the scattering operators of $4/5d^n$ based Mott insulators with t_{2g} was published in Ref. (52). There, the operators are given in terms of the 1 effective angular momentum and the spin degree of freedom. I checked that my results are equivalent to the projection of the operators found in that article onto the $j = 3/2$ manifold for $4/5d^1$ electrons.

After calculating the scattering operators $\hat{\mathcal{O}}_i^{L_\mu}$, the RIXS cross section in Eq. (5.32) can be calculated using the same techniques used to evaluate the INS dynamical structure factor (Section 5.1.4). The results for some representative operators are shown in Fig. 29. The spectral weight is distributed over a broad continuum, as expected for fractional excitations. A common feature for all these results is a maximum of intensity for transferred momentum at the L point, $\mathbf{q} = (\pi, \pi, \pi)$.

Interestingly, the θ^2 fermion is excited in the cross section of the L_2 edge through the operators τ^x , τ^z and $\mathbf{s}\tau^y$, in sharp contrast with the dynamical structure factor for INS. Due to the reduced bandwidth of the θ^2 fermions, the spectrum probed by RIXS (with the proper

polarization) displays a narrower energy range when compared to the one measured by INS. This feature is readily verified when comparing Figs. 29b, 29c and 29d with Fig. 27b.

The interesting feature of the L_3 -edge is that it detects pseudospin excitations directly. In principle, it would be possible to choose ε and ε' such that $P_x = P_y = 0$, but $P_z \neq 0$. The cross section is then given by

$$I(\mathbf{q}, \omega) \propto \sum_n |\langle n | s_{\mathbf{q}}^z | g \rangle|^2 \delta(E_g - E_n + \hbar\omega), \quad (5.43)$$

where $s_{\mathbf{q}}^z$ is the Fourier transform of s_j^z . At the special point $\mathbf{q} = 0$, the form factor involves the conserved quantity $\mathbf{s}_{\mathbf{q}=0} = \mathbf{s}_{\text{tot}}$ [see Eq. (3.55)], which commutes with the spin Hamiltonian. Since the ground state is a singlet of the pseudospin SU(2) symmetry, $\mathbf{s}_{\mathbf{q}=0} | g \rangle = 0$. Thus, it follows from Eq. (5.43) that

$$I(\mathbf{q} = 0, \omega) = 0 \quad (\text{for } \hat{O}_{\mathbf{q}} = s_{\mathbf{q}}^z), \quad (5.44)$$

for any transferred energy ω . This feature is clearly seen in Fig. 29a, and should be contrasted with the dynamical structure factor $S(\mathbf{q} = 0, \omega) \neq 0$ for INS in Fig. 27b. This result is explicitly confirmed by the computation of the form factor in Eq. (5.43). At the mean field level, the excited state $|n\rangle$ is a two-particle excitation, in which the particles are characterized by well-defined momenta \mathbf{k} and \mathbf{k}' . We can write $|n\rangle = |n(\mathbf{k}, \mathbf{k}')\rangle$, in which the vector \mathbf{k}' can take the values $\pm\mathbf{k} \pm \mathbf{q}$ according to the type of two-particle excitation under consideration. As shown in Appendix F (see Eq. (F.15)), the form factor in this case is

$$|\langle n(\mathbf{k}, \mathbf{k}') | s_{\mathbf{q}}^z | g \rangle|^2 = 1 - \frac{\mathbf{h}(\mathbf{k}) \cdot \mathbf{h}(\mathbf{k}')}{|\mathbf{h}(\mathbf{k})||\mathbf{h}(\mathbf{k}')|}. \quad (5.45)$$

This form factor clearly vanishes for $\mathbf{q} = 0$. Therefore, this RIXS cross section could be used to detect the hidden SU(2) symmetry of the spin-orbital model for double perovskites.

The dynamic structure factor for the operator $s\tau^y$ calculated at mean-field level also vanishes at $\mathbf{q} = 0$ (see Fig. 29b). The reason is that the Majorana representation $s^a\tau^y = -i\eta^a\theta^2/4$, involves only θ^2 and η fermions, whose mean-field Hamiltonians are diagonalized by the same unitary transformation $U_{\mathbf{k}}$ given by Eq. (4.25). As a result, the form factor associated with $s\tau^y$ is also given by Eq. (5.45). However, since $\sum_j \mathbf{s}_j \tau_j^y$ does not commute with the Hamiltonian, the vanishing of the spectral weight at $\mathbf{q} = 0$ in this case is an artifact of the mean-field approximation.

I conclude this section with final remarks on the usefulness of RIXS to probe $4/5d^1$ Mott insulators. Throughout this section I considered only the cubic case, because of its simplicity and relevance to study the QSOL candidate Ba_2YMoO_6 . But it is also possible to compute the scattering cross sections of distorted systems. Appendix G provides the expression for Eq. (5.39) including effects of tetragonal distortion that were calculated in Ref. (1). These results indicate that RIXS is another tool to investigate the onset of quadrupolar orders in double perovskites, such as the one recently proposed on the osmate $\text{Ba}_2\text{NaOsO}_6$. (187)

The discussion throughout this work was restricted to one-site operators, but this technique can, in principle, probe operators involving two or three sites. (51) The symmetry arguments presented here can be extended to these operators. When this is done, it can be shown that the chiral operator $\mathbf{s}_i \cdot (\mathbf{s}_j \times \mathbf{s}_k)$ could be probed and would couple with the polarization factor $\boldsymbol{\varepsilon}^{I*} \cdot \boldsymbol{\varepsilon}$ (see Table I of Ref. (51)) RIXS could in principle detect the P and Θ symmetry breaking of the chiral spin-orbital liquid in the elastic limit. Even though this signal would be weak (since a three-site operator would lead to a less intense cross section than a single-site), it is already a remarkable result that RIXS can probe some type of order in a QSOL. Out of the elastic limit, the RIXS cross section is influenced by Z_2 gauge fluctuations. As happened with the INS, the evaluation of these fluctuations will be left to a separate and detailed study.

6 CONCLUSIONS AND OUTLOOK

I have presented a study of realistic microscopic models for $4/5d^1$ Mott insulators, in which strong SOC leads to an effective $j = 3/2$ local moment. These minimal models display multipolar interactions and large continuous symmetries that enhance quantum fluctuations. The latter can induce exotic forms of magnetism, including QSOL states. I first analyzed the multipoles of these angular momentum and showed that they can be rewritten in terms of $s = 1/2$ pseudospins \mathbf{s} and pseudo-orbitals $\boldsymbol{\tau}$. These operators allow simpler interpretations of the continuous symmetries emerging in double perovskites and Kitaev material-like compounds in the limit of vanishing Hund's coupling. In the case of the double perovskites, the total pseudospin $\sum_i \mathbf{s}_i$ is a conserved quantity. For the materials in generalized honeycomb lattices, the SU(4) symmetry can be made explicit through a Klein transformation on \mathbf{s} and a two-sublattice transformation on $\boldsymbol{\tau}$. The results discussed in this thesis can help guide theoretical modeling, design and interpretation of experiments in compounds with similar $j = 3/2$ physics.

I also studied the energetics and experimental responses of fermionic QSOLs proposed from parton mean-field theory. The energetics study was performed with VMC computations and showed that the QSOLs displayed competitive energies and could describe the ground state. It was then possible to compare the experimental data available for the double perovskite Ba_2YMoO_6 (30–33) and the expected response of the chiral spin-orbital liquid. The chiral QSOL reproduces the sharp drop in the spin-lattice relaxation rate at low temperatures (31) and the broad peak in the specific heat. (30, 31) It is necessary to remember, however, that parton mean-field theory is an uncontrolled approximation that includes contributions of unphysical states. The controlled computation of thermodynamical quantities for QSLs has only been possible for the Kitaev model by combining its integrability with Monte Carlo calculations. (132–134) The problem of improving the computation of thermodynamical quantities for fermionic QSOLs is still open.

Turning to the spectroscopic technique, the QSOL does not lead to a three-peak structure observed in the INS cross section measured in polycrystalline samples. (32) It is also difficult to interpret the two Curie regimes observed in the susceptibility. (30) The current results for this phase do not support a QSOL in double perovskites, and a dimer-singlet phase explains the experimental data available for Ba_2YMoO_6 in a more natural way. (139) This seemingly disappointing result must be balanced with the positive methodological accomplishments. The study performed in this thesis started from the microscopic degrees of freedom up to the expected responses of a $j = 3/2$ QSOL and showed that its absence of order does not imply absence of distinguishable features in experiments.

It was also demonstrated that RIXS is a promising technique to probe $j = 3/2$ compounds. The RIXS scattering operators for $4/5d^1$ Mott insulators directly probe \mathbf{s} and $\boldsymbol{\tau}$ in the case of

fixed polarization. This leads to a peculiar feature to the RIXS cross section of the chiral QSOL at the L_3 -edge, namely, the suppression of the spectral weight for $\mathbf{q} = 0$ transferred momentum due to the $SU(2)$ symmetry. The applicability of RIXS as a spectroscopic technique for strongly correlated systems stumble upon certain technical limitations. The most important at the moment is its dependence of the measured cross section with the photon polarization, which works as a double-edged sword. On the one hand, it gives the potential of probing the dynamics of certain degrees of freedom that are kept unavailable for INS. On the other hand, since the final polarization of the photon is not controlled, it also means that the measured RIXS cross sections display a combination of responses from different degrees of freedom. The data must be then further analyzed in order to give useful information. The challenges of producing better photon detectors are great, but there are reasons for optimism concerning this issue. The synthesis of the Kitaev material $H_3LiIr_2O_6$ was announced this year with several experimental results indicating a QSL ground state. (116) This is an interesting compound to be probed with RIXS, since this technique can probe the Majorana excitations of the Kitaev model in the L_3 -edge with a fixed polarization. (130, 131) Given the deserved attention of this experimental problem, the better control of the photon polarization in RIXS can be considered the next benchmark in RIXS instrumentation. This factor combined with the steady progress of RIXS applicability makes it reasonable to state that the RIXS theory designed here may be tested in the following years.

Concerning the experimental features of $4/5d^1$ compounds isostructural to the Kitaev materials, there is only one synthesized material in this category (α - $ZrCl_3$) and no experimental results available to determine the nature of its ground state. (39) One recently proposed route to produce similar Mott insulators in generalized honeycomb lattices is through metal-organic frameworks. (39, 108) Since the superexchange path in these frameworks would be topologically identical to the ones observed in Kitaev materials, $4/5d^1$ compounds would display the same $SU(4)$ symmetrical model. (39) Would they be good QSOL candidates? The $SU(4)$ limit probably hosts a QSOL ground state and the results of VMC calculations indicate that they should be stable against tetramerization. The results I have found with LFWT also indicate that simpler orders are unstable. But the state observed in actual experiments will depend on the role of perturbations induced by Hund's coupling, further-neighbor interactions, direct exchange, distortions, etc. There is no tenable theoretical solution to a problem with so many possible variables, and the answer to this question will depend upon an interplay between theory and experiment, as performed for double perovskites.

I close with some open issues and suggesting some venues for future research in $j = 3/2$ compounds, starting with the more immediate question of the Jahn-Teller effects in these materials. The models considered throughout this thesis presupposed the retention of cubic symmetry, since it is an important part of the physics of Ba_2YMoO_6 and the Kitaev materials. However, distortion is generally observed in $4/5d^1$ double perovskites. (29) Provided the spin-orbit coupling is more relevant than this distortion, the pseudospin and pseudo-orbital remain good degrees of freedom to describe the physics of this compounds. Indeed, the effects of

tetragonal distortion on RIXS scattering were already computed. (1) The distortion lifts the degeneracy between B and C orbitals, and hence favors an orbital ordering. This generically leads to a quadrupolar order, whose order parameters are given in terms of mean values of τ^x and τ^z . (29) The study of distortion and Jahn-Teller effects are further encouraged by NMR experiments indicating the breaking of local point symmetry in the osmium-based compound $\text{Ba}_2\text{NaOsO}_6$ by tetragonal distortions at low temperatures. (187) A quadrupolar order was suggested to explain these results. Even more recently, a study based on *ab initio* techniques indicated that the dynamic Jahn-Teller effect can be important to understand the physics of double perovskites. (188) The machinery developed throughout this thesis may simplify the treatment of this problem and shed light on the physics of quadrupolar orders and excitations.

It would be also important to study the stability of the QSOLs with a renormalization group (RG) approach. Just like parton mean-field theory is different from the usual mean field theory, the enlarged Hilbert space generated by the parton construction is also inherited by the RG. To overcome this problem, a methodology was designed allowing RG calculations for fermionic QSLs in recent years, the so-called pseudofermion functional renormalization group (pf-FRG). (80, 189–194) Its principle is the same of other functional renormalization group (FRG) techniques: it allows the determination of the exact flow equation of the vertex function Γ^Λ , a Legendre transformation of the more usual Green's function. (195) The flow is defined by a system with infinitely many coupled equations, and approximate schemes involving the truncation of these equations are necessary in actual computations. The pf-FRG was developed using the physics of the Mott insulating phase of cuprates as motivation. (189) It distinguishes from other FRG schemes because it slightly changes the Hamiltonian of interest in a way that is equivalent to project the parton states to the physical Hilbert space. The pf-FRG was soon adapted to discuss the phase diagram of the Heisenberg-Kitaev model with temperature (190) and can be used to compute the DSF of complex materials in the elastic limit. (80) More directly connected to this thesis, the pf-FRG was discussed for models with $\text{SU}(N)$ symmetry in real and momentum space. (193, 194) After a more careful analysis of stable ordered states of the model (3.59), it would be interesting to study the stability of the $\text{SU}(4)$ QSOLs under Hund's coupling induced perturbations using pf-FRG.

Finally, I ask if there are compounds implementing an exactly solvable $j = 3/2$ model. There are in fact several examples of these models available in the literature (154, 196–200) but they never found the same amount of attention given to the Kitaev model due to the lack of experimental motivation. In this thesis, I developed the necessary theoretical machinery that can facilitate the analysis of compounds with $j = 3/2$, and foster research for the synthesis of other materials implementing the physics of these integrable models. Let me briefly discuss two examples to point out some similarities and differences between them and the Kitaev model.

Consider the Gamma Matrix Model (GMM) on the square lattice (196)

$$\begin{aligned}\hat{H}_{\text{GMM}} &= \sum_j [J_x \Gamma_j^1 \Gamma_{j+\hat{x}}^2 + J_y \Gamma_j^3 \Gamma_{j+\hat{y}}^4] + \sum_i [J'_x \Gamma_j^{15} \Gamma_{j+\hat{x}}^{25} + J'_y \Gamma_j^{35} \Gamma_{j+\hat{y}}^{45}] \\ &= 16 \sum_i s_i^x s_{i+\hat{x}}^y (J_x \tau_i^y \tau_{i+\hat{x}}^y + J'_x \tau_i^x \tau_{i+\hat{x}}^x) - 8 \sum_i (J_y s_i^z \tau_i^y \tau_{i+\hat{y}}^x + J'_y s_i^z \tau_i^x \tau_{i+\hat{y}}^y)\end{aligned}\quad (6.1)$$

and the SU(2)-invariant Kitaev model on the honeycomb lattice (154)

$$\hat{H}_{\text{SU}(2)} = \sum_{\langle ij \rangle_\gamma} J_\gamma \mathbf{s}_i \cdot \mathbf{s}_j \tau_i^\gamma \tau_j^\gamma, \quad (6.2)$$

in which γ labels different bond orientations. The Γ^a matrices in Eq. (6.1) are 4×4 matrices satisfying the Clifford algebra. The models in Eqs. (6.1) and (6.2) are nearest-neighbor models with bond-dependent interactions like Eq. (2.48). Their integrability depends upon a Majorana parton representation of the operators and leads to an emerging Z_2 gauge field. This mapping allows any state to be described as a direct product of a “flux” state $|F\rangle$ and a “matter” state $|M\rangle$. (21) The Hamiltonians can be diagonalized in a fixed gauge, and the ground state sector can be determined with the application of Lieb’s theorem (124) or using numerical methods. The similar form of the projection operator makes it reasonable that an identity similar to Eq. (2.68) or its extensions (see Ref. (125)) can be found.

The $j = 3/2$ models also display interesting physical differences in relation to the Kitaev model. First, the interactions occur between different components of Γ^a and Γ^{ab} in the GMM (Eq. (6.1)) that are equivalent to multipoles described in terms of \mathbf{s} and $\boldsymbol{\tau}$. The Z_2 gauge fluxes are conserved quantities of the GMM just like in the Kitaev model and ensure ultra-short correlations, that is, correlations only between nearest neighbors. (21) The model in Eq. (6.2) is also integrable and the bond-directional interactions play an important role in finding the exact solution. However, in contrast to the Kitaev model and the GMM, it possesses a global SU(2) symmetry and excitations in three Majorana flavors. These flavors combine themselves into $S = 1$ fermionic excitations leading to a static spin correlation function with a power-law decay, in clear contrast to the Kitaev model. (154)

It would be very interesting to calculate the DSF measured through the INS for exactly solvable $j = 3/2$ models, i.e., the quantity

$$S(\mathbf{q}, \omega) = \frac{1}{N} \sum_{\mathbf{R}_m \mathbf{R}_n} \sum_{a,b} e^{-i\mathbf{q} \cdot (\mathbf{R}_m - \mathbf{R}_n)} \int dt e^{i\omega t} \langle 0 | j_m^a(t) j_n^a(0) | 0 \rangle \quad (6.3)$$

where $|0\rangle$ is the direct product of a Z_2 flux state $|F_0\rangle$ and a matter state of Majorana fermions $|M_0\rangle$. RIXS cross sections can also be evaluated by substituting the $j_m^a(t)$ and $j_n^b(0)$ in Eq. (6.3) for their pseudospin and pseudo-orbital counterparts. Such cross section can be evaluated in parallel with the DSF. It is expected that the matrix element in Eq. (6.3) for $j = 3/2$ models with ultra-short correlations (196, 199) can be mapped to a local quantum quench problem. (125) This is a formidable non-equilibrium problem in quantum mechanics, but it is still solvable since it

is written in terms of quadratic operators. If the mapping to a quench is possible, the methods developed to uncover the dynamics of the Kitaev QSL (125) can be adapted to compute Eq. (6.3) exactly. Comparisons with the Kitaev model and the responses obtained with mean field parton approximations will be useful to interpret these results.

The exact DSF of QSLs with power-law decay of the correlation function (154, 200) has not been calculated yet. Even if there is a mapping of the matrix element in Eq. (6.3) to a quantum quench, the evaluation of $S(\mathbf{q}, \omega)$ is not possible by computing only nearest neighbors correlators. The recently developed augmented parton mean-field theory is probably the best formalism to deal with this problem. (176) This technology is suited to find approximate expressions of $S(\mathbf{q}, \omega)$ for the perturbed Kitaev model. In principle, the technique can be used to understand the evolution of the DSF with an applied magnetic field. Interestingly enough, this field induces a power-law correlation (201) of the same type that is observed on the ground state of $j = 3/2$ models with continuous symmetry. (154, 200) Therefore, I expect that adapting the augmented parton MFT to $j = 3/2$ states will be the best approach to find a controlled approximation of the DSF of these QSOLs.

Overall, one of the pleasing aspect of this thesis was to work out the construction of a model in a condensed matter system from its microscopic degrees of freedom (reductionism) and then argue in favor of an exotic behavior in the thermodynamic limit (emergence). This process depended on both basic and well-grounded quantum mechanics and sophisticated methods that are still under development. It was also part of a much larger ongoing project of understanding new phases of matter with direct interplay between theorists and experimentalists. For these reasons, I expect that the topics discussed here will be of general interest and generate other lines of inquiry in the coming years.

BIBLIOGRAPHY

- 1 NATORI, W. M. H.; DAGHOFER, M.; PEREIRA, R. G. Dynamics of a $j = \frac{3}{2}$ quantum spin liquid. **Physical Review B**, v. 96, n. 12, p. 125109, 2017.
- 2 COLEMAN, P. **Heavy fermions and the Kondo lattice: a 21st century perspective**. 2015. Available from: <<https://arxiv.org/pdf/1509.05769.pdf>>. Accessible at: 07 June 2018.
- 3 NATORI, W. M. H.; ANDRADE, E. C.; PEREIRA, R. G. **SU(4)-symmetric spin-orbital liquids on the hyperhoneycomb lattice**. 2018. Available from: <<https://arxiv.org/pdf/1802.00044.pdf>>. Accessible at: 07 June 2018.
- 4 NATORI, W. M. H. et al. Chiral spin-orbital liquids with nodal lines. **Physical Review Letters**, v. 117, n. 1, p. 017204, 2016.
- 5 MACHAMER, P.; SILBERSTEIN, M. (Ed.). **The Blackwell guide to the philosophy of science**. Massachusetts: Blackwell Publishers, 2002. (Blackwell philosophy guides, v.7).
- 6 ANDERSON, P. W. More is different. **Science**, v. 177, n. 4047, p. 393–396, 1972.
- 7 KADANOFF, L. P. More is the same; phase transitions and mean field theories. **Journal of Statistical Physics**, v. 137, n. 5, p. 777, 2009.
- 8 KIVELSON, S.; KIVELSON, S. A. Defining emergence in physics. **Npj Quantum Materials**, v. 1, p. 16024, 2016. doi.org/10.1038/npjquantmats.2016.24.
- 9 COLEMAN, P. **Emergence and reductionism: an awkward Baconian alliance**. 2017. Available from: <<https://arxiv.org/pdf/1702.06884.pdf>>. Accessible at: 07 June 2018.
- 10 BALENTS, L. Spin liquids in frustrated magnets. **Nature**, v. 464, n. 2, p. 199–208, 2010.
- 11 SAVARY, L.; BALENTS, L. Quantum spin liquids: a review. **Reports on Progress in Physics**, v. 80, n. 1, p. 016502, 2017.
- 12 ANDERSON, P. Resonating valence bonds: a new kind of insulator? **Materials Research Bulletin**, v. 8, n. 2, p. 153 – 160, 1973.
- 13 HASAN, M. Z.; KANE, C. L. Colloquium: topological insulators. **Reviews of Modern Physics**, v. 82, n. 4, p. 3045, 2010.
- 14 QI, X.-L.; ZHANG, S.-C. Topological insulators and superconductors. **Reviews of Modern Physics**, v. 83, n. 4, p. 1057, 2011.
- 15 CHIU, C.-K. et al. Classification of topological quantum matter with symmetries. **Reviews of Modern Physics**, v. 88, n. 3, p. 035005, 2016.
- 16 TREBST, S. **Kitaev materials**. 2017. Available from: <<https://arxiv.org/pdf/1701.07056.pdf>>. Accessible at: 07 June 2018.
- 17 WINTER, S. M. et al. Models and materials for generalized Kitaev magnetism. **Journal of Physics: condensed matter**, v. 29, n. 49, p. 493002, 2017.

-
- 18 HERMANN, M.; KIMCHI, I.; KNOLLE, J. Physics of the Kitaev model: fractionalization, dynamical correlations, and material connections. **Annual Review of Condensed Matter Physics**, v. 9, n. 1, p. 17–33, 2018.
- 19 JACKELI, G.; KHALIULLIN, G. Mott insulators in the strong spin-orbit coupling limit: from Heisenberg to a quantum compass and Kitaev models. **Physical Review Letters**, v. 102, n. 1, p. 017205, 2009.
- 20 KITAEV, A. Anyons in an exactly solved model and beyond. **Annals of Physics**, v. 321, n. 1, p. 2–111, 2006.
- 21 BASKARAN, G.; MANDAL, S.; SHANKAR, R. Exact results for spin dynamics and fractionalization in the Kitaev model. **Physical Review Letters**, v. 98, n. 24, p. 247201, 2007.
- 22 BERNEVIG, B. A.; HUGHES, T. L.; ZHANG, S.-C. Quantum spin Hall effect and topological phase transition in HgTe quantum wells. **Science**, v. 314, n. 5806, p. 1757–1761, 2006.
- 23 KONIG, M. et al. Quantum spin Hall insulator state in HgTe quantum wells. **Science**, v. 318, n. 5851, p. 766–770, 2007.
- 24 KANE, C. L.; MELE, E. J. Quantum spin Hall effect in graphene. **Physical Review Letters**, v. 95, n. 22, p. 226801, 2005.
- 25 _____. Z_2 topological order and the quantum spin Hall effect. **Physical Review Letters**, v. 95, n. 14, p. 146802, 2005.
- 26 WITCZAK-KREMPA, W. et al. Correlated quantum phenomena in the strong spin-orbit regime. **Annual Review of Condensed Matter Physics**, v. 5, n. 1, p. 57, 2014.
- 27 VASALA, S.; KARPPINEN, M. $A_2BB'O_6$ perovskites: a review. **Progress in Solid State Chemistry**, v. 43, n. 1, p. 1 – 36, 2015.
- 28 ABRAGAM, A.; BLEANEY, B. **Electron paramagnetic resonance of transition ions**. Oxford: Oxford University Press, 1970.
- 29 CHEN, G.; PEREIRA, R.; BALENTS, L. Exotic phases induced by strong spin-orbit coupling in ordered double perovskites. **Physical Review B**, v. 82, n. 17, p. 174440, 2010.
- 30 VRIES, M. A. de; MCLAUGHLIN, A. C.; BOS, J.-W. G. Valence bond glass on an fcc lattice in the double perovskite Ba_2YMoO_6 . **Physical Review Letters**, v. 104, n. 17, p. 177202, 2010.
- 31 AHAREN, T. et al. Magnetic properties of the geometrically frustrated $s = \frac{1}{2}$ antiferromagnets, La_2LiMoO_6 and Ba_2YMoO_6 : evidence for a collective spin-singlet ground state. **Physical Review B**, v. 81, n. 22, p. 224409, 2010.
- 32 CARLO, J. P. et al. Triplet and in-gap magnetic states in the ground state of the quantum frustrated fcc antiferromagnet Ba_2YMoO_6 . **Physical Review B**, v. 84, n. 10, p. 100404, 2011.
- 33 VRIES, M. A. de et al. Low-temperature spin dynamics of a valence bond glass in Ba_2YMoO_6 . **New Journal of Physics**, v. 15, p. 043024, 2013. doi:10.1088/1367-2630/15/4/043024.

- 34 WIEBE, C. R. et al. Spin-glass behavior in the $s=1/2$ fcc ordered perovskite $\text{Sr}_2\text{CaReO}_6$. **Physical Review B**, v. 65, n. 14, p. 144413, 2002.
- 35 _____. Frustration-driven spin freezing in the $s=1/2$ fcc perovskite $\text{Sr}_2\text{MgReO}_6$. **Physical Review B**, v. 68, n. 13, p. 134410, 2003.
- 36 YAMAMURA, K.; WAKESHIMA, M.; HINATSU, Y. Structural phase transition and magnetic properties of double perovskites Ba_2CaMO_6 ($M=\text{W, Re, Os}$). **Journal of Solid State Chemistry**, v. 179, n. 3, p. 605–612, 2006.
- 37 STITZER, K. E.; SMITH, M. D.; LOYE, H.-C. z. Crystal growth of Ba_2MOsO_6 ($M=\text{Li, Na}$) from reactive hydroxide fluxes. **Solid State Sciences**, v. 4, n. 3, p. 311–316, 2002.
- 38 ERICKSON, A. S. et al. Ferromagnetism in the Mott insulator $\text{Ba}_2\text{NaOsO}_6$. **Physical Review Letters**, v. 99, n. 1, p. 016404, 2007.
- 39 YAMADA, M. G.; OSHIKAWA, M.; JACKELI, G. **Emergent $SU(4)$ symmetry in $\alpha\text{-ZrCl}_3$ and crystalline spin-orbital liquids**. 2017. Available from: <<https://arxiv.org/pdf/1709.05252.pdf>>. Accessible at: 07 June 2018.
- 40 LI, Y. Q. et al. $SU(4)$ theory for spin systems with orbital degeneracy. **Physical Review Letters**, v. 81, n. 16, p. 3527–3530, 1998.
- 41 WANG, F.; VISHWANATH, A. Z_2 spin-orbital liquid state in the square lattice Kugel-Khomskii model. **Physical Review B**, v. 80, n. 6, p. 064413, 2009.
- 42 CORBOZ, P. et al. Spin-orbital quantum liquid on the honeycomb lattice. **Physical Review X**, v. 2, n. 4, p. 041013, 2012.
- 43 LAJKÓ, M.; PENC, K. Tetramerization in a $SU(4)$ Heisenberg model on the honeycomb lattice. **Physical Review B**, v. 87, n. 22, p. 224428, 2013.
- 44 KUGEL, K. I.; KHOMSKII, D. I. The Jahn-Teller effect and magnetism: transition metal compounds. **Soviet Physics Uspekhi**, v. 25, n. 4, p. 231, 1982.
- 45 NUSSINOV, Z.; BRINK, J. van den. Compass models: theory and physical motivations. **Reviews of Modern Physics**, v. 87, n. 1, p. 1–59, 2015.
- 46 GROS, C. Physics of projected wavefunctions. **Annals of Physics**, v. 189, n. 1, p. 53–88, 1989.
- 47 AMENT, L. J. P.; KHALIULLIN, G. Theory of Raman and resonant inelastic x-ray scattering from collective orbital excitations in YTiO_3 . **Physical Review B**, v. 81, n. 12, p. 125118, 2010.
- 48 AMENT, L. J. P. et al. Resonant inelastic x-ray scattering studies of elementary excitations. **Reviews of Modern Physics**, v. 83, n. 2, p. 705–767, 2011.
- 49 KIM, J. et al. Magnetic excitation spectra of Sr_2IrO_4 probed by resonant inelastic x-ray scattering: establishing links to cuprate superconductors. **Physical Review Letters**, v. 108, n. 17, p. 177003, 2012.
- 50 _____. Excitonic quasiparticles in a spin-orbit Mott insulator. **Nature Communications**, v. 5, p. 4453, 2014. doi:10.1038/ncomms5453.

- 51 SAVARY, L.; SENTHIL, T. **Probing hidden orders with resonant inelastic x-ray scattering**. 2015. Available from: <<https://arxiv.org/pdf/1506.04752.pdf>>. Accessible at: 07 June 2018.
- 52 KIM, B. J.; KHALIULLIN, G. Resonant inelastic x-ray scattering operators for t_{2g} orbital systems. **Physical Review B**, v. 96, n. 8, p. 085108, 2017.
- 53 GOLDSTONE, J.; SALAM, A.; WEINBERG, S. Broken symmetries. **Physical Review**, v. 127, n. 3, p. 965–970, 1962.
- 54 HOLSTEIN, T.; PRIMAKOFF, H. Field dependence of the intrinsic domain magnetization of a ferromagnet. **Physical Review**, v. 58, n. 12, p. 1098–1113, 1940.
- 55 LOVESEY, S. W. **Theory of neutron scattering from condensed matter: polarization effects and magnetic scattering**. Oxford: Oxford University Press, 1984. v. 2.
- 56 WEGNER, F. J. Duality in generalized Ising models and phase transitions without local order parameters. **Journal of Mathematical Physics**, v. 12, n. 10, p. 2259–2272, 1971.
- 57 KOGUT, J. B. An introduction to lattice gauge theory and spin systems. **Reviews of Modern Physics**, v. 51, n. 4, p. 659–713, 1979.
- 58 WEN, X.-G. **Quantum field theory of many-body systems**. Oxford: Oxford University Press, 2004.
- 59 WEN, X. G.; NIU, Q. Ground-state degeneracy of the fractional quantum Hall states in the presence of a random potential and on high-genus Riemann surfaces. **Physical Review B**, v. 41, n. 13, p. 9377–9396, 1990.
- 60 WEN, X.-G. Quantum orders and symmetric spin liquids. **Physical Review B**, v. 65, n. 16, p. 165113, 2002.
- 61 KITAEV, A. Fault-tolerant quantum computation by anyons. **Annals of Physics**, v. 303, n. 1, p. 2 – 30, 2003.
- 62 BOER, J. H. de; VERWEY, E. J. W. Semi-conductors with partially and with completely filled 3 d -lattice bands. **Proceedings of the Physical Society**, v. 49, n. 4S, p. 59, 1937.
- 63 MOTT, N. F.; PEIERLS, R. Discussion of the paper by de Boer and Verwey. **Proceedings of the Physical Society**, v. 49, n. 4S, p. 72, 1937.
- 64 MOTT, N. F. The basis of the electron theory of metals, with special reference to the transition metals. **Proceedings of the Physical Society A**, v. 62, n. 7, p. 416, 1949.
- 65 _____. The transition to the metallic state. **Philosophical Magazine**, v. 6, n. 62, p. 287–309, 1961.
- 66 _____. **Metal-insulator transitions**. London/Philadelphia: Taylor & Francis, 1990.
- 67 FAZEKAS, P. **Lecture notes on electron correlation and magnetism**. Singapore: World Scientific, 1999. (Series in modern condensed matter physics, v.5).
- 68 MAEKAWA, S. et al. **Physics of transition metal oxides**. Berlin Heidelberg: Springer-Verlag, 2004.

-
- 69 LACROIX, C.; MENDELS, P.; MILA, F. (Ed.). **Introduction to frustrated magnetism**. Berlin Heidelberg: Springer-Verlag, 2011. (Springer-Series in solid state sciences, v.164).
- 70 KHOMSKII, D. **Transition metal compounds**. Cambridge: Cambridge University Press, 2014.
- 71 ANDERSON, P. W. Antiferromagnetism. theory of superexchange interaction. **Physical Review**, v. 79, n. 2, p. 350–356, 1950.
- 72 _____. New approach to the theory of superexchange interactions. **Physical Review**, v. 115, n. 1, p. 2–13, 1959.
- 73 HUBBARD, J. Electron correlations in narrow energy bands. **Proceedings of the Royal Society of London A**, v. 276, n. 1365, p. 238–257, 1963.
- 74 NÉEL, L. Antiferromagnetism and ferrimagnetism. **Proceedings of the Physical Society A**, v. 65, n. 11, p. 869, 1952.
- 75 MARSHALL, W. Antiferromagnetism. **Proceedings of the Royal Society of London A**, v. 232, n. 1188, p. 48–68, 1955.
- 76 FAZEKAS, P.; ANDERSON, P. W. On the ground state properties of the anisotropic triangular antiferromagnet. **Philosophical Magazine**, v. 30, n. 2, p. 423–440, 1974.
- 77 CAPRIOTTI, L.; TRUMPER, A. E.; SORELLA, S. Long-range Néel order in the triangular Heisenberg model. **Physical Review Letters**, v. 82, n. 19, p. 3899–3902, 1999.
- 78 HAN, T.-H. et al. Fractionalized excitations in the spin-liquid state of a kagome-lattice antiferromagnet. **Nature**, v. 492, n. 7429, p. 406–410, 2012.
- 79 KERMARREC, E. et al. Spin dynamics and disorder effects in the $s = \frac{1}{2}$ kagome Heisenberg spin-liquid phase of kapellasite. **Physical Review B**, v. 90, n. 20, p. 205103, 2014.
- 80 BALZ, C. et al. Physical realization of a quantum spin liquid based on a complex frustration mechanism. **Nature Physics**, v. 12, p. 942, 2016. doi.org/10.1038/nphys3826.
- 81 ANDERSON, P. W. The resonating valence bond state in La_2CuO_4 and superconductivity. **Science**, v. 235, n. 4793, p. 1196–1198, 1987.
- 82 BEDNORZ, J. G.; MÜLLER, K. A. Possible high- T_c superconductivity in the Ba-La-Cu-O system. **Zeitschrift für Physik B condensed matter**, v. 64, n. 2, p. 189–193, 1986.
- 83 BARDEEN, J.; COOPER, L. N.; SCHRIEFFER, J. R. Microscopic theory of superconductivity. **Physical Review**, v. 106, n. 1, p. 162–164, 1957.
- 84 TAKAGI, H. et al. High- T_c superconductivity of La-Ba-Cu oxides. ii. specification of the superconducting phase. **Japanese Journal of Applied Physics**, v. 26, n. 2A, p. L123, 1987.
- 85 JAHN, H. A.; TELLER, E. Stability of polyatomic molecules in degenerate electronic states. i. orbital degeneracy. **Proceedings of the Royal Society A**, v. 161, n. 905, p. 220–235, 1937.
- 86 BASKARAN, G.; ZOU, Z.; ANDERSON, P. The resonating valence bond state and high- T_c superconductivity - a mean field theory. **Solid State Communications**, v. 63, n. 11, p. 973 – 976, 1987.

- 87 KIVELSON, S. A.; ROKHSAR, D. S.; SETHNA, J. P. Topology of the resonating valence-bond state: solitons and high- T_c superconductivity. **Physical Review B**, v. 35, n. 16, p. 8865–8868, 1987.
- 88 SU, W. P.; SCHRIEFFER, J. R.; HEEGER, A. J. Solitons in polyacetylene. **Physical Review Letters**, v. 42, n. 25, p. 1698–1701, 1979.
- 89 KALMEYER, V.; LAUGHLIN, R. B. Equivalence of the resonating-valence-bond and fractional quantum Hall states. **Physical Review Letters**, v. 59, n. 18, p. 2095–2098, 1987.
- 90 BERRY, M. V. Quantal phase factors accompanying adiabatic changes. **Proceedings of the Royal Society of London A: mathematical, physical and engineering sciences**, v. 392, n. 1802, p. 45–57, 1984.
- 91 KHARE. **Fractional statistics and quantum theory**. Singapore: World Scientific, 2005.
- 92 LAUGHLIN, R. B. Superconducting ground state of noninteracting particles obeying fractional statistics. **Physical Review Letters**, v. 60, n. 25, p. 2677–2680, 1988.
- 93 READ, N.; CHAKRABORTY, B. Statistics of the excitations of the resonating-valence-bond state. **Physical Review B**, v. 40, n. 10, p. 7133–7140, 1989.
- 94 AFFLECK, I.; MARSTON, J. B. Large- n limit of the Heisenberg-Hubbard model: implications for high- T_c superconductors. **Physical Review B**, v. 37, n. 7, p. 3774–3777, 1988.
- 95 WEN, X. G.; WILCZEK, F.; ZEE, A. Chiral spin states and superconductivity. **Physical Review B**, v. 39, n. 16, p. 11413, 1989.
- 96 GUTZWILLER, M. C. Effect of correlation on the ferromagnetism of transition metals. **Physical Review Letters**, v. 10, n. 5, p. 159–162, 1963.
- 97 KANAMORI, J. Superexchange interaction and symmetry properties of electron orbitals. **Journal of Physics and Chemistry of Solids**, v. 10, n. 2, p. 87 – 98, 1959.
- 98 CHALOUKKA, J.; KHALIULLIN, G. Magnetic anisotropy in the Kitaev model systems Na_2IrO_3 and RuCl_3 . **Physical Review B**, v. 94, n. 6, p. 064435, 2016.
- 99 KHALIULLIN, G. Orbital order and fluctuations in Mott insulators. **Progress of Theoretical Physics Supplement**, v. 160, p. 155, 2005. doi.org/10.1143/PTPS.160.155.
- 100 SINGH, Y.; GEGENWART, P. Antiferromagnetic Mott insulating state in single crystals of the honeycomb lattice material Na_2IrO_3 . **Physical Review B**, v. 82, n. 6, p. 064412, 2010.
- 101 SINGH, Y. et al. Relevance of the Heisenberg-Kitaev model for the honeycomb lattice iridates A_2IrO_3 . **Physical Review Letters**, v. 108, n. 12, p. 127203, 2012.
- 102 PLUMB, K. W. et al. α - RuCl_3 : A spin-orbit assisted Mott insulator on a honeycomb lattice. **Physical Review B**, v. 90, n. 4, p. 041112, 2014.
- 103 MANDAL, S.; SURENDRAN, N. Exactly solvable Kitaev model in three dimensions. **Physical Review B**, v. 79, n. 2, p. 024426, 2009.
- 104 HERMANNNS, M.; TREBST, S. Quantum spin liquid with a Majorana Fermi surface on the three-dimensional hyperoctagon lattice. **Physical Review B**, v. 89, n. 23, p. 235102, 2014.

-
- 105 HERMANN, M.; O'BRIEN, K.; TREBST, S. Weyl spin liquids. **Physical Review Letters**, v. 114, n. 15, p. 157202, 2015.
- 106 HERMANN, M.; TREBST, S.; ROSCH, A. Spin-Peierls instability of three-dimensional spin liquids with Majorana Fermi surfaces. **Physical Review Letters**, v. 115, n. 17, p. 177205, 2015.
- 107 O'BRIEN, K.; HERMANN, M.; TREBST, S. Classification of gapless Z_2 spin liquids in three-dimensional Kitaev models. **Physical Review B**, v. 93, n. 8, p. 085101, 2016.
- 108 YAMADA, M. G.; DWIVEDI, V.; HERMANN, M. Crystalline Kitaev spin liquids. **Physical Review B**, v. 96, n. 15, p. 155107, 2017.
- 109 WELLS, A. F. **Three-dimensional nets and polyhedra**. Hoboken: John Wiley & Sons Inc, 1977.
- 110 MODIC, K. A. et al. Realization of a three-dimensional spin-anisotropic harmonic honeycomb iridate. **Nature Communications**, v. 5, n. 6, p. 4203, 2014.
- 111 TAKAYAMA, T. et al. Hyperhoneycomb Iridate β -Li₂IrO₃ as a Platform for Kitaev Magnetism. **Physical Review Letters**, v. 114, n. 7, p. 077202, 2015.
- 112 CHALOUPKA, J.; JACKELI, G.; KHALIULLIN, G. Kitaev-Heisenberg model on a honeycomb lattice: possible exotic phases in iridium oxides A₂IrO₃. **Physical Review Letters**, v. 105, n. 2, p. 027204, 2010.
- 113 _____. Zigzag magnetic order in the iridium oxide Na₂IrO₃. **Physical Review Letters**, v. 110, n. 9, p. 097204, 2013.
- 114 RAU, J. G.; LEE, E. K.-H.; KEE, H.-Y. Generic spin model for the honeycomb iridates beyond the Kitaev limit. **Physical Review Letters**, v. 112, n. 7, p. 077204, 2014.
- 115 WINTER, S. M. et al. Challenges in design of Kitaev materials: magnetic interactions from competing energy scales. **Physical Review B**, v. 93, n. 21, p. 214431, 2016.
- 116 KITAGAWA, K. et al. A spin-orbital-entangled quantum liquid on a honeycomb lattice. **Nature**, v. 554, p. 341, 2018. doi.org/10.1038/nature25482.
- 117 BAEK, S.-H. et al. Evidence for a field-induced quantum spin liquid in α -RuCl₃. **Physical Review Letters**, v. 119, n. 3, p. 037201, 2017.
- 118 BANERJEE, A. et al. Excitations in the field-induced quantum spin liquid state of α -RuCl₃. **npj Quantum Materials**, v. 3, n. 1, p. 8, 2018.
- 119 SEARS, J. A. et al. Phase diagram of α -RuCl₃ in an in-plane magnetic field. **Physical Review B**, v. 95, n. 18, p. 180411, 2017.
- 120 YADAV, R. et al. **Pressure-tuned magnetic interactions in honeycomb Kitaev materials**. 2018. Available from: <<https://arxiv.org/pdf/1802.01051.pdf>>. Accessible at: 07 June 2018.
- 121 LIU, H.; KHALIULLIN, G. Pseudospin exchange interactions in d^7 cobalt compounds: possible realization of the Kitaev model. **Physical Review B**, v. 97, n. 1, p. 014407, 2018.

- 122 SANO, R.; KATO, Y.; MOTOME, Y. Kitaev-Heisenberg hamiltonian for high-spin d^7 Mott insulators. **Physical Review B**, v. 97, n. 1, p. 014408, 2018.
- 123 ELLIOTT, S. R.; FRANZ, M. Colloquium: Majorana fermions in nuclear, particle, and solid-state physics. **Reviews of Modern Physics**, v. 87, n. 1, p. 137–163, 2015.
- 124 LIEB, E. H. Flux phase of the half-filled band. **Physical Review Letters**, v. 73, n. 16, p. 2158–2161, 1994.
- 125 KNOLLE, J. **Dynamics of a quantum spin liquid**. Heidelberg: Springer International Publishing, 2016. (Springer theses).
- 126 KNOLLE, J. et al. Dynamics of a two-dimensional quantum spin liquid: signatures of emergent Majorana fermions and fluxes. **Physical Review Letters**, v. 112, n. 20, p. 207203, 2014.
- 127 _____. Dynamics of fractionalization in quantum spin liquids. **Physical Review B**, v. 92, n. 11, p. 115127, 2015.
- 128 SMITH, A. et al. Neutron scattering signatures of the 3d hyperhoneycomb Kitaev quantum spin liquid. **Physical Review B**, v. 92, p. 180408, 2015.
- 129 _____. Majorana spectroscopy of three-dimensional Kitaev spin liquids. **Physical Review B**, v. 93, n. 23, p. 235146, 2016.
- 130 HALÁSZ, G. B.; PERKINS, N. B.; BRINK, J. van den. Resonant inelastic x-ray scattering response of the Kitaev honeycomb model. **Physical Review Letters**, v. 117, n. 12, p. 127203, 2016.
- 131 HALÁSZ, G. B.; PERREAULT, B.; PERKINS, N. B. Probing spinon nodal structures in three-dimensional Kitaev spin liquids. **Physical Review Letters**, v. 119, n. 9, p. 097202, 2017.
- 132 NASU, J.; UDAGAWA, M.; MOTOME, Y. Vaporization of Kitaev spin liquids. **Physical Review Letters**, v. 113, n. 19, p. 197205, 2014.
- 133 _____. Thermal fractionalization of quantum spins in a Kitaev model: temperature-linear specific heat and coherent transport of Majorana fermions. **Physical Review B**, v. 92, n. 11, p. 115122, 2015.
- 134 NASU, J.; MOTOME, Y. Spin correlation and Majorana spectrum in chiral spin liquids in a decorated-honeycomb Kitaev model. **Journal of Physics: conference series**, v. 683, n. 1, p. 1–10, 2016.
- 135 LIEB, E.; SCHULTZ, T.; MATTIS, D. Two soluble models of an antiferromagnetic chain. **Annals of Physics**, v. 16, n. 3, p. 407 – 466, 1961.
- 136 OSHIKAWA, M. Commensurability, excitation gap, and topology in quantum many-particle systems on a periodic lattice. **Physical Review Letters**, v. 84, n. 7, p. 1535–1538, 2000.
- 137 SONG, X.-Y.; YOU, Y.-Z.; BALENTS, L. Low-energy spin dynamics of the honeycomb spin liquid beyond the Kitaev limit. **Physical Review Letters**, v. 117, n. 3, p. 037209, 2016.
- 138 SMITH, J.; KMETKO, E. Magnetism or bonding: a nearly periodic table of transition elements. **Journal of the Less Common Metals**, v. 90, n. 1, p. 83 – 88, 1983.

- 139 ROMHÁNYI, J.; BALENTS, L.; JACKELI, G. Spin-orbit dimers and noncollinear phases in d^1 cubic double perovskites. **Physical Review Letters**, v. 118, n. 21, p. 217202, 2017.
- 140 PÄRSCHKE, E. M.; RAY, R. **Influence of multiplet structure on photoemission spectra of spin-orbit driven Mott insulators: application to Sr_2IrO_4** . 2018. Available from: <<https://arxiv.org/pdf/1802.04158.pdf>>. Accessible at: 07 June 2018.
- 141 STAMOKOSTAS, G. L.; FIETE, G. A. Mixing of $t_{2g} - e_g$ orbitals in $4d$ and $5d$ transition metal oxides. **Physical Review B**, v. 97, n. 8, p. 085150, 2018.
- 142 KOGA, A.; NAKAUCHI, S.; NASU, J. Role of spin-orbit coupling in the Kugel-Khomskii model on the honeycomb lattice. **Physical Review B**, v. 97, n. 9, p. 094427, 2018.
- 143 FEINER, L. F.; OLÉS, A. M.; ZAAANEN, J. Quantum melting of magnetic order due to orbital fluctuations. **Physical Review Letters**, v. 78, n. 14, p. 2799–2802, 1997.
- 144 KHALIULLIN, G.; OUDOVENKO, V. Spin and orbital excitation spectrum in the Kugel-Khomskii model. **Physical Review B**, v. 56, n. 22, p. R14243–R14246, 1997.
- 145 JOSHI, A. et al. Elementary excitations in magnetically ordered systems with orbital degeneracy. **Physical Review B**, v. 60, n. 9, p. 6584–6587, 1999.
- 146 KUGEL, K. I. et al. Spin-orbital interaction for face-sharing octahedra: realization of a highly symmetric $\text{SU}(4)$ model. **Physical Review B**, v. 91, n. 15, p. 155125, 2015.
- 147 SANTINI, P. et al. Multipolar interactions in f -electron systems: the paradigm of actinide dioxides. **Reviews of Modern Physics**, v. 81, n. 2, p. 807–863, 2009.
- 148 SHIINA, R. et al. Interplay of field-induced multipoles in CeB_6 . **Journal of the Physical Society of Japan**, v. 67, n. 3, p. 941, 1998.
- 149 LUTTINGER, J. M.; TISZA, L. Theory of dipole interaction in crystals. **Physical Review**, v. 70, n. 11-12, p. 954–964, 1946.
- 150 PATI, S. K.; SINGH, R. R. P.; KHOMSKII, D. I. Alternating spin and orbital dimerization and spin-gap formation in coupled spin-orbital systems. **Physical Review Letters**, v. 81, n. 24, p. 5406–5409, 1998.
- 151 ITOI, C.; QIN, S.; AFFLECK, I. Phase diagram of a one-dimensional spin-orbital model. **Physical Review B**, v. 61, n. 10, p. 6747–6756, 2000.
- 152 KIMCHI, I.; VISHWANATH, A. Kitaev-Heisenberg models for iridates on the triangular, hyperkagome, kagome, fcc, and pyrochlore lattices. **Physical Review B**, v. 89, n. 1, p. 014414, 2014.
- 153 KIMCHI, I.; COLDEA, R. Spin dynamics of counterrotating Kitaev spirals via duality. **Physical Review B**, v. 94, n. 20, p. 201110, 2016.
- 154 YAO, H.; LEE, D.-H. Fermionic magnons, non-abelian spinons, and the spin quantum Hall effect from an exactly solvable spin-1/2 Kitaev model with $\text{SU}(2)$ symmetry. **Physical Review Letters**, v. 107, n. 8, p. 087205, 2011.
- 155 LEE, E. K.-H. et al. Heisenberg-Kitaev model on the hyperhoneycomb lattice. **Physical Review B**, v. 89, n. 4, p. 045117, 2014.

- 156 TSVELIK, A. M. New fermionic description of quantum spin liquid state. **Physical Review Letters**, v. 69, n. 14, p. 2142–2144, 1992.
- 157 COLEMAN, P.; MIRANDA, E.; TSVELIK, A. Odd-frequency pairing in the Kondo lattice. **Physical Review B**, v. 49, n. 13, p. 8955–8982, 1994.
- 158 BISWAS, R. R. et al. SU(2)-invariant spin liquids on the triangular lattice with spinful Majorana excitations. **Physical Review B**, v. 83, n. 24, p. 245131, 2011.
- 159 HERFURTH, T.; STREIB, S.; KOPIETZ, P. Majorana spin liquid and dimensional reduction in Cs₂CuCl₄. **Physical Review B**, v. 88, n. 17, p. 174404, 2013.
- 160 FIETE, G. A. et al. Topological insulators and quantum spin liquids. **Physica E: low-dimensional systems and nanostructures**, v. 44, n. 5, p. 845 – 859, 2012.
- 161 BASKARAN, G. Novel local symmetries and chiral-symmetry-broken phases in S=1/2 triangular-lattice Heisenberg model. **Physical Review Letters**, v. 63, n. 22, p. 2524–2527, 1989.
- 162 ARMITAGE, N. P.; MELE, E. J.; VISHWANATH, A. Weyl and Dirac semimetals in three-dimensional solids. **Reviews of Modern Physics**, v. 90, n. 1, p. 015001, 2018.
- 163 WILCZEK, F.; ZEE, A. Appearance of gauge structure in simple dynamical systems. **Physical Review Letters**, v. 52, n. 24, p. 2111, 1984.
- 164 ZAK, J. Berry's phase for energy bands in solids. **Physical Review Letters**, v. 62, n. 23, p. 2747–2750, 1989.
- 165 BURKOV, A. A.; HOOK, M. D.; BALENTS, L. Topological nodal semimetals. **Physical Review B**, v. 84, n. 23, p. 235126, 2011.
- 166 CHIU, C.-K.; SCHNYDER, A. P. Classification of reflection-symmetry-protected topological semimetals and nodal superconductors. **Physical Review B**, v. 90, n. 20, p. 205136, 2014.
- 167 YANG, B.-J.; NAGAOSA, N. Classification of stable three-dimensional Dirac semimetals with nontrivial topology. **Nature Communications**, v. 5, p. 4898, 2014. doi.org/10.1038/ncomms5898.
- 168 KIM, F. H. et al. Linear flavor-wave theory for fully antisymmetric SU(N) irreducible representations. **Physical Review B**, v. 96, n. 20, p. 205142, 2017.
- 169 WHITE, R. M.; SPARKS, M.; ORTENBURGER, I. Diagonalization of the antiferromagnetic magnon-phonon interaction. **Physical Review**, v. 139, n. 2A, p. A450–A454, 1965.
- 170 CORBOZ, P. et al. Simultaneous dimerization and SU(4) symmetry breaking of 4-color fermions on the square lattice. **Physical Review Letters**, v. 107, n. 21, p. 215301, 2011.
- 171 DIETL, P.; PIÉCHON, F.; MONTAMBAUX, G. New magnetic field dependence of Landau levels in a graphenelike structure. **Physical Review Letters**, v. 100, n. 23, p. 236405, 2008.
- 172 BANERJEE, S. et al. Tight-binding modeling and low-energy behavior of the semi-Dirac point. **Physical Review Letters**, v. 103, n. 1, p. 016402, 2009.

- 173 BOSSCHE, M. van den et al. Spontaneous plaquette formation in the SU(4) spin-orbital ladder. **Physical Review Letters**, v. 86, n. 18, p. 4124–4127, 2001.
- 174 BIFFIN, A. et al. Unconventional magnetic order on the hyperhoneycomb kitaev lattice in β -Li₂IrO₃: full solution via magnetic resonant x-ray diffraction. **Physical Review B**, v. 90, n. 20, p. 205116, 2014.
- 175 YOSHITAKE, J.; NASU, J.; MOTOME, Y. Fractional spin fluctuations as a precursor of quantum spin liquids: Majorana dynamical mean-field study for the Kitaev model. **Physical Review Letters**, v. 117, n. 15, p. 157203, 2016.
- 176 KNOLLE, J.; BHATTACHARJEE, S.; MOESSNER, R. Dynamics of a quantum spin liquid beyond integrability: the Kitaev-Heisenberg- γ model in an augmented parton mean-field theory. **Physical Review B**, v. 97, n. 13, p. 134432, 2018.
- 177 PUNK, M.; CHOWDHURY, D.; SACHDEV, S. Topological excitations and the dynamic structure factor of spin liquids on the kagome lattice. **Nature Physics**, v. 10, n. 4, p. 289–293, 2014.
- 178 NEGELE, J.; ORLAND, H. **Quantum many-particle systems**. Boulder: Westview Press, 1998.
- 179 COLEMAN, P. Fluctuation–dissipation theorem and linear response theory. In: _____. **Introduction to Many-Body Physics**. Cambridge: Cambridge University Press, 2015. cap. 9, p. 292–331.
- 180 STOKES, H. T.; HATCH, D. M. Couple order parameters in the Landau theory of phase transition in solids. **Phase Transitions**, v. 34, n. 1-4, p. 53–67, 1991.
- 181 HATCH, D. M.; STOKES, H. T. Complete listing of order parameters for a crystalline phase transition: a solution to the generalized inverse Landau problem. **Physical Review B**, v. 65, n. 1, p. 014113, 2001.
- 182 POLYAKOV, A. Thermal properties of gauge fields and quark liberation. **Physics Letters B**, v. 72, n. 4, p. 477 – 480, 1978.
- 183 SENTHIL, T.; FISHER, M. P. A. Z_2 gauge theory of electron fractionalization in strongly correlated systems. **Physical Review B**, v. 62, n. 12, p. 7850–7881, 2000.
- 184 HAVERKORT, M. W. Theory of resonant inelastic x-ray scattering by collective magnetic excitations. **Physical Review Letters**, v. 105, n. 16, p. 167404, 2010.
- 185 JIA, C. et al. Using RIXS to uncover elementary charge and spin excitations. **Physical Review X**, v. 2, n. 6, p. 021020, 2016.
- 186 KRAUSE, M. O.; OLIVER, J. H. Natural widths of atomic k and l levels, $k\alpha$ x-ray lines and several kll auger lines. **Journal of Physical and Chemical Reference Data**, v. 8, n. 2, p. 329–338, 1979.
- 187 LU, L. et al. Magnetism and local symmetry breaking in a Mott insulator with strong spin orbit interactions. **Nature Communications**, v. 8, n. 14407, 2017.
- 188 IWAHARA, N.; VIERU, V.; CHIBOTARU, L. F. **Spin-orbital-lattice entangled states in cubic d^1 double perovskites**. 2018. Available from: <<https://arxiv.org/pdf/1803.06945.pdf>>. Accessible at: 07 June 2018.

- 189 REUTHER, J.; WÖLFLE, P. J_1-J_2 frustrated two-dimensional Heisenberg model: Random phase approximation and functional renormalization group. **Physical Review B**, v. 81, n. 14, p. 144410, 2010.
- 190 REUTHER, J.; THOMALE, R.; TREBST, S. Finite-temperature phase diagram of the Heisenberg-Kitaev model. **Physical Review B**, v. 84, n. 10, p. 100406, 2011.
- 191 REUTHER, J.; THOMALE, R.; RACHEL, S. Spiral order in the honeycomb iridate Li_2IrO_3 . **Physical Review B**, v. 90, n. 10, p. 100405(R), 2014.
- 192 IQBAL, Y. et al. Functional renormalization group for three-dimensional quantum magnetism. **Physical Review B**, v. 94, n. 14, p. 140408, 2016.
- 193 BUESSEN, F. L. et al. Functional renormalization group approach to $SU(N)$ Heisenberg models: real-space renormalization group at arbitrary N . **Physical Review B**, v. 97, n. 6, p. 064415, 2018.
- 194 ROSCHER, D. et al. Functional renormalization group approach to $SU(N)$ Heisenberg models: Momentum-space renormalization group for the large- N limit. **Physical Review B**, v. 97, n. 6, p. 064416, 2018.
- 195 METZNER, W. et al. Functional renormalization group approach to correlated fermion systems. **Reviews of Modern Physics**, v. 84, n. 1, p. 299–352, 2012.
- 196 YAO, H.; ZHANG, S.; KIVELSON, S. Algebraic spin liquid in an exactly solvable spin model. **Physical Review Letters**, v. 102, n. 21, p. 217202, 2009.
- 197 NUSSINOV, Z.; ORTIZ, G. Bond algebras and exact solvability of hamiltonians: spin $s = \frac{1}{2}$ multilayer systems. **Physical Review B**, v. 79, n. 21, p. 214440, 2009.
- 198 WU, C.; AROVAS, D.; HUNG, H.-H. γ -matrix generalization of the Kitaev model. **Physical Review B**, v. 79, n. 13, p. 134427, 2009.
- 199 CHUA, V.; YAO, H.; FIETE, G. A. Exact chiral spin liquid with stable spin Fermi surface on the kagome lattice. **Physical Review B**, v. 83, n. 18, p. 180412, 2011.
- 200 LAI, H.-H.; MOTRUNICH, O. I. $SU(2)$ -invariant Majorana spin liquid with stable parton fermi surfaces in an exactly solvable model. **Physical Review B**, v. 84, n. 8, p. 085141, 2011.
- 201 TIKHONOV, K. S.; FEIGEL'MAN, M. V.; KITAEV, A. Y. Power-law spin correlations in a perturbed spin model on a honeycomb lattice. **Physical Review Letters**, v. 106, n. 6, p. 067203, 2011.
- 202 EDEGGER, B. et al. Particle number renormalization in nearly half-filled Mott Hubbard superconductors. **Physical Review B**, v. 72, n. 13, p. 134504, 2005.

Appendix

APPENDIX A – ANALYSIS OF THE MULTIPOLE OPERATORS UNDER O_h OPERATIONS

In this Appendix, I discuss how the multipoles were organized in terms of irreducible representations of O_h in Table 1. I first discuss the symmetry operations of the group O , the group of all proper symmetries of the cube. They are given by

- E : identity
- $6C_4$ and $3C_4^2$: there are three proper axes of rotation for the cube that are coincident with the axis x , y , and z (see Fig 30a). To understand these operations, consider just the three rotations around the z axis. The rotation of π around this axis is its own inverse and form its own group with the identity (C_4^2 operation). The C_4 operations comprise the $\frac{\pi}{2}$ and $\frac{3\pi}{2}$ rotations around the z axis, which also form a group when conjoined with the identity.
- $6C_2$: These axes go along the lines connecting opposite middle points of the cube edges. There are six of them as shown in Fig 30b.
- $8C_3$: There are four axes connecting opposite vertices of the cube that are related with rotations of $\frac{2\pi}{3}$ and $\frac{4\pi}{3}$, all of them shown in Fig. 30c.

The character table of the group O is given in Table 4. Notice that the position vectors and the rotation operations form a basis of the irreducible representation Γ_4 .

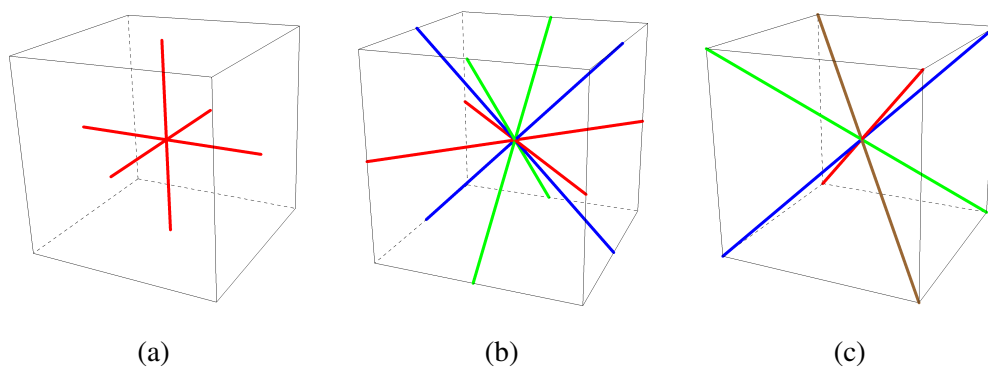


Figure 30 – Axes of symmetry of a cube related to the O symmetry group.

Source: By the author

Table 4 – Character Table of the O group

O	E	$6C_4$	$3C_4^2$	$8C_3$	$6C_2$	
Γ_1	1	1	1	1	1	$x^2 + y^2 + z^2$
Γ_2	1	-1	1	1	-1	
Γ_3	2	0	2	-1	0	$(2z^2 - x^2 - y^2, x^2 - y^2)$
Γ_4	3	1	-1	0	-1	$(x, y, z); (R_x, R_y, R_z)$
Γ_5	3	-1	-1	0	1	(xy, xz, yz)

Source: By the author.

Consider the action of the inversion operation i , whose action on each operations of the group O lead to other operations that constitute the O_h group. For example $iC_4 = S_4$ and $iC_3 = S_3$, which are improper axes of rotation. The combinations iC_4^2 and iC_2 gives rise to the mirror symmetries σ_h and σ_d , respectively. The inversion acts as the identity on the rotation operators. This can be intuitively understood by considering the effect of inversion on the angular momentum operator

$$\mathbf{L} = \mathbf{r} \times \mathbf{p}. \quad (\text{A.1})$$

The inversion reverses both \mathbf{r} and \mathbf{p} , which leads to

$$i : \mathbf{L} \rightarrow \mathbf{L}. \quad (\text{A.2})$$

Another way to see this is by verifying that all the axes of proper rotations are left invariant by the inversion operation. Since the angular momentum operator is even under the inversion operation, it is enough to consider the effect of the symmetry operations of the O cubic group, which will be done in the next section.

For clarity, let us restrict ourselves to one representative of each class defined by the group O . The $\pi/2$ and π rotations will be taken around the z -axis, the C_3 rotation will be around the (111) axis, and the C_2 rotation around the (011) axis. Then I find

$$C_{4(z)} \mathbf{J} C_{4(z)}^{-1} = (-J^y, J^x, J^z) \quad (\text{A.3a})$$

$$C_{4(z)}^2 \mathbf{J} (C_{4(z)}^2)^{-1} = (-J^x, -J^y, J^z) \quad (\text{A.3b})$$

$$C_{3(111)} \mathbf{J} C_{3(111)}^{-1} = (J^z, J^x, J^y) \quad (\text{A.3c})$$

$$C_{2(011)} \mathbf{J} C_{2(011)}^{-1} = (-J^x, J^z, J^y). \quad (\text{A.3d})$$

The traces of the matrices representing $C_{4(z)}$, $C_{4(z)}^2$, $C_{3(111)}$ and $C_{2(011)}$ are exactly the characters of the Γ_4 representation given in Table 4. Therefore, \mathbf{J} expand a basis for the Γ_4 representation. Similarly, consider the octupoles

$$T_a^\alpha = (J^\alpha)^3 - \frac{1}{2} \left[\overline{J^\alpha (J^\beta)^2} + \overline{J^\alpha (J^\gamma)^2} \right], \quad (\text{A.4})$$

where $\epsilon_{\alpha\beta\gamma} = 1$ and the bars over symbols indicate the sum with respect to all the possible permutations. The T_a operators follow the transformations of the \mathbf{J} operator and thus form another basis of the irreducible representation Γ_4 .

Consider now the octupole $\overline{J^x J^y J^z}$, which is proportional to the pseudo-orbital τ^y . Equations A.3 imply that

$$C_{4(z)} \overline{J^x J^y J^z} C_{4(z)}^{-1} = -\overline{J^x J^y J^z} \quad (\text{A.5a})$$

$$C_{4(z)}^2 \overline{J^x J^y J^z} (C_{4(z)}^2)^{-1} = \overline{J^x J^y J^z} \quad (\text{A.5b})$$

$$C_{3(111)} \overline{J^x J^y J^z} C_{3(111)}^{-1} = \overline{J^x J^y J^z} \quad (\text{A.5c})$$

$$C_{2(011)} \overline{J^x J^y J^z} C_{2(011)}^{-1} = -\overline{J^x J^y J^z}. \quad (\text{A.5d})$$

The results above reproduce the characters of the Γ_2 representation given in Table 4. Next, I the quadrupole operators in the Γ_3 representation $(Q_{3z^2-r^2}, Q_{x^2-y^2}) = ([3(J^z)^2 - \mathbf{J}^2] / \sqrt{3}, (J^x)^2 - (J^y)^2)$, which are directly proportional to (τ^z, τ^x) . Using these equivalences, the following equations are derived

$$C_{4(z)} (\tau^z, \tau^x) C_{4(z)}^{-1} = (\tau^z, -\tau^x), \quad (\text{A.6a})$$

$$C_{4(z)}^2 (\tau^z, \tau^x) (C_{4(z)}^2)^{-1} = (\tau^z, \tau^x), \quad (\text{A.6b})$$

$$C_{3(111)} (\tau^z, \tau^x) C_{3(111)}^{-1} = \left(-\frac{1}{2}\tau^z - \frac{\sqrt{3}}{2}\tau^x, \frac{\sqrt{3}}{2}\tau^z - \frac{1}{2}\tau^x \right), \quad (\text{A.6c})$$

$$C_{2(011)} (\tau^z, \tau^x) C_{2(011)}^{-1} = \left(-\frac{1}{2}\tau^z - \frac{\sqrt{3}}{2}\tau^x, -\frac{\sqrt{3}}{2}\tau^z \frac{1}{2}\tau^x \right), \quad (\text{A.6d})$$

which reproduce the characters of the Γ_3 representation. Notice that the 120° compass character of the (τ^z, τ^x) is related with their transformations under rotations.

Lastly, let us discuss the operators in the Γ_5 representation. First, the quadrupoles of this representation transform under the proper rotations of O like

$$C_{4(z)} (\overline{J^y J^z}, \overline{J^z J^x}, \overline{J^x J^y}) C_{4(z)}^{-1} = (\overline{J^z J^x}, -\overline{J^y J^z}, -\overline{J^x J^y}), \quad (\text{A.7a})$$

$$C_{4(z)}^2 (\overline{J^y J^z}, \overline{J^z J^x}, \overline{J^x J^y}) (C_{4(z)}^2)^{-1} = (-\overline{J^y J^z}, -\overline{J^z J^x}, \overline{J^x J^y}), \quad (\text{A.7b})$$

$$C_{3(111)} (\overline{J^y J^z}, \overline{J^z J^x}, \overline{J^x J^y}) C_{3(111)}^{-1} = (\overline{J^x J^y}, \overline{J^y J^z}, \overline{J^z J^x}), \quad (\text{A.7c})$$

$$C_{2(011)} (\overline{J^y J^z}, \overline{J^z J^x}, \overline{J^x J^y}) C_{2(011)}^{-1} = (\overline{J^y J^z}, -\overline{J^x J^y}, -\overline{J^z J^x}). \quad (\text{A.7d})$$

Similarly, the Γ_5 octupoles

$$T_b^\alpha = \frac{\sqrt{15}}{6} \left(\overline{J^\alpha (J^\beta)^2} - \overline{(J^\gamma)^2 J^\alpha} \right) \quad (\text{A.8})$$

transform themselves like

$$C_{4(z)} \mathbf{T}_b C_{4(z)}^{-1} = (T_b^y, -T_b^x, -T_b^z), \quad (\text{A.9a})$$

$$C_{4(z)}^2 \mathbf{T}_b (C_{4(z)}^2)^{-1} = (-T_b^x, -T_b^y, T_b^z), \quad (\text{A.9b})$$

$$C_{3(111)} \mathbf{T}_b C_{3(111)}^{-1} = (T_b^z, T_b^x, T_b^y), \quad (\text{A.9c})$$

$$C_{2(011)} \mathbf{T}_b C_{2(011)}^{-1} = (T_b^x, -T_b^z, -T_b^y), \quad (\text{A.9d})$$

and also reproduce the Γ_5 character table. This finishes the symmetry analysis of the \mathbf{J} multipoles under the cubic rotations.

APPENDIX B – KLEIN TRANSFORMATIONS

Following Ref. (152), I will derive the Klein duality transformation for general graphs with Kitaev γ bond labels and show that it has the structure of the Klein four-group $K \cong \mathbb{Z}_2 \times \mathbb{Z}_2$. The multiplication rules of this abelian group are explicitly given in Table 5.

Consider a lattice or finite graph in any dimension that connects $S = 1/2$ spins, and assume each bond (i, j) carries a Kitaev type label

$$\gamma_{i,j} \in \{\mathbb{I}, x, y, z\}. \quad (\text{B.1})$$

The set $\gamma \in \{x, y, z\}$ corresponds to Kitaev coupling $S_i^\gamma S_j^\gamma$ on that bond, where $\{x, y, z\}$ refers to the orthogonal axes of quantization of the spins. Here, I consider the duality only in the model with nearest neighbor interactions. A label is assigned to each site

$$a_i \in \{\mathbb{I}, X, Y, Z\}. \quad (\text{B.2})$$

This label will specify a rotation by π around the Bloch sphere axis S^a for $a \in \{X, Y, Z\}$, and no rotation for the identity element $a = \mathbb{I}$. Each element will be associated with a sign structure as follows

$$\begin{aligned} g[\mathbb{I}] &= (1, 1, 1), \\ g[X] &= (1, -1, -1), \\ g[Y] &= (-1, 1, -1), \\ g[Z] &= (-1, -1, 1). \end{aligned} \quad (\text{B.3})$$

Notice that both $\gamma_{i,j}$ and a_i may be interpreted as elements of the single set $K = \{\mathbb{I}, X, Y, Z\}$.

The next step is to transform the set K into a group by defining a multiplication rule over it. A possible definition is suggested by the multiplication of the associated sign structure. Take,

Table 5 – Klein four-group multiplication rules.

\times	\mathbb{I}	X	Y	Z
\mathbb{I}	\mathbb{I}	X	Y	Z
X	X	\mathbb{I}	Z	Y
Y	Y	Z	\mathbb{I}	X
Z	Z	Y	X	\mathbb{I}

Source: By the author.

for example, the $g[X]$ signs. We see that

$$\begin{aligned} g[X]g[\mathbb{I}] &= (1, -1, -1) = g[X], \\ g[X]g[X] &= (1, 1, 1) = g[\mathbb{I}], \\ g[X]g[Y] &= (-1, -1, 1) = g[Z], \\ g[X]g[Z] &= (-1, 1, -1) = g[Y]. \end{aligned}$$

Notice that the equations above reproduce the second row of Table 5, and the same procedure can be applied to other g signs. Formally, we define the Klein group product \times and rewrite the equations above like

$$\begin{aligned} X \times \mathbb{I} &= X, \\ X \times X &= \mathbb{I}, \\ X \times Y &= Z, \\ X \times Z &= Y. \end{aligned}$$

The multiplication table can be constructed solely from the equation:

$$X^2 = Y^2 = Z^2 = XYZ = \mathbb{I}, \quad (\text{B.4})$$

with \mathbb{I} being the identity. This abelian group is known as the Klein four-group and is the smallest noncyclic group.

Now, let us turn to the geometrical way of constructing a multiplication between a_i and $\gamma_{i,j}$. Let us fix the values of $\gamma_{i,j}$ and consider an arbitrary choice of a_i for each site. The geometric multiplication $(*)$ of a site i and one of its bonds (i, j) is defined by

$$a_i * \gamma_{i,j} = a_j. \quad (\text{B.5})$$

The Klein group product and the geometrical multiplication $(*)$ for a given choice $\{a_i\}$ are consistent on a bond if they give the same answer, $a_i * \gamma_{i,j} = a_i \times \gamma_{i,j}$. We say the transformation given by site labels $\{a_i\}$ is the Klein transformation if the geometrical multiplication is consistent with Klein group multiplication on every bond in the lattice.

The consistency between the Klein group product and the transformation operators a_i and a_j is given by

$$a_i \times \gamma_{i,j} = a_j, \quad (\text{B.6})$$

or

$$a_i \times a_j = \gamma_{i,j}. \quad (\text{B.7})$$

Consider now the effect of this on a Kitaev-Heisenberg coupling given by $\sum_{\alpha} J_{ij}^{\alpha} S_i^{\alpha} S_j^{\alpha}$. The effect of the transformations a_i and a_j can be written as the following map of the coupling constants:

$$J_{i,j}^{\alpha} \rightarrow g[a_i]_{\alpha} g[a_j]_{\alpha} J_{i,j}^{\alpha} = g[\gamma_{i,j}]_{\alpha} J_{i,j}^{\alpha}. \quad (\text{B.8})$$

Although one can make the geometrical and Klein group multiplication consistent on a particular bond, it seems improbable that it will be consistent in the whole lattice. Eq. (B.6) leads to a simple criterion to ensure the existence of an adequate Klein transformation: any closed loop of the lattice must satisfy

$$a_i = \gamma_{i,j} \times \gamma_{j,l} \times \dots \times \gamma_{k,i} a_i \implies \prod_{l \in \text{loop}} \gamma_l = \mathbb{I}. \quad (\text{B.9})$$

This condition is translated geometrically as follows: a Klein transformation can be defined if any closed loop, containing N_x x bonds, N_y y bonds and N_z z bonds satisfy

$$N_x, N_y, \text{ and } N_z \text{ all even or all odd.} \quad (\text{B.10})$$

APPENDIX C – PSEUDOSPIN AND PSEUDO-ORBITAL OPERATORS IN TERMS OF SU(4) GENERATORS

In this appendix I explicitly list the representations of the pseudospin and pseudo-orbital operators in terms of the S_m^n generators of the SU(4). This list is useful both for the linear-flavor wave theory and the parton mean-field theory with complex fermions.

$$s^x = \frac{1}{2} \sum_{m=1,3} (S_m^{m+1} + S_{m+1}^m), \quad (\text{C.1})$$

$$s^y = \frac{1}{2i} \sum_{m=1,3} (S_m^{m+1} - S_{m+1}^m), \quad (\text{C.2})$$

$$s^z = \frac{1}{2} \sum_{m=1,3} (S_m^m - S_{m+1}^{m+1}), \quad (\text{C.3})$$

$$\tau^x = \frac{1}{2} \sum_{n=1,2} (S_n^{n+2} + S_{n+2}^n), \quad (\text{C.4})$$

$$\tau^y = \frac{1}{2i} \sum_{n=1,2} (S_n^{n+2} - S_{n+2}^n), \quad (\text{C.5})$$

$$\tau^z = \frac{1}{2} \sum_{n=1,2} (S_n^n - S_{n+2}^{n+2}), \quad (\text{C.6})$$

$$s^x \tau^x = \frac{1}{4} (S_1^4 + S_2^3 + h.c.), \quad (\text{C.7})$$

$$s^x \tau^y = \frac{1}{4i} (S_1^4 + S_2^3) + h.c., \quad (\text{C.8})$$

$$s^x \tau^z = \frac{1}{4} (S_1^2 - S_3^4 + h.c.), \quad (\text{C.9})$$

$$s^y \tau^x = \frac{1}{4i} (S_1^4 - S_2^3) + h.c., \quad (\text{C.10})$$

$$s^y \tau^y = \frac{1}{4} (-S_1^4 + S_2^3 + h.c.), \quad (\text{C.11})$$

$$s^y \tau^z = \frac{1}{4i} (S_1^2 - S_3^4) + h.c., \quad (\text{C.12})$$

$$s^z \tau^x = \frac{1}{4} (S_1^3 - S_2^4 + h.c.), \quad (\text{C.13})$$

$$s^z \tau^y = \frac{1}{4i} (S_1^3 - S_2^4) + h.c., \quad (\text{C.14})$$

$$s^z \tau^z = \frac{1}{4} (S_1^1 - S_2^2 - S_3^3 + S_4^4). \quad (\text{C.15})$$

APPENDIX D – SYMMETRY AND TOPOLOGICAL PROPERTIES OF THE CHIRAL SPIN-ORBITAL LIQUID WITH NODAL LINES

There are now enough elements to complete the symmetry analysis of the mean-field theory related with $\mathcal{H}_1(\mathbf{k})$. I can show that the mean-field Hamiltonian preserves a symmetry isomorphic to the O_h group, which were explicitly given in Appendix A. This analysis follows closely the analysis performed in Ref. (15) for weakly correlated topological phases combined with convenient gauge transformations. Consider first the action of the time reversal operator, which conjugates complex numbers and reverses the momentum. The fact that \mathcal{H}_1 is imaginary and $\mathbf{h}(\mathbf{k}) = \mathbf{h}(-\mathbf{k})$ implies:

$$\Theta \mathcal{H}_1(\mathbf{k}) \Theta^{-1} = \mathcal{H}_1^*(-\mathbf{k}) = -\mathcal{H}_1(\mathbf{k}). \quad (\text{D.1})$$

The parity operator can be defined as the reflection by the mirror plane perpendicular to δ_3 . Its action on momentum space is given by $P : k_x \rightarrow k_x, k_y \rightarrow -k_z, k_z \rightarrow -k_y$. Its action in the sublattice space is given by the matrix

$$P = \begin{pmatrix} 0 & 0 & 1 & 0 \\ 0 & 1 & 0 & 0 \\ 1 & 0 & 0 & 0 \\ 0 & 0 & 0 & 1 \end{pmatrix}. \quad (\text{D.2})$$

The following gauge transformation that changes the sign of fermions on the $X = 1$ sublattices can be also applied

$$G_P = \begin{pmatrix} 1 & & & \\ & -1 & & \\ & & 1 & \\ & & & 1 \end{pmatrix} \quad (\text{D.3})$$

$$(PG_P)^{-1} \mathcal{H}_1(P\mathbf{k}) PG_P = -\mathcal{H}_1(\mathbf{k}). \quad (\text{D.4})$$

Combining the effects of time reversal and parity, one can show that $P\Theta G_P$ is a symmetry of the Hamiltonian (15)

$$(P\Theta G_P)^{-1} \mathcal{H}_1(P\mathbf{k}) P\Theta G_P = \mathcal{H}_1(\mathbf{k}). \quad (\text{D.5})$$

I consider now the C_3 rotation about a (111) axis leaving the $X = 1$ site invariant while permuting all other sublattices

$$C_3 = \begin{pmatrix} 1 & 0 & 0 & 0 \\ 0 & 0 & 0 & 1 \\ 0 & 1 & 0 & 0 \\ 0 & 0 & 1 & 0 \end{pmatrix}. \quad (\text{D.6})$$

Its effect on momentum is given by $R_3 : k_x \rightarrow k_z, k_y \rightarrow k_x, k_z \rightarrow k_y$. In this case, no gauge transformation is required and the following equation is immediately obtained:

$$C_3^{-1} \mathcal{H}_1(R_3 \mathbf{k}) C_3 = \mathcal{H}_1(\mathbf{k}). \quad (\text{D.7})$$

The C_2 rotation along the z axis exchanges the sites on sublattices 1 and 2, and the sublattices 3 and 4, and is given by the following matrix

$$C_2 = \begin{pmatrix} 0 & 1 & & \\ 1 & 0 & & \\ & & 0 & 1 \\ & & 1 & 0 \end{pmatrix}. \quad (\text{D.8})$$

The action of this rotation on momentum leaves k_z invariant while reversing the other components $R_2 : k_x \rightarrow -k_x, k_y \rightarrow -k_y$. Combined with the following gauge transformation

$$G_2 = \begin{pmatrix} 1 & & & \\ & -1 & & \\ & & 1 & \\ & & & -1 \end{pmatrix}, \quad (\text{D.9})$$

it is shown that

$$(C_2 G_2)^{-1} \mathcal{H}_1(R_2 \mathbf{k}) (C_2 G_2) = \mathcal{H}_1(\mathbf{k}). \quad (\text{D.10})$$

Lastly, I consider the effect of C_4 rotations along the z axis and show how they can account for the twofold degeneracy of the Majorana bands. I consider first a rotation C_4 going through an A site, whose action on the sublattice space is given by

$$C_4 = \begin{pmatrix} 1 & 0 & & \\ 0 & 1 & & \\ & & 0 & -1 \\ & & 1 & 0 \end{pmatrix}. \quad (\text{D.11})$$

In momentum space, $R_4 : k_x \rightarrow k_y, k_y \rightarrow -k_x$. Combining the action of C_4 with the gauge transformation

$$G_4 = \begin{pmatrix} 1 & & & \\ & -1 & & \\ & & -1 & \\ & & & 1 \end{pmatrix} \quad (\text{D.12})$$

leads to

$$(C_4 G_4)^{-1} \mathcal{H}_1(R_4 \mathbf{k}) (C_4 G_4) = -\mathcal{H}_1(\mathbf{k}). \quad (\text{D.13})$$

The C_4 inverts the chirality of the Ansatz, a feature that can be visualized in Fig. 14b. It is then easy to verify that $C_4 G_4 \Theta$ is a symmetry of the Hamiltonian. Consider now another C'_4 rotation, but this time exchanging A and B sublattices:

$$C'_4 = \begin{pmatrix} 0 & -1 & & \\ 1 & 0 & & \\ & & 1 & 0 \\ & & 0 & 1 \end{pmatrix}. \quad (\text{D.14})$$

Let us also define it to be a rotation in the opposite direction of R_4 , such that its action in momentum space reads $R'_4 : k_x \rightarrow -k_y, k_y \rightarrow k_x$. This also implies that $R'_4 = (R_4)^{-1}$. It is easy to check that $M = C_4 C'_4$ commutes $M^{-1} \mathcal{H}_1(\mathbf{k}) M = \mathcal{H}_1(\mathbf{k})$, and obeys $M^2 = -\mathbb{I}$. This also implies that $\mathcal{H}_1(\mathbf{k})$ can be block diagonalized by sectors labeled by the eigenvalue $\pm i$ of the matrix M :

$$U_M^\dagger \mathcal{H}_1(\mathbf{k}) U_M = \begin{pmatrix} \tilde{\boldsymbol{\sigma}} \cdot \mathbf{h}(\mathbf{k}) & \\ & -\tilde{\boldsymbol{\sigma}} \cdot \mathbf{h}(\mathbf{k}) \end{pmatrix}, \quad (\text{D.15})$$

where $\tilde{\boldsymbol{\sigma}} \equiv (-\sigma^z, \sigma^y, \sigma^x)$ and U_M is the unitary matrix that diagonalizes M . This block diagonalization makes it clear that $\mathcal{H}_1(\mathbf{k})$ displays twofold degeneracy with eigenvalues $\pm |\mathbf{h}(\mathbf{k})|$. Two degenerate states can be distinguished by the eigenvalue ± 1 of the matrix iM , in analogy to the chirality of Weyl fermions in massless Dirac equations. (162)

The band dispersion of Majorana fermions is also the analogous to the ones observed in line-node semimetals and superconductors. (165–167) The first step to understand this point is to note that the Fermi surface is constituted by nodal lines along the edges of the cubic Brillouin zone and are parameterized by, e.g., $\mathbf{k} = (\pi, \pi, k_z)$. The matrix $\mathcal{H}_1(\mathbf{k})$ in the neighborhood of these lines ($\mathbf{k} = (\pi + p_x, \pi + p_y, k_z)$ with $p_x, p_y \ll 1$) gives $\mathcal{H}_1(\mathbf{k}) \approx 2 \cos(k_z/2) (p_x \Sigma^y + p_y \Sigma^z)$. This yields a linear dispersion at low energies with k_z dependent velocity $\epsilon_\pm(\mathbf{k}) \approx 2 \cos(k_z/2) \sqrt{p_x^2 + p_y^2}$. The exception to this behavior is the point of intersection of the three nodal lines $R = (\pi, \pi, \pi)$. At this point, the band touching is quadratic and display an anisotropic dispersion $\epsilon_\pm(\mathbf{k}) \approx \sqrt{p_x^2 p_y^2 + p_y^2 p_z^2 + p_z^2 p_x^2}$.

The nodal lines described above can be characterized as topological defects with an associated generalized Berry phase, also known as a Zak phase. (163, 164) To verify this result, let us call the $\mathcal{H}_1(\mathbf{k})$ eigenstates by $\tilde{\zeta}_{\mathbf{k}\lambda}$ and relate them with the sublattice operators by an unitary matrix $U_{\mathbf{k}}$:

$$\zeta_{\mathbf{k}X} = \sum_{\lambda=1}^4 (U_{\mathbf{k}})_{X\lambda} \tilde{\zeta}_{\mathbf{k}\lambda}, \quad (\text{D.16})$$

in which $\lambda = 1, \dots, 4$ is the band index. One can define an SU(2) Berry connection $A_{\lambda\lambda'}^a$ out of the two bands of positive energy eigenstates by

$$A_{\lambda\lambda'}^a(\mathbf{k}) = i \left\langle \tilde{\zeta}_\lambda(\mathbf{k}) \left| \partial_{k_a} \tilde{\zeta}_{\lambda'}(\mathbf{k}) \right. \right\rangle. \quad (\text{D.17})$$

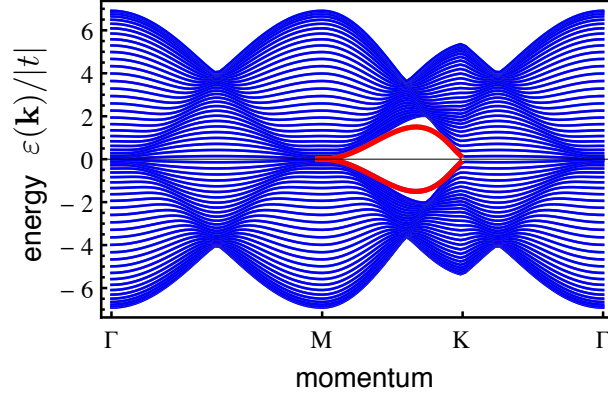


Figure 31 – Spectrum of the chiral spin-orbital liquid Ansatz for double perovskites in a slab geometry with open boundary conditions in the (111) direction. The surface states are indicated by the thick red lines in the middle of the gap between the M and K points.

Source: NATORI; ANDRADE; MIRANDA; PEREIRA (4)

The states $|\tilde{\zeta}_\lambda(\mathbf{k})\rangle$ and $|\tilde{\zeta}_{\lambda'}(\mathbf{k})\rangle$ are degenerate, but orthogonal, vectors that are also tuned to diagonalize $A^z(\mathbf{k})$. The Zak phase is defined by the Wilson loop

$$\Phi = \mathcal{P} \exp \left[-i \oint dk_a A^a(\mathbf{k}) \right], \quad (\text{D.18})$$

where \mathcal{P} denotes path ordering. I parametrize \mathbf{k} to be in a small neighborhood of the nodal line $\mathbf{k} \approx (\pi + \epsilon \cos \alpha, \pi + \epsilon \sin \alpha, k_z)$, with $\alpha \in [-\pi, \pi)$ and $\epsilon \ll 1$. The following approximation is valid in this case

$$A^x = -\frac{1}{2\epsilon} \sin \alpha \sigma^y + \mathcal{O}(\epsilon^0), \quad A^y = \frac{1}{2\epsilon} \cos \alpha \sigma^y + \mathcal{O}(\epsilon^0), \quad (\text{D.19})$$

which is precisely the ϵ dependence of a vortex line. The phase $\Phi = -\mathbb{I}$ was found, which is equivalent to a π Berry phase. Furthermore, I could also verify the presence of protected state surface states by calculating the spectrum of the mean-field Hamiltonian with open boundary conditions in the (111) direction (Fig. 31). There appear two pairs of doubly degenerate bands separated from the continuum, with dispersions terminating at the projection of the nodal lines. Remarkably, the positive-energy surface states are spatially separated from the negative energy ones. This is a direct manifestation of the breaking of inversion symmetry.

APPENDIX E – VARIATIONAL MONTE CARLO CALCULATION OF THE CHIRAL SPIN-ORBITAL LIQUID

As stated in Subsection 3.3.3, the derivation of the spin-orbital model was incomplete in Ref. (4). The SU(2)-symmetric Hamiltonian in this limit reads

$$\mathcal{H}_{\text{SU}(2)} = \frac{4}{9} J_{\text{eff}} \sum_{\langle ij \rangle_\gamma} \left(\mathbf{s}_i \cdot \mathbf{s}_j - \frac{1}{4} \right) \left(\frac{1}{2} - \tau_i^{\alpha\beta} \right) \left(\frac{1}{2} - \tau_j^{\alpha\beta} \right), \quad (\text{E.1})$$

and distinguishes from Eq. (3.52) by the sign factor of the spin-independent terms. The VMC computation of the chiral spin orbital liquid should be redone. Nevertheless, this computation is useful to show how VMC can be performed for $J = 3/2$ QSOLs out of the special case of the SU(4) Heisenberg model.

We have to enforce the local constraint in Eq. (4.6) exactly using the VMC algorithm. Just like in the SU(4) case, we start by rewriting the Majorana fermions in terms of three complex fermions (41)

$$c_i^\dagger = \frac{1}{2} (\eta_i^2 + i\theta_i^2), \quad d_i^\dagger = \frac{1}{2} (\eta_i^1 + i\eta_i^3), \quad f_i^\dagger = \frac{1}{2} (\theta_i^1 + i\theta_i^3). \quad (\text{E.2})$$

The local constraint is now translated into the fact that a given site must have an even number of Dirac fermions. In this case there are three possible states at each site defined as

$$|x_i\rangle = c_i^\dagger d_i^\dagger |0\rangle, \quad |y_i\rangle = d_i^\dagger f_i^\dagger |0\rangle, \quad |z_i\rangle = f_i^\dagger c_i^\dagger |0\rangle \quad (\text{E.3})$$

Given a real space configuration specified by the locations of the doubly occupied sites, $X \equiv \{x_i\}$, $Y \equiv \{y_i\}$, $Z \equiv \{z_i\}$, the wave function assigns an amplitude $\Psi(\{x_i\}, \{y_j\}, \{z_m\})$ similar to Eq. (4.71). The local constraint only fixes the parity of the number of fermions but not the number itself. Moreover, our Hamiltonian contains terms which not only create/annihilate two particles, e.g. $|x_i\rangle \leftrightarrow |0\rangle$, but also terms which preserve the total number of fermions while changing the number of each of the three individual fermionic flavors, e.g. $|x_i\rangle \leftrightarrow |y_i\rangle$. It is possible to write down a projected wave functions with varying particle number and perform the computation of observables with VMC. (202) However, this work was not done for the sake of computational simplicity. Instead, the ground state wave function was further restricted and we enforced a condition in which each state occupies $N/4$ distinct sites ($\{x_i\} = \{x_1, x_2, \dots, x_{N/4}\}$, etc).

The mean-field Hamiltonian was defined using the same order parameters written in Eq. (4.15) but applied to Eq. (E.1). The mean field Hamiltonian in terms of the three complex

fermions in Eq. (E.2) is given by

$$\begin{aligned}
\mathcal{H}_{MF} = & -\frac{NJ}{6} + \frac{J}{36} \sum_{\langle jl \rangle \in \alpha} \left[(3u_{jl}^2 + 3\bar{w}_{jl}^\alpha u_{jl} - w_{jl}^\alpha v_{jl}) + i(4u_{jl} + 2\bar{w}_{jl}^\alpha) d_j^\dagger d_l \right. \\
& + i(2u_{jl} + \bar{w}_{jl}^\alpha - w_{jl}^\alpha) c_j^\dagger c_l + i(2u_{jl} + \bar{w}_{jl}^\alpha + w_{jl}^\alpha) c_j^\dagger c_l^\dagger + i(3u_{jl} - v_{jl}) f_j^\dagger f_l + \text{h.c.} \left. \right] \\
& - \frac{J}{36} \sum_{\langle jl \rangle \in XY} \left[i(3u_{jl} + v_{jl}) f_j^\dagger f_l^\dagger + \text{h.c.} \right] + \frac{J}{36} \sum_{\langle jl \rangle \in YZ} \left[i(3u_{jl} e^{i\pi/3} + v_{jl} e^{-2i\pi/3}) f_j^\dagger f_l^\dagger + \text{h.c.} \right] \\
& + \frac{J}{36} \sum_{\langle jl \rangle \in XZ} \left[i(3u_{jl} e^{i\pi/3} - v_{jl} e^{-2i\pi/3}) f_j^\dagger f_l^\dagger + \text{h.c.} \right]. \tag{E.4}
\end{aligned}$$

The three fermion flavors are decoupled and we may thus write the mean-field wave function as a product of three Slater determinants. The d -fermion sector of the Hamiltonian in E.4 corresponds to free fermions and thus their mean-field ground state is obtained by filling up the states with negative energy. For the c and f -fermions, the Hamiltonian is BCS-like and their ground state is given by the vacuum of their respective Bogoliubov quasiparticles. (46) The different status of the d fermion is expected from symmetry: the hidden global SU(2) symmetry of the original Hamiltonian implies the global U(1) symmetry corresponding to the conservation of the total number of Dirac fermions defined by a combination of η Majorana fermions. On the other hand, there is no continuous symmetry associated with θ Majorana fermions; as a result, the total number of c and f fermions is not conserved. The need to work with BCS-type wave functions in our case should be contrasted with the case of SU(4) symmetric models (41), where the SU(4) symmetry implies the conservation of the numbers of all three flavors of Dirac fermions.

After constructing the mean-field wave function, a variational Monte Carlo calculation was implemented to calculate the Gutzwiller-projected ground state energy $E_{\text{gs}}^{\text{VMC}}$. The algorithm works exactly in the same way specified in Subsection 4.2.3 since we restricted ourselves to real space configurations in which each state occupies $N/4$ sites. The results were obtained for lattices of size $N = 4L^3$ with $L = 4, 6,$ and 8 . We find that the change in the ground state energy with N is smaller than the Monte Carlo error bars for the system sizes considered here. The results for $L = 8$ were then taken as the converged ones.

The ground state energy $E_{\text{gs}}^{\text{VMC}}$ was calculated for the wavefunctions obtained from the two sets of mean-field parameters quoted in this Appendix. These two sets of parameters were obtained from self-consistency of the mean-field theory. For $u = v = 0.258$, $\bar{w} = 0.317$, and $w = -0.081$ we obtain $E_{\text{gs}}^{\text{VMC}} = -0.39(1) NJ$. As for $u = -v = 0.258$, $\bar{w} = 0.318$, and $w = 0.161$ we obtain $E_{\text{gs}}^{\text{VMC}} = -0.40(1) NJ$. The Gutzwiller projection decreases the mean-field energy down to values comparable to a VBS state computed for Eq. (E.1) ($E_{\text{VBS}} = -0.417 NJ$). (29)

APPENDIX F – COMPUTATION OF PARTON MEAN-FIELD CORRELATION FUNCTIONS

In this appendix, I outline the calculation of finite-temperature spectral functions such as the one in Eq. (5.20). Consider the correlation function

$$\chi_{lm}(\tau) = \langle T_\tau \hat{O}_l(\tau) \hat{O}_m(0) \rangle, \quad (\text{F.1})$$

where \hat{O}_l is a local operator acting on the $j = 3/2$ subspace associated with site l , $\hat{O}_l(\tau) = e^{H_{\text{eff}}\tau} \hat{O}_l e^{-H_{\text{eff}}\tau}$ is the operator evolved in imaginary time, T_τ denotes time ordering, and $\langle \cdot \rangle = \text{Tr}(\rho \cdot)$ denotes the thermal average with density matrix $\rho = e^{-\beta H_{\text{eff}}}/Z$.

Quite generally, the local operator \hat{O}_l can be written as a combination of Majorana fermion bilinears, $\zeta_l^a \zeta_l^b$, with $\zeta^a \in \{\eta^a, \theta^a\}$. Let us illustrate the procedure by taking

$$\hat{O}_l = -i\eta_l^1 \eta_l^2 = 2s_l^z. \quad (\text{F.2})$$

Within the mean-field approximation, the correlation function can be written as

$$\chi_{lm}(\tau) = \mathcal{G}_{ml}^{12}(-\tau) \mathcal{G}_{lm}^{21}(\tau) - \mathcal{G}_{ml}^{11}(-\tau) \mathcal{G}_{lm}^{22}(\tau), \quad (\text{F.3})$$

where

$$\mathcal{G}_{lm}^{ab}(\tau) = -\langle T_\tau \eta_l^a(\tau) \eta_m^b(0) \rangle \quad (\text{F.4})$$

is the noninteracting fermion Green's function. If \mathbf{R}_l belongs to the X sublattice, $X = 1, \dots, 4$, and \mathbf{R}_m to the Y sublattice, we can write for $0 < \tau < \beta$ [using momentum conservation and Eq. (D.16)]

$$\begin{aligned} \mathcal{G}_{lm}^{ab}(\tau) = & -\frac{8}{N} \sum_{\mathbf{k} \in \frac{1}{2}BZ} \sum_{\lambda} \left[(U_{\mathbf{k}})_{X\lambda} \left(U_{\mathbf{k}}^\dagger \right)_{\lambda Y} \langle \eta_{\mathbf{k}\lambda}^a \eta_{-\mathbf{k}\lambda}^b \rangle e^{i\mathbf{k} \cdot (\mathbf{R}_l - \mathbf{R}_m)} e^{-\epsilon_{\mathbf{k}\lambda}^{(\eta)} \tau} \right. \\ & \left. + (U_{\mathbf{k}})_{Y\lambda} \left(U_{\mathbf{k}}^\dagger \right)_{\lambda X} \langle \eta_{-\mathbf{k}\lambda}^a \eta_{\mathbf{k}\lambda}^b \rangle e^{-i\mathbf{k} \cdot (\mathbf{R}_l - \mathbf{R}_m)} e^{\epsilon_{\mathbf{k}\lambda}^{(\eta)} \tau} \right] \end{aligned} \quad (\text{F.5})$$

The thermal average yields

$$\langle \eta_{\mathbf{k}\lambda}^a \eta_{-\mathbf{k}\lambda}^b \rangle = \delta^{ab} n_F(-\epsilon_{\mathbf{k}\lambda}^{(\eta)}). \quad (\text{F.6})$$

Taking the Fourier transform of Eq. (F.5), we obtain

$$\begin{aligned} \mathcal{G}(\mathbf{k}, \omega_n) &= \int_0^\beta d\tau e^{i\omega_n \tau} \frac{1}{N} \sum_{l,m} e^{-i\mathbf{k} \cdot (\mathbf{R}_l - \mathbf{R}_m)} \mathcal{G}_{lm}^{11}(\tau) \\ &= \frac{1}{2} \sum_{X,Y} \frac{(U_{\mathbf{k}})_{X\lambda} \left(U_{\mathbf{k}}^\dagger \right)_{\lambda Y}}{i\omega_n - \epsilon_{\mathbf{k}\lambda}^{(\eta)}} \end{aligned} \quad (\text{F.7})$$

where $\omega_n = (2n + 1)\pi/\beta$, $n \in \mathbb{Z}$, are fermionic Matsubara frequencies.

Similarly, we obtain the Fourier transform of the correlation in Eq. (F.3):

$$\chi(\mathbf{q}, \omega_m) = \frac{1}{N} \sum_{\mathbf{k} \in \frac{1}{2}\text{BZ}} \sum_{\lambda_1, \lambda_2} \left\{ \begin{aligned} & \frac{\mathcal{F}_{\lambda_1 \lambda_2}^{(1)}(\mathbf{k}, \mathbf{q}) \left[n_F(\epsilon_{\mathbf{k}-\mathbf{q}, \lambda_1}^{(\eta)}) - n_F(\epsilon_{\mathbf{k} \lambda_2}^{(\eta)}) \right]}{i\omega_m - \epsilon_{\mathbf{k} \lambda_2}^{(\eta)} + \epsilon_{\mathbf{k}-\mathbf{q}, \lambda_1}^{(\eta)}} \\ & + \frac{\mathcal{F}_{\lambda_1 \lambda_2}^{(2)}(\mathbf{k}, \mathbf{q}) \left[n_F(-\epsilon_{-\mathbf{k}+\mathbf{q}, \lambda_1}^{(\eta)}) - n_F(\epsilon_{\mathbf{k} \lambda_2}^{(\eta)}) \right]}{i\omega_m - \epsilon_{\mathbf{k} \lambda_2}^{(\eta)} - \epsilon_{-\mathbf{k}+\mathbf{q}, \lambda_1}^{(\eta)}} \\ & + \frac{\mathcal{F}_{\lambda_1 \lambda_2}^{(3)}(\mathbf{k}, \mathbf{q}) \left[n_F(\epsilon_{\mathbf{k}, \lambda_2}^{(\eta)}) - n_F(\epsilon_{\mathbf{k}+\mathbf{q}, \lambda_1}^{(\eta)}) \right]}{i\omega_m - \epsilon_{\mathbf{k}+\mathbf{q}, \lambda_1}^{(\eta)} + \epsilon_{\mathbf{k}, \lambda_2}^{(\eta)}} \\ & + \frac{\mathcal{F}_{\lambda_1 \lambda_2}^{(4)}(\mathbf{k}, \mathbf{q}) \left[n_F(\epsilon_{\mathbf{k}, \lambda_2}^{(\eta)}) - n_F(-\epsilon_{-\mathbf{k}-\mathbf{q}, \lambda_1}^{(\eta)}) \right]}{i\omega_m + \epsilon_{-\mathbf{k}-\mathbf{q}, \lambda_1}^{(\eta)} + \epsilon_{\mathbf{k}, \lambda_2}^{(\eta)}} \end{aligned} \right\} \quad (\text{F.8})$$

where $\omega_m = 2\pi m/\beta$, $m \in \mathbb{Z}$, are bosonic Matsubara frequencies. The form factors are given by

$$\begin{aligned} \mathcal{F}_{\lambda_1 \lambda_2}^{(1)}(\mathbf{k}, \mathbf{q}) &= \left| \sum_X e^{i\mathbf{G} \cdot \delta_X} \left(U_{\mathbf{k}-\mathbf{q}+\mathbf{G}}^\dagger \right)_{\lambda_1 X} (U_{\mathbf{k}})_{X \lambda_2} \right|^2, \\ \mathcal{F}_{\lambda_1 \lambda_2}^{(2)}(\mathbf{k}, \mathbf{q}) &= \left| \sum_X e^{i\mathbf{G} \cdot \delta_X} (U_{-\mathbf{k}+\mathbf{q}+\mathbf{G}})_{X \lambda_1} (U_{\mathbf{k}})_{X \lambda_2} \right|^2, \\ \mathcal{F}_{\lambda_1 \lambda_2}^{(3)}(\mathbf{k}, \mathbf{q}) &= \left| \sum_X e^{i\mathbf{G} \cdot \delta_X} \left(U_{\mathbf{k}}^\dagger \right)_{\lambda_2 X} (U_{\mathbf{k}+\mathbf{q}+\mathbf{G}})_{X \lambda_1} \right|^2, \\ \mathcal{F}_{\lambda_1 \lambda_2}^{(4)}(\mathbf{k}, \mathbf{q}) &= \left| \sum_X e^{i\mathbf{G} \cdot \delta_X} \left(U_{-\mathbf{k}-\mathbf{q}+\mathbf{G}}^\dagger \right)_{\lambda_1 X} \left(U_{\mathbf{k}}^\dagger \right)_{\lambda_2 X} \right|^2, \end{aligned} \quad (\text{F.9})$$

where $\mathbf{G} = 2\pi(n_x, n_y, n_z)$ with $n_a \in \mathbb{Z}$ are reciprocal lattice vectors chosen such that the momenta $\pm \mathbf{k} \pm \mathbf{q} + \mathbf{G}$ in each form factor lies in $\frac{1}{2}\text{BZ}$.

After an analytical continuation $i\omega_m \rightarrow \omega + i0^+$, we can take the imaginary part of the retarded correlation function $\chi''(\mathbf{q}, \omega)$ in a standard way. In the regime $\beta\omega \ll 1$, we can approximate the factors of Fermi-Dirac distributions using $n_F(\epsilon + \omega) - n_F(\epsilon) \approx \omega dn_F/d\epsilon$. We then obtain the expression for the contribution from the η fermions to the spin-lattice relaxation rate

$$\begin{aligned}
\left(\frac{1}{T_1}\right)_\eta &\propto \frac{\pi}{4N} \sum_{\lambda_1, \lambda_2} \sum_{\mathbf{k} \in \frac{1}{2}\text{BZ}} \sum_{\mathbf{q} \in \text{BZ}} \frac{|A(\mathbf{q})|^2}{\cosh^2\left(\beta\epsilon_{\mathbf{k}\lambda_2}^{(\eta)}/2\right)} \times \\
&\times \left[\mathcal{F}_{\lambda_1\lambda_2}^{(1)}(\mathbf{k}, \mathbf{q}) \delta(\epsilon_{\mathbf{k}-\mathbf{q}, \lambda_1}^{(\eta)} - \epsilon_{\mathbf{k}\lambda_2}^{(\eta)}) \right. \\
&+ \mathcal{F}_{\lambda_1\lambda_2}^{(2)}(\mathbf{k}, \mathbf{q}) \delta(\epsilon_{-\mathbf{k}+\mathbf{q}, \lambda_1}^{(\eta)} + \epsilon_{\mathbf{k}\lambda_2}^{(\eta)}) \\
&+ \mathcal{F}_{\lambda_1\lambda_2}^{(3)}(\mathbf{k}, \mathbf{q}) \delta(\epsilon_{\mathbf{k}+\mathbf{q}, \lambda_1}^{(\eta)} - \epsilon_{\mathbf{k}\lambda_2}^{(\eta)}) \\
&\left. + \mathcal{F}_{\lambda_1\lambda_2}^{(4)}(\mathbf{k}, \mathbf{q}) \delta(\epsilon_{-\mathbf{k}-\mathbf{q}, \lambda_1}^{(\eta)} + \epsilon_{\mathbf{k}, \lambda_2}^{(\eta)}) \right]. \tag{F.10}
\end{aligned}$$

Eq. (F.10) can be further simplified since $|\epsilon_{\mathbf{k}\lambda_i}^{(\eta)}| = |\epsilon_{\mathbf{k}\lambda_j}^{(\eta)}|$ for $\lambda_i, \lambda_j = 1, \dots, 4$ (see Eq. (4.30)). For $\mathcal{F}_{\lambda_1\lambda_2}^{(1)}(\mathbf{k}, \mathbf{q})$, the sum over eigenstates yields

$$\begin{aligned}
\sum_{\lambda_1, \lambda_2} \mathcal{F}_{\lambda_1\lambda_2}^{(1)}(\mathbf{k}, \mathbf{q}) \delta(\epsilon_{\mathbf{k}-\mathbf{q}, \lambda_1}^{(\eta)} - \epsilon_{\mathbf{k}\lambda_2}^{(\eta)}) &= 2\mathcal{F}^\eta(\mathbf{k}, \mathbf{k} - \mathbf{q}) \\
&\times \delta(|\epsilon_{\mathbf{k}-\mathbf{q}}^{(\eta)}| - |\epsilon_{\mathbf{k}}^{(\eta)}|), \tag{F.11}
\end{aligned}$$

where

$$\mathcal{F}^\eta(\mathbf{k}, \mathbf{k} - \mathbf{q}) = 1 + \frac{\mathbf{h}(\mathbf{k}) \cdot \mathbf{h}(\mathbf{k} - \mathbf{q})}{|\mathbf{h}(\mathbf{k})||\mathbf{h}(\mathbf{k} - \mathbf{q})|}. \tag{F.12}$$

The expressions obtained for other sums differ from (F.11) only by the combination of vectors \mathbf{k} and \mathbf{q} . Eq. (F.12) is the form factor \mathcal{F}^η stated in Eq. (5.22). Notice that the reciprocal lattice vector \mathbf{G} does not appear in this final expression.

From $\chi(\mathbf{q}, \omega)$ we can also recover the RIXS dynamical structure factor of s^z . Taking the zero temperature limit, we find

$$\begin{aligned}
\lim_{T \rightarrow 0^+} \chi''(\mathbf{q}, \omega) &\propto \frac{\pi}{4N} \sum_{\lambda_1, \lambda_2} \sum_{\mathbf{k} \in \frac{1}{2}\text{BZ}} \sum_{\mathbf{q} \in \text{BZ}} \sum_i \\
&\times \mathcal{F}_{\lambda_1\lambda_2}^{(i)}(\mathbf{k}, \mathbf{q}) \delta_{\lambda_1\lambda_2}^{(i)}(\omega, \mathbf{k}, \mathbf{q}), \tag{F.13}
\end{aligned}$$

in which

$$\begin{aligned}
\delta_{\lambda_1\lambda_2}^{(1)}(\omega, \mathbf{k}, \mathbf{q}) &= \Theta(-\epsilon_{\lambda_1})\Theta(\epsilon_{\lambda_2})\delta(\omega - (\epsilon_{\mathbf{k}\lambda_2}^{(\eta)} - \epsilon_{\mathbf{k}-\mathbf{q}, \lambda_1}^{(\eta)})), \\
\delta_{\lambda_1\lambda_2}^{(2)}(\omega, \mathbf{k}, \mathbf{q}) &= \Theta(\epsilon_{\lambda_1})\Theta(\epsilon_{\lambda_2})\delta(\omega - (\epsilon_{-\mathbf{k}+\mathbf{q}, \lambda_1}^{(\eta)} + \epsilon_{\mathbf{k}\lambda_2}^{(\eta)})), \\
\delta_{\lambda_1\lambda_2}^{(3)}(\omega, \mathbf{k}, \mathbf{q}) &= \Theta(\epsilon_{\lambda_1})\Theta(-\epsilon_{\lambda_2})\delta(\omega - (\epsilon_{\mathbf{k}+\mathbf{q}, \lambda_1}^{(\eta)} - \epsilon_{\mathbf{k}\lambda_2}^{(\eta)})), \\
\delta_{\lambda_1\lambda_2}^{(4)}(\omega, \mathbf{k}, \mathbf{q}) &= \Theta(-\epsilon_{\lambda_1})\Theta(-\epsilon_{\lambda_2})\delta(\omega + \epsilon_{-\mathbf{k}-\mathbf{q}, \lambda_1}^{(\eta)} + \epsilon_{\mathbf{k}, \lambda_2}^{(\eta)}). \tag{F.14}
\end{aligned}$$

Once again, summing over the eigenstates, we find for $\omega = 0$

$$\begin{aligned}
\sum_{\lambda_1, \lambda_2} \mathcal{F}_{\lambda_1\lambda_2}^{(1)}(\mathbf{k}, \mathbf{q}) \delta_{\lambda_1\lambda_2}^{(1)}(0, \mathbf{k}, \mathbf{q}) &= \left(1 - \frac{\mathbf{h}(\mathbf{k}) \cdot \mathbf{h}(\mathbf{k} - \mathbf{q})}{|\mathbf{h}(\mathbf{k})||\mathbf{h}(\mathbf{k} - \mathbf{q})|}\right) \\
&\times \delta(|\epsilon_{\mathbf{k}-\mathbf{q}}^{(\eta)}| - |\epsilon_{\mathbf{k}}^{(\eta)}|), \tag{F.15}
\end{aligned}$$

with similar expressions for other summations. The expression in brackets is just the form factor written in Eq. (5.45). As stated in the main text, it is clear that this form factor will vanish when $\mathbf{q} = 0$.

The procedure outlined in this appendix can be generalized for the θ fermions as well. In particular, if $\hat{O}_l = -i\eta_l^a \theta_l^2$, the corresponding form factor of a RIXS experiment will be exactly the one given in Eq. (F.15). For operators involving the fermions θ^1 and θ^3 , it is not possible to find exact expressions to the form factors, since there is no closed form to the matrix $V_{\mathbf{k}}$ (see Eq. 4.34). The response functions must then be computed numerically.

APPENDIX G – RIXS SCATTERING OPERATORS UNDER TETRAGONAL DISTORTION

The combined effect of the spin-orbit coupling and the distortion on the d orbitals is modeled by the Hamiltonian

$$H_{\text{ion}} = -\lambda \mathbf{l} \cdot \mathbf{S} + \delta (l^z)^2, \quad (\text{G.1})$$

where δ is the energy scale associated with the distortion. Notice that the time-reversal symmetry of H_{ion} is preserved, which means that the eigenstates can still be organized into three Kramers pairs. In analogy with Eq. (2.45), we define

$$\begin{aligned} A_\sigma &= 2\sigma (\sin \varphi d_{0,-\sigma} - \cos \varphi d_{-2\sigma,\sigma}), \\ B_\sigma &= \cos \varphi d_{0,-\sigma} + \sin \varphi d_{-2\sigma,\sigma}, \\ C_\sigma &= d_{2\sigma,\sigma}, \end{aligned} \quad (\text{G.2})$$

in which the angle φ is defined by

$$\tan(2\varphi) = \frac{2\sqrt{2}\lambda}{\lambda + 2\delta}. \quad (\text{G.3})$$

In general, we write the RIXS scattering operators like

$$\begin{aligned} \hat{\mathcal{O}}^{L_\mu} &= U a_{\mu,U} \tau^z + Q_2 a_{\mu,Q_2} \tau^x + Q_3 a_{\mu,Q_3} \tau^z \\ &+ \sum_{a=x,y,z} T_a a_{\mu,T_a} s^a \tau^y \\ &+ \sum_{a=x,y,z} P_a (a_{\mu,P_a} s^a + b_{\mu,P_a} s^a \tau^x + c_{\mu,P_a} s^a \tau^z), \end{aligned} \quad (\text{G.4})$$

where $\mu = 2, 3$ for the $L_{2,3}$ edge, the polarization factors given by Eq. (5.36) and the coefficients a_μ are functions of the angle parameter φ in Eq. (G.3). These coefficients are listed in Table 6 that also highlight the coefficients in the cubic limit, which were expressed in Eqs. (5.40) and (5.42).

Table 6 – Coefficients of the scattering operators in Eq. G.4 as a function of the angle parameter φ . The columns with the cubic limit values are obtained by taking $\varphi = \arcsin(1/\sqrt{3})$.

	L_3 edge	Cubic	L_2 edge	Cubic
$a_{\mu,U}$	$\frac{1}{9} (\cos^2 \varphi - \sqrt{2} \sin 2\varphi + 3 \sin^2 \varphi - 1)$	0	$\frac{1}{9} (\cos^2 \varphi + \sqrt{2} \sin 2\varphi - 2)$	0
a_{μ,Q_2}	$\frac{\sqrt{3}}{18} (\cos^2 \varphi - \sqrt{2} \sin 2\varphi + 2 - 6 \sin^2 \varphi)$	0	$\frac{\sqrt{3}}{18} (\cos^2 \varphi + \sqrt{2} \sin 2\varphi + 4)$	$\frac{\sqrt{3}}{3}$
a_{μ,Q_3}	$2\sqrt{2} (\cos \varphi - \sqrt{2} \sin \varphi)$	0	$2 (\sqrt{2} \cos \varphi + \sin \varphi)$	$\frac{\sqrt{3}}{3}$
a_{μ,T_x}	$-\frac{2\sqrt{2}}{3} (\cos \varphi - \sqrt{2} \sin \varphi)$	0	$-\frac{4}{3} (\sqrt{2} \cos \varphi + \sin \varphi)$	$-\frac{4\sqrt{3}}{3}$
a_{μ,T_y}	$-\frac{2\sqrt{2}}{3} (\cos \varphi - \sqrt{2} \sin \varphi)$	0	$-\frac{4}{3} (\sqrt{2} \cos \varphi + \sin \varphi)$	$-\frac{4\sqrt{3}}{3}$
a_{μ,T_z}	$\frac{4\sqrt{2}}{3} (\cos \varphi - \sqrt{2} \sin \varphi)$	0	$-\frac{4}{3} (\sqrt{2} \cos \varphi + \sin \varphi)$	$-\frac{4\sqrt{3}}{3}$
a_{μ,P_x}	$\frac{1}{3} \left(2 + \frac{3\sqrt{2}}{2} \sin 2\varphi \right)$	$\frac{4}{3}$	$-\frac{2}{3}$	$-\frac{2}{3}$
a_{μ,P_y}	$\frac{1}{3} \left(2 + \frac{3\sqrt{2}}{2} \sin 2\varphi \right)$	$\frac{4}{3}$	$-\frac{2}{3}$	$-\frac{2}{3}$
a_{μ,P_z}	$\frac{1}{3} (4 \cos^2 \varphi + \sqrt{2} \sin 2\varphi)$	$\frac{4}{3}$	$-\frac{1}{3} (\cos^2 \varphi + \sqrt{2} \sin 2\varphi)$	$-\frac{2}{3}$
b_{μ,P_x}	$\frac{2\sqrt{2}}{3} (\cos \varphi - \sqrt{2} \sin \varphi)$	0	$\frac{4}{3} (\sqrt{2} \cos \varphi + \sin \varphi)$	$\frac{4\sqrt{3}}{3}$
b_{μ,P_y}	$-\frac{2\sqrt{2}}{3} (\cos \varphi - \sqrt{2} \sin \varphi)$	0	$-\frac{4}{3} (\sqrt{2} \cos \varphi + \sin \varphi)$	$-\frac{4\sqrt{3}}{3}$
b_{μ,P_z}	0	0	0	0
c_{μ,P_x}	$\frac{1}{3} (4 - 3\sqrt{2} \sin 2\varphi)$	0	$-\frac{4}{3}$	$-\frac{4}{3}$
c_{μ,P_y}	$\frac{1}{3} (4 - 3\sqrt{2} \sin 2\varphi)$	0	$-\frac{4}{3}$	$-\frac{4}{3}$
c_{μ,P_z}	$-\frac{2}{3} (\sqrt{2} \sin 2\varphi - 4 \sin^2 \varphi)$	0	$\frac{1}{3} (5 + \cos 2\varphi + 2\sqrt{2} \sin 2\varphi)$	$\frac{8}{3}$

Source: NATORI; DAGHOFER; PEREIRA (1)